

Exploring antiferromagnetic domain wall mechanics through scanning nitrogen vacancy magnetometry

Inauguraldissertation

zur
Erlangung der Würde eines Doktors der Philosophie
vorgelegt der
Philosophisch-Naturwissenschaftlichen Fakultät
der Universität Basel

von

NATASCHA HEDRICH

2021

Originaldokument gespeichert auf dem Dokumentenserver der Universität Basel
<https://edoc.unibas.ch>



This work is licensed under a Creative Commons
Attribution-NonCommercial-NoDerivatives 4.0 International License.

The complete text may be reviewed here:
<http://creativecommons.org/licenses/by-nc-nd/4.0/>

Genehmigt von der Philosophisch-Naturwissenschaftlichen Fakultät
auf Antrag von
Prof. Dr. Patrick Maletinsky
Prof. Dr. Martino Poggio
Prof. Dr. Toeno van der Sar

Basel, den 25.05.2021

Prof. Dr. Marcel Mayor
Dekan

“... was ist das?”

“Das ist, äh, eine Doktorarbeit.”

“Eine Doktorarbeit? ... Jetzt bin ich aber erleichtert. Ich dachte schon, es sei eine schreckliche Krankheit.”

“Das ist eine Doktorarbeit gewissermaßen auch.”

Rumo & die Wunder im Dunkeln, Walter Moers

Abstract

As computing requirements and data volumes continue to increase, the need for faster, more efficient memories has become a driving force in many research areas. One proposed alternative to current ferromagnetic (FM) storage technology is antiferromagnetic (AFM) memories, which promise faster, more energy-efficient switching and higher bit densities. Developing such technologies requires progress on two fronts. On the one hand, we must understand and harness the AFM magnetic textures central to the proposed memory devices. At the same time, we require technologies capable of addressing these typically hard-to-access systems. In this thesis, we use magnetometry based on the nitrogen vacancy (NV) center in diamond to address both sides of this problem.

NV magnetometry, in particular scanning magnetometry, can be employed in a variety of environmental conditions, providing access to a wide range of materials and phenomena. Furthermore, the high magnetic field sensitivity and spatial resolution achievable with this technique enable us to address the nanoscale magnetic textures of interest. However, sensitivity and resolution are limited by our ability to collect the NV center photoluminescence (PL) and by how close we can bring the NV to the magnetic field source, respectively. Here, we aim to improve on the state-of-the-art scanning NV magnetometry probe with a novel design based on a truncated parabolic pillar. The parabolic nature of the pillar leads to excellent directional emission of the PL, allowing us to demonstrate median PL rates of 2.1 MHz and collection efficiencies of 57%. As such, we realize improved sensitivities compared to the state-of-the-art scanning probes while simultaneously achieving nanoscale resolution through the truncated end facet of the pillar.

We then use these improved scanning probes to study the magnetic properties of a magnetoelectric AFM – chromia (Cr_2O_3). Due to its room-temperature AFM ordering and the ability to switch the magnetic order with electric fields, this material is a popular candidate for spintronics applications. In our study, we demonstrate control over the magnetic orientation of a bulk Cr_2O_3 crystal and employ its magnetoelectric properties to nucleate domain walls (DWs). Using NV magnetometry, we characterize the surface magnetization of Cr_2O_3 and investigate the DW structure. We furthermore demonstrate an interaction between the DW and patterned surface topography, allowing us to develop a model of the DW mechanics. In particular, we observe a Snell’s law-like behavior of the DW in the presence of topographical steps and pinning of the DW to the edges of these steps. We use this pinning, together with local heating of the Cr_2O_3 crystal, to exert control over the motion of the DW.

These results bring us one step closer to achieving AFM-based memories. Having shown the ability to generate, control, and move DWs in an AFM crystal, we have laid the groundwork for a DW-based memory. Moreover, by improving the understanding of antiferromagnetic DW mechanics, we highlight material properties of Cr_2O_3 that may benefit and guide future material research.

Contents

Title	a
Abstract	e
Contents	g
List of symbols and abbreviations	k
1. Introduction	1
2. Fundamentals of NV magnetometry	5
2.1. The NV center in diamond	5
2.1.1. Spin states of the NV center	7
2.1.2. Charge states of the NV center	8
2.1.3. Additional properties of the NV center	10
2.2. Magnetometry with the NV center	11
2.2.1. Measuring the magnetic field	11
2.2.2. ODMR variations	13
2.2.3. Sensitivity	15
2.2.4. Spatial resolution	16
2.3. Conclusions	18
3. Truncated parabolic scanning probes for magnetometry	19
3.1. Parabolic reflector concept	21
3.1.1. Geometric optics picture	21
3.1.2. Simulating devices	22
3.1.3. Fabrication	26
3.2. Characterization	28
3.2.1. Saturation behavior of single NV centers	29
3.2.2. The excited state lifetime	30
3.2.3. The charge state	32
3.2.4. Collection efficiency	33
3.2.5. Angular emission	35
3.3. Applications to magnetometry	37
3.3.1. Sensitivity	37
3.3.2. Resolution	39
3.4. Conclusions and Outlook	42
3.4.1. Outlook	42

4. Mechanics of antiferromagnetic domain walls in Chromia	45
4.1. Magnetism of Chromia	46
4.1.1. Introduction to Magnetic Order	46
4.1.2. Magnetoelectricity	48
4.1.3. Chromia	49
4.1.4. Surface magnetization	51
4.1.5. Measuring the surface magnetization	53
4.2. Domain walls in Chromia	57
4.2.1. Introduction to domain walls	57
4.2.2. Magnetoelectric annealing	59
4.2.3. Nanoscale analysis of the domain wall	62
4.3. The mechanics of DWs	64
4.3.1. Domain wall refraction at topographic features	65
4.3.2. Elasticity of the DW	70
4.3.3. Domain Wall Dragging	73
4.4. Thin Films	76
4.4.1. Raising the Néel Temperature	77
4.5. Outlook and Conclusions	80
4.5.1. Summary	83
5. Summary and outlook	85
5.1. Summary	85
5.2. Outlook	87
A. Appendix	91
A.1. Fabrication	91
A.1.1. Diamond fabrication	91
A.1.2. Chromia fabrication	94
A.2. Setup details	96
A.2.1. Characterization setup	96
A.2.2. Room-temperature NV magnetometry setup	97
A.2.3. Temperature calibration	99
A.3. Poissonian analysis of NV number	102
A.4. Approach curves	103
A.5. Domain wall theory	105
A.5.1. Angular Profile Derivation	105
A.5.2. Domain Wall Stray Field	106
A.6. Metropolis-Hastings algorithm	109
A.7. Error Analysis	111
B. Additional Measurements	113
B.1. Artificial Spin ice	113
B.1.1. Introduction	114
B.1.2. The Samples	117
B.1.3. DC magnetometry	118
B.1.4. AC magnetometry	121
B.1.5. Conclusions	124

B.2. Skyrmions	126
B.2.1. Introduction	126
B.2.2. Imaging skyrmions	128
B.2.3. Conclusions	130
C. Bibliography	131
Acknowledgments	151
Curriculum Vitae	153

List of symbols and abbreviations

General symbols

T	Temperature
τ	Evolution time
\mathcal{T}	Measurement time
$[001]$	Crystal vector
(001)	Crystal plane
\mathbf{n}_s	Surface normal
ν	Frequency
f	Focal length
n	Index of refraction
$\bar{\square} \left(\widetilde{\square} \right)$	Mean (Median)

NV center

θ_{NV}	Polar angle of NV axis
ϕ_{NV}	Azimuthal angle of NV axis
d_{NV}	Distance between NV and source
$\hat{\mathbf{S}}, \hat{S}_x, \hat{S}_y, \hat{S}_z$	Spin operator and components
\mathbf{S}	Spin vector
$B_{\parallel}/B_{\text{NV}}$	Magnetic field (along NV axis)
B_{\perp}	Magnetic field (perpendicular to NV axis)
D_0	Zero-field splitting
Δ_Z	Zeeman splitting
T_1	Spin relaxation time
T_2^*	Spin dephasing time
T_2	Spin coherence time
t_e	Excited state lifetime
Γ_e	Excited state decay rate
Γ_e^r (Γ_e^{nr})	(Non)radiative decay rate
γ_{-0} (γ_{0-})	Ionization (Recombination) rate
Γ_{-} (Γ_0)	NV ⁻ (NV ⁰) PL rate
Γ_{NV}	Measured PL rate
Γ_{sat}	Saturation PL rate
Γ_{bg}	Background PL rate

\mathcal{I}_{na}	Simulated power collected at objective
\mathcal{I}_{wg}	Simulated power at waveguide
\mathcal{I}_{bd}	Simulated power of dipole in bulk diamond
\mathcal{I}	Simulated power of dipole in pillar
$\mathcal{I}^s(\mathcal{I}^p)$	$s-$ ($p-$) polarized component of \mathcal{I}
P	Optical power
P_{sat}	Saturation power
s	P/P_{sat}
ϵ	Detection probability
ϵ_{setup}	Optical path efficiency
ϵ_{dev}	Collection efficiency
η_B	Magnetic field sensitivity
\mathcal{S}	Magnetic field-sensitive signal

Material Properties

\mathbf{B}	Magnetic flux density (Magnetic field)
\mathbf{H}	Magnetic flux intensity
\mathbf{E}	Electric field
\mathbf{D}	Displacement field
\mathbf{F}	Free energy
\mathbf{m}	Magnetic moment
$\boldsymbol{\mu}$	Magnetic moment unit vector
\mathbf{M}	Magnetization
σ_m	Surface magnetization
\mathbf{L}	Néel vector
\mathbf{P}	Polarization
χ	Susceptibility
\mathcal{H}_{an}	Anisotropy Hamiltonian
\mathcal{H}_{ex}	Exchange Hamiltonian
\mathcal{H}_{di}	Dipole Hamiltonian
\mathcal{K}	Anisotropy constant (lattice)
K	Anisotropy constant (micromagnetics)
\mathcal{J}	Exchange parameter (lattice)
A	Exchange stiffness (micromagnetics)
\mathbf{D}_{12}	DMI vector
\mathcal{E}	Energy
a, b, c	Crystal axes
$w(t)$	Width (Thickness) of a structure

t_m	Thickness of magnetic layer
ξ	DW surface
ϕ_{DW}	Azimuthal DW angle
ℓ_m	Magnetic length
ρ	Tension coefficient
$T_{\text{Néel}}$	Néel temperature
$\theta_1(\theta_2)$	DW angle in bulk (on mesa) relative to mesa
k, k_0, k_1	Slope of DW in bulk/ at bulk surface/ on mesa surface

Analytics

\mathcal{P}	Probability
P_{Pois}	Poissonian distribution
\mathcal{D}	Propagator

Constants

$g_e = 2.0028$	Electronic g -factor
$\gamma_{\text{NV}} = 2.80 \text{ MHz/G}$	Gyromagnetic ratio of NV spin
$h = 6.626 \cdot 10^{-34} \text{ m}^2 \text{ kg/s}$	Planck's constant
$\hbar = 1.055 \cdot 10^{-34} \text{ m}^2 \text{ kg/s}$	Reduced Planck's constant
$k_B = 1.381 \cdot 10^{-23} \text{ J/K}$	Boltzmann constant
$\mu_B = 9.274 \cdot 10^{-24} \text{ J/T}$	Bohr magneton
$\mu_0 = 4\pi \cdot 10^{-7} \text{ N/A}^2$	Vacuum permeability

Abbreviations

AFM	Antiferromagnet(ic)
ASI	Artificial spin ice
BFP	Back focal plane
CW	Continuous wave
DMI	Dzyaloshinskii-Moria interaction
DW	Domain wall
FM	Ferromagnet(ic)
ICP/RIE	Inductively coupled plasma/ Reactive ion etch
MFM	Magnetic force microscopy
MSE	Mean square error
MW	Microwave
NA	Numerical aperture
NV	Nitrogen Vacancy
NV ⁻	Negatively charged NV center

NV ⁰	Neutral NV center
ODMR	Optically detected magnetic resonance
PL	Photoluminescence
PEEM XMCD	Photoemission electron microscopy - X-ray magnetic circular dichroism
PM	Paramagnet(ic)
SOC	Spin-orbit coupling
SQUID	Superconducting quantum interference device
TIR	Total internal reflection
TPSP	Truncated parabolic scanning pillar
WF	Write field
ZFS	Zero field splitting
ZPL	Zero-phonon line

1. Introduction

From phones and watches to fridges and traffic lights, smart devices have become a fundamental part of daily life. Though the scale of the computers that form the foundation of this “smart” revolution has drastically changed since the earliest realizations, they are still based on the same principles. They rely on controlling the flow of electronic charges through series of transistors, capacitors, and integrated circuits. While the progress in electronics has enabled us to perform operations, store and access information at very high rates, such systems tend to be highly volatile. Once the power is turned off, that information is gone. For this reason, non-volatile data storage methods are crucial to modern computing. However, as we near physical limits on data density and computation speeds, the need for alternative technologies will continue to grow.

One source of such alternatives is the field of study known as spin electronics or spintronics. Here, the goal is to harness the electronic spin in magnetic systems as an alternative or complementary degree of freedom to the electron charge [1, 2]. A classic example of harnessing magnetic systems for data storage is ferromagnetic (FM) memories as found in hard drives. These memories rely on the reading and writing of information to and from nanoscale domains in a magnetic material. In the '90s, spintronics found great commercial success through the development of spin valves, which use the giant magnetoresistive effect to read out magnetic bits [3]. The discovery of other techniques for manipulating spins, including spin-transfer torque [4] or spin-orbit torque [5], has continued to push the development of new memory technologies due to the promise of low energy consumption, fast switching times, and non-volatility. Devices based on magnetic textures such as domain walls (DWs) or skyrmions have also been suggested as alternate forms of magnetic memories. These devices could eliminate the need for a moving read/write head and enable higher bit densities [6–8]. Such magnetic textures have also been proposed in new, non-volatile logic elements [9, 10].

Critical to the development of spintronic technologies is the identification, fabrication, and characterization of new magnetic materials. Historically, FMs have been used due to the ease with which one can read and write magnetic regions. Unfortunately, switching of magnetic domains in such materials is typically limited to GHz speeds [11] and their susceptibility to magnetic fields makes the stored data vulnerable to strong external fields.

Therefore, a promising development in spintronics has been to move away from traditional FM materials to antiferromagnetic (AFM) materials. Antiferromagnets lack an overall magnetic moment and are therefore robust against external magnetic fields [12]. Additionally, the observation of THz switching and spin excitation has proven very attractive [13, 14]. However, due to their robustness against magnetic fields, controlling the magnetic order of AFMs with such fields is typically difficult.

For this reason, the ability to control the magnetic state of the material through the application of electric fields rather than currents is a particularly appealing quality as it could significantly reduce the energy cost of manipulating the material state [15]. Electric field switching is achievable, for example, using multiferroic materials, which exhibit simultaneous magnetic, electric, or elastic orderings, or in magnetoelectric materials, which exhibit coupled magnetic and electric properties. One material, which has shown much promise in this direction is chromia or Cr_2O_3 , an insulating magnetoelectric crystal. Recent demonstrations of electric field-based reading and switching of the magnetic order in Cr_2O_3 highlight its potential for future spintronic technologies [16–18].

To guide future application directions and discover new functionalities, an understanding of the underlying physics and magnetic ordering in materials such as Cr_2O_3 is paramount. To achieve this, we require techniques to image and study the magnetic ordering and textures in a diverse range of systems. However, the fundamentally nanoscale range of such magnetic textures and the high-frequency nature of their dynamics place rather strict requirements on the methods used to investigate them. One of the most common techniques is magnetic force microscopy (MFM). Here, the signal arises from the interaction between a magnetic tip and the stray magnetic field, allowing for very high spatial resolution [19]. Similarly, magnetometry based on superconducting quantum interference devices (SQUIDs) relies on measuring the magnetic flux and shows incredible sensitivities [20]. Photoemission electron microscopy based on X-ray magnetic circular dichroism (XMCD-PEEM), on the other hand, measures the interaction between X-ray polarization and the magnetic orientation of a crystal, providing very high temporal resolution in a pump-probe configuration [21]. In recent years, another technique that has proven very successful for imaging nanoscale spin textures such as skyrmions [22, 23] and DWs in FMs [24] but also domain structures in AFM multiferroics [25, 26] is magnetometry based on the nitrogen vacancy (NV) defect in diamond.

The NV center is an atomic diamond defect, which due to its electronic spin state, exhibits excellent sensitivity to stray magnetic fields. Such stray fields may arise from magnetic spin textures or even from a single atomic layer of magnetic moments. One of the enabling factors here is the long spin coherence time, which may be used to detect not only static (DC) but also oscillating (AC) signals in a wide range of materials [27]. Furthermore, in scanning NV magnetometry, where the NV is placed at the apex of a diamond pillar probe, real-space imaging of magnetic systems may be performed with nanoscale resolution [28–30]. The high sensitivity and nanoscale resolution are two significant advantages of this technique, but it also benefits from impressive stability over a wide range of temperatures [31]. This versatility of NV magnetometry and its ability to measure magnetic textures in real space makes this a powerful technique and allows us to address typically difficult-to-image materials and magnetic textures.

Scope of this thesis

Over the course of this thesis, we aim to show how NV magnetometry may be used to develop a better understanding of the magnetic properties of Cr_2O_3 through imaging and characterization of the mechanics of DWs. In doing so, we hope to open up a path to novel AFM memory devices. In the process, we will also address the issue of improving the performance of NV magnetometry through diamond fabrication.

We begin in Chap. 2, by introducing the underlying principles of NV magnetometry, starting with the structure of the NV center and its spin energy levels. From here, we see how to achieve all-optical spin initialization and readout. We then discuss the NV center charge state, which forms an often overlooked source of background for the readout process. Following this, we dive into a description of NV magnetometry. Specifically, we discuss the magnetic field dependence of the NV spin states and how to determine the local stray field through optically detected magnetic resonance imaging. We conclude this section with a theoretical discussion of the primary driving factors of this technique: the magnetic field sensitivity and spatial resolution.

We will see that the spatial resolution is determined by how close the NV can be brought to the source of the magnetic fields, while the sensitivity is strongly influenced by our ability to collect the NV photon emission. Unfortunately, the latter of these two points is hindered by reflection from the diamond surface due to the high index of refraction of diamond. For this reason, in Chap. 3, we explore how both of these aspects can be addressed by engineering the diamond environment. Specifically, we present a novel form of scanning diamond probe, whose parabolic tip shape leads to excellent waveguiding of the NV emission and high collection efficiencies. To quantify this, we first present simulations of our devices. We then motivate the design and highlight the improved collection efficiency and angular emission compared to traditional cylindrical scanning probes. We also briefly examine the fabrication techniques used to create these structures before moving into a detailed characterization of our devices. We conclude by again returning to a discussion of the sensitivity and spatial resolution achieved through these structures.

Finally, we turn to the ultimate goal of this thesis, a study of DW mechanics in Cr_2O_3 . In Chap. 4, we first give a theoretical introduction into the typical energies involved in magnetic systems as well as the origins of the magnetoelectric effect. We then focus on the physical and magnetic structure of Cr_2O_3 in more detail, including a description of the surface magnetization, an important source of stray magnetic fields. We then use scanning NV magnetometry to characterize the magnitude and temperature dependence of this surface moment. Following this introduction, we move to a description of DWs. We demonstrate the ability to nucleate these DWs in a bulk Cr_2O_3 single crystal using a method known as magnetoelectric annealing. We then attempt to use NV magnetometry to extract both the DW type and width. Quantitative stray field images of the DWs obtained through NV magnetometry allow us to analyze the behavior of the DW as it interacts with raised structures patterned on the Cr_2O_3 surface. We observe both pinning and a Snell's law-like deflection of the DW, which we proceed to explain through simulations and analytic calculations using energy minimization arguments. Combining the pinning we have observed with local heating from a focused laser, we also demonstrate control over the DW position in the crystal – an essential step for realizing novel AFM memories. Finally, we shift to

a discussion of recent results focusing on raising the critical temperature of thin-film Cr_2O_3 . We finish by bringing together the results of this chapter into a proposal of a new form of DW-based magnetic memory and explore possible future directions for Cr_2O_3 studies.

In Chap. 5, we conclude our discussion. We present a summary of the critical results and look towards the future. For instance, we explore necessary improvements to the scanning setup that will allow us to expand the functionality of scanning NV magnetometry. We also present several potentially exciting research directions, focusing on further AFM systems that promise to yield exciting physics.

2. Fundamentals of NV magnetometry

As the miniaturization of technology is pushed to its physical limits, sensing and imaging of magnetic fields (magnetometry) at the nanoscale have become essential tools. In spintronics, nanoscale magnetic textures such as skyrmions [2, 8, 23] and domain walls (DWs) [6, 32] may be used to encode digital information; in biology, sensing of minute magnetic fields from bacteria can help us learn more about cellular processes [33]. These are just two cases in a wide range of magnetometry applications spanning all of the natural sciences. What unites these applications are two universal requirements: high sensitivity and high spatial resolution. One method to achieve both of these points is sensing with the nitrogen vacancy (NV) center.

Though diamonds have been recognized for their hardness, purity, and optical properties for thousands of years, the realization that their defects could be used as a powerful technological tool is much more recent. Since their initial characterization in the 1970s [34], NV centers have become extremely popular. Many of the properties that have made diamond so attractive, such as its biocompatibility and wideband optical transparency, also make the NV a promising platform for sensing magnetic fields [27, 31, 35], electric fields [36, 37], strain [38, 39] and temperature [40, 41] in a wide range of materials and even in biological systems [42, 43].

To see how we can achieve high sensitivity and high-resolution imaging of anti-ferromagnetic systems, we will spend this chapter investigating the NV's properties, focusing on magnetic field sensing at room temperature. We will begin by examining the NV spin and charge states before moving into an introduction of NV magnetometry. Our goal is to build up the theoretical building blocks used later in this thesis when we explore NV centers in fabricated diamond structures and their ability to image DW mechanics in an antiferromagnetic (AFM) crystal.

2.1. The NV center in diamond

In an ideal diamond, carbon will form a diamond-cubic structure, with each carbon atom being connected to four others, resulting in rigid tetrahedral sub-structures. However, one may introduce defects into this lattice, for example, by removing or replacing one of these carbon atoms. In particular, when one carbon atom is replaced by a nitrogen atom and one of its neighboring carbon atoms is missing leaving behind a “vacancy”, the resulting combined defect is known as the NV center.

Such defects may occur naturally in diamond due to remaining atmospheric nitrogen during the growth process but can also be controllably generated. Recently, the generation of NV centers based on the natural nitrogen content in diamond has been achieved through high-power lasers [44, 45]. The most common method though, involves bombarding the diamond with nitrogen ions [46, 47] and subsequently annealing the diamond. In this way, the vacancies generated through the bombardment

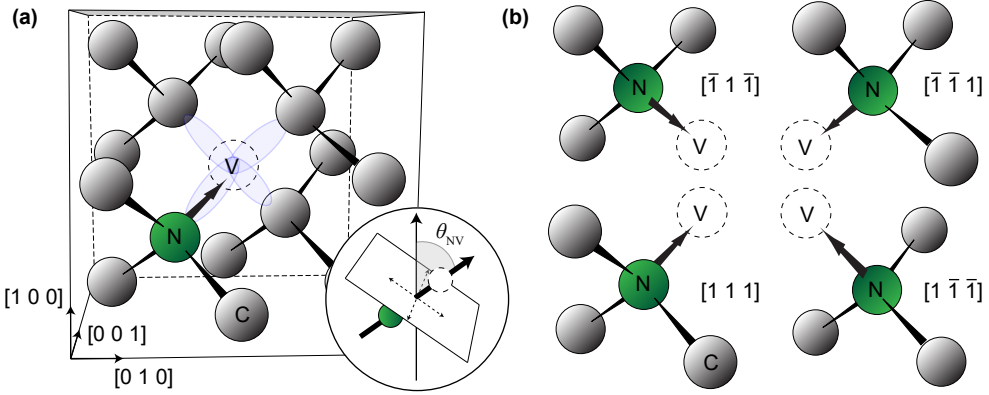


Figure 2.1.: The structure of the NV center. (a) The diamond lattice, hosting a single substitutional nitrogen atom (green) next to a vacancy (dashed line). Dangling bonds (light blue) from the nitrogen and nearby carbons (gray) contribute electrons to the NV state. Here, the (100) diamond surface is colored in gray. The NV axis (thick arrow) is shown in the circular inset, forming an angle $\theta_{\text{NV}} = 54.7^\circ$ with the $[100]$ axis. Additionally, we show the NV center optical dipoles (dotted lines) in the plane perpendicular to the NV axis. (b) Four possible orientations of the NV, with the NV axis shown as an arrow and labeled with the corresponding crystallographic description.

migrate, forming NV centers with the implanted nitrogen [48]. The resulting point-like defect is shown in Fig. 2.1a.

Here, the line connecting the substitutional nitrogen and the vacancy forms a natural symmetry axis, referred to as the NV axis. This axis can have one of four orientations in the lattice, given by the $[111]$, $[\bar{1},1,\bar{1}]$, $[1,\bar{1},\bar{1}]$ and $[\bar{1},\bar{1},1]$ axes [49], as shown in Fig. 2.1b. From here on in, we will assume a $[100]$ -oriented diamond surface. In this case, the top diamond surface, shown in gray in Fig. 2.1a, corresponds to the (100) plane. This orientation leads to a polar angle $\theta_{\text{NV}} = 57.4^\circ$ between the $[100]$ crystal axis and the NV axis [50], as shown in the inset of Fig. 2.1a.

Due to the missing atom at the vacancy site, dangling bonds from the nearby carbon atoms result in three unpaired electrons. The nitrogen supplies five more electrons, three of which are covalently bonded to the nearby carbons, while the remaining two will occupy the orbital states formed by the dangling bonds. This five-electron state constitutes what is known as the neutral, or NV^0 charge state. However, more commonly, one additional electron will be drawn in from the surrounding environment, giving rise to the negative, or NV^- charge state. We will explore the difference between these two charge states of the NV center in more detail in Sec. 2.1.2, but for the time being, when we refer to the NV center, we will be restricting ourselves to the negative charge state.

2.1.1. Spin states of the NV center

Calculations of the energy levels of the NV center based on the six-electron configuration [51, 52] reveal an $S=1$ spin triplet ground and excited state. Both states may be characterized by the spin eigenstates $|m_s\rangle$ of the \hat{S}_z operator with respect to the NV axis, such that $\hat{S}_z|m_s\rangle = \hbar m_s|m_s\rangle$, where $m_s = 0, \pm 1$. At room temperature, the $|0\rangle$ and $|\pm 1\rangle$ spin ground states are split in energy by spin-spin interactions, leading to a zero-field splitting (ZFS) of $D_0 = 2.87$ GHz, as shown in Fig. 2.2. The magnetic dipole transitions between the $|0\rangle$ and $|\pm 1\rangle$ states may therefore be driven by an external microwave (MW) frequency field. Excitation between the orbital ground and excited states, on the other hand, is achieved via a spin-preserving optical transition. While the NV may be excited resonantly at 637 nm, we typically use an off-resonant, 532 nm continuous wave (CW) laser to drive the optical transition for all three spin states.

Let us now use the energy level diagram in Fig. 2.2 to discuss one of the most important characteristics of the NV center, namely the ability to optically initialize and read out the NV spin states. To understand this, we require one additional point: the metastable singlet state of the NV center [53], shown to the right in Fig. 2.2. While the $|0\rangle$ state decays primarily radiatively (red, wavy arrows) with only weak non-radiative decay (gray, dashed arrows) to the singlet state, the $|\pm 1\rangle$ states have an over 50% probability for non-radiative decay. In Fig. 2.2, we denote the strength of the non-radiative decay channels by the gray scale of the dashed arrows.

As the singlet state has a significantly longer lifetime (~ 150 ns [54]) than the $|\pm 1\rangle$ and $|0\rangle$ excited states (~ 7 ns and ~ 13 ns respectively in bulk diamond [55]), a significant portion of the $|\pm 1\rangle$ population will be shelved into this metastable state. During this shelving period, the $|0\rangle$ state will undergo multiple cycles of optical excitation and radiative decay. This process will therefore lead to a contrast in photoluminescence (PL) between the $|0\rangle$ (bright) and $|\pm 1\rangle$

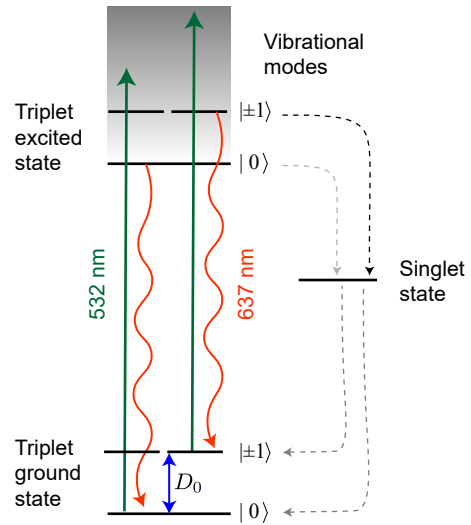


Figure 2.2.: Electronic state of the NV^- . Energy levels of the NV, highlighting the triplet ground and excited state and the metastable singlet state. Here, we show the $|0\rangle$ and $|\pm 1\rangle$ states, separated by the ZFS, D_0 . Non-resonant excitation by a 532 nm laser is shown with solid, green arrows, and MW driving of the spin states is shown in blue. (Non-) Radiative decays are shown as (dashed) solid arrows. The non-radiative decay channel strength is shown with the intensity of the line, emphasizing the non-spin-conserving nature of decay via the singlet state.

(dark) states of up to 30% [56]. In this way, we can differentiate between the spin states using only optical detection methods. Furthermore, as the decay from the singlet state is not spin-conserving [53], we will begin to transfer population from the $|\pm 1\rangle$ states into the $|0\rangle$ state. This process allows us to initialize the NV center optically. Together with the MW driving of the spin states, we are able to manipulate, readout, and initialize the spin state of the NV center.

2.1.2. Charge states of the NV center

While we will continue to focus on the negative charge state of the NV center throughout this thesis, it is important to reiterate that this is not the only available charge state. Though often neglected in discussions of NV magnetometry, the charge state has been used as a successful alternative method for reading out the spin state of the NV center [57]. Unfortunately, PL emission from the NV^0 state also forms a fluorescence background signal for our readout technique. As such, understanding where this background comes from will also help us to overcome it.

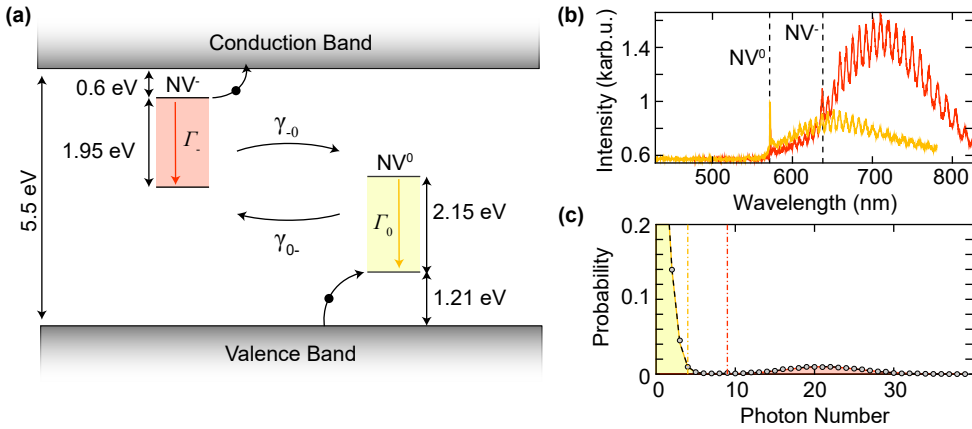


Figure 2.3.: The NV charge state. (a) Simplified energy levels of the NV^- (red) and NV^0 (yellow) and their energetic position within the diamond bandgap. Two-photon processes can lead to ionization of the NV^- or recombination with the NV^0 , at a rate γ_{-0} and γ_{0-} respectively, as shown with black arrows. The radiative decay rates of the two NV charge states are given by Γ_- and Γ_0 . (b) Emission spectra of a single NV center in a diamond pillar. The emission is measured with a spectrometer (HRS-500-S, Princeton Instruments) while exciting the NV center with a CW 532 nm laser. Here, the NV center undergoes a change in charge state, from being primarily NV^- (red) to predominantly NV^0 (yellow). The ZPLs of the two charge states are shown with black, dashed lines and labeled accordingly. Oscillations in the emission spectrum arise from the cavity formed in the diamond pillar. (c) Charge state measurement showing a histogram of the detected number of photons. The NV^0 (yellow) and NV^- (red) distributions are fit according to Ref. [57], as shown with a dashed black line. The dot-dashed yellow and red lines show the resulting thresholds needed to distinguish the two charge states.

Figure 2.3a, shows the simplified NV^- and NV^0 energy diagrams relative to the conduction and valence bands of diamond [58]. It is possible for the excited NV^- to absorb a second photon, thereby moving the excess electron (black circle) to the nearby conduction band as shown [59]. This process leaves the NV in the neutral charge state. Conversely, a similar two-photon process can excite an electron from the valence band, allowing it to combine with the NV^0 , forming the negative charge state. These two processes are commonly known as ionization and recombination. The rate at which these two processes occur is characterized by two light-intensity dependent rates, γ_{-0} and γ_{0-} respectively, which tend to be long compared to the lifetime of the NV^- excited states.

Despite the difference in their energy level diagrams [58], both NV^- and NV^0 show similar emission spectra, as shown in Fig. 2.3b. Here, we present the emission spectrum of a shallow NV center within a diamond pillar, excited with a CW 532 nm laser. Following a tri-acid clean [60], the NV center is found to be primarily NV^- (red) but becomes predominantly NV^0 (yellow) after some time. From these spectra, we can identify the broad phonon-mediated sideband of both charge states as well as their sharp zero phonon lines (ZPL) at 575 nm for the NV^0 and 637 nm for the NV^- [61]. Due to the significant overlap between the two spectra, it can be challenging to differentiate the PL of the two charge states. Unfortunately, the NV^0 does not show the same spin-state dependent PL as the NV^- . Therefore, without careful control [57], any time spent in the NV^0 state will reduce the NV^- spin readout contrast.

One way in which one can control the charge state fluctuations is to reduce the ionization rate. Whereas the NV^- and NV^0 PL rates (Γ_- and Γ_0 respectively) depend linearly on the excitation power below saturation, both γ_{-0} and γ_{0-} show a quadratic power dependence [59]. Therefore, working at low excitation powers can lead to higher charge stability. To reduce the NV^0 background, one can use the wavelength dependence of the two spectra in Fig. 2.3b. Specifically, we see that the NV^0 spectrum is shifted to slightly shorter wavelengths compared to the NV^- spectrum. While the broad, overlapping phonon sidebands prevent us from completely filtering out the NV^0 emission, one can use a long-pass filter to remove a large portion of the NV^0 PL while losing only a fraction of the NV^- PL.

The frequency shift between the NV^- and NV^0 spectra is also key to distinguishing the charge states. In particular, there is a small wavelength interval around 594 nm in which one can optically excite NV^- while only weakly exciting NV^0 . By driving the NV center with a laser within this wavelength range and using a long-pass filter, we can obtain a factor of 20 difference in the PL rate of the two charge states [57]. Specifically, we drive the NV with 0.49 μW of 594 nm CW excitation over 812.5 μs while simultaneously counting the detected photons. We see the result of such a measurement in Fig. 2.3c. Here, we have created a histogram of the number of measured photons over 100 000 repetitions. We observe two well-separated distributions which we associate with the NV^0 state (yellow) and NV^- state (red), where we see the clear difference in PL rate between the two charge states, from which we define thresholds on the expected number of counts when in a given charge state [57]. In this way, we can determine the charge state before and after a secondary measurement, allowing us to select those events in which the NV was in the negative charge state, thereby completely removing the NV^0 background. We will revisit this technique in the next chapter.

2.1.3. Additional properties of the NV center

In general, the optical initialization and readout of the NV center spin and charge state is an attractive property as it makes NV magnetometry a very accessible technique. The NV center brings with it several other advantages as well. For example, though our focus lies on room temperature magnetometry, we would be remiss not to mention the incredible temperature compatibility of the NV center. In particular, we are able to perform NV spin readout at temperatures below 100 mK [62] and exceeding 600 K [63]. At cryogenic temperatures, one also gains access to an orbital degree of freedom of the NV excited states, which at room temperature is inaccessible due to phonon-mediated orbital averaging [56, 64]. As strain and electric fields couple primarily to the orbital degree of freedom [65, 66], low temperatures can help us explore new aspects of the NV center. This broad temperature compatibility of the NV also presents a significant advantage over other sensing techniques such as SQUIDS, which only function at cryogenic temperatures [20].

Another advantage of the NV center is that it is non-invasive. As such, it is less likely to inadvertently influence the magnetic textures we wish to measure, as compared to other techniques such as MFM, which relies on a magnetized tip. We are assuming that we do not change the magnetic system through our optical or MW excitation of the NV, which is a reasonable assumption considering the typically low driving strengths used. NV magnetometry also benefits from the low toxicity of the diamond host. This makes diamond biocompatible and allows, for example, nanodiamonds to be inserted directly into living cells as a popular alternative to traditional fluorescence markers [67].

The final property that we wish to discuss here is the coherence time i.e., the time over which the quantum phase of the NV spin remains intact. Deep in the diamond bulk, the loss of coherence of the NV center is typically caused by the fluctuation of nearby ^{13}C spins, which appear naturally in diamond [68]. Near the diamond surface however, the emergence of additional spins and charges typically leads to much faster decoherence. Generally, the decoherence of the NV center is associated with three processes – spin relaxation, homogeneous spin dephasing, and inhomogeneous spin dephasing – with corresponding relaxation times commonly labeled T_1 , T_2 and T_2^* , respectively.

Each of these processes results from spin noise in the nearby surroundings of the NV center, but are differentiated by the frequency of the spin noise leading to the loss in coherence. While the T_2^* time-characterized processes are primarily sensitive to slow fluctuations exceeding the time of typical magnetometry measurements, the T_2 time-characterized processes are most sensitive to fluctuations on the order of $1/T_2$, typically in the 1-100 kHz range. These long coherence times are crucial in for example, quantum computing, where they have propelled the popularity of the NV as a quantum bit [69, 70]. Finally, T_1 time-characterized processes are associated with magnetic field noise resonant with the ground state spin transitions of the NV center i.e., at GHz frequencies. Bulk NV centers boast remarkably long spin relaxation times, exceeding seconds at cryogenic temperatures [71] and reaching μs even when approaching 1000 K [72].

While the loss of spin coherence may be unfavorable when trying to maintain a given spin superposition, it can also be a valuable detection tool. For example, the

changing coherence time in the presence of spin noise may be used to perform AC magnetometry with the NV center. Such spin noise may originate from spin waves for example [73], thereby allowing us to detect and image dynamics in magnetic systems.

2.2. Magnetometry with the NV center

We have now explored some of the properties that make the NV center such a versatile sensor. Among other accomplishments, NV magnetometry has aided in realizing magnetic field measurements under extreme conditions [74] and in answering long-standing questions in the magnetics community [75]. We now turn to a discussion of the basic principles of this technique.

2.2.1. Measuring the magnetic field

In discussing the energy level diagram of the NV center, we have always assumed the NV $|\pm 1\rangle$ states to be degenerate. However, in the presence of an external symmetry-breaking field, this will no longer be the case, a fact that will be key to using the NV as a sensor. Let us, therefore, consider the simplified Hamiltonian¹ of the NV ground state in the presence of a magnetic field, \mathbf{B} :

$$\hat{\mathcal{H}}/h = D_0 \hat{S}_z^2 + \gamma_{\text{NV}} \mathbf{B} \cdot \hat{\mathbf{S}}. \quad (2.1)$$

Here, $\hat{\mathbf{S}}$ is the spin operator vector of the electronic spin, and $\gamma_{\text{NV}} = 2.8 \text{ MHz/G}$ is the NV gyromagnetic ratio. We focus on three aspects of this Hamiltonian, namely the shift of the energy levels in the presence of a magnetic field parallel (B_{\parallel}) or perpendicular (B_{\perp}) to the NV axis, as well as temperature. We summarize these three cases in Fig. 2.4. In the left panel of Fig. 2.4a, we show the energy levels for the B_{\parallel} case, where the $|\pm 1\rangle$ states shift linearly with the field according to the Zeeman splitting, $\Delta_Z = 2\gamma_{\text{NV}} B_{\parallel}$, while the $|0\rangle$ state remains unchanged. In contrast, B_{\perp} will lead to a mixing of the electron spin states, resulting in a quadratic shift of D_0 with B_{\perp} , in addition to a small splitting as shown in the left panel of Fig. 2.4b. Finally, though not explicitly stated in the Hamiltonian, D_0 is temperature dependent, allowing us to use the NV as a thermometer [40, 76]. As shown in the left panel of Fig. 2.4c, the ZFS decreases with approximately $\frac{dD_0}{dT} = -72.4 \text{ kHz/K}$ near room temperature.

Though many techniques exist to measure these field and temperature-dependent shifts of the NV energy levels, perhaps the simplest is optically detected magnetic resonance (ODMR). Key here is the spin-dependent PL rate discussed earlier. This widely applicable technique has enabled the detection of many nanoscale magnetic phenomena, including spin spirals in AFMs [25], skyrmions [77], and even ferromagnetic DW hopping [24]. ODMR measurements rely on sweeping a MW driving frequency over the NV spin transition frequencies while recording the PL of the NV center. Under these conditions, due to the reduced PL rate of the $|\pm 1\rangle$ states, one will observe a dip in PL when the resonance condition between the $|0\rangle$ and $|\pm 1\rangle$ spin states is met.

¹Note that here, we have ignored any discussion of interactions with the nuclear spin, which leads to the hyperfine structure of the NV center. For a more detailed discussion of these effects, and the full NV Hamiltonian, see [65].

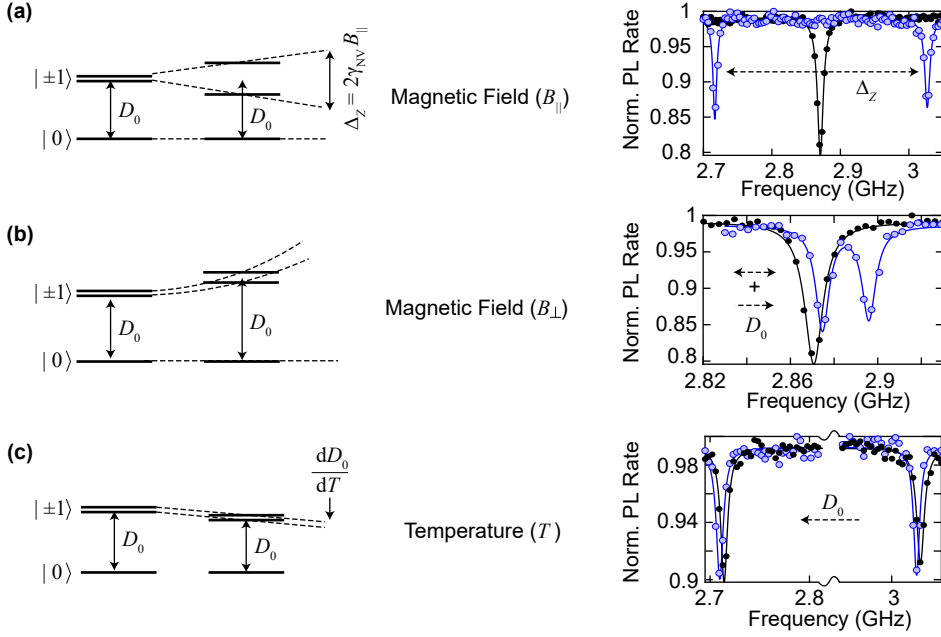


Figure 2.4.: Influence of external stimuli on the NV ground state. (a) Influence of an external, static magnetic field, applied along the NV axis, on the electronic ground state of the NV. (Left) The $|\pm 1\rangle$ states experience a Zeeman splitting, while D_0 remains unchanged. (Right) An example of an ODMR trace taken at zero applied field (black circles) and with a field of ~ 5.5 mT, applied parallel to the NV axis (blue, hollow circles). The ODMR trace shows the splitting of the $|\pm 1\rangle$ states. (b) Effect of a static magnetic field applied perpendicular to the NV axis. (Left) Schematic of the NV ground state levels, showing the resulting increase in D_0 and slight splitting of the $|\pm 1\rangle$ levels. (Right) Representative ODMR trace at zero applied field (black) and an external field of ~ 6 mT, applied perpendicular to the NV (blue). (c) Effect of temperature on the ground state of the NV center. (Left) The shift of the $|\pm 1\rangle$ energy levels due to the temperature dependence of D_0 . (Right) An ODMR trace taken at room temperature (black) and $\sim 66^\circ\text{C}$ (blue), showing the shift in D_0 .

We focus on CW ODMR in particular, where the NV is simultaneously driven with a CW 532 nm laser while sweeping the MW field. Such ODMR measurements are shown in the right panels of Fig. 2.4 for a range of different experimental conditions. In the absence of an external magnetic field, the degeneracy of the $|\pm 1\rangle$ states results in a single resonance at $D_0 = 2.87$ GHz, as shown in black in Figures 2.4a and b. However, upon applying a static field, we see two resonances emerge corresponding to the $|0\rangle \rightarrow |-1\rangle$ and $|0\rangle \rightarrow |+1\rangle$ transitions, as shown in blue. In the case of a field B_{\parallel} applied parallel to the NV axis, the resulting separation of the resonances will be the Zeeman splitting Δ_Z . By extracting Δ_Z , we can determine the magnetic field amplitude parallel to the NV axis. However, as we can not differentiate between a field parallel (positive splitting) or anti-parallel (negative splitting) to the NV axis, we often apply a small bias magnetic field. This bias allows us to extract the sign as

well as the amplitude of an unknown magnetic field.

In Fig. 2.4b, we show the case of a field B_{\perp} , applied perpendicular to the NV axis. We see a splitting in addition to the shift of D_0 towards higher frequencies, as discussed previously. Due to the quadratic dependence on B_{\perp} , for magnetic fields below several mT, these effects are much smaller than the linear splitting induced by a magnetic field parallel to the NV axis [31]. For this reason, B_{\perp} may often be neglected in the presence of weak stray fields. This procedure can also be extended to full vector magnetometry. By measuring the field with different NV orientations, one can directly extract each magnetic field component [78, 79]. Alternatively, from a 2D scan of a single magnetic field component e.g., B_{\parallel} , one can obtain the complete magnetic field vector at increasing distances from the magnetic origin [27, 80].

Finally, in Fig. 2.4c, we see the slight shift in D_0 towards smaller frequencies, indicating an increase in temperature. As this shift is on the order of kHz while the width of a single ODMR line is typically ~ 6 MHz, identifying the small temperature-dependent shifts using this method requires very careful measurements.

2.2.2. ODMR variations

Obtaining a full ODMR spectrum can be time-consuming, as such a measurement generally takes upwards of 10s. One solution is to focus only on a single ODMR resonance line. In the absence of strong perpendicular magnetic fields or large variations in temperature, which would shift the ZFS, and therefore the ODMR lines, this process can significantly reduce the measurement time. Here, we will focus on three techniques used in this context to speed up ODMR acquisition.

Firstly, as shown in Fig. 2.5a, it is possible to extract the magnetic field based on a single ODMR line, a technique we refer to as single line tracking. In this procedure, we assume that the magnetic field gradients result in changes in the Zeeman splitting that are small compared to the width of the MW frequency window. Under these conditions, the shift between two subsequent measurements should be visible within the same frequency window, as shown by the red and blue ODMR spectra in Fig. 2.5a. We therefore fit the ODMR line by a Lorentzian for each measurement and shift the subsequent frequency window to be centered on the extracted ODMR minimum. In this way, we maintain a narrow frequency window, allowing us to measure with fewer points than required for a full spectrum, thereby shortening the measurement time. However, this method is limited to small magnetic field gradients and still requires up to several seconds of measurement time per spectrum to obtain sufficient signal to noise.

Shown in Fig. 2.5b is a second method that relies on measuring only a single point of the ODMR trace. Rather than varying the MW driving field frequency, we set it to a fixed value, in this example, at the center of the ODMR line. As the magnetic field at the NV changes, the resonance shifts relative to the set MW frequency, leading to a change in the measured PL rate. Therefore, we will observe a reduced PL rate only where the resonance condition between NV spin transition and static MW driving frequency is met. This method is known as isofield, or iso-B imaging [81, 82]. While this method is fast, it also only yields contour maps of the magnetic field, and is therefore primarily a qualitative technique.

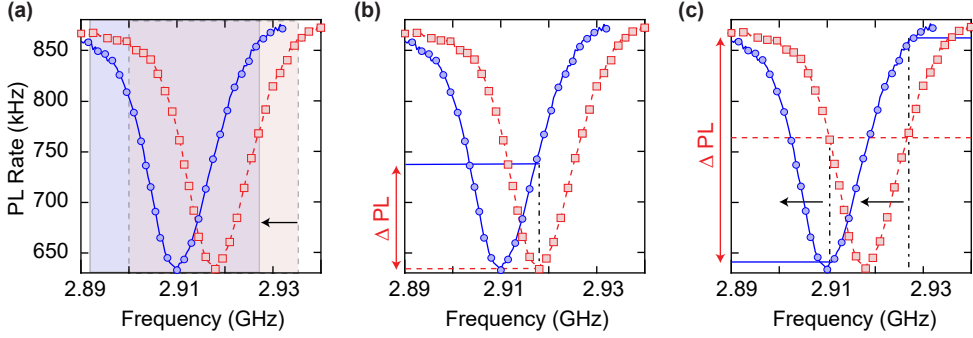


Figure 2.5.: Three variations on CW ODMR-based magnetometry. In each subfigure, the red squares show the initial ODMR line, and the blue circles denote the shifted ODMR line following a wait-time or moving to a new pixel. **(a)** Single line tracking. We measure the original (red) and shifted (blue) ODMR lines and shift the frequency sweep window (red area) to be centered around the shifted ODMR (blue area) for the subsequent measurement. **(b)** Iso-field measurement. We fix the MW driving to a single value, shown with a black dash-dotted line. As the resonance shifts with the external field, the measured PL rate (red dotted line) increases (blue solid line). This behavior results in minimal PL only when the resonance condition is met. **(c)** Feedback tracking of the ODMR line. We set two MW sources to frequencies on either flank of the resonance as shown with black dash-dotted lines. We alternate between these two MW sources and measure the corresponding PL rate. The two measured PL rates (red dashed line) are the same for the red curve. As the ODMR shifts (blue), the PL rate at one frequency will decrease, while the other increases (blue, solid lines), allowing us to determine the direction of the shift and correct the applied MW frequency accordingly, as shown with the black arrows.

We can modify this second technique slightly to obtain fully quantitative magnetic field maps as in the first method. To do so, we again set the MW drive to a single frequency, located on a flank of the ODMR line as shown in Fig. 2.5c. We also apply a second MW source, which we set to a frequency on the opposite flank of the same ODMR line. We then lock the MW frequencies to each other to ensure that they remain a linewidth apart. Now, we switch between these two MW sources in $\sim 5 \mu\text{s}$ intervals while simultaneously measuring the PL obtained under driving with one or the other. Ideally, the PL counts measured in either case should be the same. However, as the resonance shifts due to a local magnetic field applied along the NV axis, the PL of one flank will decrease while the other increases. We therefore use the PL difference as the error signal for a PI loop, with which we match the MW driving frequencies to the instantaneous NV spin transition frequency. In this way, we are again able to track the frequency of the ODMR line [83]. We refer to this technique as feedback imaging. As we measure only two points, we can measure quickly with typical integration times of 0.1 s. However, this integration time also limits how fast we can scan through a strong magnetic field gradient without losing track of the ODMR line. This technique is used most commonly in the remainder of this thesis.

2.2.3. Sensitivity

Having developed the necessary background for understanding NV magnetometry, we now turn our attention to the two most important characteristics of any magnetometry technique: sensitivity and spatial resolution. We begin with the sensitivity.

Put simply, sensitivity (η_B) refers to the smallest detectable magnetic field for a signal-to-noise ratio of 1. Formally, we can write this as follows [31, 84]:

$$\eta_B = \delta B \sqrt{\mathcal{T}}, \quad (2.2)$$

where δB is the detectable change in magnetic field and \mathcal{T} is the measurement time. Looking at the specific case of an ODMR-type measurement, the measured signal $\mathcal{S}(B)$ in a time \mathcal{T} will be given by $(\partial \mathcal{S} / \partial B)(\delta B)(\mathcal{T})$ while the noise is limited by the photon shot noise $N = \sqrt{\Gamma_{\text{NV}} \mathcal{T}}$ [31]. Here, Γ_{NV} is the PL rate of the NV center. Taking $\mathcal{S}/N = 1$ as in our definition of η_B , we can rewrite Eq. 2.2 as follows:

$$\eta_B = \frac{\sqrt{\Gamma_{\text{NV}}}}{(\partial \mathcal{S} / \partial B)|_{\text{max}}} \quad (2.3)$$

From this expression, we see that the stronger our signal varies with the magnetic field, the smaller η_B becomes i.e., the better our sensitivity.

We can further develop this concept for DC, ODMR-based magnetometry by a closer inspection of the denominator in Eq. 2.3. In particular, due to the fluctuating nuclear-spin bath surrounding the NV center, the natural lineshape of the detected resonance will be approximated by a Gaussian with a FWHM limited by the T_2^* time of the NV [85]. Therefore, we wish to find

$$(\partial \mathcal{S} / \partial B)|_{\text{max}} = \frac{1}{\gamma_{\text{NV}}} (\partial \mathcal{S} / \partial \nu)|_{\text{max}} \text{ for } \mathcal{S}(\nu) = \Gamma_{\text{NV}} [1 - C \exp\{-(\nu - \nu_0)/(2\sigma^2)\}],$$

where σ is the standard deviation of the Gaussian, C is the contrast, and ν_0 is the center frequency [85]. Evaluating the second derivative of this expression and setting it to zero, we find that the maximum slope is given by $(P_F \Delta \nu) / (C \Gamma_{\text{NV}})$, where $\Delta \nu = 2\sqrt{2 \ln 2} \sigma$ is the FWHM of the Gaussian and $P_F = \sqrt{e/(8 \ln 2)}$. Inserting this into Eq. 2.3, we obtain the following expression:

$$\eta_{B,\text{ODMR}} = P_F \frac{1}{\gamma_{\text{NV}}} \frac{\Delta \nu}{C \sqrt{\Gamma_{\text{NV}}}}. \quad (2.4)$$

Note that under optical and MW driving, the ODMR spectrum is subject to power broadening, leading to a Lorentzian line shape, which will result in a modification of $P_F = 4/(3\sqrt{3})$. Each of the parameters is presented in Fig. 2.6 with an example of an ODMR measurement under strong driving, fit with two Lorentzians.

From the expression in Eq. 2.4, we see that improving the sensitivity of ODMR detection can take multiple routes. Each of the three parameters - C , Γ_{NV} , and $\Delta \nu$ will be affected by the driving conditions, thereby providing some control over the sensitivity [85]. We will explore this point in more detail in Chap. 3.3.1. However, there are also fundamental limits on these three parameters that require modification of the fundamental NV properties or more complex measurement techniques to improve the sensitivity further.

One possibility, as discussed in Sec. 2.1.2, is to increase the contrast by controlling the NV charge state. As mentioned, charge state stability may be improved by using low optical excitation powers. Additionally, using a long-pass filter in the signal detection path helps remove some of the NV^0 background. Though this leads to an overall drop in PL, the remaining PL should display a larger spin contrast. Unfortunately, the charge state selection technique discussed briefly in Sec. 2.1.2 is currently not practical for ODMR measurements for the following reason: though the overall measurement time for an ODMR spectrum is on the order of seconds, this is averaged over thousands of repetitions, each a factor of ~ 15 shorter than a single charge state measurement [86]. However, this method is very promising for longer measurement protocols such as those seen in AC magnetometry.

Alternatively, one can focus on improving either the linewidth or the PL rate Γ_{NV} . The fundamental linewidth of an ODMR is determined by the inverse coherence time of the NV center and can suffer when the NV center is brought close to the diamond surface (see Sec. 2.1.3). However, recent results in modifying the diamond termination show great promise for extending this coherence time [87, 88]. Another option for extending the coherence time is through complex pulsing schemes [89, 90]. At the same time, to increase Γ_{NV} , we typically rely on diamond engineering [29, 91]. This allows us to overcome the total internal reflection that is the primary limiting factor when collecting the NV PL. This point will be the focus of the next chapter.

Overall, the balance of the NV properties influencing the contrast, PL rate, and line width is a nontrivial problem, and discussing it in detail is beyond the scope of this thesis. Luckily, many in-depth reviews of this topic exist [90, 92, 93].

2.2.4. Spatial resolution

Finally, we discuss the spatial resolution of NV magnetometry. As the NV center is a single atomic defect, the spatial resolution does not depend on sensor size, unlike SQUIDS [20], nor on the diffraction limit as in optical techniques. Instead, the spatial

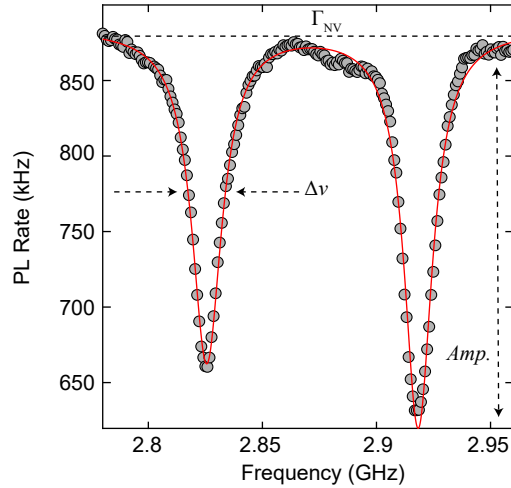


Figure 2.6.: Calculating sensitivity from an ODMR spectrum. Example of an ODMR spectrum taken with 26 μW of 532 nm excitation and an effective MW driving field of $\sim 36 \mu\text{T}$, fit with the sum of two Lorentzians. Due to this strong driving of the NV, we see significant broadening ($\Delta\nu = 15.5 \pm 0.5 \text{ MHz}$). However, this also yields excellent contrast $C = \text{Amp}/\Gamma_{\text{NV}} = 27 \pm 3\%$. With a base PL rate $\Gamma_{\text{NV}} = 0.88 \pm 0.01 \text{ MHz}$, we find that the resulting sensitivity, using Eq. 2.4, is $1.7 \pm 0.7 \mu\text{T}$.

resolution of a scanning NV magnetometer is given by the distance between the NV center and the source of the magnetic signal. To understand why, we will use a simple argument borrowed from the Rayleigh criterion in optics. Let us consider two magnetic dipoles, oriented perpendicular to a given sample surface and separated by a distance d . The field of a single magnetic dipole is given by:

$$\mathbf{B} = \frac{\mu_0}{4\pi} \left[\frac{(\mathbf{m} \cdot \mathbf{r})\mathbf{r}}{r^5} - \frac{\mathbf{m}}{r^3} \right], \quad (2.5)$$

where \mathbf{m} is the magnetic moment, and \mathbf{r} is the position vector. In Fig. 2.7, we plot the z -component of the stray field for these two dipoles, normalized to their maximum amplitudes, as a function of the distance h between a vertically-oriented NV center and the sample plane (inset). At a distance $h = d$, we see that the distance between the peaks of the two field profiles is equal to the width of a single profile. Beyond this point, these two objects will no longer be “resolvable”. Thus, analogous to the Rayleigh criterion, when located at a distance d_{NV} from the source, the minimal resolvable distance between two magnetic dipoles i.e., the spatial resolution, is also d_{NV} .

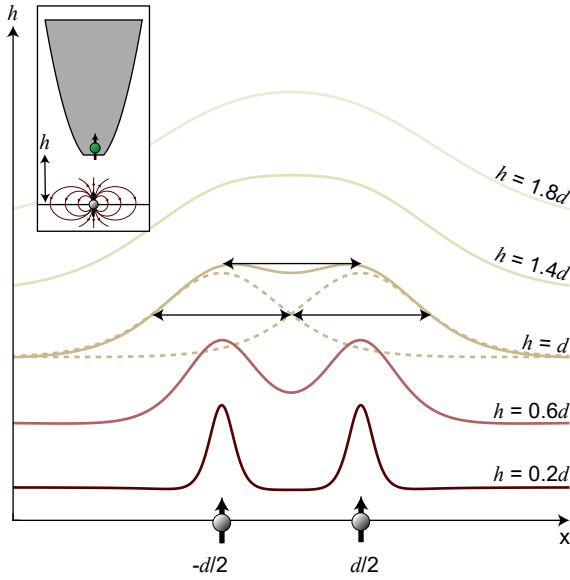


Figure 2.7.: An intuitive picture of spatial resolution. Here, we show the normalized z -component of the stray magnetic field arising from two dipoles placed a distance d apart and detected by an NV with an orientation shown in the inset. We plot the stray magnetic field for different distances h from the sample plane where the dipoles are located. At a distance $h = d$, we see that the FWHM (black arrows) of the individual profiles (dashed lines) are equal to the distance between maxima. Hence, our ability to resolve two distinct magnetic sources is limited by the distance between NV and source.

One can also argue the spatial resolution in a more quantitative and general manner using the propagation of magnetic fields. This procedure is typically done in Fourier space, where the propagation of a given Fourier component of the stray magnetic field directly above the sample, to a plane at a distance $d_{\text{NV}} > 0$, corresponds to multiplication with $e^{-d_{\text{NV}}q}$. Here, q is the in-plane wavevector of a given magnetization pattern $\mathbf{m}(\mathbf{r}) = (\mathbf{m}_{x,y}(\mathbf{r}), m_z(\mathbf{r}))$ at $z = 0$. Thus, the decay of the magnetic field with distance depends on the spatial frequency of the magnetic texture in question.

Returning to a real-space description, let us examine, for example, the z -component of the field. We find that [27]:

$$B_z(\mathbf{r}, d_{\text{NV}}) = -\mu_0/2 [\alpha_z(\mathbf{r}, d_{\text{NV}}) \star \nabla^2 m_z(\mathbf{r}) + \alpha_{x,y}(\mathbf{r}, d_{\text{NV}}) \star \nabla \cdot \mathbf{m}_{x,y}(\mathbf{r})], \quad (2.6)$$

where \star represents a 2D convolution between the magnetization and the resolution function $\alpha_{x,y,z}$. In particular,

$$\begin{aligned} \alpha_z(\mathbf{r}, d_{\text{NV}}) &= \frac{1}{2\pi (\mathbf{r}^2 + d_{\text{NV}}^2)^{\frac{1}{2}}} \\ \alpha_{x,y}(\mathbf{r}, d_{\text{NV}}) &= \frac{d_{\text{NV}}}{2\pi (\mathbf{r}^2 + d_{\text{NV}}^2)^{\frac{3}{2}}} \end{aligned} \quad (2.7)$$

Here, $r = (x, y)$. In this form, we can see more clearly how d_{NV} determines the magnetic field features that can be resolved. From this discussion, one should realize the importance of having an NV as close to the diamond surface as possible in order to improve the spatial resolution. We will explore this requirement in more detail in Chap. 3.3.2.

2.3. Conclusions

In our discussion of the NV center and NV magnetometry, we have occasionally made comparisons to common techniques used in the magnetism community. As we have seen, each of these techniques comes with advantages and disadvantages, which allow for unique contributions to the field of magnetism. An excellent review comparing some of the techniques described in this chapter has recently been published [94]. NV magnetometry, in particular, benefits immensely from the ability to address a diverse range of materials in a large number of environmental scenarios.

Of course, the key to this versatility is the NV center itself, and in this chapter, we have explored some of the basic properties of this valuable diamond defect. Apart from some contextual statements, we have limited ourselves to a discussion of the properties relevant to room temperature magnetometry, which will form the focus of the remainder of this thesis. In Sec. 2.1, we have delved into the electronic energy levels of the NV, where we discussed the spin $S=1$ triplet ground and excited state, whose $|0\rangle$ and $|\pm 1\rangle$ spin states form the basis of NV magnetometry. Due to the different decay channels and, subsequently, the differing PL rates of the spin states, we are able to initialize and read out the state of the NV optically. We also discussed a second degree of freedom of the NV center: the charge state. In particular, we explored how to characterize the background signal it forms for our magnetometry techniques. Finally, in Sec. 2.2, we moved to a discussion of NV magnetometry itself, providing the necessary background to understand how ODMR-based DC magnetometry is performed. We also described some variations on the traditional ODMR measurement, which will be used throughout this thesis. We concluded this section by discussing the two defining parameters of NV magnetometry - sensitivity and spatial resolution. Specifically, we explored how the other aspects discussed in this chapter can influence the sensitivity and how the spatial resolution may be given by the distance between NV and magnetic field source. In the next chapter, we will expand on this discussion in the context of a novel diamond probe for scanning NV magnetometry.

3. Truncated parabolic scanning probes for magnetometry

In the previous chapter, we introduced a powerful tool for addressing nanoscale magnetic field imaging: the nitrogen vacancy (NV) center. One of its strengths – the all-optical communication with the NV center – however, also turns out to be one of its most significant challenges. In Sec. 2.2.3, we showed that the sensitivity of our DC magnetometry technique improves with increasing photoluminescence (PL) collection efficiency. Unfortunately, the high index of refraction of diamond ($n = 2.4$) results in significant total internal reflection (TIR) at a diamond-air interface, preventing us from achieving high PL collection efficiencies in planar diamond structures. Thankfully, this material property may also be manipulated to our advantage through the fabrication of photonic structures.

Photonic engineering of diamond structures has existed for many years now [95, 96]. In quantum information applications, for example, where the spatial resolution is not of relevance, a large variety of structures have been fabricated with the primary goal of extracting as many photons as possible from the diamond. Diamond solid immersion lenses, as shown in Fig. 3.1a, have achieved single-NV PL detection rates of approximately 1 MHz through the minimization of oblique reflections at the diamond-air interface [97, 98]. More exotic structures such as dielectric antennas [99], metalenses (Fig. 3.1b) [100], and bull’s eye gratings (Fig. 3.1c) [101], have also been used to achieve high PL rates by creating conditions in which wide-angle emission is directed out of the plane of the diamond, towards the detection area.

In scanning applications, where the NV must be brought near and scanned relative to the surface of a secondary material, a single-sided waveguide has proven to be the most practical and popular solution. In such a structure, the NV is traditionally located close to the end-facet of a long, tapered [102] or cylindrical [28–30] pillar (as shown in Fig. 3.1d and e, respectively). The pillar is monolithically combined with a larger diamond slab typically referred to as a cantilever. This geometry allows the NV to be brought close to a sample while simultaneously providing a waveguide for the PL. The PL then exits the diamond at the backside of the cantilever, where it is collected through an objective. These structures achieve nanoscale spatial resolutions [103], but the collection efficiency tends to fall below 50% even in optimized cases [104].

Recently, one of the highest collection rates to date (approximately 4 MHz) has been achieved through the fabrication of a single-sided diamond parabolic reflector (Fig. 3.1f) [91]. This technique requires an NV placed at the focus of a parabolic diamond structure and uses the TIR of diamond to direct the PL parallel to the pillar axis, as shown in Fig. 3.2b. In this way, one can minimize reflections at the backside of the structure, where the PL is collected through a single oil-immersion lens. This waveguiding of the PL is achieved for a wide range of wavelengths and is robust against deviations from the ideal curvature and displaced emitters.

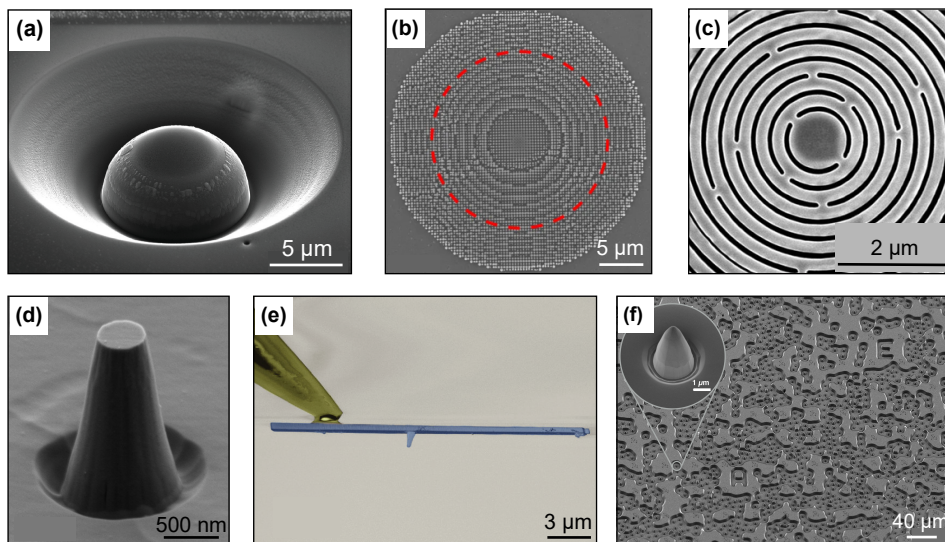


Figure 3.1.: Engineering the diamond environment. These images present various approaches towards photonic engineering of the diamond environment to optimize the collection of PL from emitters located within the diamond. **(a)** All-diamond solid immersion lens produced through focused ion beam milling. Reproduced from [98], with the permission of AIP Publishing. **(b)** A diamond metalens designed to collimate the emission of a bulk NV center and fabricated using electron beam lithography and ICP-RIE etching (a typical top-down approach). Adapted with permission from [100]. **(c)** A bull’s eye grating fabricated through etching with a Si hard mask and achieving PL rates up to 4.5 MHz. Adapted with permission from [101]. Copyright 2015 American Chemical Society. **(d)** A tapered pillar, achieving up to 1.7 MHz PL rates and fabricated using a top-down approach. Reprinted with permission from [102]. Copyright 2015 American Chemical Society. **(e)** Cylindrical pillars used for scanning applications fabricated using a top-down approach. Reprinted from [29], with the permission of AIP Publishing. **(f)** Parabolic diamond reflectors achieving PL rates up to 4 MHz through grayscale lithography of the diamond. Adapted with permission from [91]. Copyright 2018 American Chemical Society.

However, for scanning applications, which will be the focus for the rest of this thesis, the parabolic reflector is limited in two aspects. Firstly, immersing a diamond probe with oil to make use of the improved collection of the oil-immersion lens is not possible in scanning setups. Secondly, placing the NV at the focus of a parabola leads to a significant diamond thickness between the NV and source, leading to a poor spatial resolution.

This chapter will address the limitations of both the parabolic reflector and classical scanning probe by combining them into a single device: the truncated parabolic scanning pillar (TPSP). We will examine the behavior of the NV dipole in such structures and discuss how this structure helps to realize high collection efficiencies and narrowly collimated emission. We will then turn to an extensive characterization

of typical, fabricated devices containing single NVs, touching upon some of the NV properties discussed in Chap. 2, such as the charge state. Finally, we conclude with a discussion of these pillars in scanning applications, focusing on the sensitivity and spatial resolution introduced in the previous chapter. Most of the results presented here have been published in Ref. [32].

3.1. Parabolic reflector concept

In our TPSP design, we wish to harness the excellent photonic properties of the parabolic reflector in a typical scanning probe geometry. To do so, we replace the classical, cylindrical pillar with a parabolic reflector but with one significant modification: the truncation of the pillar apex. By truncating the parabola, we can still use the channeling of the PL while simultaneously bringing the NV close to the surface of the diamond. In this way, we minimize the NV-to-source distance, thereby maximizing our spatial resolution.

3.1.1. Geometric optics picture

The use of parabolic reflectors is by no means a revolutionary concept. Rather, it has found its way into many areas of daily life, from car headlights to the Hubble spacecraft and satellite dishes. The general motivation behind parabolic reflectors is that any emission from the focus will always be reflected in a direction parallel to the axis of symmetry and vice versa, making collection extremely efficient.

We use this property in the geometric optics consideration shown in Fig. 3.2. In Fig. 3.2a, we show the general geometry of our scanning probe, including the collection and excitation through the objective. The inset shows an example of a completed TPSP, which we will describe in more detail in Sec. 3.1.3. For now, we will focus on the tip of this device, as shown in Fig. 3.2b. We first present an ideal diamond parabolic reflector with an NV located at the focus (f) of the parabola, described by:

$$4fy = x^2. \quad (3.1)$$

In Fig. 3.2b and c, we have chosen $f = 61$ nm based on typical device parameters. In this simplified geometric optics picture, we clearly see the effect of the parabolic structure, which is to guide the emission from the focus into a directed, collimated beam. Thus, the structure acts as an optical waveguide. As the angle between the waveguided emission and back surface of the diamond cantilever is now zero, the reflection from the cantilever will be minimized, allowing us to collect $\sim 80\%$ of the emission that reaches this point.

To minimize the distance between the NV center and the diamond surface, we truncate the parabola just below the NV. This case is shown in Fig. 3.2c for a truncation 20 nm below the focus, the typical depth of the NVs within our devices. The majority of the rays that reflect from the end facet are then further reflected by the walls of the significantly larger pillar leading to a similar, highly directional emission at the backside of the cantilever. As such, the TPSP behaves as a nearly ideal parabolic reflector despite the truncated end facet.

However, placing an NV center near the diamond surface, will also modify the emission behavior of the defect. In bulk diamond, the optical dipoles of an NV center

can radiate unimpeded. In a diamond structure, on the other hand, the modified diamond surface will alter the supported photonic modes. The resulting modification of the local density of states will then lead to changes in the excited state lifetime i.e., the radiative lifetime of the NV center [104].

An intuitive picture of the latter result is given in Ref. [105] for a generic dipole near a mirror. Following these arguments, we imagine placing the NV center near the diamond surface (a poor mirror) such that constructive interference of the emission is achieved above the NV center. This constructive interference mimics an increase in the radiation probability of the NV center, or equivalently, a decrease in the radiative lifetime of the NV. Conversely, destructive interference will lead to no radiation at all, and so the radiative lifetime is effectively infinite. In our TPSP geometry, this modification of the radiative lifetime of the NV arises not only due to the fact that the dipole exists close to a flat diamond end facet but also due to the overall pillar shape. As such, for a given NV center within a TPSP, we expect to see a change in the radiative lifetime of the NV center, thereby affecting the amount of emitted PL.

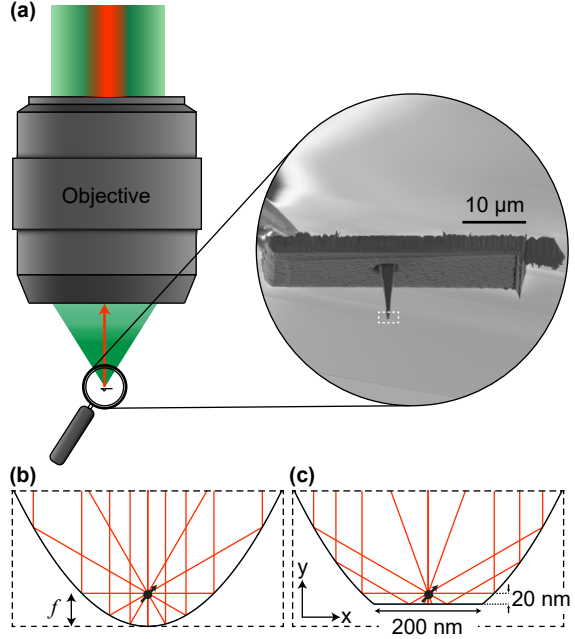


Figure 3.2.: The TPSP. (a) Schematic showing the excitation of and collection from a single scanning device. Inset: An SEM image of a TPSP with the associated diamond cantilever. (b) Ray diagram demonstrating the functionality of a parabolic tip. The (assumed isotropic) emission of the NV, located at the focus f , is reflected from the walls of the device, parallel to the axis of the pillar. (c) A similar ray diagram for a TPSP truncated 20 nm below the focus.

3.1.2. Simulating devices

Though this geometric optics argument provides a useful picture to motivate our use of the parabolic reflector, it is not entirely accurate as the length scales of the device are on the order of the wavelength of the NV emission. To properly capture the benefits of the TPSP and understand the behavior of the NV within the structure, we turn to finite-difference time-domain simulations of scanning probes. In these simulations, Maxwell's equations are solved on a discrete grid, resulting in a full vectorial solution of the electromagnetic field within a given geometry. Here, we use the Lumerical simulation package.

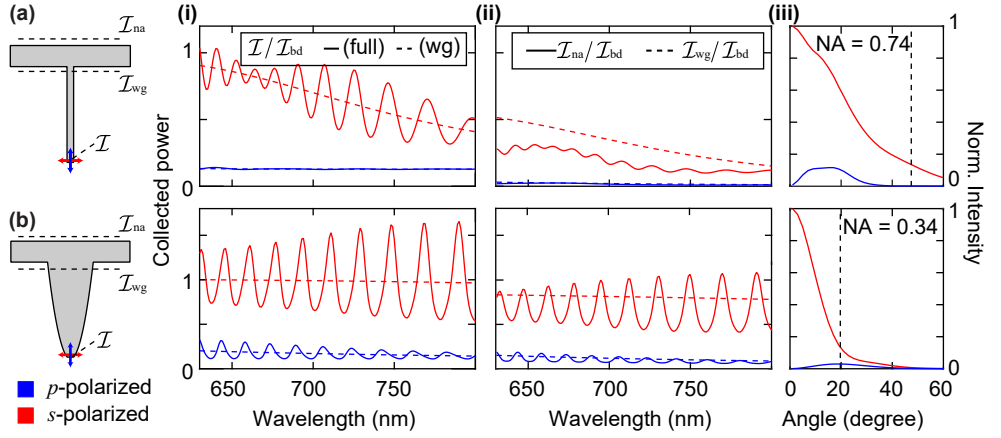


Figure 3.3.: Simulations of a cylindrical pillar vs. TPSP Lumerical simulations of an s - (red) or p -polarized (blue) dipole in (a) a cylindrical pillar and (b) TPSP, both having a 200 nm-diameter end facet. (i) Comparison between the dipole emission (\mathcal{I}) normalized to the emission of a bulk dipole (\mathcal{I}_{bd}) as a function of wavelength for the full device simulation (solid lines) and for the waveguide alone (dashed lines). Oscillations arise due to the cavity formed between the pillar end facet and the cantilever backside. (ii) The waveguided power (\mathcal{I}_{wg}) and the power collected within an NA = 0.8 at the cantilever backside (\mathcal{I}_{na}) as a function of wavelength. (iii) The normalized intensity collected at the backside of the device, shown as a function of the polar angle. Here, we integrate the power contained in an annulus $[\phi, \phi + \delta\phi]$, divided by the area of the annulus. The resulting NA, given by the point where the normalized intensity drops to $1/e^2$ of its maximum, is shown with a black dashed line.

Within the framework of this software, we define scanning probes consisting of a waveguide or pillar, attached to a large diamond slab similar to that shown in the inset of Fig. 3.2a. In particular, we focus on two waveguide geometries: our novel TPSP with a 200 nm-diameter truncated facet and the traditional scanning probe, consisting of a 200 nm-diameter cylindrical pillar [106]. Both of these geometries are highlighted in the leftmost panels of Fig. 3.3.

In each case, we simulate the electromagnetic field of a broadband dipole emitter, placed 20 nm from the end facet of the pillar, and centered on the pillar axis. To simplify our simulations, we will consider s - and p -polarized dipoles oriented perpendicular, respectively parallel, to the pillar axis. Given the 35.3° formed between the NV dipole plane and the normal axis of the (100) diamond surface (see Fig. 2.1a), the emission of the NV can be decomposed into a $2/3$ s - and $1/3$ p -polarized contribution [107]. This decomposition allows us to perform simulations for the simpler s - and p -polarized dipoles while still accurately describing the NV.

We will focus on three quantities, which we extract from our simulations for each of these dipole orientations: the emitted power of the dipole, \mathcal{I} , the power passing through the base of the waveguide, \mathcal{I}_{wg} , and the power collected at the backside of the full structure, \mathcal{I}_{na} . The positions at which these values are extracted are shown in the leftmost panels of Fig. 3.3. Specifically, \mathcal{I}_{na} is the power collected within

the numerical aperture (NA) of a typical objective (NA=0.8). These parameters are then normalized to the total emitted power of an ideal dipole in bulk diamond, \mathcal{I}_{bd} to isolate the change in the dipole emission described in the previous section. These three quantities also yield three useful characterization parameters: the Purcell factor ($\mathcal{I}/\mathcal{I}_{\text{bd}}$), which describes the change in emission rate, the waveguiding efficiency of the pillar ($\mathcal{I}_{\text{wg}}/\mathcal{I}$), and the collection efficiency of the whole device ($\mathcal{I}_{\text{na}}/\mathcal{I}$).

Let us begin by considering the emitted dipole power, \mathcal{I} , as shown in Fig. 3.3a(i) and b(i). Here, we plot $\mathcal{I}/\mathcal{I}_{\text{bd}}$ as a function of the wavelength over the typical NV center emission from 630 nm to 800 nm. However, the behavior we observe depends on whether we only consider the waveguide or the full structure.

Focusing first on the waveguide simulation (dashed lines in Fig. 3.3a(i), b(i)), we see that the emission of the p -polarized dipole (blue) is strongly suppressed in both structures. Thus, for the moment, we will focus on the s -polarized dipole (red) instead. In the cylindrical pillar (Fig. 3.3a(i)), the dipole emission for the s -polarized dipole drops by 50% over the entire wavelength range. For the parabolic pillar (Fig. 3.3b(i)), on the other hand, the emitted power of the dipole closely resembles that of a bulk dipole even over the wide range of wavelengths.

Turning to the full structure simulation (solid lines), we observe interference fringes in the collected power. These result from the cavity that forms between the end-facet of the pillar and backside of the cantilever, resulting in a Purcell effect. The emission behavior of the dipole in the parabolic and cylindrical pillar can be summarized by averaging over the wavelengths¹ shown in Fig. 3.3a(i) and b(i). These values are given in Table 3.1, where we observe an average Purcell factor of 0.99 for the parabolic pillar but only 0.65 for the cylindrical one. The Purcell factor highlights the first advantage of the parabolic pillar: an improved emission compared to its cylindrical precursor. Due to the rapid expansion of the diamond pillar from the end facet, the dipole experiences a more bulk-like environment, resulting in high broadband emission.

Let us move on to the waveguided and collected power plotted in Fig. 3.3a(ii) and b(ii). We see that for the cylindrical pillar (Fig. 3.3a(ii), dashed line), $\mathcal{I}_{\text{wg}}/\mathcal{I}_{\text{bd}}$ drops by an additional factor of approximately two relative to $\mathcal{I}/\mathcal{I}_{\text{bd}}$ in Fig. 3.3a(i). This drop indicates that a large portion of the dipole emission is lost from the waveguide before reaching the base of the pillar. On the other hand, the parabolic pillar (Fig. 3.3b(ii), dashed line) shows very little change compared to $\mathcal{I}/\mathcal{I}_{\text{bd}}$ in Fig. 3.3b(i).

Geometry	Dipole	$\mathcal{I}/\mathcal{I}_{\text{bd}}$	$\mathcal{I}_{\text{wg}}/\mathcal{I}_{\text{bd}}$	$\mathcal{I}_{\text{na}}/\mathcal{I}_{\text{bd}}$
Cylindrical (Fig. 3.3a)	s	0.65	0.32	0.18
	p	0.13	0.02	0.02
Parabolic (Fig. 3.3b)	s	0.99	0.81	0.68
	p	0.17	0.12	0.10

Table 3.1.: Summary of the emitted ($\mathcal{I}/\mathcal{I}_{\text{bd}}$), waveguided ($\mathcal{I}_{\text{wg}}/\mathcal{I}_{\text{bd}}$), and collected ($\mathcal{I}_{\text{na}}/\mathcal{I}_{\text{bd}}$) power in cylindrical and parabolic scanning probes as extracted from simulations. These values have been integrated over the entire wavelength range from 630 nm to 800 nm.

¹We average as follows: $\mathcal{I}/\mathcal{I}_{\text{bd}} = \frac{1}{N} \sum_{i=1}^N (\mathcal{I}/\mathcal{I}_{\text{bd}})^{\lambda_i}$. Here, N is the number of simulated wavelengths λ_i and $(\mathcal{I}/\mathcal{I}_{\text{bd}})^{\lambda_i}$ is the Purcell factor for a given wavelength.

In Table 3.1, we see an average waveguiding efficiency ($\mathcal{I}_{\text{wg}}/\mathcal{I}$) of 82% and 49% when normalized to $\mathcal{I}/\mathcal{I}_{\text{bd}}$ for the parabolic and cylindrical pillars, respectively. This factor of 1.6 improvement in the parabolic geometry over the cylindrical one highlights the performance of our TPSP model. We will now consider the full structure (solid lines). Despite the large oscillations in the TPSP emission (Fig. 3.3b(ii)), the wavelength-averaged collection efficiency $\mathcal{I}_{\text{na}}/\mathcal{I}$ still reaches 69% compared to 28% (normalized to $\mathcal{I}/\mathcal{I}_{\text{bd}}$) for the cylindrical case, as summarized in Table 3.1).

Recall that all the values we have stated here are for the s -polarized dipole. As mentioned in our discussion of $\mathcal{I}/\mathcal{I}_{\text{bd}}$, in Fig. 3.3a(i) and b(i), we see that the emitted power \mathcal{I} of the p -polarized dipole is suppressed by a factor of ~ 7 . In addition to the lifetime effects mentioned in Sec. 3.1.1, an additional reason for this suppression is the coupling of the emission to the waveguide. While the s -polarized dipole exhibits good modal overlap with the propagating waveguide modes of the pillar, the p -polarized dipole emission is not well transmitted in the waveguide. This is supported by the fact that the collection efficiency (normalized to $\mathcal{I}/\mathcal{I}_{\text{bd}}$) for the p -polarized dipole also drops to 59% and 15% for the TPSP and cylindrical pillar, respectively. It further manifests itself in the far-field modes, which are Gaussian for the s -polarized dipole but donut-shaped for the p -polarized dipole. Based on the combined simulation results, we can conclude that the majority of NV emission we observe will come from the s -polarized components of the dipoles.

Finally, we will use the full-structure simulations to simulate the far-field emission patterns of these devices. In Fig. 3.3a(iii) and b(iii), we show the emitted intensity measured at the cantilever backside, averaged over the azimuthal angle and full wavelength range (630 nm to 800 nm), and plotted as a function of the polar angle. From these plots, we quantify the angular emission of the devices by determining the NA of the devices, shown as a black dashed line. We do so by selecting the angular position where the emission intensity has dropped to $1/e^2$ of its maximum. This analysis shows a factor of 2 improvement in the NA of the parabolic device compared to the cylindrical one. The reduced NA represents a further advantage of the TPSP design. This difference in NA can also be understood in an intuitive sense by considering the pillar geometry. As the base of the cylindrical pillar is small compared to the simulated wavelengths, it will act as a narrow aperture, and the dipole emission will undergo much stronger diffraction when entering the wider diamond cantilever. The broad angular emission of the cylindrical pillar also contributes to the reduced collection efficiency as large emission angles will lead to more TIR at the cantilever surface. The parabolic pillar, on the other hand, due to its continuous expansion, circumvents this diffractive behavior.

The results of these simulations can be summarized with two important realizations. Firstly, in comparison to the cylindrical pillar, we have seen that simulations of the parabolic pillar show a much higher dipole emission and collection thereof. Comparing the average collection efficiency for these two structures in Table 3.1, we see a roughly fourfold improvement. The improved collection efficiency will lead to an increase in the collected PL, and thus our sensitivity as discussed in Chap. 2.2.3. Secondly, from the far-field simulations, we see that the parabolic pillar also results in a significantly more directed emission, which allows us to collect the NV PL signal with a narrower NA objective. Such objectives are typically associated with larger working distances and higher transmission rates, which allow for more convenient operation.

3.1.3. Fabrication

Naturally, having understood and designed an ideal TPSP, the next challenge is to fabricate such a structure. Following already well-established techniques [29, 102], we begin with a 50 μm -thick plate of (100)-cut, type-IIa diamond (Element Six). The diamond is implanted with a nitrogen density of 2×10^{11} ions/ cm^{-2} and energy of 12 keV at a 7° angle and then annealed to achieve approximately 20 nm-deep NV centers, typical for scanning probes [92]. We will realize these structures using a combination of electron-beam lithography and inductively-coupled plasma reactive ion etching (ICP-RIE, Sentech) to define the structures. The details of this fabrication procedure may be found in Appendix A.1.1.

We begin by writing the masks (FOX-16, Dow Corning) for 20 $\mu\text{m} \times 40 \mu\text{m}$ cantilevers, and etching these structures to a depth of approximately 2 μm , on the top i.e., implanted side of the diamond. We subsequently pattern circular, 1 μm -diameter masks aligned to the cantilevers. These circular masks will define our pillars. The pillar etch itself consists of two stages. In the first stage, the diamond is etched using an O_2 plasma chemistry (interspersed with occasional CF_4 steps [108]) to produce a tapered diamond pillar approximately 6 μm in length and 2 μm in diameter at the base. Here, the taper arises due to the etching of the diamond along the natural crystal facets [109].

In the second stage, we introduce the novel procedure used to achieve the parabolic shape of the pillar tip that is central to our device concept. Essential at this point in the etch is that the mask

has developed a conical shape as seen in Fig. 3.4a(i). We will now make use of the preferential etching of the FOX mask by CF_4 [102, 108]. Specifically, we change the rate at which the angle of the mask is transferred to the diamond by controlling the relative etch rates between diamond and FOX (see Appendix A.1.1). Through short steps with increasing CF_4 concentration, we develop a gradually increasing taper angle (Fig. 3.4a(i-iv)). The resulting structure then approximates a parabola with a focus ~ 20 nm above the end facet, ideally corresponding to the NV center depth.

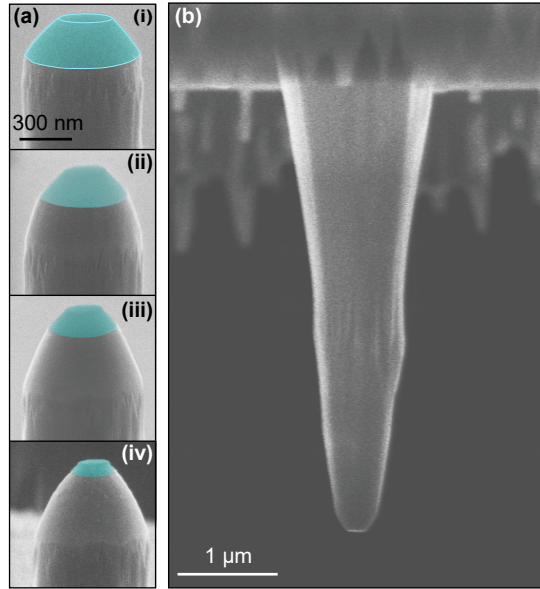


Figure 3.4.: The fabricated device. (a) SEM images of the parabolic etching steps. (i-iv) The progression of the mask (teal) as it is etched together with the diamond via an O_2/CF_4 plasma with increasing CF_4 concentration. (b) SEM image of the completed TPSP device.

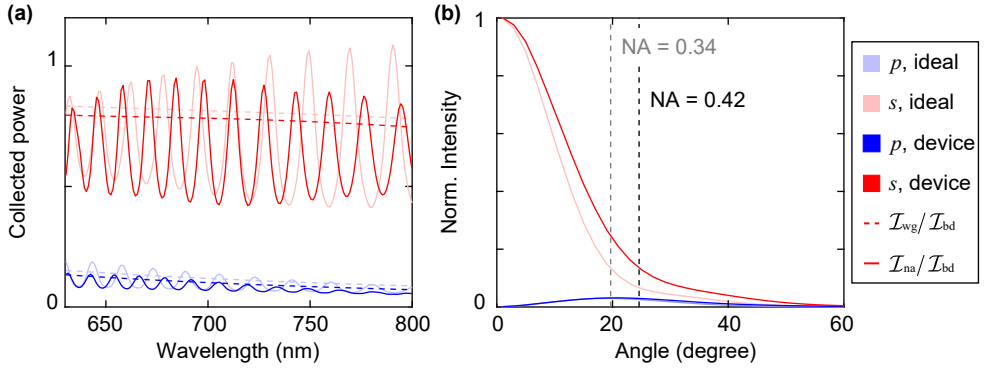


Figure 3.5.: Simulations of the fabricated device. (a) A comparison of the collected emission of the fabricated device (dark lines) and an ideal TPSP (faint lines) from simulations. The solid lines show $\mathcal{I}_{na}/\mathcal{I}_{bd}$, while the dashed lines give the value of $\mathcal{I}_{wg}/\mathcal{I}_{bd}$ as a function of wavelength for an s - (red) and p - (blue) polarized dipole. (b) A similar comparison showing the angular dependency of the fabricated and ideal TPSP devices. The NA of the respective devices is shown by the labeled dashed black and gray lines, respectively.

Finally, we remove the remaining mask, leaving us with a tapered pillar with a truncated, parabolic tip, as shown in Fig. 3.4b. The diamond is then etched from the opposite side relative to the pillars to release the structures in preparation for scanning magnetometry [29].

If we compare the fabricated structures to the ideal parabolic pillar, we notice that the tapered pillar leads to a much steeper diamond sidewall. To understand the influence of this deviation, we return to simulations. We extract the geometry of the fabricated structure from a profile image as in Fig. 3.4b, which we then compare to the ideal TPSP using the same simulation procedure outlined in the previous section. In Fig. 3.5a, we focus on the waveguided ($\mathcal{I}_{wg}/\mathcal{I}_{bd}$, dashed lines) and collected power ($\mathcal{I}_{na}/\mathcal{I}_{bd}$, solid lines). We observe good agreement between the ideal (pale lines) and fabricated devices (dark lines). As before, we summarize the wavelength-averaged values in Table 3.2, from which we extract a collection efficiency of 65% for the s -polarized dipole of the fabricated device. Comparing this value to the 69% collection

Geometry	Dipole	$\mathcal{I}/\mathcal{I}_{bd}$	$\mathcal{I}_{wg}/\mathcal{I}_{bd}$	$\mathcal{I}_{na}/\mathcal{I}_{bd}$
Fabricated	s	0.98	0.78	0.64
	p	0.16	0.10	0.08
Parabolic	s	0.99	0.81	0.68
	p	0.17	0.12	0.10

Table 3.2.: Summary of the emitted ($\mathcal{I}/\mathcal{I}_{bd}$), waveguided ($\mathcal{I}_{wg}/\mathcal{I}_{bd}$), and collected ($\mathcal{I}_{na}/\mathcal{I}_{bd}$) power observed in simulations of the fabricated parabolic pillar and compared to the ideal parabolic device. These values have been averaged over the range from 630 nm to 800 nm.

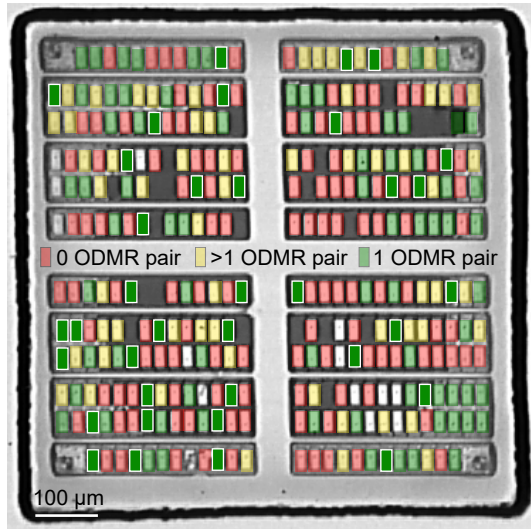
efficiency of the ideal device, we see that the fabricated device represents an excellent approximation of an ideal TPSP. Additionally, the angular distribution of the emission in the far-field shown in Fig. 3.5b demonstrates performance (dark lines) comparable to that of the ideal TPSP (pale lines) with only a 20% increase in the NA. As such, we expect our fabricated devices should exhibit high collection efficiencies and well-collimated emission patterns.

3.2. Characterization

We now wish to verify the improved performance of the fabricated devices introduced in the previous section. To do so, we require a detailed characterization of the optical properties of both the NV center and the pillar itself, which we will explore in this section. In a single round of fabrication, we typically etch a $\sim 1 \text{ mm} \times 1 \text{ mm}$ area of the diamond, which we refer to as a write field (WF), resulting in approximately 300 devices, as shown in Fig. 3.6. Characterization of these devices is carried out in a homebuilt confocal microscope equipped with 532 nm and 594 nm CW lasers and a wavelength-tunable, supercontinuum picosecond pulsed laser (SuperK Extreme, NKT Photonics). More details concerning this setup may be found in Appendix A.2.1.

We begin with a pre-characterization of the devices, where we focus on extracting three parameters of interest for scanning magnetometry: the NV PL rate, the contrast of the ODMR spectrum, and the number of NV centers in the pillar. We have already discussed the importance of the first two parameters in Chap. 2.2.3. For scanning magnetometry, we additionally aim for single-NV devices. Such devices allow us to, for instance, avoid confusion due to multiple ODMR lines when performing feedback scans as introduced in Chap. 2.2.2.

Figure 3.6.: Characterization of devices in a completed write field. An optical image of a single etched WF containing 308 devices. The devices are color-coded based on the number of ODMR lines detected in the initial characterization: red denotes no ODMR detected, yellow, more than one pair of ODMR lines, and green, a single pair of lines. Some devices (those without color) were precluded from characterization due to missing pillars or large defects at the pillar location. Of the resulting 109 single NV structures, 36 were selected for further analysis and are marked with a white border.



All three parameters can typically be well-addressed through a single ODMR measurement [110, 111]. Here, we apply a small bias field without aligning it to any given NV axis, such that one should observe different splittings for each of the four NV orientations. The first two parameters are then obtained by fitting the ODMR lines with Gaussian lineshapes. Additionally, the number of resonance pairs in the spectrum gives an indication of the number of NV centers in the pillar. Through this procedure, of the 294 devices characterized, we identified 109 devices containing a single ODMR pair and 60 devices containing multiple ODMR pairs, with the remaining devices showing no ODMR at all. These results are summarized in Fig. 3.6.

Though an ODMR spectrum is generally a good indication of the number of NV centers, a pillar can contain two NVs with the same orientation, resulting in a single pair of resonances. In particular, this means that of our 109 single ODMR pair devices, we would expect some to contain multiple NV centers (see Appendix A.3 for more details). In the next characterization step, we select 36 of these potentially single-NV devices from across the WF. In the following sections, our goal is to characterize these devices thoroughly. We will begin by verifying the single-NV nature of the devices through autocorrelation ($g^{(2)}(\tau)$) measurements, which may be used to indicate the presence of a single quantum emitter. In the remaining characterization, we examine the saturation PL, excited-state lifetime, and charge state of the NV centers. Finally, we will discuss the pillar-defined properties, namely the collection efficiency and angular emission, which we will compare to simulations.

3.2.1. Saturation behavior of single NV centers

We begin our investigation of the NV centers in our TPSP devices by verifying the single-NV nature of the 36 selected devices. Figure 3.7a shows the result of a $g^{(2)}(\tau)$ measurement performed on one of these devices. These measurements are realized by recording the correlations between photons arriving at two single-photon counters in a Hanbury Brown-Twiss configuration. In particular, we record a histogram of the events in which a photon is detected on the first counter followed by a second photon on the second counter. We bin the data by the time between photon arrivals, which is measured using a time-of-flight analyzer (P7889, FastComtec). Ideally, if the source is a single quantum emitter, the resulting $g^{(2)}$ trace will be characterized by a $g^{(2)}(0) < 0.5$ [112]. However, the $g^{(2)}$ by itself is not sufficient to guarantee that a device contains only a single NV center [110], which is why we also take the ODMR trace into account. As we observe a $g^{(2)}(0) = 0.16 \pm 0.02$ in combination with the single ODMR pair, this device contains, with high likelihood, only a single NV. Of the 36 selected devices showing a single pair of ODMR lines, only 25 show $g^{(2)}(0) < 0.5$.

We will now focus the remaining analysis on these 25 single-NV devices. In particular, we will begin with one of the most common figures of merit for assessing the performance of scanning devices: the saturation PL rate. A representative example of a saturation measurement of the NV PL rate, Γ_{NV} , as a function of 532 nm excitation power P is shown in Fig. 3.7b. The measured PL rate (black points) includes the emission of the NV together with a linear background signal, and as such, we fit the saturation curve with [113]:

$$\Gamma_{\text{NV}}(P) = \frac{\Gamma_{\text{sat}} P}{P + P_{\text{sat}}} + \Gamma_{\text{bg}} P. \quad (3.2)$$

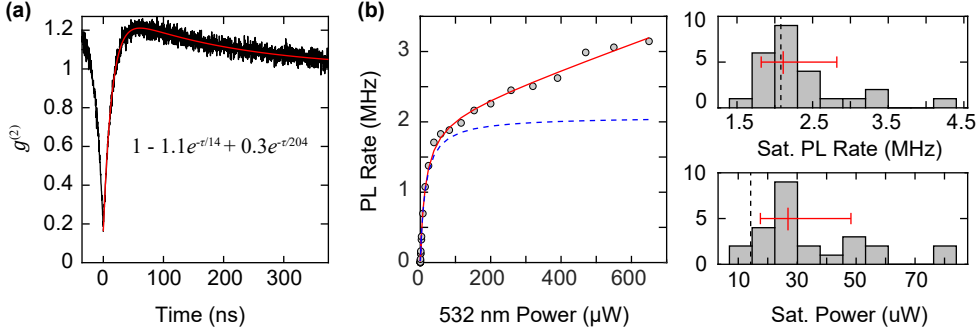


Figure 3.7.: Identifying and characterizing single NV centers. (a) Autocorrelation measurement of a representative NV center. The data are fit by the equation shown in the plot [113] to normalize the $g^{(2)}$ and obtain a $g^{(2)}(0) = 0.16 \pm 0.02$, confirming that the device indeed hosts a single NV center. (b) PL rate collected from the same representative device as a function of the excitation power. The gray circles give the measured data, which we fit in red with Eq. 3.2, yielding a saturation PL rate $\Gamma_{\text{sat}} = 2.1 \pm 0.2$ MHz and $P_{\text{sat}} = 14 \pm 3$ μ W. The blue dashed line gives the background-subtracted fit. The right-hand panels show histograms containing the saturation PL (top) and power (bottom) extracted from all 25 single NV devices. The results of the measurement to the left are shown with black dashed lines, and the median and 1σ intervals of the combined measurements are given by the red bars.

Here, Γ_{sat} is the saturated PL rate, P_{sat} is the saturation power, and Γ_{bg} is the background emission per unit excitation power. We plot the raw NV contribution in Fig. 3.7b as a dashed blue line to show the saturation behavior of the NV more clearly. From the expression in Eq. 3.2, we obtain $\Gamma_{\text{sat}} = 2.1 \pm 0.2$ MHz and $P_{\text{sat}} = 14 \pm 3$ μ W. Considering all the characterized devices, we obtain a median $\tilde{\Gamma}_{\text{sat}} = 2.1$ MHz and $\tilde{P}_{\text{sat}} = 27$ μ W with 1σ confidence intervals of [1.9, 2.8] MHz and [20, 48] μ W, respectively. Histogrammed statistics of the measurements are provided in the right panel of Fig. 3.7b, where $\tilde{\Gamma}_{\text{sat}}$ and \tilde{P}_{sat} and their respective 1σ intervals are shown with red bars. The sample measurement in Fig. 3.7b is marked with a black, dashed line.

To our knowledge, these values represent the highest recorded saturation PL rate for NV centers in scanning probes. Furthermore, it represents a factor of five improvement over the previous generation of devices [29, 30]. As such, it highlights the improved waveguiding efficiency of the TPSP compared to its cylindrically-shaped predecessors.

3.2.2. The excited state lifetime

While the saturation PL rate is a figure of merit of great practical relevance, it does not provide complete information about the photonic properties of the NV center and the TPSP. As discussed in Sec. 3.1.1, the presence of the diamond surface will influence the emission behavior of the NV center. In particular, in this section, we will discuss the change in the radiative decay rate, Γ_e^r . Experimentally, we can access this parameter through the excited state PL lifetime $t_e = 1/\Gamma_e$, where Γ_e is the total

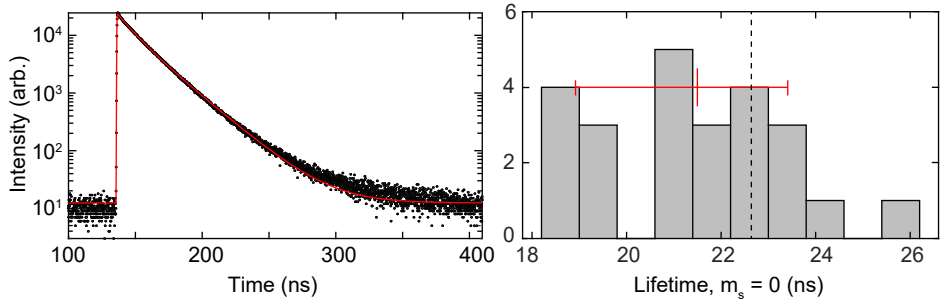


Figure 3.8.: Excited-state lifetime of the NV center. Semi-log plot of the measured NV PL following a picosecond pulse excitation as a function of time. The measurement is fit by the sum of two exponentially modified Gaussians [114] to extract the excited state lifetime of the $|0\rangle$ and $|\pm 1\rangle$ states. The right panel presents a histogram of the $|0\rangle$ state lifetime for 24 single NV devices. Again, the left-hand panel measurement is shown with a black dashed line, and the median and 1σ band are given by red bars.

decay rate of the NV excited state and consists of the radiative component Γ_e^r and a non-radiative one Γ_e^{nr} .

To measure t_e , we excite the NV with a picosecond pulsed laser at a repetition rate of 2.44 MHz and average power of 0.26 μ W tuned to a 12 nm band centered around 532 nm. The photons emitted following an excitation pulse are then measured with an avalanche photodiode, and their arrival time is recorded with the P7889 time-of-flight analyzer, resulting in the plot shown in Fig. 3.8. This histogram now contains the emission from the short-lived $|\pm 1\rangle$ excited states and the longer-lived $|0\rangle$ excited state (see Sec. 2.1.1), leading to a bi-exponential decay.

In practice, our measurements will begin to pump the NV center into the $|0\rangle$ state. In combination with the substantial non-radiative decay of the $|\pm 1\rangle$ states, the majority of the emission we measure will therefore be the result of radiative decay from the $|0\rangle$ excited state. Thus, we approximate the measured radiative decay rate as $\Gamma_e^r \approx 1/t_e^0$. For the measurement shown in Fig. 3.8, we obtain $t_e^0 = 23 \pm 1$ ns. The median $|0\rangle$ state lifetime, \tilde{t}_e^0 is found to be 21.5 ns with a 1σ confidence interval of [18.9, 23.4] ns. Comparing this to the value of t_e^0 in bulk [55], we obtain $\tilde{\Gamma}_e^r \approx 0.57 \Gamma_{e,bd}^r$.

Let us also compare this ratio of the radiative decay rate to that expected from simulations. Recall that we have simulated the Purcell factor $\mathcal{I}/\mathcal{I}_{bd}$ for both s - and p -polarized dipoles. The Purcell factor gives us the change in radiative decay rate for each of these dipole orientations, but we wish to estimate the value for the NV dipole. Therefore, we recall that the NV dipole has a $2/3$ s - and $1/3$ p -projection, allowing us to write the overall suppression of Γ_e^r in the pillar as follows:

$$\Gamma_e^r \approx \Gamma_{e,bd}^r \left[\frac{2}{3} \left(\frac{\mathcal{I}}{\mathcal{I}_{bd}} \right)^s + \frac{1}{3} \left(\frac{\mathcal{I}}{\mathcal{I}_{bd}} \right)^p \right], \quad (3.3)$$

where $(\mathcal{I}/\mathcal{I}_{bd})^{s(p)}$ is the Purcell factor for the s - and p -polarized dipoles respectively. Taking the values from Table 3.2, we obtain $\Gamma_e^r \approx 0.7\Gamma_{e,bd}^r$. The discrepancy between

the simulated and measured values suggests the presence of additional radiative suppression in our TPSPs. This suppression can, for example, be caused by lateral shifts of the NV from the pillar axis, which further modify the optical environment by bringing the NV closer to one of the sidewalls.

3.2.3. The charge state

One further aspect of the NV center – the NV charge state – tends to be overlooked in the characterization of scanning probes. As introduced in Chap. 2.1.2, the charge state of the NV center fluctuates between the NV^- state we are interested in and the NV^0 state, which forms one source of background fluorescence. To overcome this unwanted signal, we remove some of the NV^0 emission with a 594 nm long-pass filter and 635 nm dichroic mirror. Unfortunately, this also means that the time spent in the NV^0 state will reduce the PL signal collected from NV^- [59]. Therefore, for a proper assessment of the device performance, it is essential to take the charge state of the NV center into account.

We follow a slightly modified version of the procedure in Bluvstein et al. [110] to determine the charge state. We begin by characterizing the rates and thresholds introduced in Chap. 2.1.2 by exciting the NV with 0.49 μW of 594 nm excitation and simultaneously measuring the PL collected within an 812.5 μs measurement window. We fit the resulting photon number distributions according to a Poissonian model of the photon statistics as described in the SI of Ref. [57]. In particular, this model allows us to extract the ionization, recombination, and PL rates of both charge states.

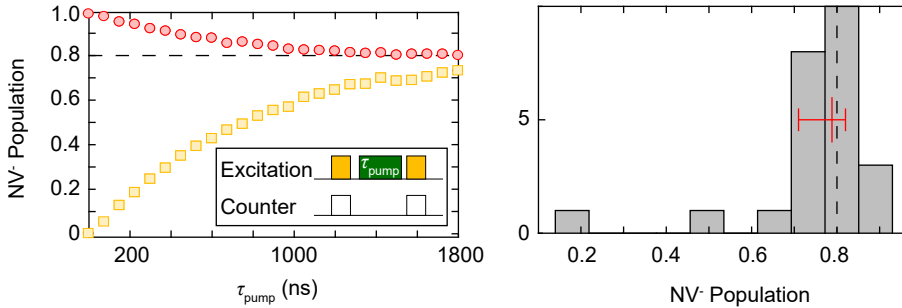


Figure 3.9.: Steady-state charge state of the NV. The NV^- population measured as a function of the 532 nm pump pulse length. The inset shows the pulse sequence used to measure this data. We separate the data based on the charge state at the beginning of the measurement: yellow if the NV begins in NV^0 or red if it begins in NV^- . The steady-state charge state of the NV is derived from the asymptotic convergence of the two curves (shown with a black, dashed line). The right-hand panel shows a histogram of the steady-state NV^- population measured for 24 single NV devices. The measurement in the left-hand panel is shown with a black dashed line and the median and 1σ band are shown in red.

From these rates, we define thresholds on the number of detected photons to differentiate the two charge states. We then perform a pump-probe measurement in which a 532 nm pump pulse of varying length is inserted between two 250 μ s-long 594 nm probe pulses as shown in the inset to Fig. 3.9. Together with our pre-defined thresholds, these probe pulses allow us to determine the initial and final charge states based on the number of detected photons within a single measurement window. This measurement is repeated 100,000 times, allowing us to plot the percentage of cases where the NV center ends in the NV^- as a function of the pump pulse length, differentiated by the initial NV charge state as shown in Fig. 3.9. We see that the two curves representing measurements starting and ending in NV^- (red) or starting in NV^0 and ending in NV^- (yellow) seem to converge for pump pulses exceeding 2 μ s in length. Therefore, the convergence point of these two curves gives the steady-state NV^- population, which is $80 \pm 2\%$ in this particular measurement. Considering once more all measured devices, the median NV^- population is measured to be 79% with a 1σ confidence interval of [71, 82] %.

3.2.4. Collection efficiency

This finally brings us to our goal of determining the collection efficiency ϵ_{dev} of our TPSPs. Experimentally, we can not measure ϵ_{dev} directly as it will be combined with the optical path efficiency ϵ_{setup} . Instead, we will measure the detection probability ϵ , together with the optical path efficiency ϵ_{setup} , which we can then use to determine $\epsilon_{\text{dev}} = \epsilon/\epsilon_{\text{setup}}$. Typical measurements of ϵ rely on short, intense pulses to transfer ground state population into the excited state in order to measure the fraction of excitations that result in photonic detection. However, these measurements suffer from two drawbacks. Firstly, these high-energy pulses will often lead to ionization of the NV^- state, decreasing the measured PL rates. Secondly, obtaining an accurate estimate of the background is challenging.

We address both issues by making use of the NV charge state. Specifically, we again perform a pump-probe measurement (see Fig. 3.9), where our pump pulse is now a single picosecond pulse tuned to a spectral band between 590 nm and 620 nm. We additionally measure the percentage of events resulting in a photon detection event. Unlike the pulse sequence presented in Fig. 3.9, we additionally measure the PL within a 275 ns window, starting several clock cycles (12.5 ns each) before each excitation pulse. Here, we use an FPGA (myRio, National Instruments) to perform these rapid operations. As the window extends far beyond the measured NV excited state lifetime of 23 ns, we are certain to collect any PL resulting from the excitation pulse. Additional 594 nm probe pulses (125 μ s) before and after the excitation pulse allow us to determine the NV charge state. We then record the number of events in which a photon is detected and group these events according to the measured charge state. This measurement is repeated for increasing pump powers, resulting in the curves shown in Fig. 3.10.

By requiring both the initial and final states to be either NV^- or NV^0 , a change in charge state in the 275 ns counter window will be very unlikely, thereby eliminating the first drawback we mentioned. Furthermore, as the pump pulse is outside the excitation band of NV^0 , any photons detected when starting and ending in NV^0 must originate from the background. In this way, we can directly measure the background

fluorescence² and circumvent the second pitfall. We finally subtract the background (yellow diamonds) from the NV^- signal (red squares) to obtain the true, charge-state corrected detection probability (gray circles) as a function of pump power (Fig. 3.10). Using this procedure, we record a maximum collection efficiency $\epsilon = 0.12$ for the device under investigation. Finally, we estimate our optical path efficiency (see Appendix A.2.1 for details) and use the measured detection probability to determine the charge-state corrected collection efficiency $\epsilon_{\text{dev}} = 57\%$. This value represents a distinct improvement over previous approaches [104].

Let us also compare this measured collection efficiency to what we would expect from our device simulations. To do so, we need to evaluate the total emitted power \mathcal{I}^{NV} and power collected at the objective $\mathcal{I}_{\text{na}}^{\text{NV}}$ for the NV dipole. Again, we recall that the emitted field of the NV dipole can be broken down into a $2/3$ s - to $1/3$ p - polarization, allowing us to draw on simulations of each dipole component as summarized in Table 3.2. In particular, simulations of the full NV dipole indicate that we can estimate the total emitted power of the dipole by summing the individual measured powers with the relevant prefactor, such that

$$\mathcal{I}^{\text{NV}}/\mathcal{I}_{\text{bd}} = \frac{2}{3}(\mathcal{I}/\mathcal{I}_{\text{bd}})^s + \frac{1}{3}(\mathcal{I}/\mathcal{I}_{\text{bd}})^p.$$

Here, we have normalized to the emission of the bulk dipole \mathcal{I}_{bd} to reflect the simulated quantities. Furthermore, for a single dipole orientation,

$$\epsilon_{\text{sim}}^{s(p)} = (\mathcal{I}_{\text{na}}/\mathcal{I}_{\text{bd}})^{s(p)} / (\mathcal{I}/\mathcal{I}_{\text{bd}})^{s(p)},$$

gives the ratio of collected power to that emitted by the dipole i.e., the collection efficiency. Multiplying the collection efficiency with the corresponding emitted power,

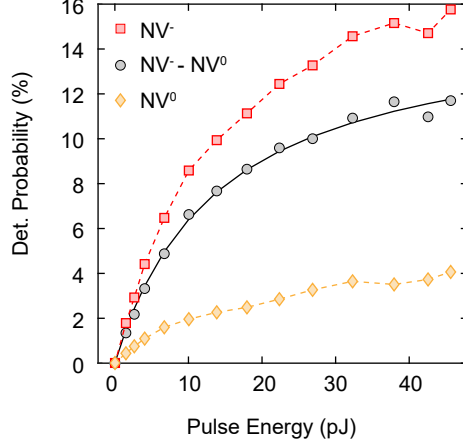


Figure 3.10.: Charge-corrected detection probability. The percentage of events in which a photon is detected following a single picosecond excitation pulse, differentiated based on the charge state measured before and after excitation. Events in which the NV begins and ends in the NV^0 state (yellow diamonds) represent a measurement of the background and are therefore subtracted from the events where the NV begins and ends in the NV^- state (red squares) to obtain the charge-state corrected detection probability (gray circles) as a function of the excitation pulse energy. We see that the curve seems to saturate above 40 pJ leading to a maximum detection probability of $\sim 12\%$.

²We assume the background is the same for all excitation wavelengths

we obtain

$$\mathcal{I}_{\text{na}} = \frac{2}{3}(\mathcal{I}/\mathcal{I}_{\text{bd}})^s \epsilon_{\text{sim}}^s + \frac{1}{3}(\mathcal{I}/\mathcal{I}_{\text{bd}})^p \epsilon_{\text{sim}}^p.$$

Taking the ratio of these two expressions and simplifying, we find that

$$\epsilon_{\text{dev}} \approx \left(\frac{\mathcal{I}_{\text{na}}}{\mathcal{I}} \right)^{\text{NV}} \approx \frac{\frac{2}{3}(\mathcal{I}_{\text{na}}/\mathcal{I}_{\text{bd}})^s + \frac{1}{3}(\mathcal{I}_{\text{na}}/\mathcal{I}_{\text{bd}})^p}{\frac{2}{3}(\mathcal{I}/\mathcal{I}_{\text{bd}})^s + \frac{1}{3}(\mathcal{I}/\mathcal{I}_{\text{bd}})^p}. \quad (3.4)$$

Using the values summarized in Table 3.2, we obtain an expected collection efficiency of 64%. Though this value exceeds that which we measured, it is surprisingly close considering that the simulations assume an NV placed perfectly in the center of the end facet, ideal excitation, and other factors that could change our collection efficiency.

3.2.5. Angular emission

In the final part of our characterization, we wish to verify one last aspect of our TPSP design: the highly directional emission seen in Fig. 3.5b. Experimentally, we can address this aspect by imaging the device's back focal plane (BFP). Located at the rear focal point of the collecting objective, the BFP is a Fourier transform of the object plane. Therefore, it can be used to determine the angular distribution of the photons originating from the object plane; in our case, the NV center within the TPSP. This plane can be imaged on a regular CCD camera as described in [115].

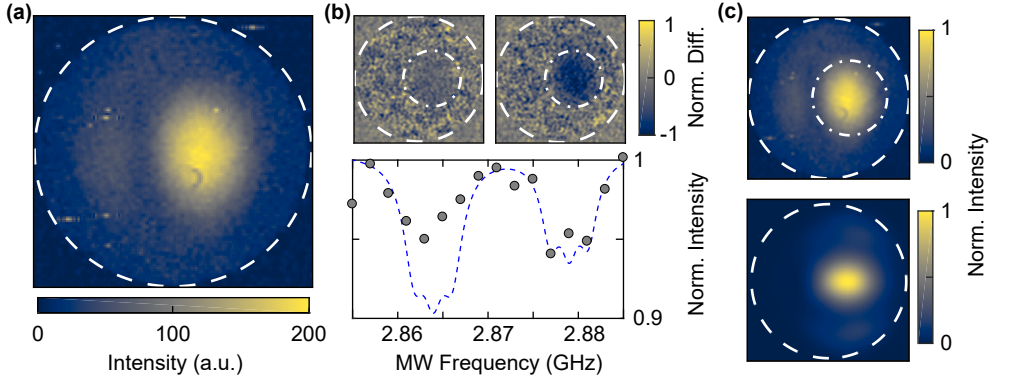


Figure 3.11.: Back focal plane imaging (a) A typical BFP image captured with a CCD camera. We highlight the edge of the objective (NA = 0.8) with a white dashed line. (b) BFP images showing the PL difference when driving with an off-resonant (left) or resonant (right) MW showing a drop in emission localized to the region within the white dash-dotted line. The bottom plot shows the intensity within the white dash-dotted line, normalized to the non-driven case as a function of the applied MW frequency. We compare these points to the measured ODMR for the same tip (blue, dashed line). (c) The same BFP image as in (a) showing the NA = 0.37 of the device, determined by fitting two 2D Gaussians to the normalized intensity (white, dash-dotted line). The bottom image shows the BFP of a simulated TPSP tilted by 5° relative to the cantilever normal.

An example of a BFP image of the emission from a TPSP device is shown in Fig. 3.11a. In such an image, we observe a drop in the pixel white-level at the angular limit of the collected light. We mark this boundary, which corresponds to the NA of our objective (NA = 0.8) [99], with a dashed white line. Within this area, we obtain a localized region of high intensity, which we attribute to the PL originating from the NV center.

To verify that this observed emission indeed originates from the NV center, we perform a set of BFP measurements while simultaneously driving with a fixed MW frequency. We process our BFP measurements as grayscale images and extract the white level of each pixel, which we refer to as the pixel intensity. We then subtract the intensity of the BFP taken in the absence of MW driving from that taken with driving. This process is repeated for several frequencies across the ODMR range. In doing so, we observe that the resulting difference images show a distinct, localized drop in intensity when the microwave is resonant with one of the two NV transitions (Fig. 3.11b, top-right panel). This intensity reduction is made even more apparent when compared to the off-resonant case (Fig. 3.11b, top-left panel). Here, we highlight this region with a dash-dotted circle. In the bottom panel of Fig. 3.11b, we plot the pixel intensity of the driven case, integrated over the region within the dash-dotted circle, and normalized to the non-driven case. We see a correspondence with the ODMR lines of the NV center shown with a blue dashed line, thus confirming our hypothesis that the BFP emission indeed originates from the NV. Furthermore, the observed drop in intensity is localized within the dash-dotted area, implying that the small lobe to the left in Fig. 3.11a does not come from the NV. Instead, this is likely background emission, possibly due to fluorescent contamination on the device or ambient lighting.

Let us now turn to the question of NA and explore how we use these BFP images quantitatively. We will again take the intensity matrix of our BFP images, which we fit using the sum of two 2D Gaussians. One of these Gaussians is fixed to be concentric with the objective aperture to imitate a broad background, while the second is allowed to vary freely in center coordinates and width to fit the signal arising from the NV. From this fit, we extract the $1/e^2$ point of the narrower signal Gaussian, which is then plotted as a white, dash-dotted line in the top panel of Fig. 3.11c. Though not stated, the dash-dotted lines in Fig. 3.11b are obtained in the same way.

To relate the $1/e^2$ point of the Gaussian fit (in pixels) to an effective NA, we use the radius of the NA = 0.8 circle (white, dashed line) identified previously as a conversion factor. In this way, we obtain an NA = 0.37 for the image shown in Fig. 3.11c. The BFP was measured for a total of ten devices, resulting in a median NA = 0.44 with a 1σ confidence interval within [0.41, 0.55]. Comparing this to the simulated NA in Fig. 3.5b, we find that the simulated NA = 0.42 fits well within this range.

We note that the emission pattern in this device is markedly off-center. This angular offset of the emission may be explained through a tilt of the pillar relative to the cantilever surface. Figure 3.11c (bottom) shows the simulated far-field emission extracted for a pillar angled at 5° from the cantilever normal. Here, we observe a comparable shift in the emission relative to the pillar axis shown with crosshairs. Simulations of emitters placed away from the symmetry axis of the pillar show a distortion of the emission for large displacements but can not explain the experimentally observed offset.

Thus, we have succeeded in verifying the narrow angular emission of the TPSPs seen

in simulations. Through the in-depth characterization of the novel scanning probes presented in this section, we have highlighted the improved photonic properties of these devices. In particular, we have achieved the highest PL rates in scanning probes to date and photon collection efficiencies exceeding 50%. Due to this significant improvement, the device concept has also been submitted for patenting.

3.3. Applications to magnetometry

Our goal in this thesis is to utilize the TPSP probes in scanning magnetometry. While the basic concepts of ODMR-based magnetometry have been discussed in Chap. 2.2, let us shortly discuss the physical implementation of DC scanning NV magnetometry. This technique relies on the spatial scanning of the NV center relative to the surface of a magnetic sample. By dividing the scanning area into a raster pattern and recording the ODMR frequency via one of the three methods detailed in Chap. 2.2.2, we obtain real-space images of the stray magnetic field at a height d_{NV} from the sample surface. We realize this scanning procedure by using our TPSP like the tip of an atomic force microscope, as described in Ref. [29]. In particular, the TPSP is glued to the end of a pulled quartz capillary, which in turn is glued to one tine of a quartz tuning fork. We excite oscillations in the tuning fork with a piezo and use the oscillation amplitude of the tuning fork to maintain in-contact operation through a feedback loop while the sample of interest is scanned below the TPSP. This procedure also allows us to reliably and repeatedly scan over topographic features reaching $1.5\text{ }\mu\text{m}$ in height. Here we also benefit from the hardness of diamond, which makes these scanning probes very robust. This technique is described in more detail in a number of publications [29, 31, 92, 116].

This section, will finally focus on characterizing the key parameters for NV magnetometry with this new TPSP design: stray field sensitivity and spatial resolution. In particular, we examine if the favorable photonic properties of the TPSP discussed in the previous sections will also translate to high magnetic field sensitivity and spatial resolution.

3.3.1. Sensitivity

To estimate the DC sensitivity achievable with the TPSP devices characterized in the previous section, we will be following a procedure based on that presented by Dréau et al. [85]. In this analysis, we will find that the hyperfine structure of the NV center, which we have neglected thus far, will play a role. In particular, interactions between the electron spin and ^{14}N nuclear spin will lead to splitting of a single ODMR line into three resonances, corresponding to the three projections of the nuclear spin. In Eq. 2.4, we have described the ideal DC ODMR sensitivity, assuming that the ODMR line is well described by a single Gaussian or Lorentzian function. In their study, Dréau et al. work at high applied fields, specifically at the excited state level anticrossing at 51 mT, where the polarization of the ^{14}N nuclear spin again results in only a single resonance. However, to remain consistent with the conditions under which we typically perform magnetometry measurements, we will consider moderate bias fields of $<3\text{ mT}$. Additionally, laser and MW induced power-induced broadening

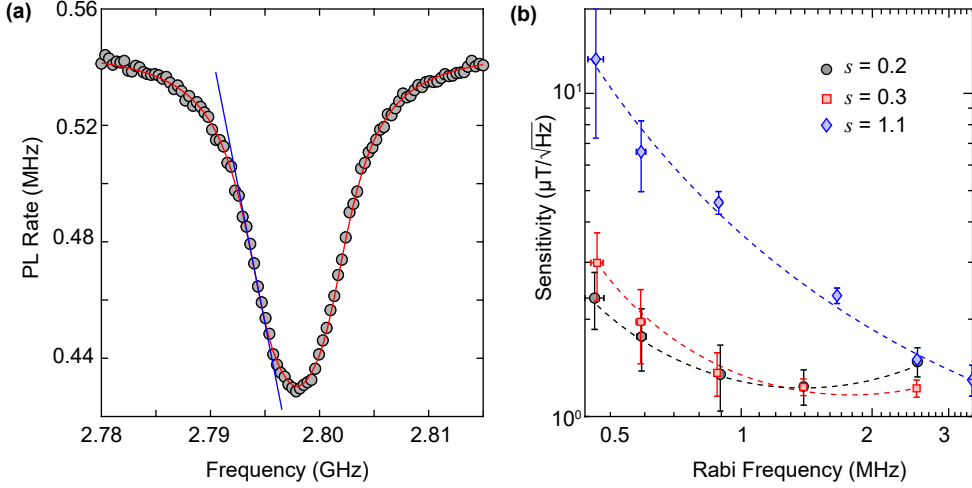


Figure 3.12.: Determining the sensitivity. (a) ODMR spectrum taken at $s = 0.3$ (where $s = P/P_{\text{sat}}$ and $P_{\text{sat}} = 37 \mu\text{W}$) and a MW Rabi frequency of 2.5 MHz. The spectrum (black points) is fit with the sum of three Voigt lines separated by 2.16 MHz (red line). The maximum slope is shown with a solid blue line. (b) Sensitivity of the TPSP device determined by Eq. 3.5 as a function of the MW driving amplitude. The measurements are repeated for three different optical powers resulting in an $s = 0.2$ (black circles), $s = 0.3$ (red squares), and $s = 1.1$ (blue diamonds). The lines are guides to the eye. The error bars represent the standard deviation extracted from three independent estimates of the maximum slope based on the Voigt fit, smoothed, and raw data.

of the individual hyperfine lines in our typical measurement regimes will lead to an ODMR spectrum as shown in Fig. 3.12a, taken with $12 \mu\text{W}$ of 532 nm excitation ($s = P/P_{\text{sat}} = 0.3$) and a MW power corresponding to a Rabi time of 2.5 MHz. Here, we are unable to resolve the individual hyperfine lines, but at the same time, a single Gaussian or Lorentzian line also provides a poor fit. In this regime, applying Eq. 2.4 will not provide a good approximation of the achievable sensitivity.

Therefore, we will rely on the slope of the ODMR spectrum to extract our sensitivity instead. Recall that the sensitivity may be evaluated with the following expression:

$$\eta_B = \frac{1}{\gamma_{\text{NV}}} \frac{\sqrt{\Gamma_{\text{NV}}}}{(\partial\Gamma_{\text{NV}}/\partial\nu)|_{\text{max}}}. \quad (3.5)$$

Here, Γ_{NV} is the PL rate measured at the point of maximum slope $(\partial\Gamma_{\text{NV}}/\partial\nu)|_{\text{max}}$. For the ODMR trace in Fig. 3.12a, we estimate the maximum slope (shown in blue in Fig. 3.12a) by calculating the gradient of the data, yielding $\eta_B = 1.12 \mu\text{T}/\sqrt{\text{Hz}}$. Due to the noise in the measurement, such an approach typically results in an overestimate of the slope. To avoid this, we also estimate the slope by smoothing the data using a Savitzky-Golay filter, resulting in an estimate of $\eta_B = 1.26 \mu\text{T}/\sqrt{\text{Hz}}$. However, as the choice of filter and filter order is arbitrary, we make one final estimate of the slope by fitting the data. In this way, we achieve similar smoothing without mak-

ing assumptions regarding the smoothing function. In particular, we fit the ODMR shown in Fig. 3.12a (red) with the sum of three Voigt functions, allowing us to accurately represent the hyperfine structure of the NV center while smoothly transitioning between a Gaussian and Lorentzian lineshape in the presence of power broadening. Using this procedure, we obtain a sensitivity estimate of $\eta_B = 1.29 \mu\text{T}/\sqrt{\text{Hz}}$. We then take the mean and deviation of these three estimates to obtain our final estimate of the sensitivity: $\eta_B = 1.22 \pm 0.07 \mu\text{T}/\sqrt{\text{Hz}}$ for this particular ODMR.

We then repeat this analysis for various MW and optical driving conditions, summarized in Fig. 3.12b for the same device shown in Fig. 3.12a ($P_{\text{sat}} = 37 \mu\text{W}$). Here, we give the sensitivity as a function of the MW Rabi frequency for three different laser powers: $s = 0.2$, shown with black circles, $s = 0.3$, shown with red squares, and $s = 1.1$, shown with blue diamonds. Note that the lines shown in this figure are guides to the eye. Like Dréau et al., we observe an optimum in the sensitivity that varies with the MW driving amplitude. For a given optical power, increasing the MW driving will first result in an improved sensitivity before power broadening and contrast saturation again lead to a decrease in sensitivity. While a similar optimum is expected as a function of excitation power, it is much broader, and therefore, not visible in Fig. 3.12b. Comparing all results within our parameter set, we observe an optimal sensitivity of $\sim 1.2 \mu\text{T}/\sqrt{\text{Hz}}$.

Finally, let us also compare these results to those presented by Dréau et al. In particular, we have realized a factor of 1.7 improvement on the CW ODMR sensitivity limit of $2 \mu\text{T}/\sqrt{\text{Hz}}$ that they identify³. However, if we compare our estimated sensitivity to values that they obtain for similar driving conditions, we observe a factor of approximately 3 improvement. This improvement is also consistent with the increase in saturation count rate ($\sim 2 \text{ MHz}$), achieved with the device shown in Fig. 3.12. While we have already achieved a regime in which we realize excellent sensitivities, comparisons to Dréau et al. suggest that we should be able to improve on these values. One possibility is by working in a regime where we are able to resolve the hyperfine lines, either by further reducing the power or through pulsed ODMR [85].

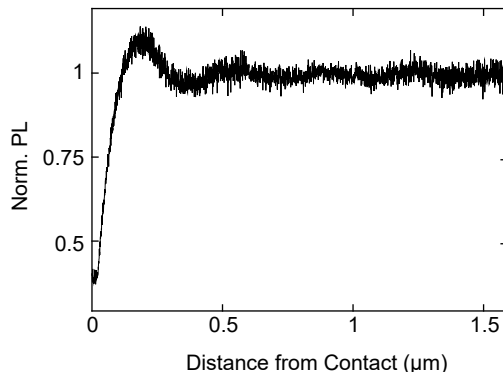
3.3.2. Resolution

We now complete the characterization of our novel scanning NV probes with a discussion of the spatial resolution. In Chap. 2.2.4, we have shown that the spatial resolution of NV center magnetometry is given by the distance d_{NV} between the NV center and source of magnetic signal. However, measuring this distance is not a trivial process.

A useful method for getting a qualitative sense of the distance is to record the collected PL as the NV approaches a dielectric sample surface, also known as an approach curve. We typically observe that the detected PL begins to oscillate and drop off very sharply shortly before coming into ‘contact’ as shown in Fig. 3.13. Here, contact is defined to be the point at which the tuning fork amplitude falls to 80% of its out-of-contact value. Generally, the oscillations will be due to a combination of standing waves in the excitation laser arising from reflections off the sample surface and changes in the NV emission behavior. Close to the sample surface, as shown

³Dréau et al. measure a bulk NV center with 250 kHz saturation count rates, using an oil objective.

Figure 3.13.: Approach curve over a dielectric surface. Measured NV PL rate as a function of the distance between the diamond tip and a dielectric surface. We observe oscillations in the PL and a rapid drop in the last ~ 200 nm, which could be used to determine the distance between NV and surface.



in Fig. 3.13, the oscillations are primarily due to changes in the Purcell factor (see Sec. 3.1.1) [117]. However, to extract the distance based on this portion of the approach curve, we require better modeling of the NV center emission. In Appendix A.4, we present first attempts at simulating this behavior. On the other hand, far from the sample i.e., at distances exceeding $\sim 2 \mu\text{m}$, oscillations will be primarily due to the standing waves in the excitation laser [118]. These laser-based oscillations have been used to estimate d_{NV} , as shown in the SI of Reference [118], but these estimates are associated with large uncertainties. For this reason, we typically use this approach curve in a qualitative manner.

The most common technique for quantitatively determining d_{NV} however, is to use the stray field of a well-understood and easily modeled structure. An ideal source would be a 1D current-carrying wire, whose stray field is described by the Biot-Savart Law. Unfortunately, obtaining this kind of ideal 1D current-carrying wire is difficult. One possibility could be to use current-carrying carbon nanotubes, but based on first attempts, the resulting signals tend to be much too small to be detected in DC magnetometry, and scanning in contact may result in tearing of the device.

A similarly simple source, is a uniform, out-of-plane magnetized stripe. For such a structure, the stray field can be described as a 1D current running along the edge of the stripe [24], as shown in Fig. 3.14a. The stray field projection onto the NV axis, as shown in Fig. 3.14b, can then be fit using this current model to determine d_{NV} . This method is well-established and forms the basis of most claims of spatial resolution, including those we present here.

Let us now turn to a quantitative discussion of d_{NV} extracted for these TPSP devices using the “stripe method” mentioned above. In Fig. 3.14c, we summarize measurements performed with six of our TPSP devices over either a FM CoFeB stripe (NV 1 and NV 6) or an AFM Cr_2O_3 mesa (NV 2-5). In particular, we present a standard box plot analysis for these devices with each measurement of the NV-to-sample spacing shown as a gray circle and the median shown in red.

Taking the mean of the median values shown, we find $\bar{d}_{\text{NV}} = 69 \pm 13$ nm, though values of d_{NV} down to 35 nm have been achieved. These values are comparable to other scanning NV devices and bring us to a regime where we can address a range of spin textures. However, the values of d_{NV} that we find are still a factor of three

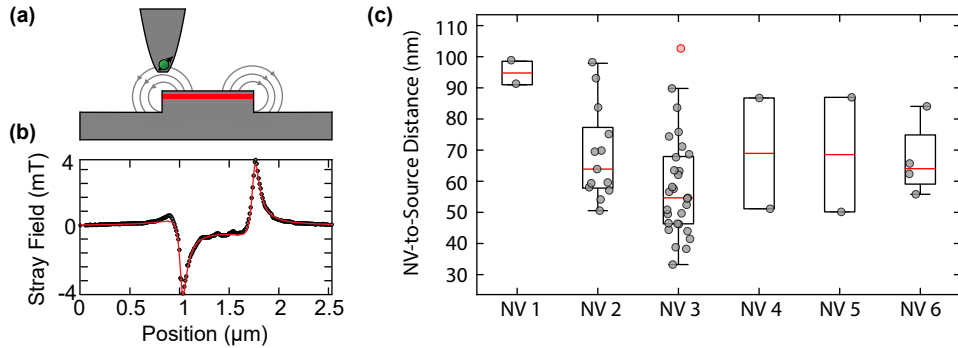


Figure 3.14.: Determination of the spatial resolution. (a) A schematic detailing the stray field arising from the edges of a FM stripe, which we model as arising from two oppositely-flowing line currents shown at the corners of the stripe. (b) The stray field arising from the measurement in (a) and fit with the two-current model (red curve). From here, we extract a value of $d_{\text{NV}} = 45 \pm 5$ nm. (c) A box plot summary of d_{NV} measured for six TPSP devices. Each point denotes an individual measurement with the median shown with a red line, a box denoting the interquartile range, and whiskers drawn to the maximum and minimum values (except for the outlier marked in red).

larger than the expected distance between the NV center and the diamond surface. In our design, if the truncated end facet of the diamond can be brought into contact with the magnetic stray field source, d_{NV} should only be defined by our implantation parameters and so is expected to be on the order of 20 nm [92, 119]. There are several reasons why we might obtain these values.

First and foremost, the estimated depth of the NV center is based on simulations and has yet to be independently confirmed. As such, the NV centers may indeed form deeper in the diamond than expected. Furthermore, a larger NV-to-sample spacing could arise from a tilt in the pillar or uneven sample surface. Mounting of the scanning probe is done by hand [92], resulting in an expected accuracy of $\pm 2^\circ$. A tilt of 2° , can lead to a separation of 3.5 nm to 7 nm depending on the position of the NV in the pillar. Even such small tilts can thus change d_{NV} by $\sim 10\%$. Note that despite the tilt of the pillar seen in BFP measurements (Fig. 3.11c), we believe that based on our fabrication procedure, the diamond end facet should still lie parallel to the cantilever. This particular tilt would, therefore, result in a slightly skewed parabola but not an increased d_{NV} .

One additional factor that will lead to changes in the distance between NV and sample surface is dirt on the diamond end facet. Experience shows that the scanning devices, though remarkably robust, suffer from collecting contamination on their surface. This process is undoubtedly a more significant issue in room-temperature magnetometry, where ambient conditions and open scanning setups allow dust and other particulate matter to accumulate. Such contamination can be mitigated by sealing the scanning setup when in use, but it is difficult to avoid altogether. For this reason, the temporal and spatial proximity of magnetometry measurement and distance calibration is essential. This final point will be used later in Chap. 4.

3.4. Conclusions and Outlook

In this chapter, we have presented a novel form of diamond NV scanning magnetometry probe. By combining the excellent waveguiding properties of the parabolic reflector and the truncation of traditional scanning probes, we were able to realize a device that achieves both high magnetic field sensitivity and high spatial resolution.

In Sec. 3.1, we introduced our truncated parabolic scanning probes by motivating the design through a simple geometric optics picture. We then expanded this picture through detailed simulations showing the improvement in collection efficiency and angular emission of the TPSP relative to its precursor, the cylindrical pillar. Following these idealized simulations, we showed that it is possible to fabricate such structures, highlighting the fabrication process and verifying their performance again through simulations.

Moving to Sec. 3.2, our goal was to characterize these newly fabricated devices. We began with a general, ODMR-based investigation to identify single NV structures, a subset of which we used to perform in-depth measurements of the saturation PL and power, lifetime, and charge state. In the process, we observed a median saturation PL photon count rate of 2.1 MHz – a factor of 5 higher than typical PL rates in the previous pillar models, and to our knowledge, the highest PL rates demonstrated for NV-based scanning probes to date. Having next presented a method to measure the charge state, we then used similar techniques to measure the charge-state corrected collection efficiency of the TPSP. The 57% collection efficiency that we were able to demonstrate again highlights the benefits of our TPSP design. To round out the comparison between measurements and simulations, we addressed the angular emission of these devices through BFP measurements, observing a median NA of 0.44. This value agrees well with simulation results and could, in the future, be used to further simplify and optimize our collection optics.

Finally, in Sec. 3.3, we returned to the question of sensitivity and spatial resolution introduced in Chap. 2. In particular, we observed a DC ODMR sensitivity of up to $1.2 \mu\text{T}/\sqrt{\text{Hz}}$ and a mean NV-to-sample distance of $69 \pm 13 \text{ nm}$. Though this does not represent a significant improvement in spatial resolution over past approaches, we have improved the sensitivity by a factor of 2 compared to previous estimates and measurements [85, 92].

3.4.1. Outlook

While these TPSPs exhibit some excellent properties, there is still room for further improvements. There are many, often complementary paths that one could take to improve both the sensitivity and spatial resolution of these devices. Here, we will present some of these directions.

The first possibility we will explore is the use of different diamond orientations. Thus far, we have restricted our discussion to (100)-oriented diamond, in which the NV is oriented at a 54° angle to the surface normal. However, this means that the NV dipole will exhibit both *s*- and *p*-polarized components, the latter of which experiences strong suppression in our diamond structures. For this reason, working with (111)-oriented diamond, where the NV may lie along the pillar axis, can be highly beneficial [120, 121]. This orientation would result in a solely *s*-polarized

dipole, which would produce the maximal PL rate. An additional benefit is that these (111)-oriented diamond probes simplify the magnetometry process, allowing us to measure the out-of-plane component of the stray magnetic field directly [79, 120].

A different route to improving the sensitivity of our devices is to stabilize the spin coherence and charge state of the NV, for example, through controlled surface termination [122, 123]. Furthermore, lower implantation densities or implantation of ^{12}C rather than nitrogen (where one would then use the natural nitrogen in the diamond as an NV) could reduce the defects that negatively impact the coherence times. However, both of these options would result in very low NV densities, necessitating the use of deterministic alignment, where one targets a particular NV when patterning the diamond pillars. Work along these lines has already begun in the group.

On the other hand, one can also focus on improvements of the TPSP itself. Though the parabolic tip of the pillar ensures that the majority of the emission impinges normal to the back surface of the cantilever, one still loses 17% of PL due to reflection from the diamond surface. Thus, adding an anti-reflection coating to the back surface of the pillar would further improve our collection efficiency, hence, our PL rate. An anti-reflection coating could be achieved through a ~ 100 nm film of SiO_2 ($n_{\text{SiO}_2} = 1.5$), a readily available material. The challenge here is to achieve a smooth coating following etching and cleaning of the diamond surface, which would likely remove any deposited oxide layers.

Though sensitivity is an important aspect of NV magnetometry, we have a second, critical parameter to improve - the NV-to-sample distance. One obvious path to improvement is obtaining shallower NV centers. This may be achieved through lower energies during implantation or through soft oxygen plasmas in which we remove nm's of diamond at a time, bringing deep NV centers closer to the surface [127]. However, shallow NV centers come with drawbacks, such as reduced coherence times. An alternative approach to achieving a higher spatial resolution is using overgrown diamond to achieve sharp, pyramidal-like pillars [124], as seen in Fig. 3.15a. Though this design of the pillar provides less high-quality waveguiding than the TPSP, the sharp point of the pyramidal tips ensures that the NV is always at the lowest point of the pillar, provided we can ensure that the NV is placed precisely at the tip of the pyramid. This is a challenge that is yet to be overcome.

To bring this chapter to an end, let us take a final look towards future forms of scanning magnetometry. Our current form of scanning setup involves atomic force microscopy-style scanning of the diamond cantilever and pillar, attached to a tuning fork through a thin, pulled quartz rod [29]. Both excitation and collection are then free-space and rely on our ability to collect the PL through an objective. However, one could also modify this to achieve a fiber-coupled sensor. By placing the diamond pillar directly on the end of an optical fiber, as shown in Fig. 3.15b, one can excite and read out the NV center directly, considerably reducing the need for optical elements, which lead to significant optical losses. Additionally, one could imagine placing the MW excitation antenna directly on the fiber, as seen in Fig. 3.15c [125], thereby leading to a compact scanning system. Such a scenario would also make this technique much more accessible for commercial users. We have made first attempts of such a fiber-coupled geometry, but to date, have observed only poor coupling between the NV PL and fiber core. Improving the match between the optical modes of the diamond pillar and the fiber is crucial and may be achieved by modifying either the pillar

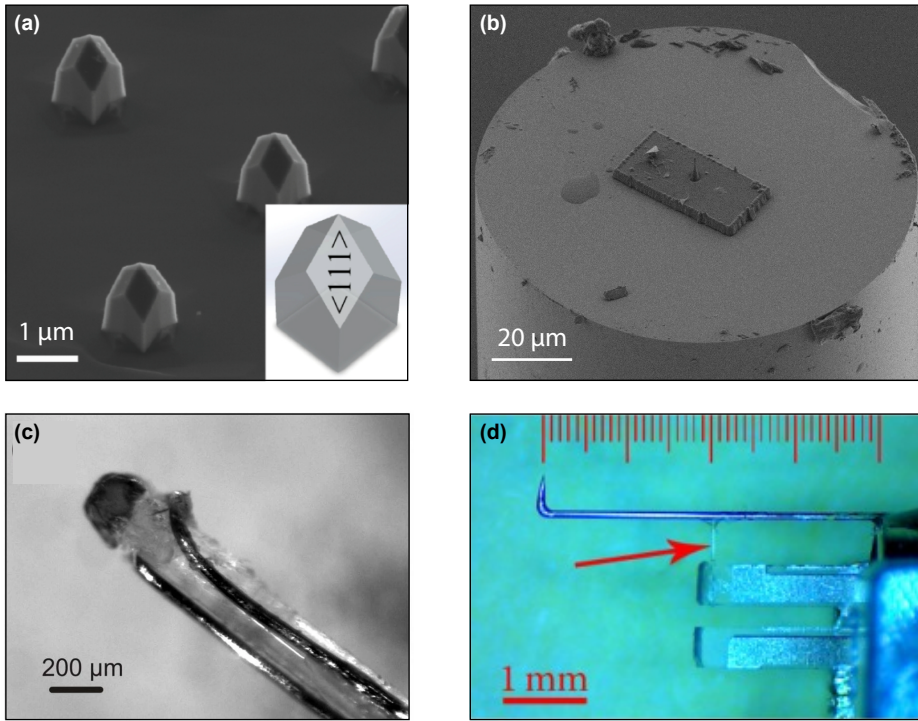


Figure 3.15.: Future directions for NV magnetometry (a) Overgrown diamond pillars exhibiting a sharp, pyramidal apex. Adapted with permission from [124]. (b) A scanning probe device glued to the end of an optical fiber for coupling to the NV. (c) A nanodiamond (dark) glued to the end of an optical fiber with a MW antenna brought close by wrapping a 50 μm copper wire around the fiber end. Reproduced with permission from [125]. (d) A bent, tapered optical fiber used for SNOM experiments. The fiber is glued to a tuning fork using a small glass rod to allow for scanning. Reproduced with permission from [126].

to have a larger base diameter or by reducing the lateral extent of the fiber. The latter is also important for realizing scanning, as the cladding diameter is typically much larger than the size of the diamond scanning probe. As such, tilting of the fiber would make achieving reliable scanning difficult. One possibility in this direction is to use current scanning nanoscale optical microscopy technology, which relies on bent, tapered optical fibers [126] as shown in Fig. 3.15d. Placing the diamond on the end of one of these structures could be an ideal scanning solution.

4. Mechanics of antiferromagnetic domain walls in Chromia

At this point, let us look back at our original motivation for this thesis. In Chap. 1, we highlighted some of the paths taken in the field of spintronics to address the question of improving the efficiency, reliability, and speed of modern computing and memory devices [128, 129]. Magnetic storage, for example, has the distinct advantage of being inexpensive and non-volatile. However, current technologies rely on ferromagnetic (FM) materials, which exhibit slow switching, require high switching currents or fields, and can be accidentally erased by applying strong, external magnetic fields. To combat these issues, antiferromagnetic (AFM) spintronics has focused on replacing these FM technologies with AFM ones. These materials have attracted much attention due to the promise of low energy costs and high switching speeds [130], all while being robust against external fields.

One material, which has drawn considerable interest from the AFM spintronics community is chromia (Cr_2O_3). Early records of this material date back to the 1830s as the primary component of certain green pigments [131]. It was not until about 130 years later that people became interested in Cr_2O_3 for its magnetic properties [132, 133]. Chromia remains AFM above room temperature and undergoes a second-order phase transition to a paramagnetic (PM) state at a Néel temperature $T_{\text{Néel}} = 307 \text{ K}$ [133, 134]. In 1960, Cr_2O_3 became the first material theorized to exhibit magnetoelectric properties, i.e., coupling between its magnetic and electric properties [132]. In the same year, this theory was confirmed experimentally [133]. Since then, many studies have focused on characterizing the magnetic structure of the material and harnessing these magnetoelectric properties. For example, it was realized quite early that one could control the magnetic order parameter through magnetoelectric annealing: the simultaneous application of magnetic and electric fields while cooling through the critical temperature [134, 135]. This procedure paved the way for later switching experiments [16, 17] and helped realize the first measurements of magnetic domains, regions of uniform magnetic orientation, in Cr_2O_3 .

However, despite all of these studies, there are still significant gaps in our knowledge regarding the underlying magnetic structure of Cr_2O_3 . For instance, there are no experimental studies that have measured the nanoscale magnetic structure of Cr_2O_3 . Furthermore, though direct imaging of domains in Cr_2O_3 has been achieved [136, 137], the boundaries between adjacent domains – the domain walls (DWs) – have remained more or less unexplored in experiments to date. In general, DWs play an important role in influencing advances in spintronics. Mobile DWs have, for example, been proposed as a key component of novel memory devices such as racetrack memories [7]. On a fundamental level, DWs can also yield information about underlying material properties [138], such as the presence of chiral energy terms. They may also demonstrate unique characteristics e.g., increased electrical conductivity, in comparison to

the rest of the material [139], which may be harnessed in applications. Thus, the understanding and control of DWs in any material, and in particular in chromia, may open up new avenues in AFM spintronics.

Our goal in this chapter is to address these knowledge gaps and expand our current understanding of DWs in Cr_2O_3 . We will begin with an introduction to the structure and material properties of Cr_2O_3 before investigating the magnetic signal of bulk Cr_2O_3 . We then present a study of DWs, which yielded unexpected, novel results on the DW mechanics. Finally, we will conclude by expanding into studies of thin-film chromia, which are of interest in technological applications. The success of these studies lies in the excellent magnetic field sensitivity and nanoscale resolution of the NV center introduced in Chapters 2 and 3.

All the measurements shown in this chapter have been performed on a home-built confocal NV magnetometry setup, equipped with a CW 532 nm excitation laser. Microwaves for spin manipulation are applied using a gold loop antenna. We additionally apply a small bias magnetic field along the NV axis to ensure quantitative imaging. For more details on this setup, see Appendix A.2.2. The majority of measurements are performed using the truncated parabolic scanning probe (TPSP) devices characterized in Chap. 3.2 and unless stated otherwise, all stray field images are obtained using feedback tracking of the ODMR spectrum. The bulk crystal results presented in the following chapter have been published in Ref. [140], and the submission of the thin film results is in progress at the time of writing.

4.1. Magnetism of Chromia

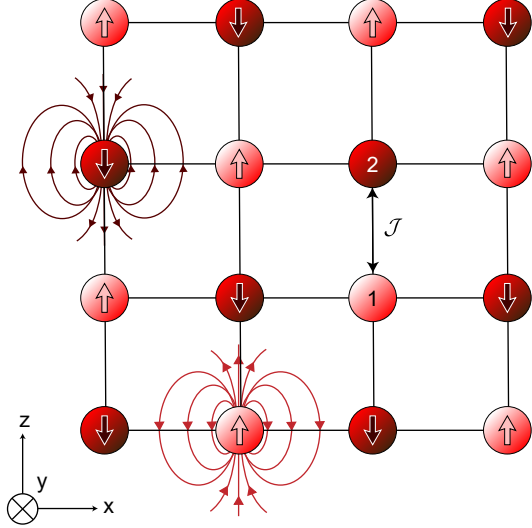
4.1.1. Introduction to Magnetic Order

Before exploring the specifics of Cr_2O_3 , we will consider a simplified magnetic system, which we will use to discuss the three most common energy terms in any magnetic material. This simple model will provide a framework within which to discuss the relevance of our later results and prepare the way for a discussion of DWs. We begin with a generic Heisenberg model, where every lattice point is occupied by a magnetic atom, as shown in Fig. 4.1. Each atom carries a magnetic moment, \mathbf{m} , which a priori, can point anywhere in 3D space. To understand the magnetic structure of such a lattice, we need to build up a Hamiltonian based on the interactions at a single lattice site, between nearest neighbors (e.g., 1-2 in Fig. 4.1), next-nearest neighbors, and so on.

We will restrict ourselves to three magnetic energy terms, the first being the magnetic anisotropy. This term describes the tendency for the magnetic moments to align to a particular, energetically favorable direction, primarily due to spin-orbit coupling [141]. Here we will assume a uniaxial magnetocrystalline anisotropy, as present in Cr_2O_3 . In this case, the crystal structure introduces a single axis along which the lattice spins will align to reduce the overall energy, also known as the easy axis. This energy contribution can be described as follows:

$$\mathcal{H}_{\text{an}} = \frac{-\mathcal{K}_u S^2}{2} \sum_i (\mu_i^z)^2, \quad (4.1)$$

Figure 4.1.: Magnetic interactions on a lattice. Each lattice point (red circles) represents a magnetic atom. Exchange interactions (\mathcal{J}) between nearest neighbors (e.g., 1-2) are AFM, and those between next-nearest neighbors are FM. Single-site uniaxial anisotropy leads to a preferential orientation along the easy-axis (here, the z -axis). Dipolar interactions arise due to the magnetic fields generated by each magnetic atom.



where \mathcal{K}_u is the uniaxial anisotropy constant, S is the spin length, and $\boldsymbol{\mu}_i$ is the unit vector representing the direction of the magnetic moment on the i -th lattice site. In particular, in Fig. 4.1, we select an easy axis pointing along the z -direction, $\mathcal{K}_u > 0$. For $\mathcal{K}_u < 0$, the magnetic moments will tend to align to an easy-plane, in this case, parallel to the xy plane.

The next energy term we consider is the exchange energy. This ubiquitous interaction arises due to the Pauli exclusion principle in the overlapping of atomic orbitals of two lattice sites and may be described as follows:

$$\mathcal{H}_{\text{ex}} = \frac{\mathcal{J}S^2}{2} \sum_{i,\delta} (\boldsymbol{\mu}_i \cdot \boldsymbol{\mu}_\delta). \quad (4.2)$$

Note that the exchange interaction tends to be short-range, and so the sum is over nearest neighbors (δ) of lattice site i . Furthermore, \mathcal{J} is the exchange parameter. If $\mathcal{J} < 0$, then the interacting spins will align parallel to each other i.e., ferromagnetically, whereas $\mathcal{J} > 0$ leads to anti-parallel i.e., AFM alignment as seen in Fig. 4.1. We highlight the AFM coupling by coloring the magnetic atoms either light red or dark red according to their spin orientation (spin up and down, respectively).

The last energy term we will discuss here is the dipolar energy. Though weak in comparison to the other two terms, it has a considerable long-range effect. Here, each dipole in the lattice is affected by the magnetic field generated by the others, as shown in the bottom left of Fig. 4.1. This interaction may be written as follows:

$$\mathcal{H}_{di} = \frac{\mu_0 g^2 \mu_B^2 S^2}{8\pi} \sum_{i \neq j} \left[\frac{\boldsymbol{\mu}_i \cdot \boldsymbol{\mu}_j}{r_{ij}^3} - \frac{3(\boldsymbol{\mu}_i \cdot \mathbf{r}_{ij})(\boldsymbol{\mu}_j \cdot \mathbf{r}_{ij})}{r_{ij}^5} \right], \quad (4.3)$$

where g is the g -factor of the atom on the lattice sites, μ_0 is the vacuum permeability, μ_B is the Bohr magneton, and \mathbf{r}_{ij} is the vector connecting lattice site i to site j .

These long-range dipolar interactions play an important role in FMs as the primary source of stray fields; in AFMs, this term will be small and can often be ignored.

These are by no means the only interaction terms that may be present in magnetic systems. We have, for instance, ignored the Dzyaloshinskii-Moriya interaction (DMI), which introduces chirality [141, 142]. However, these three terms represent the most important energy contributions and are sufficient to describe a wide range of physical phenomena. In particular, this discussion may be applied to any uniaxial, achiral AFM, including chromia, as we will see in Sec. 4.1.3.

4.1.2. Magnetoelectricity

As previously discussed, initial interest in Cr_2O_3 developed due to its magnetoelectric properties. To understand the origin of this particular property, let us first write down the general form of the free energy i.e., the energy stored by the magnetic or electric field per unit volume, for a magnetoelectric dielectric medium [143]:

$$F = F_0 + \frac{1}{2} \mathbf{H} \cdot \mathbf{B} + \frac{1}{2} \mathbf{E} \cdot \mathbf{D} - \boldsymbol{\alpha} \mathbf{E} \cdot \mathbf{B}. \quad (4.4)$$

Here, F_0 is the energy in the absence of external fields, and \mathbf{B} and \mathbf{H} are the magnetic flux density and magnetic intensity, respectively. Similarly, \mathbf{E} and \mathbf{D} represent the electric and displacement fields. The crucial component for a magnetoelectric medium is the last term in Eq. 4.4, which involves the magnetoelectric susceptibility tensor $\boldsymbol{\alpha}$. Expanding these terms (see Ref.[144]) and taking the derivative of the free energy with respect to E and H , one obtains the typical description of the polarization and magnetization of a linear magnetoelectric material such as Cr_2O_3 :

$$\begin{aligned} P_i &= -\frac{\partial F}{\partial E_i} \\ &= \chi_{ij}^e E_j + \alpha_{ij} B_j, \end{aligned} \quad (4.5)$$

and

$$\begin{aligned} M_i &= -\frac{\partial F}{\partial B_i} \\ &= \chi_{ij}^m B_j + \alpha_{ij} E_j. \end{aligned} \quad (4.6)$$

Here, $\chi_{ij}^{m(e)}$ is the magnetic (electric) susceptibility and repeated indices represent a sum over those terms. From these equations, we see that, as expected, the electric field will induce a polarization and the magnetic field induces a magnetization. However, due to the presence of the magnetoelectric susceptibility, applying an electric field to a magnetoelectric material will also induce a magnetization, and vice versa, applying a magnetic field induces an electric polarization. This interplay of the electric and magnetic properties is particularly interesting for applications, as it enables the switching and readout of the material's magnetic state through the application of electric [16, 17, 145] or magnetic [146] fields.

The key ingredient for obtaining a magnetoelectric response is the crystal symmetry, specifically, symmetry breaking [132, 147]. Let us consider two particular symmetries – spatial inversion and time-inversion – which will lead to a sign change in \mathbf{E} and

\mathbf{B} , respectively [147]. Applying these properties to the expression in Eq. 4.4, we see that the second and third terms remain invariant under these individual symmetry operations, but the $\mathbf{E} \cdot \mathbf{B}$ product in the final term will change its sign. One important requirement for the free energy of a system is that it remains invariant under symmetry operations corresponding to the symmetry of the crystal [148]. As such, in order to have a non-zero magnetoelectric term in the free energy, the crystal must break both time-reversal and spatial inversion symmetries. In magnetic crystals such as Cr_2O_3 , the breaking of these symmetries results from the magnetic ordering, which we will explore in the next section.

4.1.3. Chromia

In Sec. 4.1.1, we developed a general model of AFM order in a square lattice. Here, we will now explore how to adapt this treatment based on the specific crystal structure of Cr_2O_3 . On an atomic scale, Cr_2O_3 has a corundum-type crystal structure with a rhombohedral primitive unit cell illustrated in Fig. 4.2a. Though not all ions are shown, each Cr^{3+} ion is bound to six O^{2-} ions, forming slightly distorted octahedrons. For a [001]-oriented Cr_2O_3 crystal, which will be the focus in this chapter, the moments of these ions are antiferromagnetically coupled along the z -axis [149] as shown in Fig. 4.2a. The unit cell picture can also be extended to include a larger portion of the crystal. In Fig. 4.2b, we show two cross-sections of the crystal along the (100) plane, highlighting two potential spin orientations in the lattice. We will now use the hexagonal lattice description of Cr_2O_3 and the corresponding crystal axes, c and a , as shown to the right. Here, the O ions appear as single layers separating the Cr ions. We also number the Cr ions to draw attention to the parallels between this atomic structure and the unit cell in Fig. 4.2a. Importantly, this picture highlights the development of the up-down-up-down structure of magnetic moments on the Cr ions, indicative of long-range AFM order.

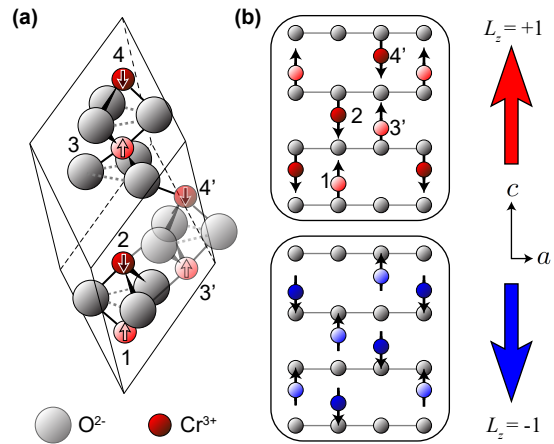


Figure 4.2.: Crystal and spin structure of Cr_2O_3 . (a) The rhombohedral primitive unit cell of Cr_2O_3 showing the positions of the Cr and O ions. Note that not all O ions in the unit cell are shown for clarity. Instead, we show the bonds to the next unit cell with semi-transparent lines. The magnetic moment of the Cr ions is shown with an arrow. (b) Simplified lattice structure highlighting two magnetic states of Cr_2O_3 with opposite Néel vectors. The numbering of the Cr ions is used to compare equivalent atoms in (a) and (b).

Each Cr ion in the antiferromagnetically coupled pairs (1-2 and 3-4) can be assigned to one of two sublattices. In Fig. 4.2, we color these sublattices with different shades to emphasize the difference between magnetic moments pointing up (light) or down (dark). Note that within a given sublattice, the spins are ordered ferromagnetically. Furthermore, this structure allows us to address the symmetry breaking mentioned in the previous section. Structurally, the unit cell of Cr_2O_3 , as seen in Fig. 4.2a, has an inversion center in the center of the cell. However, with the magnetic ordering of the Cr ions, inversion around this point will lead to a reversal of the magnetic moments. Similarly, time-reversal will also lead to a reversal of each magnetic moment, and so we see that the magnetic ordering breaks both inversion and time-reversal symmetries.

Let us now return to the general model introduced in Sec. 4.1.1. If we wish to apply this simple, cubic model to Cr_2O_3 , we must understand how the energy terms need to be adapted to achieve an accurate representation. The first energy term is dominated by a uniaxial, magnetocrystalline anisotropy leading to a $\mathcal{K}_u > 0$. However, magnetoelastic contributions due to tension in the crystal may modify the anisotropy constant. As such, we account for such variations through the use of an effective anisotropy constant \mathcal{K} [150, 151].

The exchange mechanism in Cr_2O_3 is less straight forward. For a long time, it was disputed due to the complicated crystal structure [152, 153]. However, recent derivations of the magnetic structure from first-principles seem to suggest that the exchange interaction is indeed dominated by nearest-neighbor interactions i.e., between atoms 1 and 2 as introduced in Eq. 4.2 [149, 154]. Therefore, the exchange term in Cr_2O_3 may be described by the same functional form, with an effective exchange constant $\mathcal{J}' > 0$.

Finally, the dipolar contribution in Cr_2O_3 is typically more than two orders of magnitude smaller than the anisotropy [155], meaning that it can be ignored in our description. As such, we obtain the following spin-lattice Hamiltonian:

$$\mathcal{H} = \mathcal{H}_{ex} + \mathcal{H}_{an} = \frac{\mathcal{J}' S^2}{2} \sum_{i,\delta} (\boldsymbol{\mu}_i \cdot \boldsymbol{\mu}_\delta) - \frac{\mathcal{K} S^2}{2} \sum_i (\mu_i^z)^2, \quad (4.7)$$

where the sum in the exchange term is over nearest neighbors belonging to opposite sublattices.

For a two-sublattice AFM as Cr_2O_3 , it is convenient to introduce two vector quantities. The first is the total magnetization vector \mathbf{M} :

$$\mathbf{M} = (\boldsymbol{\mu}_1 + \boldsymbol{\mu}_2) / 2. \quad (4.8)$$

While this vector represents the primary order parameter in FMs, in Cr_2O_3 , the two magnetic moments are ideally equal and opposite, leading to $|\mathbf{M}| = 0$. The vanishing magnetization is one of the key properties of collinear AFMs such as Cr_2O_3 , where the spins point precisely opposite each other. It is this lack of overall magnetic moment that makes AFMs robust against external magnetic fields.

Though there is no net magnetization, we can still define a second vector quantity, known as the Néel vector or Néel order parameter, \mathbf{L}^1 :

$$\mathbf{L} = (\boldsymbol{\mu}_1 - \boldsymbol{\mu}_2) / 2. \quad (4.9)$$

¹Typically, \mathbf{L} may be defined as $\mathbf{L} = \boldsymbol{\mu}_1 - \boldsymbol{\mu}_2 + \boldsymbol{\mu}_3 - \boldsymbol{\mu}_4$ [141]. However, as $\boldsymbol{\mu}_1 = \boldsymbol{\mu}_3$ and $\boldsymbol{\mu}_2 = \boldsymbol{\mu}_4$ in our case, we can simplify \mathbf{L} to the form in Eq. 4.9.

Analogously to \mathbf{M} in FMs, \mathbf{L} will be used to describe the magnetic ordering of the Cr_2O_3 domains. In particular, the direction of \mathbf{L} for the two magnetic orientations in Fig. 4.2b is shown to the right of the figure as a bold arrow.

Up to now, we have focused on an atomic lattice model, which is useful for simulations and when addressing the magnetic structure on an atomic level. However, when discussing magnetic structures such as DWs in the nanoscale regime, it is often necessary to describe the system based on a micromagnetic i.e., continuum formalism. In particular, this requires reframing Eq. 4.7 in the micromagnetic limit. Using the Néel vector we just introduced, our Hamiltonian description will be equivalent to the following [156]:

$$\mathcal{E} = A \int \sum_{\nu=x,y,z} (\partial_\nu \mathbf{L})^2 d\mathbf{r} + K \int (1 - L_z^2) d\mathbf{r}. \quad (4.10)$$

Here, the first term is the exchange energy, and the second term here is the anisotropy. Note that we have also introduced new constants, specifically A , the exchange stiffness constant. Note that A and K may be related to the lattice-defined constants through the following relations: $A = \mathcal{J}' S^2 / 2a$ and $K = \mathcal{K} S^2 / 2a^3$, where a is the lattice constant [142].

4.1.4. Surface magnetization

In Eq. 4.8, we have stated that the overall magnetization \mathbf{M} of Cr_2O_3 vanishes. However, the existence of a non-zero surface moment density is well-supported by experiments [26, 145, 157]. Currently, there are several alternative descriptions to describe the origin of this surface moment.

We will begin with a structural argument by considering the surface of Cr_2O_3 . Though the exact (001) surface termination is disputed, particularly in ambient conditions [158–160], it is believed that the most stable termination is the one shown in Fig. 4.3a. Here, the (001) surface bisects one Cr ion pair (e.g., 1-2 as shown in Fig. 4.2a), leading to a single sublattice of spins on the top. The opposite spin sublattice will be present at the bottom surface of the crystal to maintain the overall compensation of spins. One important feature of this termination is that it is robust against surface roughness [26, 145]. Thus, though each up-pointing sublattice site is compensated by a down-pointing sublattice site, leading to an overall $\mathbf{M} = 0$, the spatial separation of the top and bottom surface results in a locally uncompensated moment layer. If this is indeed the correct termination, we would expect one Cr ion per unit cell, carrying a moment of $3\mu_B$ in the fully magnetized state. As the hexagonal Cr_2O_3 unit cell has a cross-sectional surface area of 0.2 nm^2 at the (001) surface, this would give a surface magnetization of $\sim 14 \mu_B / \text{nm}^2$.

Alternatively, one can apply the same symmetry properties used to motivate the magnetoelectric properties of Cr_2O_3 to explain the origin of an intrinsic surface magnetization [161, 162]. As these arguments do not rely on a given surface termination, a surface magnetization is expected to be present in all magnetoelectric materials. One method is to consider the magnetic symmetry of Cr_2O_3 in the presence of the surface normal vector \mathbf{n}_s . It has been argued that \mathbf{n}_s reduces the magnetic point group analogously to an electric field [162]. In a magnetoelectric material where an applied electric field induces a magnetization, the existence of the electric field-like

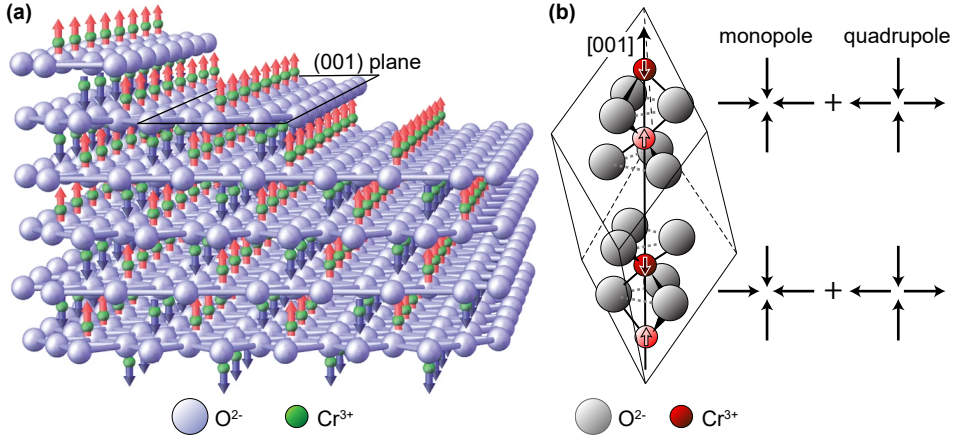


Figure 4.3.: Origin of the surface magnetic moment. (a) The lattice structure of Cr_2O_3 showing the extended lattice of O (gray) and Cr (green) ions. The structure is terminated by a spin-polarized layer, independent of steps in the (001) surface highlighted in black. On the other hand, the bulk of the lattice hosts both sublattices, which then compensate each other. Modified from [145] with permission from Springer Nature: Nature Materials (2010). (b) The unit cell of Cr_2O_3 now showing all atoms within the cell with the [001] axis shown. The moments of the Cr ions can be represented by a negative magnetoelectric monopole moment and additional quadrupole moments, as shown to the right [161].

surface normal should then induce an equivalent surface magnetization [162]. However, Ref. [162] provides no quantitative value for the surface moment.

A closely related but more quantitative method of arguing a surface moment was recently given by Spaldin [161]. Recall that in Sec. 4.1.2, we argued that inversion and time-reversal symmetry breaking is necessary to explain the existence of the magnetoelectric effect. In Ref. [161], the same symmetry breaking arguments are used to decompose the magnetic structure of Cr_2O_3 into magnetoelectric monopolar and quadrupolar terms, as shown in Fig. 4.3b. When summed over a semi-infinite plane, this multipolar expansion leads to an intrinsic surface magnetization σ_m . Spaldin presents two estimates of σ_m depending on the surface termination, namely $2.4 \mu_B/\text{nm}^2$ for a (001) surface cleaving at the oxygen plane (see Fig. 4.2b) or $12.0 \mu_B/\text{nm}^2$ for the termination shown in Fig. 4.3a. In this description, we have the additional effect that the quadrupolar terms cancel out, leading to no net magnetization on surfaces perpendicular to the (001) plane.

We can also use this multipolization technique to make a statement on the energetics of the system. Let us shortly look back at the magnetoelectric free energy term in Eq. 4.4, which we wrote as $F_{\text{me}} = -\alpha_{ij} E_i B_j$. If we then apply, for example, parallel electric and magnetic fields along the c axis of the crystal, the minimal F_{me} energy will be achieved for a positive value of α_{ij} , corresponding in turn to one of the two order parameters introduced in Eq. 4.9. Conversely, anti-parallel magnetic and electric fields will favor the opposite order parameter. If this description holds, one should be able

to use this behavior to prepare a particular magnetic state through magnetoelectric annealing [135] and ideally relate the prepared state to one of the two possible surface terminations mentioned above. These two points will be explored in more detail in Sec. 4.2.2.

Regardless of the origin, two essential aspects of this surface magnetization are maintained. Firstly, the surface magnetization is roughness insensitive. That is, the presence of steps at the material boundary does not change the direction or magnitude of the surface magnetization. Secondly, the surface magnetization will be intrinsically linked to the bulk magnetic order. This second point is very relevant as it allows us to access \mathbf{L} through magnetometry.

4.1.5. Measuring the surface magnetization

We have now spent quite some time developing a model of Cr_2O_3 and explaining its theoretical magnetic structure. After this detailed introduction, we will begin our investigation of Cr_2O_3 with a pristine single crystal. All bulk Cr_2O_3 measurements presented here have been performed on half of a $5\text{ mm} \times 5\text{ mm}$ square, 1 mm-thick, single crystal of Cr_2O_3 (Mateck) with (001) surface termination polished to a roughness below 2 nm as verified with atomic force microscopy. Our goal here will be to confirm the value of the surface magnetization presented in the previous section.

Unfortunately, this pristine surface poses an issue for NV magnetometry. Early characterization of the crystal with second harmonic generation [136] indicates that these crystals tend to form mm-sized domains. Over typical length scales for NV magnetometry imaging ($\sim 50\text{ }\mu\text{m}$), the crystal will therefore appear to be uniformly magnetized, resulting in negligibly small magnetic stray fields. One solution to this problem is to introduce topographic steps through fabrication. Though atomic steps provide no measurable stray field², changes in the surface height of many 10's of nanometers can produce sizable fields thanks to the vertical displacement of the surface moments on the top and bottom surface of the step [26]. Therefore, we pattern a series of rectangular, $10\text{ }\mu\text{m} \times 2\text{ }\mu\text{m}$ masks using the same FOx-based electron beam lithography as described in Chap. 3.1.3. We then etch the surface of the crystal with an Ar/Cl_2 -based RIE ICP plasma, and upon removal of the mask, are left with a uniform grid of micron-scale mesas with a mean height $\bar{t} = 166(4)\text{ nm}$ and width $\bar{w} = 2.4(3)\text{ }\mu\text{m}$, as shown in Fig. 4.4a. Details of this etching process may be found in Appendix A.1.2.

Similar to our discussion in Chap. 3.3.2, we model the stray field of the patterned mesas as arising from two currents located at the top and bottom edges of the step as shown in Fig. 4.4b. We then use this model to extract the surface magnetization σ_m of the sample. Assuming a mesa oriented along the y -direction, we obtain the following two-current description of the stray magnetic field from a single edge, projected on the NV axis [24]:

²For a 2.5 nm step and a mean $d_{\text{NV}} = 69\text{ nm}$ (see Chap. 3.3.2), we expect a stray field of $0.89\text{ }\mu\text{T}$. This value is well within our noise level.

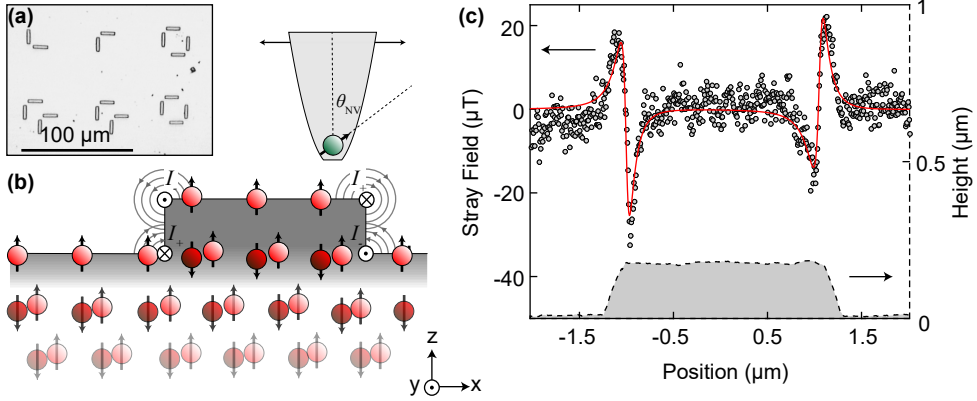


Figure 4.4.: Investigating the surface magnetization of Cr_2O_3 . (a) The surface of the Cr_2O_3 crystal following fabrication. Here, each rectangular mesa is $\sim 10\mu\text{m} \times 2\mu\text{m}$ in size. (b) Depiction of a uniformly magnetized mesa structure with a (001) termination showing the magnetic moments of the Cr ions. The resulting surface magnetization leads to a stray field that can be modeled as four currents running along the edges of the mesa, shown here with gray arrows. (c) Stray field and topography of a representative mesa, measured using NV magnetometry. The stray field is fit by Eq. 4.11 (red line) resulting in $\sigma_m = 2.4 \pm 0.2 \mu_B/\text{nm}^2$, $d_{\text{NV, left}} = 46 \pm 3 \text{ nm}$ and $d_{\text{NV, right}} = 53 \pm 3 \text{ nm}$. The topography (gray area with dashed line) is scaled by independent atomic force microscopy measurements.

$$B_{\text{NV}} = \sin \theta_{\text{NV}} \cos \phi_{\text{NV}} B_x + \sin \theta_{\text{NV}} \sin \phi_{\text{NV}} B_y + \cos \theta_{\text{NV}} B_z, \text{ where}$$

$$\begin{aligned} B_x &= \frac{-\mu_0 \sigma_m}{2\pi} \left(\frac{d_{\text{NV}}}{(x - x_0)^2 + d_{\text{NV}}^2} - \frac{(d_{\text{NV}} + t)}{(x - x_0)^2 + (d_{\text{NV}} + t)^2} \right), \\ B_y &= 0, \text{ and} \\ B_z &= \frac{\mu_0 \sigma_m}{2\pi} \left(\frac{x - x_0}{(x - x_0)^2 + d_{\text{NV}}^2} - \frac{x - x_0}{(x - x_0)^2 + (d_{\text{NV}} + t)^2} \right). \end{aligned} \quad (4.11)$$

Here, d_{NV} is the distance between NV and sample as before, t is the mesa thickness, x_0 is the location of the mesa edge, and θ_{NV} and ϕ_{NV} are the polar and azimuthal angles of the NV axis, respectively. As this model describes only one edge of the mesa, we can also allow for different d_{NV} values for the left- and right-hand sides. Such offsets may arise due to a tilting of the scanning probe away from the sample normal [120].

Due to the many fit parameters in Eq. 4.11, faithfully extracting σ_m from data is not trivial. As such, narrowing down sources of error for the other parameters, such as the NV angles, is an important task. For a given NV center, the diamond structure will limit the possible polar and azimuthal angles, but extracting the exact values of θ_{NV} and ϕ_{NV} requires further characterization. To overcome this difficulty, we examine the surface magnetization by measuring 29 independent line scans, all taken with the same scanning probe across multiple mesas with different orientations

relative to the NV axis. By changing the relative orientation between the NV axis and mesa, we can examine different magnetic field projections, thereby helping us narrow down the NV angles. Another source of uncertainty is the width and height of the mesa, which are independently determined through comparison to atomic force microscopy measurements of the topography (see Appendix A.2.2).

We analyzed these 29 line scans by fitting our model in Eq. 4.11 to the data using the Metropolis-Hastings (MH) algorithm (see Appendix A.6 for details). The algorithm outputs a set of likelihood distributions for each of the fitting parameters from which we estimate σ_m , d_{NV} , θ_{NV} , and ϕ_{NV} together with their uncertainties. The advantage of the MH algorithm is that it allows us to easily explore a wide range of starting parameters to ensure that we reach the overall best fit. In this way, we can also improve our determination of d_{NV} and σ_m .

An example of one such fit, performed at room temperature, is shown in Fig. 4.4c. We repeat this procedure for each of the 29 line scans and combine the resulting distributions for the NV angles. In doing so, we find that our NV center is described by the following angles, $\theta_{\text{NV}} = 60.7^\circ \pm 2.9^\circ$ and $\phi_{\text{NV}} = 260.6^\circ \pm 0.8^\circ$. In Fig. 4.4c the fit also yields two different values of d_{NV} , for either side of the mesa: $d_{\text{NV, left}} = 46 \pm 3$ nm and $d_{\text{NV, right}} = 53 \pm 3$ nm. This difference is an indication that there may indeed be a small tilt of the pillar.

From our fits, we extract $\sigma_m = 2.4 \pm 0.2 \mu_B/\text{nm}^2$, which agrees well with other measurements [26, 157]. If σ_m is linked to the bulk Néel vector, we should also observe that σ_m follows the same temperature dependence as expected for $|\mathbf{L}|$. In particular, we should see the surface magnetization disappear at $T_{\text{Néel}} \approx 307$ K and a critical behavior mirroring that of $|\mathbf{L}|$ below $T_{\text{Néel}}$. For this reason, the aforementioned line scans were also taken at a range of global sample temperatures from room temperature (~ 296 K) up to ~ 340 K.

The results of the stray field analysis as a function of temperature are summarized in Fig. 4.5. Here, we plot the mean of σ_m for each measurement in light gray. The gray bars show the range of potential values, extracted as shown in right-hand plot, and based on the Gaussian likelihood distributions. In black, we give the mean and standard deviation of the set σ_m measurements performed at a given temperature. In particular, focusing on the results taken at room temperature, we observe a mean surface magnetization $\bar{\sigma}_m = \pm (2.1 \pm 0.3) \mu_B/\text{nm}^2$.

To analyze the temperature-dependence of these data, we fit them with a power law:

$$\sigma_m = \sigma_{m_0} \left(1 - \frac{T - T_0}{T_{\text{Néel}}} \right)^\beta. \quad (4.12)$$

Here, β is the critical exponent. In this case, β describes the evolution of the magnetic order parameter near a second-order phase transition. Furthermore, σ_{m_0} is the surface magnetization at low temperatures, and T_0 is a temperature offset used to take into account the temperature calibration uncertainty (see Appendix A.2.3). We have assumed an ideal bulk $T_{\text{Néel}}$ of 307 K, which is reasonable in the absence of excessive strain [163] or doping [164].

Our fit results in $|\sigma_{m_0}| = 5.5 \pm 0.9 \mu_B/\text{nm}^2$, $T_0 = -2.0 \pm 0.1$ K and $\beta = 0.24 \pm 0.04$. Here, T_0 falls within our temperature calibration uncertainty. Moreover, the value of β agrees well with previous measurements performed on a similar Cr_2O_3 crystal [165].

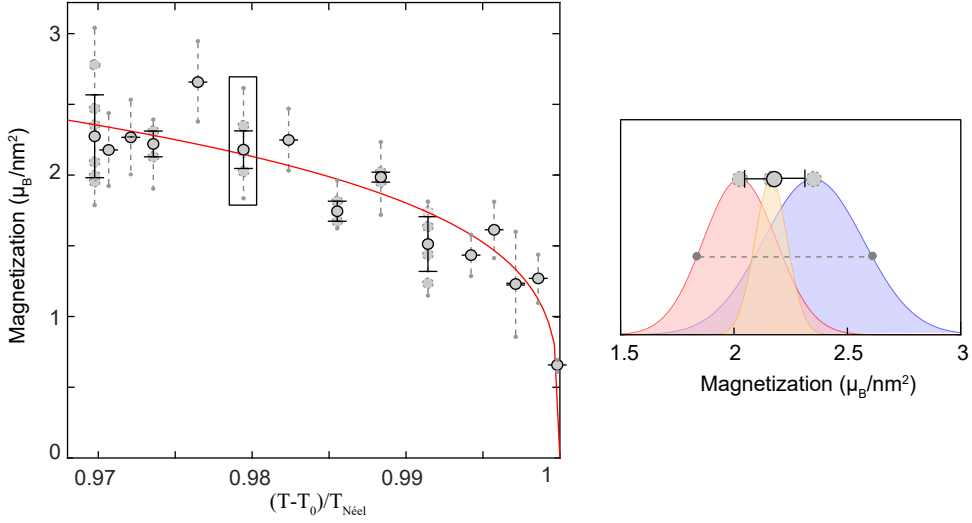


Figure 4.5.: Temperature dependence of σ_m . Measured surface magnetization as a function of the relative temperature, fit with Eq. 4.12 in red. A solid gray circle shows the mean at each temperature, while each measurement is presented with a dashed gray circle. The solid error bars show the standard deviation of the measurements at a given temperature. As each instance of σ_m is determined by a fit to the Gaussian likelihood distribution arising from the MH algorithm, we also show the maximum and minimum values of σ_m (measured at half max) with a gray dashed line. The right-hand panel shows how each component is determined based on the data points highlighted in the main figure with a black box. The normalized likelihood distribution of each measurement is shown with colored curves, where the mean of each is highlighted with a gray circle. As in the main figure, we highlight the maximum and minimum values with a gray dashed line. The overall mean and standard deviation is shown with a solid circle and black error bars.

In Ref. [165], Borisov et al. identify a bulk-defined $\beta \approx 0.2 - 0.3$. They additionally show a cross-over regime within 1 K of the Néel temperature, where $\beta \rightarrow 0.8$, which they attribute to the surface of the crystal. As we fit our data far from this cross-over temperature, our measured value of β supports the fact that the magnetization is indeed linked to the bulk ordering.

As such, we have shown that we can directly measure the roughness-insensitive surface magnetization of Cr_2O_3 using scanning NV magnetometry. We have identified a room temperature value $\sigma_m = 2.1 \pm 0.3 \mu_B/\text{nm}^2$, surprisingly close to the estimate made by Spaldin for an oxygen-terminated (001) surface at zero temperature [161]. However, as these estimates are likely based on low-temperature approximations, a more appropriate comparison would be $\sigma_{m0} = 5.5 \pm 0.9 \mu_B/\text{nm}^2$. Unfortunately, this value is not consistent with any of the estimates given in Sec. 4.1.4. It is possible though, that the Cr-terminated surface becomes disordered near room temperature, resulting in a reduced magnetization. We will explore this further in Sec. 4.2.2.

4.2. Domain walls in Chromia

Thus far, we have always implicitly assumed a mono-domain state with a homogeneous order parameter. Though this is useful for exploring the surface magnetization, the material information we can learn from such a magnetic state is limited. Instead, we are interested in an inhomogeneous magnetization, where the material is split into regions of differing \mathbf{L} i.e., magnetic domains. On a fundamental level, understanding domain formation and domain structure can yield important information about the exchange interactions and anisotropy of magnetic materials. Furthermore, these domains are of great interest in the spintronics and magnetics community, for instance, for their use in storing information [7]. In FM materials, the formation of magnetic domains is a natural consequence of minimizing the strong, long-range dipolar interactions that otherwise lead to a significant external stray field. There is no such energetic advantage for an ideal AFM with no net magnetization and no stray fields.

Nevertheless, the existence of domains in Cr_2O_3 was established early on [134, 136, 166]. However, little experimental evidence exists on the transition between two domains in Cr_2O_3 . In this region i.e., the DW, the spins must rotate from one order parameter orientation to another. We will spend this section investigating DWs in Cr_2O_3 , harnessing the nanoscale resolution of NV magnetometry in an attempt to observe the internal structure of the DW.

4.2.1. Introduction to domain walls

Let us begin by looking into a theoretical description of these DWs. Due to the uniaxial anisotropy along the c -axis in bulk Cr_2O_3 , $\mathbf{L} = \pm \mathbf{e}_z$ within a domain. Therefore, between two domains with opposite order parameters, the spins must rotate 180° , as shown in Fig. 4.6a. We can also use the Néel vector to provide a simplified picture of the DW, as shown in Fig. 4.6b. In particular, we define the plane of the DW ξ , as being the surface where $L_z = 0$. Generally, the spins of a 180° DW will rotate in a given plane at an angle ϕ_{DW} relative to ξ . However, we often deal with two special cases where either $\phi_{\text{DW}} = 0$, such that the spins rotate within the ξ plane as shown in the top panel of Fig. 4.6b, or $\phi_{\text{DW}} = \pi/2$, such that the rotation is perpendicular to the ξ plane as shown in the bottom panel. These two cases are known as Bloch and Néel DWs, respectively.

To find the exact form of the rotation within these DWs, we will return to Eq. 4.10. Here, we introduced the energy of chromia in our simple model using the Néel order parameter:

$$\mathcal{E} = \int \left[A \left((\partial_x \mathbf{L})^2 + (\partial_y \mathbf{L})^2 + (\partial_z \mathbf{L})^2 \right) + K (1 - L_z^2) \right] d\mathbf{r}. \quad (4.13)$$

Let us first frame this in a local spherical coordinate system such that $\mathbf{L} = (\cos \phi_{\text{DW}} \sin \theta, \sin \phi_{\text{DW}} \sin \theta, \cos \theta)$. For a given DW, ϕ_{DW} will be constant, while θ varies across the DW. In the absence of chiral terms, which tend to prefer a Néel DW, the DWs will be predominantly Bloch. Therefore, we will focus on the Bloch DW as shown in the top panel of Fig. 4.6b, where ξ lies parallel to the xz plane, and the DW extends along the x -direction. In this case, $\phi_{\text{DW}} = 0$, and so $\mathbf{L} = (\sin \theta, 0, \cos \theta)$.

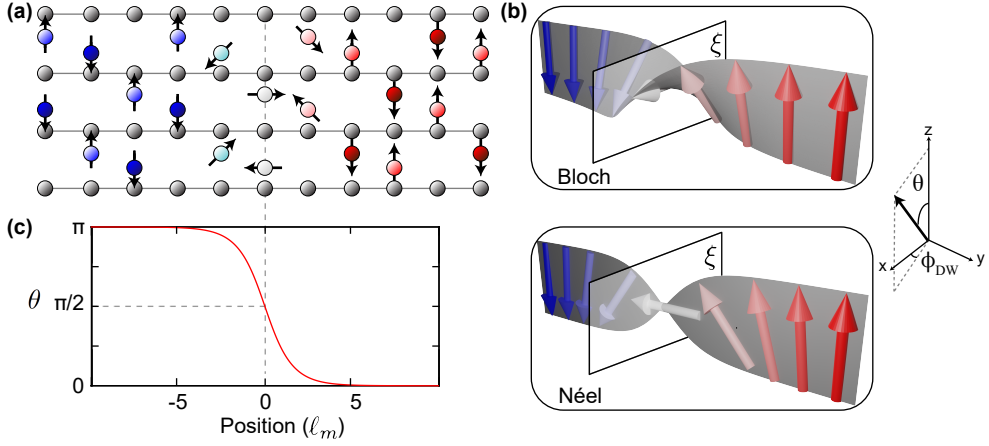


Figure 4.6.: Introduction to DWs. (a) Simplified lattice illustrating the rotation of the magnetic moments between two domains with differing Néel vectors. Here we show a Néel DW. (b) Néel vector representations of Bloch (top) and Néel (bottom) DWs relative to the DW plane ξ , defined as the plane in which $L_z = 0$. The axes to the right show the spatial orientation of these representations. (c) DW profile showing the change in θ for the negative solution in Eq. 4.15, as a function of position (in units of the magnetic length ℓ_m) normal to ξ . This result is independent of ϕ_{DW} . Dashed lines highlight the location of the DW surface.

Substituting this into Eq. 4.13, we find that:

$$\mathcal{E} = \int \left[A \left(\frac{d\theta}{dy} \right)^2 + K \sin^2 \theta \right] dy. \quad (4.14)$$

Determining the DW form now reduces to finding the angular progression that minimizes this energy. Solving this energy minimization problem yields the following angular profile:

$$\theta(y) = 2 \tan^{-1} \left(e^{\pm y/\ell_m} \right), \quad (4.15)$$

where $\ell_m = \sqrt{A/K}$ is called the magnetic length and is used to characterize the DW width. Thus, the width of the DW is determined by the exchange and anisotropy constants, a key result that will be used throughout this chapter. We plot this result in Fig. 4.6c. Note that the results we have shown here hold for not only both Bloch and Néel DW cases, but any angle ϕ_{DW} (a more general and detailed derivation may be found in Appendix A.5.1). The total symmetric exchange and anisotropy energies alone will not differentiate between the two DW types. To lift the degeneracy between these two cases, one requires the addition of strain, dipolar terms, or DMI. In FMs, for example, it is the dipolar interaction that favors the formation of Bloch DWs.

From Eq. 4.15, we can also extract the full spatial profile of a general DW by calculating the x , y , and z components:

$$\mathbf{L} = \left[\operatorname{sech} \left(\frac{y}{\ell_m} \right) \cos(\phi_{\text{DW}}), \operatorname{sech} \left(\frac{y}{\ell_m} \right) \sin(\phi_{\text{DW}}), \tanh \left(\frac{y}{\ell_m} \right) \right]. \quad (4.16)$$

Here $\phi_{\text{DW}} = 0$ for a Bloch wall and $\phi_{\text{DW}} = \pi/2$ for a Néel wall. However, to perform an in-depth analysis of a DW, we must first be able to localize and generate such a structure.

4.2.2. Magnetoelectric annealing

As mentioned in Sec. 4.1.5, Cr_2O_3 has been shown to form mm-scale domain structures [136], and as such, searching for a single DW with NV magnetometry can be like finding a needle in a haystack. To make this problem more tractable, we again use the mesas patterned on the crystal surface. In addition to acting as a probe of the surface magnetization, these structures serve as markers for localizing the DW on the sample surface. In particular, we measure the surface magnetization at mesas distributed across the sample surface and looking for flips in the sign of the magnetization, heralding the presence of a DW. Through this procedure, we find that the sample as received, is in a mono-domain state, forcing us first to generate a DW. To do so, we make use of magnetoelectric annealing [134, 135].

In this process, we will harness the magnetoelectric response of Cr_2O_3 to preferably select one of the two order parameter orientations through the simultaneous application of collinear magnetic and electric fields while cooling the sample through $T_{\text{Néel}}$ (see Sec. 4.1.2 and 4.1.4). Applying uniform fields allows us to prepare the sample in a uniform state. If instead, we apply parallel magnetic and electric fields along one half of the sample, and anti-parallel fields on the other half, as shown in Fig. 4.7a, we will generate two uniformly magnetized regions with a single DW between them.

To achieve this, we place the sample within a split gate capacitor consisting of two top contacts separated by a $\sim 750 \mu\text{m}$ gap and a single back contact. The contacts consist of $\sim 100 \text{ nm}$ of gold evaporated onto a quartz slide. We additionally place $\sim 10 \mu\text{m}$ -thick flakes of mica between the contacts and the sample. We found this procedure necessary to avoid electroplating gold onto the Cr_2O_3 surface. The entire capacitor structure is then placed between two large permanent magnets, producing a uniform field of $\sim 550 \text{ mT}$ between them, measured using a teslameter (FM 302, Projekt Elektronik). A voltage of $\pm 750 \text{ V}$ is applied to the top electrodes while grounding the bottom electrode, thereby achieving an electric field of $\sim 0.75 \text{ MV/m}$ over the crystal, with opposing orientations on either side of the Cr_2O_3 crystal. We then heat the sample far above its $T_{\text{Néel}}$, to $\sim 75^\circ\text{C}$, with a heat gun while reading the temperature near the crystal with a local thermistor. Finally, we allow the sample to cool to room temperature by removing the heat source before removing the electric and magnetic fields.

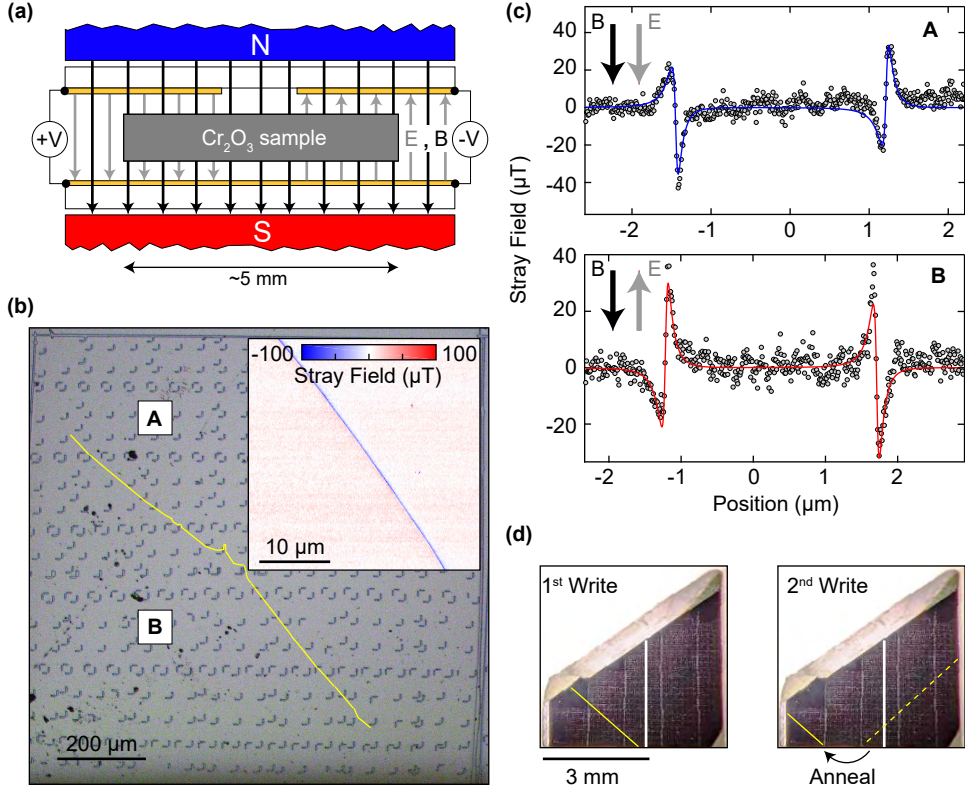


Figure 4.7.: Magnetolectric annealing of Cr_2O_3 . (a) Schematic of the poling device used to anneal the Cr_2O_3 crystal magnetolectrically. A uniform magnetic field of 550 mT is achieved via two permanent magnets, and a voltage of ± 750 V is applied between the split gate and bottom gate. The (anti)aligned fields then lead to two different orientations of the Néel parameter upon heating and subsequently cooling through $T_{\text{Néel}}$. (b) An optical micrograph of the Cr_2O_3 surface highlighting the path of the DW (yellow) as determined by multiple stray field images. The inset shows a sample stray field image of the DW far from the mesa structures, near the top left of the main image. (c) The stray magnetic field of two mesas measured on either side of the DW shown in (b) for an NV whose in-plane orientation points along the long-axis of the mesa. Furthermore, while measuring, we apply a bias field of ~ 25 G along the NV axis, pointing towards the sample plane. The flip in order parameter at the DW leads to opposite signs of σ_m for these two measurements (positive for A and negative for B). (d) Two different realizations of DWs within the Cr_2O_3 crystal. The approximate position of the split gate during magnetolectric annealing is highlighted with a thick, white line, and the final position of the DW is given by the yellow lines. In the second writing procedure, the dashed yellow line shows the DW position. Following a sample anneal in the absence of magnetic and electric fields, the DW was found in the position given by the solid yellow line, also shown in (b).

Following this magnetoelectric annealing procedure, we re-characterize the Cr_2O_3 surface and are indeed able to localize and image a single DW. Through a series of stray field images, we see that the DW tends towards a straight path, as shown with the yellow line in Fig. 4.7b. The smoothness of the DW is particularly pronounced in the absence of surface topography, as seen in the inset. Due to these observations, we believe that the DW passes through the crystal largely unimpeded by strong crystalline defects. Furthermore, we find that we can reverse this annealing procedure through the application of uniform magnetic and electric fields. This whole process is repeatable and leads to different DW orientations, as shown in Fig. 4.7d, indicating that the DWs nucleated in this procedure are not fixed by a particular crystal direction or defects.

Repeated magnetoelectric annealing highlights a further interesting aspect. After heating the crystal to $\sim 200^\circ\text{C}$ in the absence of electric and magnetic fields and subsequent cooling back to room temperature, the sample is still in a two-domain state. Thus, heating the sample to temperatures significantly above $T_{\text{Néel}}$ without applying external fields does not seem sufficient to destroy the DW. However, following this procedure, we observe a shift in the DW position as shown by the dashed and solid yellow lines in the right panel of Fig. 4.7d. First descriptions of such behavior date back to the 60s. In Ref. [134], Brown talks about a ‘memory’ effect, first observed by Martin and Anderson [167]. He suggests that this effect could be caused by local strain defects in the crystal, which would have a higher critical temperature, thereby maintaining the local magnetic order.

Performing magnetoelectric annealing with uniform fields also allows us to test some of the predictions mentioned at the end of Sec. 4.1.4. Therefore, we begin by applying parallel magnetic and electric fields uniformly across the sample. Following this procedure, we then scan across mesas oriented parallel to the in-plane NV orientation and fit the observed stray fields to obtain the sign of the magnetic moment. In this case, we find that this annealing procedure leads to a positive σ_m , i.e., a surface magnetization pointing out of the (001) surface plane. Conversely, annealing with anti-parallel fields results in a negative surface magnetization. This annealing behavior appears to be independent of the absolute orientation of the individual fields, only showing a change when the relative orientation of \mathbf{B} and \mathbf{E} are changed, as expected from the theory [161]. In Fig. 4.7c, we present two examples of the stray field associated with a positive (top) and negative (bottom) surface magnetization, taken on either side of the DW in Fig. 4.7b.

Unfortunately, we do not currently know which of the two order parameters (with a positive or negative monopolar contribution according to the definition by Spaldin [161]) are selected by parallel or antiparallel fields. For this reason, it is also not possible to relate our results to the expected termination of the Cr_2O_3 surface. Furthermore, the magnitude of $|\sigma_m|$ we find is still markedly different than the predicted values. It remains to be seen whether a re-ordering of the surface can explain the discrepancy in the low-temperature values of σ_m presented in Sec. 4.1.5. With this in mind, cryogenic measurements of Cr_2O_3 could be helpful to determine the true low-temperature value of σ_m . Additionally, measuring the surface of Cr_2O_3 with high-resolution atomic force microscopy and Lorentz transmission electron microscopy, could help clear up the termination and magnetic moments at the Cr_2O_3 surface.

4.2.3. Nanoscale analysis of the domain wall

At this point, we arrive at one of the most important open questions in Cr_2O_3 : the characterization of the DW width and the wall type. Having realized single, well-isolated DWs as shown in Fig. 4.7b, we have an ideal starting point to investigate these magnetic structures. To do so, we must first develop a model for the stray field of the DW. Here, we will continue to assume a Bloch wall ($\phi_{\text{DW}} = 0$), a reasonable assumption in the absence of DMI or similar terms that typically induce Néel order.

We already know the profile $\mathbf{L}(\mathbf{r})$ for a Bloch wall, as derived in Sec. 4.2.1. Therefore, we will use the forward propagation of the magnetic fields to obtain the expected stray field from this profile [27]. For this purpose, we use the Fourier-space description $\mathbf{B}(q, d_{\text{NV}}) = \mathcal{D}(q, d_{\text{NV}})\mathbf{L}(q)$, where q is the vector in reciprocal space and $\mathbf{L}(q)$ is the Fourier transform of the DW profile [168]. The propagator $\mathcal{D}(q, d)$ is given by:

$$\mathcal{D}(q, d) = \frac{\mu_0 M_s}{2} (e^{-dq} - e^{-(d+t_m)q}) \begin{bmatrix} -\cos^2(\phi_q) & -\frac{\sin(2\phi_q)}{2} & -i\cos(\phi_q) \\ -\frac{\sin(2\phi_q)}{2} & -\sin^2(\phi_q) & -i\sin(\phi_q) \\ -i\cos(\phi_q) & -i\sin(\phi_q) & 1 \end{bmatrix}.$$

Here, ϕ_q is the reciprocal-space azimuthal angle, t_m is the thickness of the magnetic layer, M_s is the saturation magnetization, and $e^{-dq} - e^{-(d+t_m)q}$ is the thickness loss factor (TLF). As the magnetic layer is equivalent to a single layer of spins, we find that $t_m \cdot q \ll 1$, which allows us to expand the TLF to first order in t_m . Doing so, and using $\sigma_m = M_s \cdot t_m$, we obtain $e^{-qd}(\mu_0 \sigma_m q)/2$.

By taking the inverse Fourier transform we then obtain the field components in real space at a distance d_{NV} :

$$\begin{aligned} B_x &= -\frac{\mu_0 \sigma_m}{2\pi^2 \ell_m} \text{Re} \left[-\psi^{(0)} \left(\frac{2d_{\text{NV}} + \pi\ell_m + 2ix}{2\pi\ell_m} \right) + \psi^{(0)} \left(\frac{2d_{\text{NV}} + \pi\ell_m - 2ix}{2\pi\ell_m} \right) \right], \\ B_y &= 0, \\ B_z &= \frac{\mu_0 \sigma_m}{2\pi^2 \ell_m} \text{Im} \left[-\psi^{(0)} \left(\frac{2d_{\text{NV}} + \pi\ell_m + 2ix}{2\pi\ell_m} \right) + \psi^{(0)} \left(\frac{2d_{\text{NV}} + \pi\ell_m - 2ix}{2\pi\ell_m} \right) \right]. \end{aligned} \quad (4.17)$$

Here, $\psi^{(0)}$ is the digamma function, and ℓ_m is again the magnetic length. Due to the complex functional form of Eq. 4.17 and large number of fit parameters, fitting the measured stray field is quickly plagued by large uncertainties and correlations between variables. For this reason, we will rely strongly on our analysis of the mesa stray field and the information we extracted there.

We measure the stray field of the DW in the same manner as the mesas. We again use NV magnetometry to record line scans perpendicular to the DW, making sure to capture the stray field of one or more mesas in the process. In particular, we select sections of the DW, which are straight on length scales $\gg d_{\text{NV}}$. This process is repeated for 20 line scans, which form a subset of the 29 line scans in Sec. 4.1.5.

In this way, we can use the pre-characterization of the NV angles and the values of σ_m and d_{NV} extracted via the mesa stray field for each DW measurement. These values then serve as prior information for the MH algorithm when fitting the DW. As such, we are able to appropriately attribute a broad DW stray field to the magnetic length rather than variations in d_{NV} .

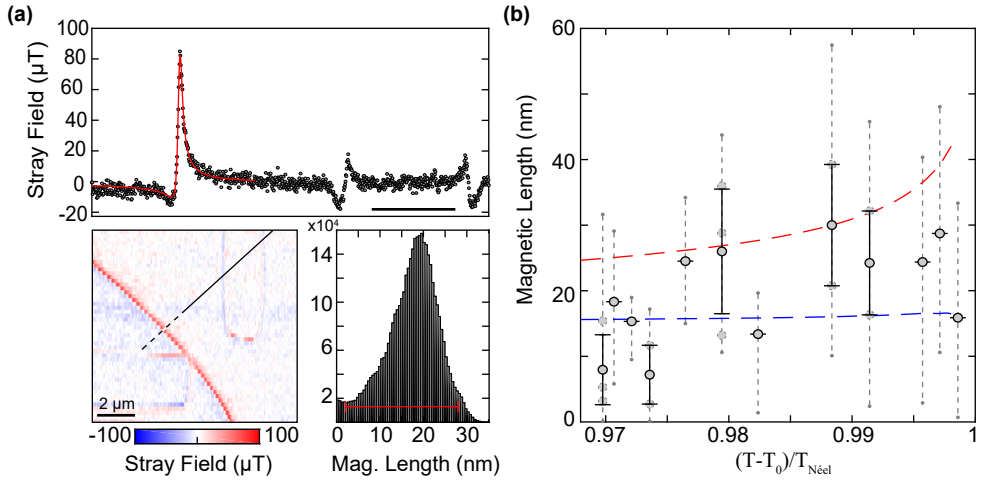


Figure 4.8.: Analysis of the DW. (a) Stray field collected from a line cut across a mesa and the DW, which is fit using Eq. 4.17 (red line). This fit results in an estimate of the magnetic length $\ell_m \in [2,28]\text{nm}$. Bottom left: a stray field image highlighting the position of the line cut for this data set, with the DW portion being shown as a dashed line. Bottom right: MH likelihood distribution showing the range of ℓ_m values extracted from the DW stray field fit. The red bar gives the 2nd and 98th percentiles of the distribution, yielding 2 nm and 28 nm, respectively. (b) The temperature dependence of ℓ_m as extracted from stray field fits similar to that shown in (a). As in Fig. 4.5, the mean of the combined measurements at a given temperature is shown with a solid gray circle while each individual measurement is shown with a dashed, gray circle. The solid error bars give the standard deviation of the measurements, and the light gray dashed lines give the 98th and 2nd percentiles of the likelihood distributions. The theoretical upper (red) and lower (blue) bounds on ℓ_m are determined based on the temperature dependence of A and K . Here, the lower bound is given by $\alpha = 2$ in Eq. 4.18.

An example of such a line scan and the resulting DW fit is shown in Fig. 4.8a. Despite our attempts to pre-characterize the NV and material properties, the fit still yields broad estimates of $\ell_m \in [2,28]$ nm. The resulting MH likelihood distribution is also strongly asymmetric, as shown in the bottom right panel of Fig. 4.8a. For this reason, the lower and upper error bounds stated here are given by the 2nd and 98th percentiles of the likelihood distributions respectively, which we chose in order to cover a reasonable range of potential ℓ_m values.

As these measurements were taken concurrently with the mesa measurements in Sec. 4.1.5, they also correspond to differing sample temperatures. As such, we also examine the change of ℓ_m as a function of temperature. The result of this analysis is shown in Fig. 4.8b. Here, we see that the individual measurements (light gray circles) are dominated by the large error bars arising from the likelihood distributions, shown with gray dashed lines. The mean value of ℓ_m at a given temperature is shown with a dark gray circle and the standard deviation with black bars. In particular, let us focus

on the measurements taken at room temperature (295 K). Though we cannot state an exact value for ℓ_m , which falls below our typical spatial resolution, we can place an upper bound on this parameter. As shown in Fig. 4.8b, the likelihood distributions we extract show that our data are consistent with a magnetic length $\ell_m < 32$ nm.

Also shown in Fig. 4.8b is a comparison to theory, for which we recall that $\ell_m = \sqrt{A/K}$. Though the temperature dependence of the anisotropy constant K is rather well defined and tabulated [169, 170], there is some dispute about the exact behavior of the exchange stiffness A . To account for the discrepancy between molecular field theory [169], which estimates a linear scaling with the magnetization, and lattice simulations [142], which give a quadratic scaling, we write:

$$A(T) = A(0) \left[\frac{\mu(T)}{\mu(0)} \right]^\alpha, \quad (4.18)$$

where $\mu(T)$ is the temperature-dependent sublattice magnetization and $\alpha \in [1, 2]$. Furthermore, $A(0) = \frac{C\mathcal{J}S^2}{2a}$, where $\mathcal{J} = 14.6$ meV [154], C is a correction factor of order 1 and $S = 1$. The estimates for α then yield upper and lower bounds plotted in Fig. 4.8b as a red and blue line, respectively. We observe reasonably good agreement between the expected theoretical range and the measured values.

In this section, we have demonstrated our ability to nucleate, measure and analyze DWs in Cr_2O_3 using NV magnetometry. Furthermore, we successfully placed an upper bound on the magnetic length of the DW of $\ell_m < 32$ nm using a Bloch wall model. Unfortunately, as the magnetic length falls below our spatial resolution, it is difficult to narrow down the precise value. This limitation furthermore prevents us from making concrete statements on the DW type. If we fit this same stray field with a Néel wall profile (profile is given in Appendix A.5.2), we obtain a similarly good fit but a smaller ℓ_m . In particular, for the data set shown in Fig. 4.8a, the median ℓ_m extracted from the Bloch DW fit is ~ 20 nm while the Néel wall shows a median of ~ 5 nm, though both give similar estimates of σ_m . As such, we are confident that the Bloch wall model does indeed offer a reliable upper bound on the DW width. To support these values, measurements performed by Wörnle et al. on similar samples have also extracted a Bloch wall with a mean ℓ_m of 34 ± 5 nm and 45 ± 8 nm [157].

In the future, achieving a realization of DWs in Cr_2O_3 where ℓ_m exceeds our spatial resolution should allow us to verify the DW type and magnetic length. Apart from improving the spatial resolution of NV magnetometry (see Sec. 3.4.1), material engineering to increase ℓ_m , through stress [171], may be helpful.

4.3. The mechanics of DWs

Originally, our approach of adding topography to the sample surface was conceived to facilitate the analysis of the surface magnetization and DWs, as discussed in the previous sections. However, we were not expecting the wealth of additional interesting

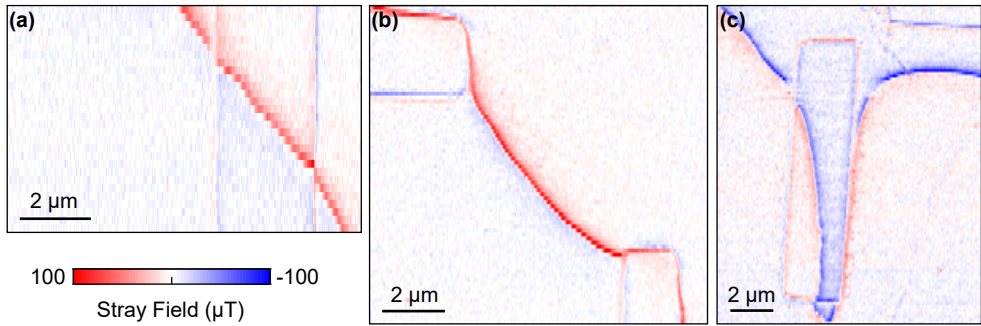


Figure 4.9.: Deviations from smooth DW behavior. Stray field images showing (a) refraction of the DW upon crossing a mesa, (b) pinning of the DW between two adjacent mesa structures, and (c) a change in the DW direction along a mesa structure. The latter is most likely caused by defects in the bulk.

physical effects that these structures would introduce. Recall that we showed that the generated DW passes through the sample largely undisturbed in the absence of surface topography, showing few deviations from a smooth curve, even over mm length scales. We have found that this is not the case when the DW crosses or passes by a mesa structure.

Figure 4.9 shows a few representative examples of deviations in the DW path near mesa structures. We have observed “refractive” behavior (Fig. 4.9a), pinning to the mesa edges (Fig. 4.9b), and even complete reversals in direction (Fig. 4.9c). While some of these phenomena, namely that in Fig. 4.9c, can be attributed to crystal defects, the others can be used to better understand DW mechanics and guide new directions in AFM spintronics. In the following section, we will focus on the first two phenomena and use the stray field images obtained through NV magnetometry to guide a DW model based on simulations and analytic calculations.

4.3.1. Domain wall refraction at topographic features

We begin with an investigation of the behavior seen in Fig. 4.9a. In Fig. 4.10a, we see an even clearer example of this behavior, which we will return to several times in this discussion. Qualitatively, the change in DW orientation resembles the refraction of a light ray when crossing through a slab with a higher index of refraction relative to the surroundings. In geometric optics, such behavior is described by Snell’s law. To make the comparison to Snell’s law more explicit, we extract the angle the DW makes with the mesa edge both off the mesa (θ_1) and on the mesa (θ_2) as shown in the inset. We do so by determining the slope from the stray field images. In particular, we map 17 instances of such refraction-like behavior over a range of DW angles spanning $\theta_1 \in (20^\circ, 70^\circ)$. Plotting these angles, or specifically, the sine of these angles, against each other as shown in Fig. 4.10b, we observe a linear behavior. Here, $\sin \theta_1 / \sin \theta_2 = 1.16 \pm 0.04$. Later in this section, we will see how this value may be related to the geometric parameters of the mesa.

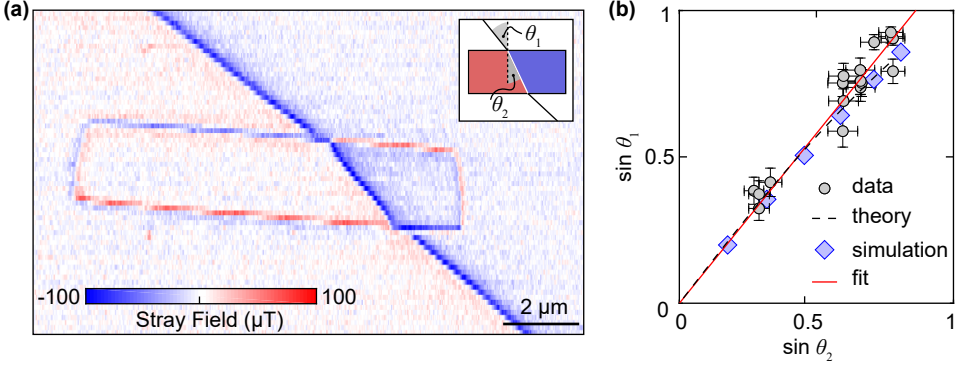


Figure 4.10.: Refraction of a DW. (a) Stray field image of a DW passing through a mesa. The DW is deflected from its otherwise straight path leading to a refractive behavior. Inset: definitions of the off-mesa (θ_1) and on-mesa (θ_2) angles. (b) A plot of the DW angles, extracted from 17 images (gray circles). A linear fit to the data (red line) results in a slope of 1.16 ± 0.04 . Numerical simulations (blue diamonds) and analytic calculations (black, dashed line) show good agreement with the experimental results for a mesa with an aspect ratio $\sim \bar{t}/\bar{w}$.

This behavior can be explained using an analogy to classical optics combined with an intuitive picture of the DW energy. If we consider the total DW energy obtained by integrating Eq. 4.10 over all space, the largest energy contributions will arise within the volume of the DW. As such, we can define a surface energy density associated with the DW surface. Though the mesa is small compared to the bulk of the crystal, the change in sample topography induced by the mesa will increase the DW energy, proportional to the added DW surface area within the mesa volume. If we now treat the DW analogously to a ray of light passing from a low index (bulk Cr_2O_3) to a high index (mesa) material, Fermat's principle of least time will require the ray (DW) to refract. Similarly, to reduce the additional energy cost induced by the mesa, the DW will assume a refractive path leading to this magnetic equivalent of Snell's law.

To obtain a more comprehensive understanding of the observed interactions between DW and mesas, we will have to expand our toolbox to include simulations and analytical descriptions of the DW. We begin by presenting the results of spin-lattice simulations based on the Hamiltonian described in Eq. 4.7 and performed by colleagues at the HZDR in Dresden using the SLiSi [172] package. In these simulations, we initialize the DW in a trajectory passing undisturbed through a mesa at a given angle relative to the mesa edge. Here, the angle is set using notches at the boundaries of the simulated volume, and the mesa is fixed to lie along the lattice planes for simplicity. The magnetization is then allowed to relax into the equilibrium state from which we extract the DW angles. We plot the results in Fig. 4.10b as blue diamonds and observe excellent agreement between the measured data and simulations, particularly for small angles.

Here, we have set $\mathcal{J} = 14.6\ \text{meV}$ and $\mathcal{K} = 1.6\ \text{meV}$. Furthermore, we select a lattice constant $a = 0.277\ \text{nm}$, giving us $\ell_m = a\sqrt{\mathcal{J}/\mathcal{K}} = 0.83\ \text{nm}$. The down-scaling of ℓ_m ,

which we achieve by scaling \mathcal{K} accordingly, keeps simulations to a reasonable size while reproducing the observed DW behavior. Under the assumption of negligible dipolar interactions, our model will scale with the magnetic length, allowing us to choose the aforementioned scaled-down parameters.

To ensure that this assumption is reasonable and to ensure that we do not bias our results due to our choice of lattice or geometry, we also perform several sanity checks. To address the influence of dipolar interactions, we include a dipolar term in the simulations that may be turned on and off using a control parameter. Comparisons of the simulation results with and without the dipolar terms show little change, and so our assumption of negligible dipolar contributions appears to be justified. We also ensure that the orientation of the simulated mesas relative to the lattice axes shows no significant effect on the DW behavior. Furthermore, we do not specify a particular DW type in our simulations, as this is determined based on the initial magnetic state. Variation of these initial conditions also shows no influence of the DW type on the relaxed DW path. Finally, we test the symmetry of our chosen lattice. In particular, we simulate a system with lower symmetry by shifting one of the two magnetic sublattices by half a lattice constant along the z -axis, with no significant effect on the DW behavior. This set of tests supports our choice of model and shows it to be an accurate representation of the Cr_2O_3 system and robust against variations in the model parameters. Not only is this simple model sufficient to explain the observed behavior, but it is also general enough that it should apply to any uniaxial AFM in the absence of chiral terms such as the DMI.

More than just reproducing the behavior of the DW observed through NV magnetometry, these simulation results also offer insights into the DW trajectory in the bulk of the sample. In Fig. 4.11a, we show cuts through the DW surface, which form the 3D morphology of the DW below the mesa. We note two points of interest. Firstly, the DW shows a smooth transition between its position on the mesa and bulk surfaces. The resulting twist of the DW propagates into the bulk below the mesa, but remains localized near the surface of the Cr_2O_3 crystal. Secondly, the simulations show bending of the DW at the edges of the mesa towards the normal axis of the side wall, resulting in the s-shaped distortion highlighted in Fig. 4.11a with a black box. This same distortion is visible at the sides of the mesa in Fig. 4.10a. These results give an important insight into the behavior of the DW. However, we can extend this further through an analytical, micromagnetic analysis performed by our colleagues in Dresden.

We begin this analytical analysis by returning to Eq. 4.10, where we described the effective energy for the Cr_2O_3 spin system, assuming uniaxial anisotropy and nearest-neighbor exchange interactions. We have one additional factor to introduce here: the boundary condition for the Néel vector at the Cr_2O_3 surface. As the surface topography plays an important role in this analysis, a description of the DW at the sample boundary will be necessary. A careful evaluation of the Landau-Lifschitz equations of motion for an achiral antiferromagnet (see Ref. [142]), leads to the following boundary condition for the Néel vector:

$$\mathbf{L} \times (\mathbf{n}_s \cdot \nabla) \mathbf{L} = 0, \quad (4.19)$$

where \mathbf{n}_s is the surface normal. This condition will be fulfilled, for example, when the derivative of \mathbf{L} along \mathbf{n}_s is zero at the crystal surface. As the derivative of DW

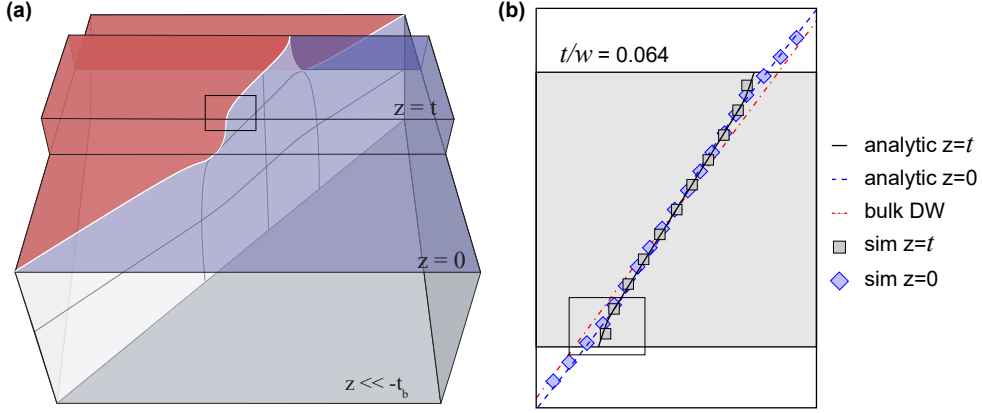


Figure 4.11.: Simulations of DW refraction. (a) 3D representation of the DW surface. Here, we observe the twisting of the DW surface below the mesa and an s-shaped distortion of the DW at the mesa surface. t_B characterizes the depth to which the twist of the DW propagates in the bulk. (b) Comparison between analytic results from Eq. 4.21 and 4.22 and simulations of the DW. We compare the profiles at the mesa surface (black line/ squares), bulk surface (blue, dashed line/ diamonds), and deep in the bulk (red, dot-dashed line) given a t/w ratio of 0.064. The s-shaped distortion of the DW on the mesa surface in (a) and (b) is highlighted with a black box.

is only non-zero perpendicular to the DW surface, this condition requires the DW surface to lie perpendicular to the mesa side wall. In particular, this leads to the s-shaped distortion seen in simulations and measurements.

We now assume a semi-infinite sample with a mesa of width w and thickness t such that $t/w > 0.01$, consistent with the fabricated structures. We set the bulk surface to be at a height $z = 0$, with the top surface of the mesa occurring at $z = t$. Finally, we set the equilibrium, bulk DW position to be the plane $y = kx$, specifically for small values of k . To describe the DW behavior within and below the mesa, we begin with a general DW profile modified from Eq. 4.15:

$$\theta = \begin{cases} 2 \tan^{-1} \left[\exp \left(\frac{y - y_0^b(x, z)}{\ell_m} \right) \right] & , z < 0, \\ 2 \tan^{-1} \left[\exp \left(\frac{y - y_0^m(x, z)}{\ell_m} \right) \right] & , z \geq 0. \end{cases} \quad (4.20)$$

Here, $y_0^{b(m)}$ describes the DW profile in the xy plane of the bulk and mesa respectively.³ Comparisons to the 3D simulations of the DW provide the following Ansatz for the DW in bulk:

$$y_0^b(x, z) = (k_0 - k)b \operatorname{sech} \left(\frac{x}{b} \right) \tanh \left(\frac{x}{b} \right) e^{-\frac{z^2}{2t_b^2}}, \quad (4.21)$$

³Note that we in fact use rotated axes x' and y' in the definition of y_0^b . Here, $(x', y') = R_{e_z}(\varphi)(x, y)$, and $R_{e_z}(\varphi)$ represents a rotation about the z -axis by an angle φ . In this way, the x -axis always lies along the DW, simplifying the description of the wall profile relative to the $y = kx$ axis.

where $b = \frac{w}{2 \sinh^{-1}(1)}$ and $t_b = \sqrt{5/14}b$. This equation holds everywhere where $z \leq 0$. In particular, we see that the twist of the DW into the bulk decays exponentially over a characteristic length scale $t_b \approx 0.34w$. Using typical values for our mesas, we find $t_b \approx 0.82 \mu\text{m}$. Therefore, we expect that these modifications of the DW profile discussed in this section exist only within the top few micrometers of the surface.

Continuing our analysis, we obtain a description of the DW profile within the volume of the mesa by minimizing the energy functional in Eq. 4.10 together with the boundary conditions described above. Such an energy minimization yields the following form for $y_0^m(x, z)$:

$$y_0^m(x, z) = \frac{4k_0}{w} \sum_{n=0}^{\infty} [\text{sech}(\lambda_n t) \cosh(\lambda_n(t - z)) \sin(\lambda_n x)]. \quad (4.22)$$

Here, $\lambda_n = \frac{(1+2n)\pi}{w}$. More details are provided in the SI of Ref. [140]. At this point, it is more informative to plot the resulting DW profiles. Shown in Fig. 4.11b is Eq. 4.21 at $z \approx 0$ (blue, dashed curve) and Eq. 4.22 at $z = t$ (black curve). Here, we consider a mesa with a $t/w = 0.064$, similar to those in our experiments. The analytically derived curves are compared to simulations at the same points (blue diamonds and black squares, respectively), showing excellent agreement between these two methods. We additionally show the slope of the DW deep in the bulk in red. In Fig. 4.11b, we see the s-shaped distortion that results at the mesa surface and the gradual twist of the DW.

Now to relate these expressions to the Snell's law-like behavior we have observed in our experiments, we first need to define the orientation of the DW relative to a mesa oriented along the x -direction as shown in Fig. 4.11b. Specifically, we define three values $-k, k_0$, and k_1 i.e., the slope the DW takes in the xy plane deep in the bulk, at the bulk surface, and at the mesa surface, respectively. Note that far from the mesa, $k = k_0$. From these terms, we can extract the angle of the DW, as in our analysis at the beginning of this section. In particular, we let $\theta_1 = \arctan(k)$ and $\theta_2 = \arctan(k_1)$. Inserting these angular forms into the typical Snell's law equation, we obtain:

$$\frac{\sin \theta_1}{\sin \theta_2} = \frac{k}{k_1} \sqrt{\frac{1 + k_1^2}{1 + k^2}}.$$

We can use this form to provide an analytic expression for the Snell's law-like behavior of the DW with respect to the geometric parameters of the mesa. Based on the DW profiles in Eq. 4.21 and Eq. 4.22, for small values of t/w , the expression above yields the following approximation:

$$\frac{\sin \theta_1}{\sin \theta_2} \approx 1 + 3.1 (\cos \theta_1)^2 \frac{t}{w} \quad (4.23)$$

As our analysis is based on a small angle approximation, $\cos \theta_1 \approx 1$, and so we find that $\sin \theta_1 / \sin \theta_2 \approx 1 + 3.1(t/w)$. For our typical mesa geometry, this yields a value of $\sin \theta_1 / \sin \theta_2 \approx 1.21$, which agrees reasonably well with our experimental value of 1.16 ± 0.04 . We also plot Eq. 4.23 as a dashed black line in Fig. 4.10b. While the agreement between Eq. 4.23 and the experimentally obtained data is excellent for

small values, we do see deviations from the linear behavior for larger angles, where the $\cos \theta_1 \approx 1$ approximation breaks down. However, the form in Eq. 4.23 agrees very well with simulations and still provides a reasonably good fit to the data. This form also highlights one significant difference to Snell's law. While the expression in geometric optics is solely a consequence of the principle of least action, the DW trajectory on the mesa is additionally constrained by the bulk DW position and the boundary condition for \mathbf{L} , hence the higher-order contributions of θ_1 .

To summarize the results of these simulations and analytical calculations, we focus on two points. The first is that we have not only been able to reproduce the DW behavior observed with NV magnetometry but have expanded our model, providing a complete 3D description of the morphology of the DW as it passes through a mesa. Secondly, the close agreement between simulations, analytics, and experimental data allows us to conclude that the DW physics in this sample are dominated by exchange and anisotropy. Other effects, including dipolar interactions and magnetoelasticity, can therefore either be neglected or are already incorporated into the effective anisotropy and exchange constants. Therefore, our next goal will be to use the knowledge acquired through this analysis to explain other phenomena, such as the pinning shown in Fig. 4.9b.

4.3.2. Elasticity of the DW

Let us consider the case of a DW passing close to the corner of a mesa. Rather than intersecting the mesa, as we have seen in the previous section, it can be energetically favorable for the DW to avoid crossing the mesa by rounding the corner instead. An excellent example of this is shown in Fig. 4.12. Just as in the previous section, we can reproduce this behavior in simulations by initializing a DW close to the corner of the mesa, as shown in the inset.

Such observations indicate that the mesa edge acts as a pinning site for the DW. In this section, we will explore this pinning more closely with the use of simulations. In Fig. 4.13a, we consider a DW initialized near a square mesa and with endpoints fixed at a position x_{DW} using notches in the simulated volume. We once again allow the simulated magnetization to relax and observe the steady-state position of the DW. In Fig. 4.13a, we plot the resulting energy of the DW (in units of

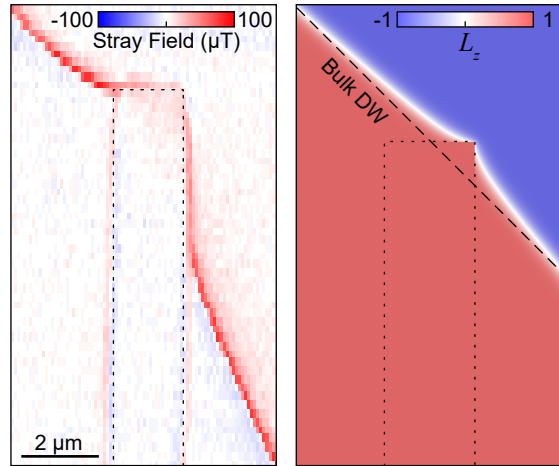


Figure 4.12.: Pinning of the DW and its elastic behavior. Stray field image of the DW, pinned around the corner of a mesa, highlighted with a black dotted line. Right: simulation reproducing this kind of pinning at a corner of the mesa.

$\sqrt{\mathcal{J}K}$) as a function of the DW endpoint position. By varying the location x_{DW} relative to the mesa, we observe two different DW behaviors.

In the first instance, a straight DW is brought near and on top of the mesa, resulting in the energy shown in Fig. 4.13a with a red line. As the path length is already minimized by going straight through the mesa, we observe no deflection of the DW. However, we observe an increase in energy when the DW is initialized on the mesa versus off the mesa. In the second case, shown in Fig. 4.13a in blue, we initialize the DW to either side of the mesa, labeled as “right pin” or “left pin”. As we move the DW endpoints past the mesa, we observe that the DW remains pinned to the side of the mesa it was initialized to, despite the increase in DW energy resulting from the deflection of the wall. Each of the scenarios discussed here is also shown graphically in Fig. 4.13b. In particular, we find that the energetically favorable path, that is, whether the DW crosses the mesa or follows the edge of the mesa, depends on the mesa geometry and the location of the DW relative to the mesa. These two aspects will define the energy penalty incurred by the increase in DW surface area. This pinning behavior also reveals an important aspect of the DW physics in this sample: elasticity. Based on our observations, it appears as though the DW acts as an elastic, deformable surface. To expand on this picture, we use lattice simulations to express the tension energy of the DW surface ξ , defined in Sec. 4.2.1, as a function of the extension of the wall.

We show the result of these simulations in Fig. 4.13c, where we see a linear increase of the tension energy with the increasing DW area. Furthermore, repeating this analysis for two different values of ℓ_m , we see that the slope of this response depends on the magnetic length of the DW, shown here with blue circles for $\ell_m = 3a$ and red diamonds for $\ell_m = 6a$, where $a = 0.277\text{ nm}$ is the lattice constant. This slope provides the tension coefficient of the DW. As such, the steeper the slope, the higher the tension of the DW surface and the more energy is required to extend the DW by a given amount. This is very much in line with the intuitive picture of an elastic sheet. What this observation also tells us is that in our simulations, the wider the DW, the softer (more elastic) it will be. The elasticity plays an important role when considering the pinning and deformation of a DW.

We can also describe the elasticity of the DW analytically. In particular, we use the description of the DW in Sec. 4.3.1 to determine the increase in DW area \mathcal{A} of a pinned DW relative to an unpinned DW. We then calculate the increase in energy, resulting in the following description of the mechanical tension of the DW:

$$\rho = \mathcal{E}/\mathcal{A} = 4\sqrt{AK}, \quad (4.24)$$

where ρ is the tension coefficient. Here, both the anisotropy and exchange contribute a factor of $2A\sqrt{AK}$. This behavior is also plotted in Fig. 4.13c as solid lines using values of A and K corresponding to the value of ℓ_m used in simulations.

We now examine the effect of the DW elasticity on the pinning we have observed. In Fig. 4.13d, we show the energy of the DW extracted from simulations as a function of the DW endpoint position. Instead of comparing different initial conditions of the DW as in Fig. 4.13a, we keep the DW orientation the same but compare the outcome for two different magnetic lengths. The blue curve, simulated for $\ell_m = 3a$, shows similar behavior to Fig. 4.13a, in which the DW is strongly pinned to one edge of the mesa.

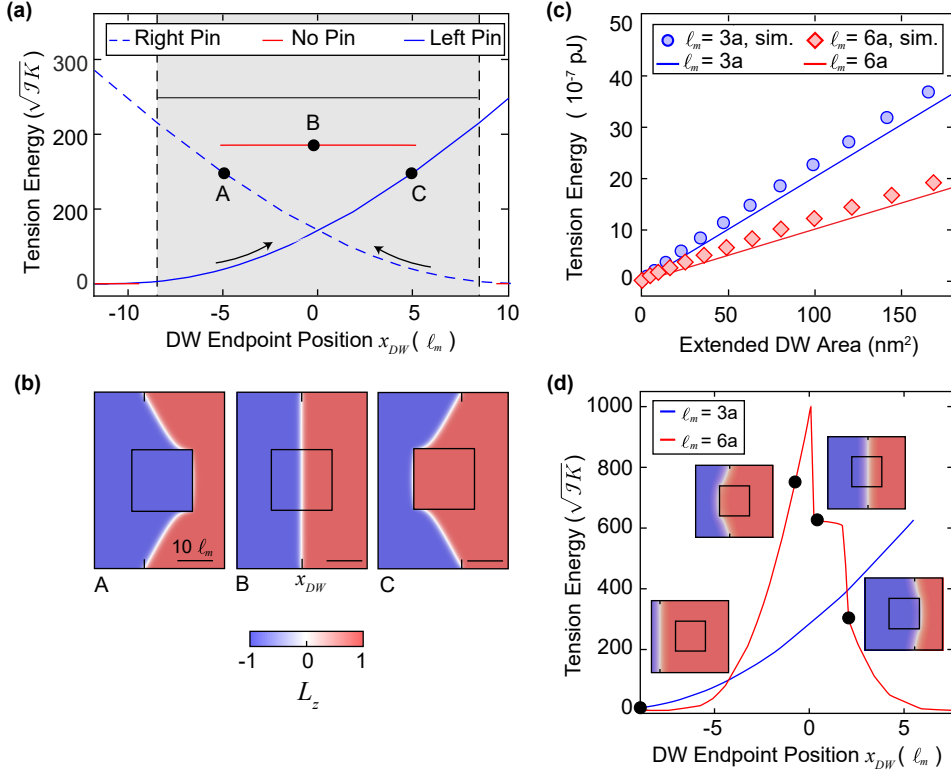


Figure 4.13.: The elastic DW surface. (a) The simulated energy of the DW ($\ell_m = 3a$) as a function of the DW endpoints. Here, the DW is initialized either to the right of the mesa (blue, dashed line), to the left of the mesa (blue, solid line), or straight between the endpoints (red line). The gray, shaded area denotes the width of the mesa in units of ℓ_m . (b) Simulations of the DW showing three (meta-) stable DW states near a mesa, as labeled in the top plot. (c) The energy of the DW arising due to the extension of the DW upon pinning along a mesa corner. We denote this energy as the tension energy and plot it as a function of the increase in DW area for two different ℓ_m values, as shown in the legend. Simulations (symbols) and analytics (lines) show good agreement. (d) Tension energy of the DW as a function of the endpoint position for two different values of ℓ_m , extracted from simulations. The blue curve ($\ell_m = 3a$) is very similar to that in (a). The red curve ($\ell_m = 6a$) shows a jump in the DW, from being pinned to lying on top of the mesa, as highlighted by the simulations in the insets.

However, for the second simulation where $\ell_m = 6a$ (shown in red), we see very different pinning behavior. While the DW remains pinned to the left edge of the mesa for some time, once the energy cost exceeds that of the straight configuration, the DW can rapidly relax to the lower energy state. In experiments, such a sudden relaxation can be triggered by the addition of an external stimulus such as local heating or magnetoelectric pressure. In simulations, this depinning is achieved through

the excess energy in the starting conditions. Further increasing x_{DW} , we see that the wall again becomes pinned at the left-hand edge of the mesa. The steady-state DW configuration is shown in Fig. 4.13d for several points along the curve.

In the case of lower ℓ_m , as well as in Fig. 4.13a, we see that though the DW may be strongly pinned to the mesa edge, at some point, the added DW surface energy will exceed that of the unpinned case. In this scenario, the DW will be in a metastable configuration. Therefore, similar to the jump seen in the red curve of Fig. 4.13d, applying a stimulus may cause a sudden relaxation of the DW position. This hysteretic process can be tuned by the mesa geometry, namely the mesa height, which gives the energy difference between on-mesa and off-mesa for the unpinned case. However, to test this simulated behavior, we must first determine a way of applying the stimulus mentioned above, which we will address in the following section.

4.3.3. Domain Wall Dragging

The first indication that we might be able to control the DW position was seen when heating the sample. In measuring the data presented in Fig. 4.5 and 4.8b, we noticed that changing the global sample temperature also occasionally led to changes in the DW position. To understand why, we return to Sec. 4.2.3, where we saw that raising the global temperature leads to a change in the exchange energy and anisotropy in the crystal. This will, in turn, change the elastic properties of the DW discussed in the previous section. In Fig. 4.14, we show the bounds on the expected value of the tension coefficient ρ plotted as a function of the relative temperature. As in Sec. 4.2.3, these bounds are determined based on the temperature-dependent behavior of A and K . Here, we see that for increasing temperatures, ρ decreases. This decrease implies a softening of the DW and increased mobility, which could explain the movement of the DW we have observed. Based on these observations, the natural consequence is to determine whether we can use local heating to move the DW in a given direction.

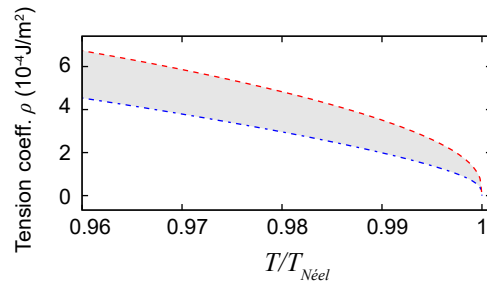


Figure 4.14.: DW tension under heating. Tension coefficient ρ of the DW, shown as a function of the relative temperature. The upper (red, dashed line) and lower (blue, dot-dashed line) bounds are obtained from the temperature dependence of A and K (see Sec. 4.2.3).

To address this question, we focus the 532 nm laser used to excite the NV center on the sample surface in the absence of the scanning probe and scan the beam across the DW. Prior to and following each laser scan, we image the DW with NV magnetometry. Scanning the laser while at room temperature shows very little response in the DW position. However, by raising the global sample temperature to ~ 304.5 K, we were

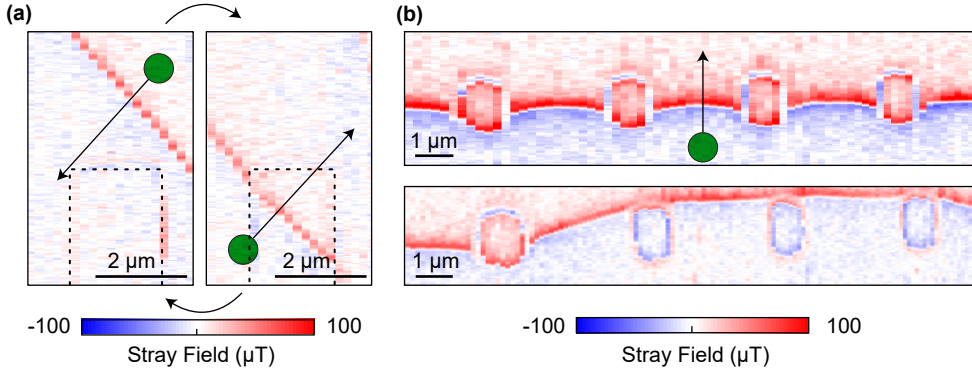


Figure 4.15.: Laser dragging of the DW. (a) Stray field images showing the DW being dragged from the corner of a $2\,\mu\text{m} \times 10\,\mu\text{m}$ mesa to on top of the mesa. This dragging is achieved by moving a focused 532 nm laser beam of $\sim 135\,\mu\text{W}$ across the surface. (b) Stray field images showing the position of the DW relative to a set of $1\,\mu\text{m} \times 1\,\mu\text{m}$ mesas prior to (top) and following (bottom) laser dragging with $\sim 1.4\,\text{mW}$. In each of the images, the green circle and arrow represent the direction of the laser dragging.

able to repeatedly move the DW, as shown in Fig. 4.15a, using a laser power of $\sim 135\,\mu\text{W}$.

Here, we show the direction of the laser scanning with a green spot and a black arrow. We scan the laser perpendicular to the DW and, through this, move the DW from lying near the mesa corner (left) to lying on the mesa (right). However, the large extent of this mesa prevents us from dragging the DW completely from one side of the mesa to the other. Therefore, in a second round of fabrication, we pattern square mesas approximately $1\,\mu\text{m} \times 1\,\mu\text{m}$ in size (Fig. 4.15b) and similar in height to the previous structures. In Fig. 4.15b, we show two realizations of the domain wall, first lying along the base of a series of mesas (top panel). Scanning across the DW at a power of $\sim 1.4\,\text{mW}$, then results in the DW being dragged across the entire width of the mesas and becoming pinned at the top edge of three of the four mesas (bottom panel). Based on the location of the DW before and after dragging, it is clear that though the laser is tightly focused, the motion of the DW takes place on a $\sim 12\,\mu\text{m}$ range. These results are consistent with simulations and with our picture of the DW as an elastic surface, where pulling one section of the surface results in a deformation of a much larger area.

The mechanism behind this laser dragging is likely similar to that in thin-film FMs [82]. Introducing the laser to a system already near the Néel temperature leads to a local increase in temperature, equivalent to reducing the DW energy. As such, the laser produces a local potential well for the DW. This is consistent with theoretical models of AFM DWs in temperature gradients, which suggest that the laser should induce an attractive potential for the DW [173, 174]. However, once the heating is removed, tension causes the DW to return to its original position unless it can be pinned along the way.

Unfortunately, this procedure is not as controlled as we would like. Though the DW may be dragged by the laser, the final location of the DW is often far from the end position of the laser. As our magnetometry images only provide snapshots of the start and end conditions, they are not sufficient to obtain an image of the pinning landscape of the crystal. To better understand this pinning process, we repeat our dragging experiments with the NV scanning probe in place. In this way, we hope to localize the DW based on its magnetic field during the dragging procedure. In Fig. 4.16, we show the results of dragging experiments performed at a global sample temperature of 304.5 K for two different realizations of a DW. Rather than plotting the stray field, we show the raw NV ODMR frequency data. Here, we compare the signal measured at a 532 nm laser power of 9.6 μW and 86 μW . We refrain from using excessive excitation powers to avoid damage to the NV center.

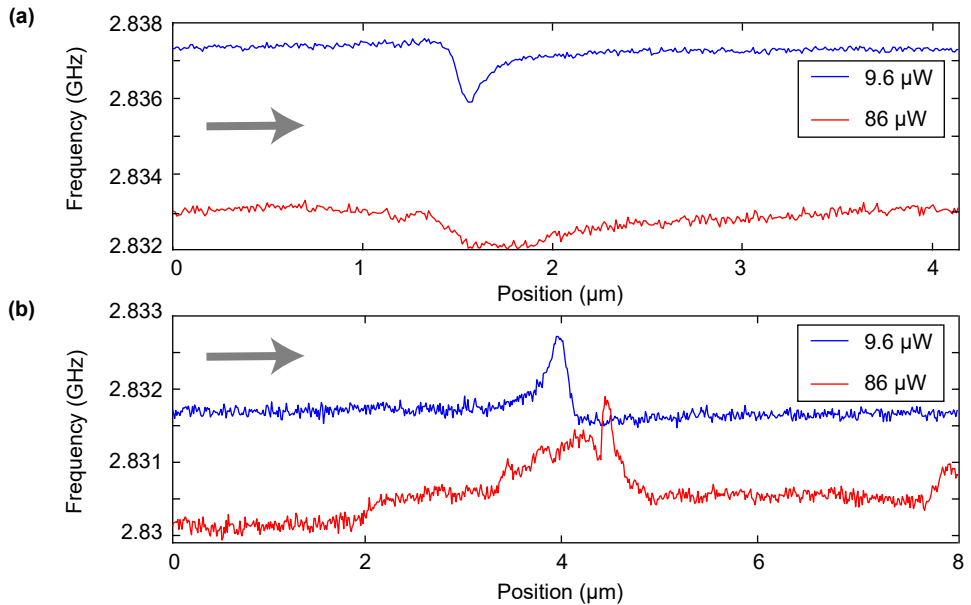


Figure 4.16.: Probing the DW pinning landscape. (a) Line scans showing the change in NV center ODMR frequency due to the measured stray magnetic field. These curves are measured with excitation powers of 9.6 μW (blue) and 86 μW (red). Here we plot the frequency of the low-frequency ODMR line, which we determine by feedback tracking, as a function of the position. The gray arrow shows the scanning direction. (b) A similar plot to (a), taken for a second DW nucleation and at a different position in the crystal. Here, we see jumps in the measured NV ODMR frequency at high powers, which we associate with pinning of the DW during the dragging process. All measurements are performed at a global sample temperature of 304.5 K. Note that the shift in frequency between the low and high power scans is primarily due to the adjusted feedback parameters to account for the power broadening of the ODMR line as we record only the frequency at the left flank of the ODMR line.

Beginning with Fig. 4.16a, we see the now familiar DW profile, taken at low excitation power. However, at high powers, this line shape becomes considerably broadened and distorted. Fig. 4.16b shows another instance of the same experiment, taken at a different location, where we observe DW dragging over a more extensive scan range (red), whereas the low power measurement (blue) shows only the local DW profile. Interpreting these data, is rather difficult. The broad peak in Fig. 4.16a could indicate an increased DW mobility resulting in dragging the DW for a short distance as the NV center passes over the wall. The additional steps in the NV signal in Fig. 4.16b, on the other hand, suggest that the DW may be dragged over larger distances, experiencing pinning along the way. If the distance between the NV center and DW changes when the DW is pinned, we could explain the changing field the NV experiences. Without a better understanding of the extent of the dragging, a quantitative analysis of observations will be difficult. Nonetheless, they are consistent with a movement of the DW and indicate that the DW can undergo pinning during the dragging process.

While laser dragging has allowed us to realize the first steps towards the type of DW manipulation necessary for AFM memory devices, future devices would likely require all-electrical switching to realize the advantages of AFM memories over their FM counterparts. In particular, we would like to use the magnetoelectric properties of Cr_2O_3 to move the DW through the application of local magnetic or electric fields [175]. This would also allow us to move the DW independently of our measurement of the stray field, thereby helping us to obtain a clearer picture of the dragging process and the pinning landscape. Currently, we cannot determine the exact DW position or orientation throughout this dragging procedure. As such, it is unclear which area of the DW is being pinned. Depending on the elasticity of the DW, we could be dragging a large portion of the wall, all of which may contribute to the observed signal.

The first tests we conducted with the application of local magnetic fields through a magnetically-coated, tapered quartz capillary showed no effect. For this reason, manipulation via electric fields would be preferable. This process will require the presence of local gates. However, one must apply a large voltage to achieve sufficiently large electric fields across the entire thickness of a bulk crystal. In his 1969 thesis [134], Brown gives a switching product $|\mathbf{E}| \cdot |\mathbf{B}| = 2 \cdot 10^5 \text{ T V/m}$ to achieve domain switching at room temperature. Assuming a magnetic field of 0.55 mT achievable in our current switching setup and an electrical breakdown in air of $\sim 1000 \text{ V/mm}$, one would have to place gates at least $360 \mu\text{m}$ apart to prevent sparking between contacts. These restrictions are prohibitive for the local generation and manipulation of DWs with surface gates. Therefore, the ultimate goal will be to move towards thin-film samples, where the thickness of Cr_2O_3 may be as low as a few tens of nanometers, allowing us to work with smaller voltages, hence, more densely-packed gates.

4.4. Thin Films

In the previous sections, we have explored the mechanics of DWs in a pinning landscape fabricated on the surface of a pristine, single crystal of Cr_2O_3 . Through this process, we have learned much about the elastic properties of the DW and have been able to demonstrate controllable pinning of the DW at the edges of fabricated surface

mesas. However, when considering potential technological applications, these large crystals are at a distinct disadvantage due to their large size, thickness, and lack of a scalable fabrication technology. In this regard, thin films of Cr_2O_3 could be very beneficial. These films have already proven useful in magnetic order switching experiments [17], where they were used to demonstrate all-electrical AFM memory bit operation.

However, one of the drawbacks of thin-film Cr_2O_3 for applications is the Néel temperature. Though Cr_2O_3 became very popular due to its room temperature ordering, the critical temperature is still far below the temperature rating of typical consumer memory devices. As such, an important aspect of materials research in Cr_2O_3 is finding ways to increase the critical temperature. In this section, we will discuss efforts by our collaborators in Dresden to do just this, where NV magnetometry helped to characterize $T_{\text{Néel}}$.

4.4.1. Raising the Néel Temperature

The question of how to raise the critical temperature of Cr_2O_3 is by no means a new one and has already been addressed using several different methods. The Binek group, among others, has realized increased $T_{\text{Néel}}$ through doping [164, 176, 177], where replacing a portion of the oxygen atoms with boron increases the exchange energy felt by the Cr ions. This increase in exchange energy then results in a higher critical temperature. Others have focused on achieving a similar increase through elastic deformations [163, 178]. Here, a reduction in the lattice constant a due to lateral compressive strain also increases the exchange interaction between Cr ions.

In the Makarov group, efforts have yielded increased $T_{\text{Néel}}$ through strain generated during the film growth process. In the past, these samples were grown epitaxially via thermal evaporation of Cr_2O_3 onto a [001]-oriented Al_2O_3 substrate. This process results in the formation of ~ 50 nm-sized columnar grains of [001]-oriented Cr_2O_3 , which extend the entire thickness (~ 200 nm) of the film, as shown in the bottom-left inset to Fig. 4.17 [26]. In contrast to these evaporated samples, recent developments have moved towards deposition of Cr_2O_3 via RF magnetron sputtering at 700°C . This procedure yields low roughness and highly uniform layers, as shown in the top-right inset to Fig. 4.17. As the sample is cooled, a mismatch in the in-plane thermal compression of Al_2O_3 and Cr_2O_3 leads to epitaxial strain in the Cr_2O_3 layer. Close to the Al_2O_3 surface, the crystal uniformity prevents the relaxation of this strain. However, further from the substrate, partial relaxation can be achieved. In particular, X-ray diffraction measurements show that the c/a ratio can increase by up to 8.5% relative to bulk values depending on the sample thickness. This strain then leads to an increase in $T_{\text{Néel}}$.

To characterize the resulting Néel temperature $T_{\text{Néel}}$ in these samples, we again turn to the excellent magnetic stray field sensitivity of NV magnetometry. In Fig. 4.17, we show a series of stray field images, presented as a function of temperature for four different thin film samples: a thermally evaporated, 200 nm film and three sputtered films with thicknesses of 200 nm, 50 nm and 25 nm. While the 200 nm evaporated film becomes PM around 33°C , each of the sputtered films shows stray fields that persist far beyond the bulk $T_{\text{Néel}}$ of 34°C .

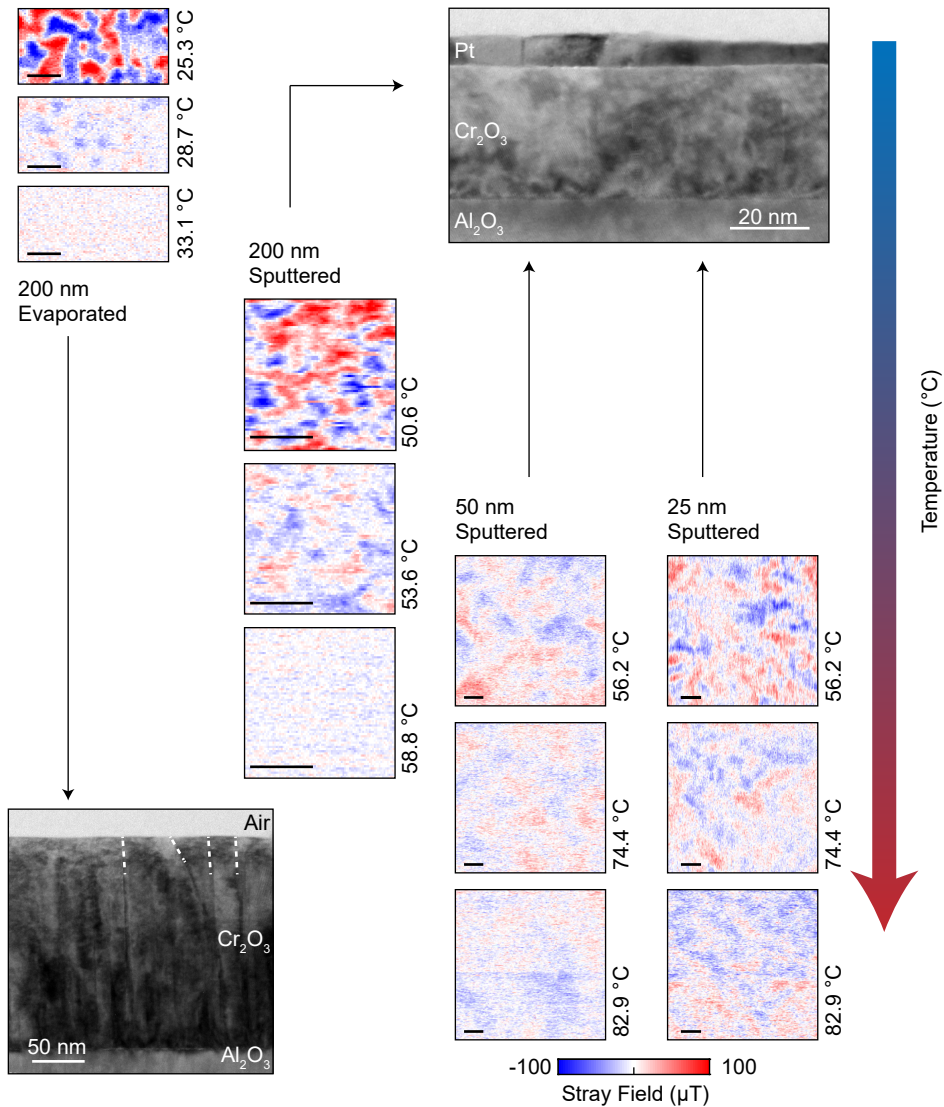


Figure 4.17.: The phase transition from AFM to PM in thin films. Series of stray field images from various thin Cr_2O_3 films taken at increasing temperatures (noted to the side of each image). The details of each thin film are noted at the end/beginning of the column. Insets show the crystal structure of the respective films taken by TEM. Whereas the old evaporated thin film (bottom) exhibits a very granular structure, highlighted with white, dashed lines, the new, sputtered films (top) show much more uniform growth. The new films also show a much higher $T_{\text{Néel}}$, resulting in measurable stray fields up to and exceeding 80°C for the thinnest (25 nm and 50 nm) films. The scale bar in each stray field figure is 500 nm.

We recall from Fig. 4.5 that one can extract $T_{\text{Néel}}$ through a study of the surface magnetization as a function of temperature. However, extracting σ_m relies on a knowledge of the orientation of the Néel vector. Ideally, a [001]-oriented thin film Cr_2O_3 should exhibit an out-of-plane magnetization much as we have seen for single crystal Cr_2O_3 thus far. However, it is unclear whether this will be the case for the 50 nm, and 25 nm films shown in Fig. 4.17 as they exhibit strong epitaxial strain, which has been shown to change the anisotropy leading to an in-plane component of the magnetization [141]. Without prior knowledge of the orientation of the magnetic moments, performing reverse propagation to extract the magnetization amplitude is not possible. Nonetheless, we can estimate $T_{\text{Néel}}$ by imaging the stray fields from the sample as a function of temperature and relying on the fact that the surface magnetization vanishes above $T_{\text{Néel}}$.

These results are very promising though unexpected when compared to measurements made with zero-offset Hall magnetometry. This technique relies on the spin Hall magnetoresistance, which induces a transverse resistance within a platinum Hall bar patterned on the top surface of the Cr_2O_3 film [16]. Therefore, the transverse resistance acts as a probe for the presence of magnetization at the interface between Cr_2O_3 and the Pt layer. In Fig. 4.18a, we compare the $T_{\text{Néel}}$ measured via NV magnetometry and zero-offset Hall magnetometry for three sample thicknesses. Though both techniques show an increased $T_{\text{Néel}}$, the values found by NV magnetometry are consistently higher.

We believe that this discrepancy arises due to the strain gradient in the films. As the strain, and correspondingly $T_{\text{Néel}}$, increases closer to the substrate, it is possible

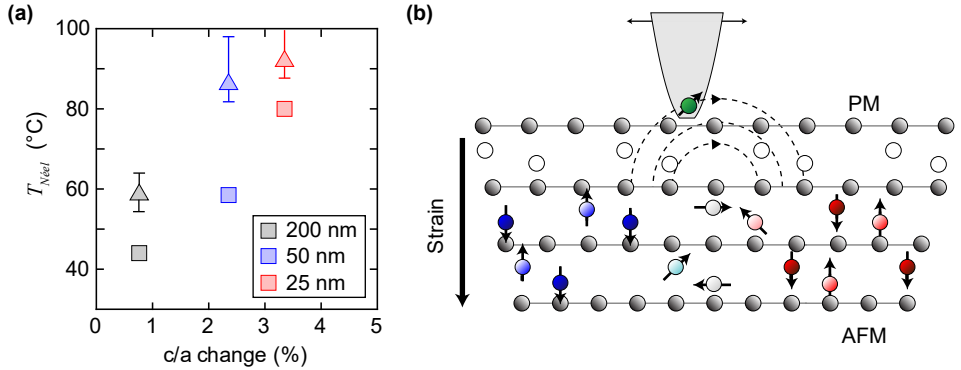


Figure 4.18.: The effect of strain on the $T_{\text{Néel}}$. (a) A plot of the approximate $T_{\text{Néel}}$, estimated by the loss of signal in NV magnetometry (triangles) and zero-offset Hall magnetometry (squares) as a function of the change in the c/a ratio for different samples thicknesses shown in the legend. We see a distinct discrepancy between the two measurements, which we attribute to a difference in the surface and bulk $T_{\text{Néel}}$. (b) A schematic showing the expansion of the Cr_2O_3 lattice towards the sample surface resulting from a relaxation of the induced strain. The strain gradient leads to a gradient in $T_{\text{Néel}}$, leading to a PM surface (white circles) while the bulk remains AFM.

that the film's surface becomes PM while AFM ordering persists deeper into the film, as shown in Fig. 4.18b. As the Hall technique is only sensitive to magnetization at the Pt/Cr₂O₃ interface, the signal is lost when the surface becomes PM. NV magnetometry, on the other hand, can still measure the stray fields produced at the AFM surface, which now lies in the bulk of the film. This makes estimating $T_{\text{Néel}}$ difficult. To obtain the critical temperature from a measurement of the stray field, one must consider not only the general power-law dependence of the magnetization with temperature but also the increasing distance between NV and AFM “surface”.

Overall, these films are much more compatible with typical industrial devices in terms of the critical temperature and the sample thickness. However, in contrast to the clean, mono-domain state of the bulk, stray field images of the thin films reveal much smaller domains on the order of 150 nm. On the one hand, this granular AFM structure could be used similarly to the granular FM films in magnetic recording [179] but would require much smaller domain sizes to be comparable to these technologies. Going in the other direction, applications such as AFM-based racetrack memories rely on our ability to controllably generate and shift DWs. Achieving this control in thin-films would first require us to reproduce the ideal DW behavior seen in bulk Cr₂O₃. In either case, further material development of Cr₂O₃ thin films and AFM materials for spintronic applications will continue to be an important research field and will strongly influence the direction of AFM applications in the future.

4.5. Outlook and Conclusions

Throughout this chapter and in motivating our study of Cr₂O₃, we have often alluded to AFM memory devices. However, current realizations of AFM memories show rather large bit sizes, and as such, do not come close to the bit densities achieved in modern FM memories [13, 17, 180]. While experiments showing memories with single antiferromagnetically coupled atoms exist [181], these are extremely difficult to produce and control, and therefore, are not yet technologically viable.

To bring together all the aspects we have studied in this chapter, we propose a new form of DW-based AFM memory. We have shown that we can engineer a controlled pinning landscape for the DW through the patterning of topographical structures. Additionally, through laser dragging, we have shown that we can reproducibly move the DW from one side of a mesa to the other, thereby flipping the order parameter at the location of the mesa. As such, we have realized topographically defined bits i.e., the mesas, whose bit value is defined by the order parameter measured on the mesa and switched through local dragging of a DW. Each of these aspects should also translate to thin film Cr₂O₃, where we have been able to show critical temperatures consistent with those required for technological applications. The resulting design, shown in Fig. 4.19, has been submitted for patenting. Not only would this memory benefit from the fast switching inherent to AFMs, but the topographical bit size would be limited only by the magnetic length of the DW and our ability to fabricate such structures. As the DW width could be further reduced, for example, through strain [171], we should be able to reach similar bit densities as in current FM memory devices.

Though we have shown each of the individual elements needed for such a memory, further improvements and demonstrations will be required before we can realize a proof-of-concept device. In particular, we need to develop better methods for the local generation and manipulation of DWs. While magnetoelectric annealing has successfully generated a single DW in a bulk Cr_2O_3 crystal, a memory device would require multiple, parallel DWs. However, as we have already discussed, achieving this in bulk is difficult. One would require an electric or magnetic field alternating on the length scales of the DW pattern we wish to generate but strong enough to select a given order parameter. The simplest method would involve a series of electric gates on the Cr_2O_3 surface. However, as mentioned at the end of Sec. 4.3.3, electrical breakdown would hinder such a nucleation pattern in the bulk crystal. For this reason, it would be advantageous to realize such a memory in thin-films, where the required electric fields would be significantly reduced. In the absence of sufficiently pristine thin films, one can also explore the intermediate case of a thin bulk crystal.

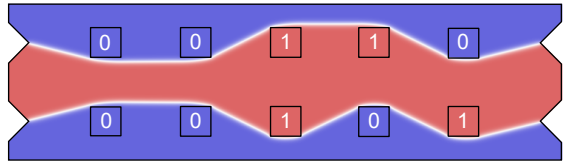


Figure 4.19.: Proposed AFM memory device. Proposal for an AFM memory device based on Cr_2O_3 . Here, the mesas define the bit location. We simulate two DWs lying between the bits such that the bit value is defined by the order parameter orientation on the mesa. The DW is held in place by pinning to the mesa edges and may be shifted by the local application of magnetoelectric pressure or thermal dragging.

Future experiments will address the domain structure and DW mechanics in $\sim 100\text{ }\mu\text{m}$ -thick Cr_2O_3 crystals. Electric gates could furthermore allow us to realize a more reliable method of DW motion than laser dragging. By applying a magnetoelectric pressure to the DW, one should be able to move the DW [175], but this has yet to be shown on single-crystal samples. As such, one avenue of future research into Cr_2O_3 will be to realize and characterize such electric field-based DW motion.

Next to such application-driven motivations, there is also a wide range of fundamental physics to explore in Cr_2O_3 . For example, there is the question of the DW type. There is also the question of the surface magnetization of Cr_2O_3 . In Sec. 4.1.4, we introduced a few of the theories currently used to explain the existence of the surface magnetization that we observe. While we have confirmed some of the predictions made in the section, the measured and theoretical surface magnetization amplitudes still show some discrepancies. In Ref. [161], Spaldin also provides a method for calculating the magnetization of non $[001]$ -oriented surfaces, which would be a further test of the magnetoelectric multipolization theory. In particular, we have received a $[104]$ -oriented crystal, on which we have performed initial measurements. As shown in Fig. 4.20a, we have etched the surface of this sample and performed magnetoelectric annealing, allowing us to realize DWs much like in the $[001]$ -oriented crystal.

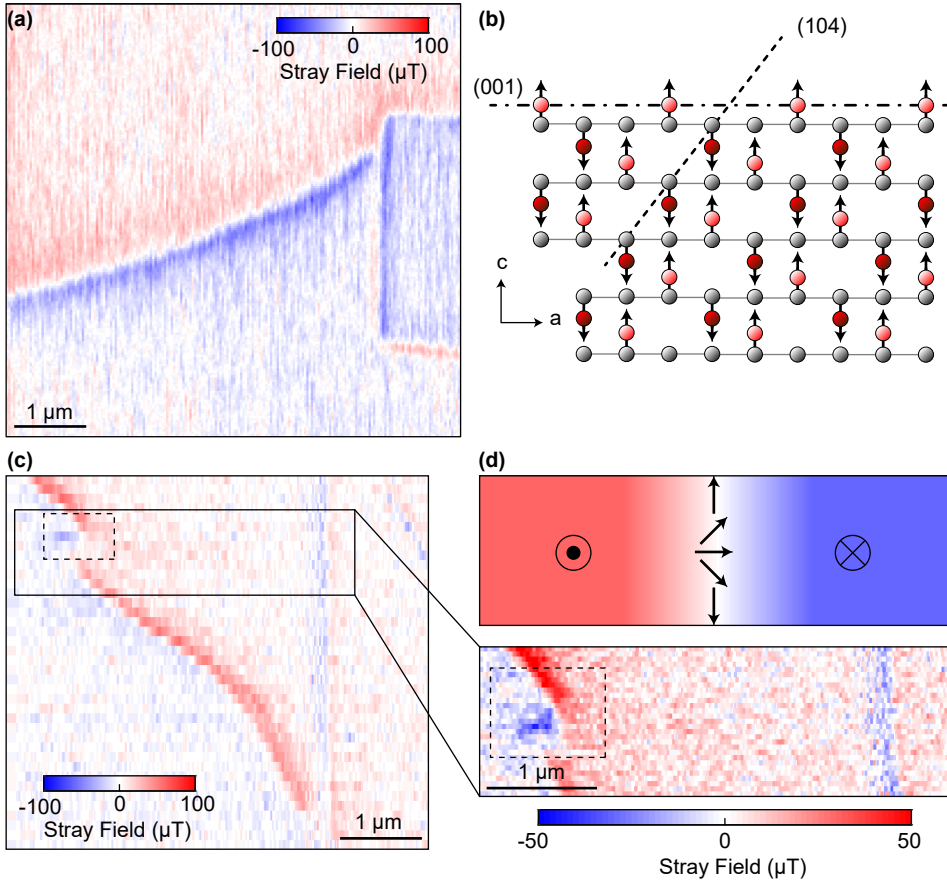


Figure 4.20.: Summary of existing questions. (a) Stray field image of a DW in Cr_2O_3 with a (104) surface. We see qualitatively similar behavior of the DW as with the [001]-oriented sample. (b) Crystal structure of Cr_2O_3 showing the cut along the (001) (dash-dotted line) and (104) surfaces (dotted line). (c) Stray field image of a DW in the [001]-oriented Cr_2O_3 lattice showing a kink or ‘break’ in the DW, highlighted with a black dashed square, created after high power laser dragging. (d) Top: Schematic showing the rotation of the magnetization in a Bloch point [182]. Bottom: Detailed scan of the DW break shown in (c), illustrating the discontinuous DW stray field, which could indicate a Bloch point.

While we observe stray fields on this sample, it is a priori not clear in which direction this magnetization points, making the analysis more difficult. One possible path to answering this question is to look at the crystal structure of Cr_2O_3 shown in Fig. 4.20b. Here, we see that the spins orient perpendicular to the (001) surface, leading to a canting relative to the (104) surface shown with a dashed line. However, whether this canting is maintained at the surface is unknown. Here, the multipolization method presented by Spaldin could provide helpful and interesting results.

There is also the question of DW dynamics. One possibility is to examine the motion of the DW itself. For example, one could investigate DW velocities in the presence of various stimuli such as electric and magnetic fields [175] or thermal gradients [173, 174]. Such experiments would also allow us to extract information about the pinning landscape of these bulk, single crystals. Alternatively, one can also investigate dynamics within the DW. Recent results on synthetic AFMs have shown how NV magnetometry may be used to image magnetic fluctuations at the DW through PL reduction of the NV [183]. To our knowledge, no such magnetic fluctuations have been seen in true AFM DWs to date.

Yet another, even more exotic research direction has presented itself through our laser dragging experiments. When scanning across the DW with high laser powers, we have occasionally observed the generation of small, apparent “breaks” in the DW, as shown in Fig. 4.20c and d. Though it is by no means clear what these magnetic signatures are, one possible explanation could be the formation of Bloch points. These are defects within the DW, in which the rotation of the magnetic moments changes direction, as shown in the top panel of Fig. 4.20d [182, 184]. As these structures have yet to be shown in experiments, this could be another exciting avenue of research. Adding to the list of potentially exotic physics in Cr_2O_3 , another exciting possibility is the generation of a magnetic monopole at the Cr_2O_3 surface due to a nearby electric charge, presented in the recent proposal by Meier et al. [185]. Needless to say, we have only just begun to scratch the surface of the interesting physics to be explored in this system.

4.5.1. Summary

Finally, let us summarize the results of this chapter. We began in Sec. 4.1 with a general introduction to magnetic ordering and magnetoelectric susceptibility, touching upon the most important energy contributions in any magnetic system - exchange, anisotropy, and dipolar interactions. We then applied this general discussion to the atomic and magnetic properties specific to Cr_2O_3 . In doing so, we developed a simple model of the material based on the exchange and anisotropy contributions. We also discussed how symmetry breaking in the crystal leads to the magnetoelectric properties that make it so attractive for applications. This latter point then brought us to the surface magnetization of Cr_2O_3 , which we proceeded to characterize using NV magnetometry performed on topographic steps on the Cr_2O_3 surface. Here, the fabricated mesas played a key role as they serve as a source of stray magnetic field in an otherwise uniformly magnetized surface. In particular, we observed an average surface magnetization of $2.1 \pm 0.3 \mu\text{T}/\sqrt{\text{Hz}}$ consistent with earlier measurements. We also showed the power-law temperature dependence of this magnetization with a critical temperature around 307 K, thereby verifying the connection between the surface magnetization and the bulk magnetic order.

Then in Sec. 4.2, we turned our attention to the DWs themselves. After an introduction to the structure of the DWs, we demonstrated the ability to nucleate these structures in the Cr_2O_3 crystal through magnetoelectric annealing. We showed that we could reproducibly and controllably select a desired order parameter of the crystal, based solely on the relative orientation of the applied magnetic and electric fields. With the aid of the mesas introduced in the previous section, we were then able to

locate and image the resulting DWs. What we found were very smooth DWs that extended over multiple millimeters, showing pristine behavior. An in-depth analysis of the DW stray field allowed us to extract an upper bound on the magnetic length of 32 nm at room temperature under the assumption of a Bloch wall. Unfortunately, with our current spatial resolution, we could not quantify the magnetic length or DW type with more precision.

This investigation of the DW was extended in Sec. 4.3, where we focused on deviations from the otherwise smooth behavior observed thus far. In doing so, we realized that the interaction between the DW and the surface topography led to a Snell's law-like refraction of the DW. This refraction was explained through minimization of the energy cost arising from the additional DW area under the mesa. We also used simulations and analytic analyses to develop a 3D model of the DW in the bulk. Not only were we able to reproduce the Snell's law behavior, but we were successful in explaining and predicting further phenomena based on our model of the DW as an elastic surface. In particular, we investigated the pinning of the DW to the mesa edges. We again used simulations to define a tension energy arising from the increased DW area. To further explore this pinning, we demonstrated DW motion through local heating with a 532 nm laser at global sample temperatures near $T_{\text{Néel}}$. In doing so, we were able to realize pinning on alternating sides of a mesa structure. First steps towards characterizing the pinning landscape of the Cr_2O_3 crystal were made by scanning across the DW with the NV center at increased powers. The ability to repeatably drag and pin the DW not only verifies the simulated behavior of the DW but also acts as a stepping stone to DW-based AFM memory devices.

Finally, in Sec. 4.4, we moved from the bulk Cr_2O_3 to thin films. While the step to thin films is somewhat application-driven, these systems are interesting in their own right. In particular, we discussed several realizations of thin film samples exhibiting increased critical temperatures. These films were grown using a new method that induces up to 8.5% strain in the film. We summarized our NV magnetometry measurements on these films, where we observed stray fields exceeding 85 °C. We were also able to explain the discrepancy seen between the critical temperature measured using Hall magnetometry and NV magnetometry through the development of a strain-dependent Néel temperature gradient.

In this chapter, our goal was to address some of the open questions surrounding the magnetic structure of Cr_2O_3 , in particular, its DWs. Throughout this chapter, not only have we demonstrated the nucleation and control of DWs, but we have also presented the building blocks of a novel form of AFM memory. Our results open up new avenues for investigating DW dynamics in AFM and magnetoelectric systems. Of course, this was only made possible through our measurement technique – NV magnetometry. Throughout Chapters 2 and 3, we have repeatedly touted the benefits of this technique and now have finally been able to use all these benefits to investigate the non-trivial system that is Cr_2O_3 . Thanks to the nanoscale spatial resolution achieved through scanning NV magnetometry, we were able to image the deviation of DWs when crossing a micron-scale mesa. Through the high stray field sensitivity, we could perform scanning measurements even close to the Néel temperature where the magnetization vanishes. These results cement the NV center as a versatile tool for investigating the magnetic properties of AFM systems and will continue to play an important role in future studies of DWs.

5. Summary and outlook

The rapid exchange of information has become a fundamental part of daily life. However, this development has caused the energy requirements for data centers worldwide to surpass the yearly energy consumption of many countries [186]. This issue is one of the motivating factors in developing new computing and memory technologies. In particular, throughout this thesis, we have focused on efforts in the field of spintronics, where the development of magnetic memories based on AFM materials promises to provide fast, energy-efficient alternatives to modern FM memories [13, 17, 180]. Of course, fundamental to this process is the characterization of potentially interesting materials and their magnetic structures, which requires an appropriate toolset.

Here, we have presented one such tool, the NV center in diamond, which has been established as a highly competitive sensor in a broad range of scientific fields. Over the last years, the NV center has found its place in range of fields including magnetometry [27, 28, 31], electrometry [37, 187], and thermometry [40, 43], and in systems ranging from biological cells [42] to geological studies [188]. This success can be attributed to its versatility, high sensitivity, and spatial resolution. It is these same properties that allow us to use NV magnetometry to answer open questions in the AFM spintronics community, inaccessible by other methods.

With this thesis, our goal was to further develop our understanding of DW mechanics in Cr_2O_3 , a magnetoelectric AFM. In addressing this goal, the key outcomes of this thesis were two-fold. Firstly, we developed a novel form of truncated parabolic scanning probes, improving on the state-of-the-art diamond scanning probes. These devices were then used to realize the Cr_2O_3 studies presented later in this thesis. In particular, we demonstrated the ability to generate and control single DWs in Cr_2O_3 , ultimately laying down the building blocks for a novel AFM memory device.

5.1. Summary

Central to any discussion of NV magnetometry is, of course, an understanding of the NV center itself. As such, we began in Chap. 2 with an introduction to the structure and electronic energy levels of the NV center. We saw that we can initialize and read out the spin state of the NV center through optical excitation while manipulating the spin state with MW excitation. We followed this up with a discussion of a second degree of freedom - the charge state. Specifically, we explored how the NV center's neutral charge state creates a significant background when measuring the NV spin state. With these building blocks in hand, we were then able to discuss the basics of NV magnetometry. We examined the magnetic field dependence of the NV energy levels and how the splitting of the $|\pm 1\rangle$ levels may be used to determine the magnetic field. Though several different techniques exist, we focused here on ODMR as a measure of static fields. We also highlighted some variations on the method which reduce

the otherwise long measurement time. We then concluded our discussion of NV magnetometry with a discussion of sensitivity and spatial resolution, two parameters that define the performance of any magnetometer. In particular, we saw the importance of having high PL collection efficiencies while simultaneously bringing the NV close to the diamond surface.

In Chap. 3, we then addressed both of these requirements in developing a new form of NV scanning probe. Though the high index of refraction of diamond makes collecting PL from the NV within a bulk diamond difficult, we could use it to our advantage. In particular, we used the total internal reflection of a truncated parabolic pillar to guide the PL towards the collection optics. Through simulations, we demonstrated a considerable improvement in both collection efficiency and angular emission of these truncated parabolic pillars. We then outlined the steps necessary to fabricate such structures before discussing the results of an extensive characterization of the resulting devices. We observed a highly directional emission with an NA of ~ 0.44 and, to our knowledge, the highest recorded PL rates for single NV, diamond scanning probes to date of 2.1 ± 0.2 MHz. We also characterized the radiative lifetime of the NV centers as well as their steady-state charge state, using the latter to finally provide an estimate of 57% for the collection efficiency of our devices. The improvements that we saw in the pillar performance allowed us to realize a DC ODMR sensitivity of up to $1.22 \pm 0.07 \mu\text{T}/\sqrt{\text{Hz}}$. This value represents a factor of >2 improvement on prior pillar designs [92]. At the same time, we achieve an average spatial resolution of 69 ± 13 nm.

This excellent performance allowed us to realize the investigation central to this thesis – a measurement of DW mechanics in AFM Cr_2O_3 – as presented in Chap. 4. We began with a general introduction to magnetic ordering and magnetoelectricity before exploring the specific magnetic properties of Cr_2O_3 . Through this discussion, we developed a simple model of this material. One feature of importance is the presence of a surface magnetization, whose theoretical origin we discussed and which we measured using NV magnetometry. The key to these measurements was patterning the Cr_2O_3 crystal surface with mesas. These acted as markers and as a source of stray magnetic fields in the uniformly magnetized sample. We then moved to a theoretical description of DWs and demonstrated the ability to nucleate single, isolated DWs through magnetoelectric poling. In the subsequent analysis of the resulting DWs, we could place an upper bound of 32 nm on the magnetic length used to characterize the width of the DW. Finally, we explored the unexpected interactions between the DW and the surface topography that we had observed. We showed several different behaviors of the DW depending on the relative location of the DW and mesa. These included a Snell’s law-like refraction of the DW and pinning of the wall to the edges of the mesas. We were able to explain both scenarios through simulations and analytical calculations. In doing so, we modeled the DW as an elastic film whose trajectory results from the minimization of the DW surface energy. Simulations further suggested an ability to pin and move the DW. We were later able to confirm this behavior experimentally through dragging of the DW using local heating with a focused laser. These bulk crystal realizations show great promise and formed the basis of a proposal for a novel AFM memory device presented later in the chapter. Finally, we presented first results on thin-film Cr_2O_3 , demonstrating the ability to raise the Néel temperature through strain introduced during the film growth. Additionally,

we observed a deviation between measurements of the Néel temperature with Hall and NV magnetometry, which we explained based on a strain-induced gradient in the critical temperature.

In conclusion, through all of these measurements, we have highlighted the versatility of the NV center as a sensor and have shown that NV magnetometry is a very promising technique for addressing AFM materials. At the same time, our observations of the mechanics of AFM DWs have revealed a number of exciting research directions, which will guide future research into the dynamics of DWs and how they may be harnessed for future memory applications.

5.2. Outlook

Throughout this thesis, our focus has been on two complementary developments. In the future, this two-pronged approach will continue to drive our research. While our goal is to explore new, interesting physics, improving our measurement technique is crucial to achieving this.

In Chap. 3.4.1, we have already explored some avenues for improving the design and performance of the diamond scanning probes. However, many of these aspects require further tests. For example, the reason for the larger-than-expected NV-to-sample distances is still unknown. A measurement of the NV depth prior to fabrication would be beneficial here. A distance determination is particularly important if we consider new pillar designs [124] where a sharp apex could help us avoid larger distances due to topography.

Improving the scanning probes is not the only approach one can take. The room temperature confocal scanning setup suffers from some drawbacks, the largest of which is the scanning method. We have mentioned the importance of characterizing the motion of the piezo, which we explore in more detail in Appendix A.2.2. To address this issue, we have developed a closed-loop scanning solution, which uses a commercial interferometry system (IDS 3010/SMF, Attocube) to obtain the real-space position of the piezo scanners. In this way, we can use the signal to controllably and repeatedly move our scanner to the desired position. The IDS can also help us determine the true length scales of structures, which is critical when fitting the stray fields. This implementation has only very recently been realized and is still under development. However, it promises to significantly improve the uncertainty in our analyses of stray magnetic fields. Such improvements to the scanning setup, magnetometry techniques, and NV center performance are vital stepping stones for future studies.

The second part of our two-prong approach focuses on new physics. The field of AFM spintronics is broad, and besides the many promising experiments proposed for Cr_2O_3 , there are many other interesting systems that one could explore. FeRh is one such system. This material undergoes a phase transition from AFM to FM around 300-400 K [189], as shown in Fig. 5.1a. It also shows great promise for spintronic applications and has been used in a proof-of-principle AFM memory device [180]. Still, as with Cr_2O_3 , many open questions exist, in particular, concerning the physics at the phase transition. Real-space imaging with PEEM-XMCD, shown in Fig. 5.1b, has already proven helpful in providing a clearer picture of this transition [190].

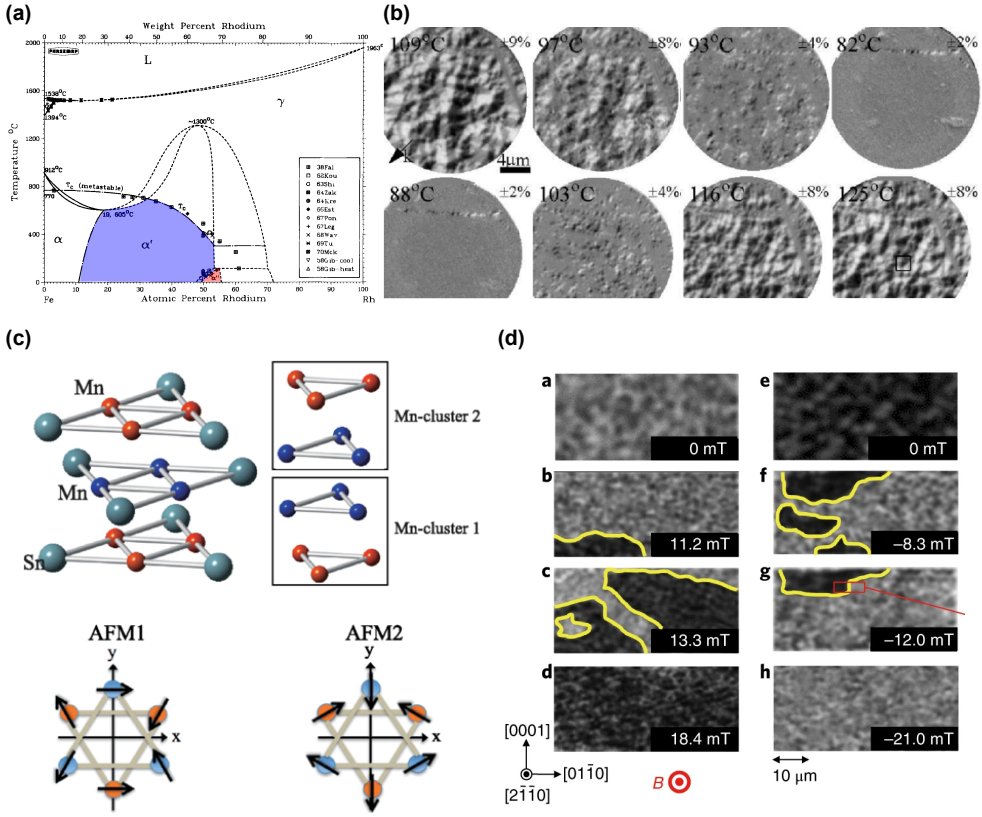


Figure 5.1.: Summary of interesting AFM systems for future study. (a) Phase diagram of FeRh as a function of temperature (vertical) and Rh concentration (horizontal). Around 50% Rh content, the material undergoes a transition from AFM (red) to FM (blue) ordering. Adapted with permission from [191]: Bul. Alloy Phase Dia., 1984. (b) PEEM-XMCD images showing the transition from AFM (top left) to FM (bottom right) in FeRh. Adapted with permission from [190]. (c) Crystal structure of Mn₃Sn with two different AFM orders shown. Reprinted with permission from [192]. Copyright 2017 by the American Physical Society. (d) MOKE imaging of the domain structure of Mn₃Sn in varying external magnetic fields, showing the flipping of the AFM order. In particular, the light gray represents the order AFM1 shown in (c), with the dark gray having all spins flipped 180° along their axis. Reproduced with permission from [193]:Nature Photonics, 2018.

However, this study was unable to address the behavior in the presence of external magnetic fields. Here, NV magnetometry could be a vital asset. Recently, first measurements of this transition using NV magnetometry have been performed, showing a reorientation of the DWs [194]. Furthermore, this material has been shown to exhibit unique spin phenomena at the phase transition [195], where the AC magnetometry capabilities of the NV center could provide local detection of these spin dynamics.

Another potentially interesting AFM system is the class of Mn₃X materials,

where X commonly refers to Sn or Ge. Unlike Cr_2O_3 , Mn_3X materials are non-collinear. These materials exhibit a hexagonal lattice, in which the Mn atoms form a honeycomb-like structure with multiple possible in-plane spin orientations, as shown in Fig. 5.1c [192]. Interest in this material first developed due to observations of a large anomalous Hall effect [196]. However, there are still multiple open questions regarding the magnetic structure of these materials. Theoretical descriptions of Mn_3Sn expect a 60° Bloch wall with a magnetic length of over $1\text{ }\mu\text{m}$ though measurements using MOKE (see Fig. 5.1d) seem to indicate Néel walls [193]. Here, the NV center could be helpful, specifically for resolving the DW structure. These are just two of the many potential material systems to be explored.

With all the interest in AFM systems, both in terms of technological applications and the interesting physics they are host to, these systems will likely prove quite fruitful in the near future. At the same time, NV magnetometry is uniquely poised to answer the questions surrounding these materials and will continue to be a highly effective tool in these studies. In the end, this thesis represents just a small drop in the much larger bucket that is the joint journey of NV magnetometry and AFM spintronics.

A. Appendix

A.1. Fabrication

A.1.1. Diamond fabrication

The basic fabrication procedure for achieving NV scanning probes in the group has mainly remained the same for the last years [62, 80, 92]. However, optimization of the process and design is constantly taking place. As discussed in Chap. 3, the most recent innovation has been the addition of truncated parabolic portions at the tip of the scanning probes. Here, we will outline the fabrication procedure for these devices. Many of the details here have been modified from the SI of Ref. [32].

We begin with a bulk, type-IIa diamond plate (Element Six) with a (100) surface. The type-IIa classification indicates that the diamond is low in impurities, with a natural nitrogen concentration of less than 5 ppb. We prepare the diamond for fabrication as follows.

1. The diamond is sliced and polished to a thickness of 50 μm by an external provider (Almax).
2. We remove $\sim 3\mu\text{m}$ of diamond from the top surface via an inductively coupled plasma reactive ion etch (ICP-RIE, Sentech), alternating between Ar/ Cl_2 and O_2 chemistries, as shown in Fig. A.1a, and as described in [29]. The goal of this step is to relieve stress within the diamond to prevent breaking in later stages.
3. The diamond is implanted with $2 \cdot 10^{11} \text{ cm}^{-2} \text{ }^{14}\text{N}$ at 12 keV and 7° tilt to the sample normal (Innovion), resulting in an estimated N depth of 20 nm (see Fig. A.1a).
4. We anneal the diamond in a vacuum to a maximum temperature of 1200 $^\circ\text{C}$ following the procedure outlined in [197].

Following this diamond preparation, we pattern the diamond surface, beginning with an array of cantilever structures and holding bars. In contrast to previous methods, we opt for patterning the entire diamond surface with multiple $1 \text{ mm} \times 1 \text{ mm}$ write fields (WFs), each containing 328 $20\mu\text{m} \times 40\mu\text{m}$ structures. We begin by mounting the diamond on a larger silicon substrate using an adhesive (Crystalbond, Pelco) and spinning a mask onto the diamond surface using the following recipe:

1. Spin Ti-based primer (Ti-Prime, MicroChemicals GmbH) onto the surface at 6000 rpm with a 3-second ramp for 40 seconds. This primer can help with adhesion between the mask and diamond.
2. Spin the flowable oxide resist (FOX-16, Dow-Corning) onto the surface at 6000 rpm for 60 seconds. This recipe should form a $\sim 300 \text{ nm}$ -thick mask.

3. Spin a conductive coating (Elektra 92 - Allresist) onto the surface at 2800 rpm for 60 seconds. This coating helps combat charging effects during patterning.

At the very beginning and following each step, the diamond is heated to 120°C for 2 minutes. The aforementioned structures are then written into the mask via electron-beam lithography (60 μm aperture, 30 keV energy, base dose of 600 $\mu\text{C}/\text{cm}^2$) and developed in TMAH for 30 s. The resulting mask is then transferred into the diamond via an ICP-RIE etching process outlined in Table A.1. This process is repeated twice, resulting in structures with a height of 2 μm , as shown in Fig. A.1b. Following this, we remove the remaining mask with a 40% buffered oxide (HF) bath.

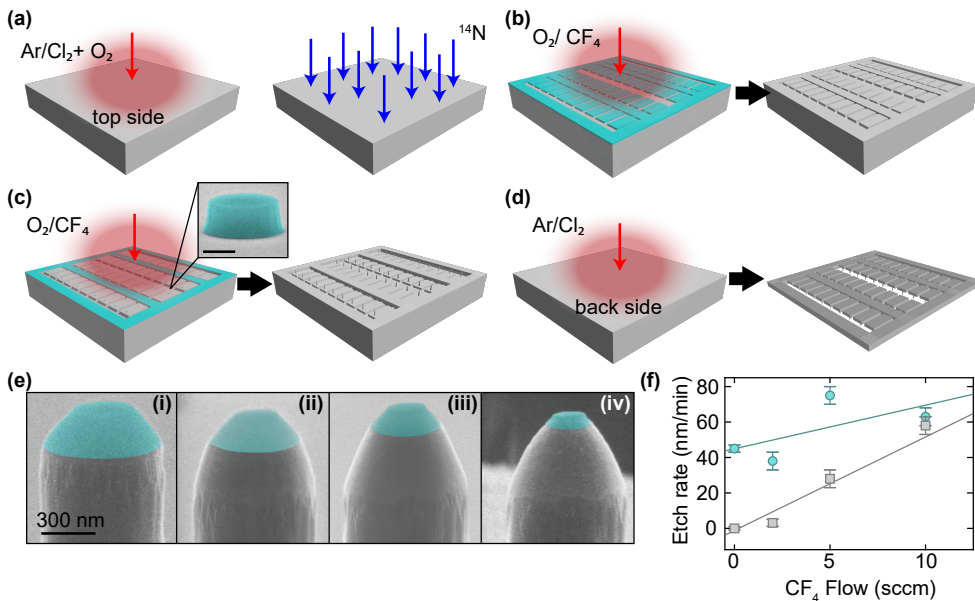


Figure A.1.: Fabrication procedure for a diamond sample. (a) The diamond is prepared using an Ar/Cl_2 and O_2 -based etch to relieve stress and is subsequently implanted with ^{14}N . (b) A FOx-16 mask is patterned on the diamond to define the holding structure and cantilever array. The mask is then etched into the diamond with an O_2/CF_4 plasma. (c) A second FOx-16 layer is patterned to achieve a pillar mask (shown in the inset, scalebar = 300 nm) and holding structure, and then etched according to the recipe outlined in Table A.2. (d) The diamond is etched from the reverse side with an Ar/Cl_2 plasma to release the structures. (e) SEM images highlighting the development of the parabolic pillar tip. (i) After the first stage of O_2 etching, the mask is eroded at the edges, leaving a trapezoidal cross-section. (ii-iv) Subsequent etching steps with increasing CF_4 flow, resulting in a controlled mask erosion and a parabolic diamond surface. (f) Etch rates of diamond (gray squares) and FOx mask (cyan circles) vs. CF_4 concentration, with linear fits (solid lines).

O ₂ Flow (sccm)	CF ₄ Flow (sccm)	Pressure (Pa)	ICP (W)	RF (W)	Time (s)
50	0	0.5	500	110	390
50	2	0.5	500	40	20

Table A.1.: Summary of the plasma parameters for etching the cantilever and holding bar structures.

In the next step, we wish to create a mask for the pillars. To do so, we use the same spinning recipe as before and proceed by defining 1 μm -diameter circular masks. These are written with electron beam lithography by aligning to the pre-etched cantilevers based on markers place in the corners of each WF. One common problem we have experienced in the past is the adhesion of the mask to the diamond surface. Recently, the use of an evaporated Si layer, which acts as an adhesion promoter, has proven quite successful in overcoming this problem [198]. However, instead have focused on obtaining an optimal exposure of the FOx mask. Therefore, we write the pillar masks as two concentric circles. In this way, the center of the mask is thoroughly exposed, resulting in excellent adhesion to the diamond. At the same time, by making the inner, double-exposed region smaller than the desired mask size, we can establish sharp mask edges. Specifically, we write the masks with a 30 keV energy electron beam, using a 30 μm aperture, base dose of 600 $\mu\text{C cm}^{-2}$, and a dose factor of 3.4. The inner mask is set to be 80% of the outer one.

The pillars themselves are etched in two stages. We begin with a tapered pillar etch as summarized in the first section of Table A.2. Here, short O₂ /CF₄ steps are used to remove resputtered material, arising from the alumina mounting wafer and mask, from the device walls [108]. The final two etch steps of stage 1 are repeated a total of 6 times to achieve a $\sim 6 \mu\text{m}$ tapered pillar. At the end of this stage, the mask has a trapezoidal cross section with a base diameter of 900 nm, as seen in Fig. A.1ei.

Stage	O ₂ Flow (sccm)	CF ₄ Flow (sccm)	Pressure (Pa)	ICP (W)	RF (W)	Time (s)
1	50	10	0.5	500	50	10
	50	0	0.5	500	110	240
	50	2	0.5	500	40	4
	50	0	0.5	500	110	240
2	50	2	0.5	500	40	120
	50	4	0.5	500	40	2 \times 60
	50	6	0.5	500	40	2 \times 45
	50	8	0.5	500	40	30
	50	10	0.5	500	40	10

Table A.2.: Summary of the plasma parameters used for etching the truncated parabolic pillar.

In the second stage, we finally introduce the parabolic nature of the pillar using the preferential etching of the mask by CF_4 . By varying the CF_4 concentration, we control the relative etch rate of the mask and diamond, as summarized in Fig. A.1f. In this way, we also control the angle of the diamond wall. The etch consists of several steps in which we introduce successively higher flow rates of CF_4 to achieve increasing diamond wall angles, as shown in Fig. A.1e(i–iv). The details of these stages are outlined in Tab. A.2. Following the final etch step, the remaining mask is removed with an HF bath. A typical final device (see Fig. 3.4b) then consists of a ~ 500 nm parabolic tip section with a ~ 200 -nm flat end facet and a ~ 6 μm -long, tapered pillar with a ~ 2 μm base diameter.

Following the pillar etch, the pillar side of the diamond is coated with a 10 nm layer of titanium and 100 nm gold to act as a protection layer. The diamond is then etched from the opposite side using an Ar/Cl_2 etch plasma until the cantilever structures are free-standing and held in place only by a thin, diamond holding bar, as shown in Fig. A.1d. The diamond is then cleaned using gold etchant and a tri-acid clean [60]. Finally, the devices may be assembled into scanning probes as described in Ref. [29].

A.1.2. Chromia fabrication

Even before patterning the mesas, initial measurements of the Cr_2O_3 surface showed a magnetic signal. However, we believe that this signal arose due to magnetic contamination rather than topography due to the large signal strength [157] and the fact that it persists far beyond the expected bulk Néel temperature, as shown in Fig. A.2. Etching of the surface through 50 repeats of a 1s Ar/Cl_2 plasma removed the top layers of the sample, at which point the magnetic signal disappeared completely.

The subsequent fabrication of the mesas on the Cr_2O_3 surface relies on many of the same techniques as introduced in the previous section. Unfortunately, the mesa writing process initially showed significant difficulties with adhesion. This difficulty was overcome by evaporating a 2 nm Ti layer onto the Cr_2O_3 instead of Ti-prime when spinning the FOx mask. Following this, we continue with the recipe as stated. The mask is written with electron beam lithography (30 kV energy and 30 μm aperture with a $630 \mu\text{C cm}^{-1}$ base dose) and developed using 30 s of TMAH.

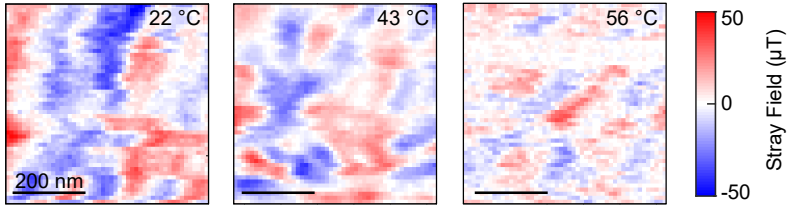


Figure A.2.: Contamination of the Cr_2O_3 surface. Full-field images taken on the unetched surface of the Cr_2O_3 sample at increasing temperatures. The signal persists far above the Néel temperature and was removed through etching with an Ar/Cl_2 plasma.

Ar Flow (sccm)	Cl ₂ Flow (sccm)	Pressure (Pa)	ICP (W)	RF (W)	Time (s)
25	40	1	400	20	100

Table A.3.: Summary of the plasma parameters for etching ~ 160 nm mesas in Cr₂O₃.

The etching is carried out using an Ar/Cl₂ ICP-RIE process, whose parameters are outlined in Table A.3. Following the etch, the mask is removed with 5 minutes in an HF bath, and the sample is cleaned with three solvent baths: first acetone, then isopropyl alcohol, and finally ethanol. To remove any remaining particulate matter, we also find First Contact (Photonic Cleaning Technologies), an optics-cleaning polymer, to be quite effective.

A.2. Setup details

In this section, we will describe the two homebuilt confocal microscopes used in this thesis. Sec. A.2.1 is modified from the SI of Ref. [32], while Sec. A.2.2 is largely modified from the methods section and SI of Ref. [140]

A.2.1. Characterization setup

We will begin with the characterization setup used in Chap. 3. Though this setup exhibits functionality exceeding that which will be described here, we will focus on the aspects relevant to the measurements provided in this thesis.

The confocal microscope is equipped with CW excitation lasers at 532 nm and 594 nm, and one can additionally couple in a tunable supercontinuum picosecond pulsed laser (SuperK Extreme, NKT Photonics). We use a 100 \times , 0.8 NA microscope objective (Olympus) to illuminate the sample and collect the PL of the NV center. The collected light is filtered by a 635 nm dichroic filter before being coupled through an $f = 18$ mm objective (Attocube) into an 8.2 μm core diameter fiber (SMF-28, Thorlabs). This arrangement provides good mode matching to the observed NA ≈ 0.45 output mode of our devices. The fiber output is further filtered by a 594 nm long-pass filter (Semrock) before being focused onto one of two avalanche photodiodes (APDs) (ARQH-33, Excelitas).

The objective is mounted on a scanning stage (P-562.3CD, PI), with a range of 200 $\mu\text{m} \times 200 \mu\text{m}$. The sample is placed below the objective, on a Newport M-562 stage with a 13 mm range, allowing us to access the entire 5 mm \times 5 mm diamond sample. Microwave excitation is provided by a 30 μm -diameter gold wire formed into a simple loop and soldered across the outer and inner conductors of a coaxial cable. A permanent magnet mounted on a moveable stage allows us to realize an adjustable bias magnetic field. Furthermore, a camera (WAT 910HX, Watec) near the objective with adjustable tubing allows us to image the sample surface and the BFP. Pulsing is controlled by an FPGA (MyRIO, NI) with custom LabView software developed by Lucas Fisher, Brendan Shields, and Oliver Frei.

In Chap. 3.2.4, we discuss the collection efficiency of our TPSP devices. To do so, we must examine the PL losses from each optical element between the NV center and the APD. For the majority of elements (e.g., mirrors and filters), we take the specified transmission over the range of wavelengths between 630 nm and 800 nm to determine the transmission efficiency. For the coupling into the SMF-28 fiber, we measure the attenuation of the supercontinuum source tuned to a band around 635 nm, which is the cutoff of our dichroic mirror. At this wavelength, the source can be coupled into the scanning probe device such that the reflection off the device is partially transmitted by the dichroic. In this way, the fiber coupling attenuation can be directly measured for the output mode of the device. The efficiencies of all components are summarized in Tab. A.4. The overall efficiency listed under total then gives us ϵ_{setup} and is used to determine the collection efficiency of our device in Chap. 3.2.4.

Component	Efficiency
Olympus LM PLAN FL N 100× microscope objective	0.85
Newport ultrabroadband mirror (x4)	0.99
Dichroic 1000 nm longpass (DMLP1000, Thorlabs)	0.99
Semrock FF635 Di01	0.94
Semrock 647 nm edgebasic longpass	0.82
Fiber coupling	0.50
Semrock 594 nm edgebasic longpass	0.99
Thorlabs E02 mirrors (x2)	0.99
Thorlabs AC254-060-B ML lens	0.99
Excelitas SPCM ARQH-33	0.67
Total	0.21

Table A.4.: Summary of setup losses at the characterization setup at the time of measurement.

A.2.2. Room-temperature NV magnetometry setup

For all magnetometry measurements shown in this thesis, the data were taken with a confocal microscopy setup similar to that of the characterization setup discussed in the previous section. It is equipped with a single CW 532 nm laser source (GEM-532, Laser Quantum), allowing us to realize several mW of excitation power measured at the objective. However, apart from the laser dragging experiments, all measurements were performed with $\lesssim 10 \mu\text{W}$ of excitation, a factor of two smaller than typical saturation powers for NVs in the TPSP devices (see Chap. 3.2.1). The laser passes through a laser line filter (FL532-10, Thorlabs) and subsequent polarization optics before reflecting off a 552 nm dichroic (LM01-552-25, Semrock) towards a fixed objective. The PL collected through the objective then passes through this dichroic and is measured at an APD (SPCM CD3531, Excelitas).

The microwave for manipulating the NV is again provided by a 30 μm -diameter gold wire in the form of a loop antenna with a typical effective driving strength of 0.25 G at the NV as determined through Rabi measurements [92]. These low excitation powers (both microwave and laser) ensure that we do not disturb the magnetic ordering of the sample. A small bias magnetic field (< 60 G) is applied along the NV axis using a permanent magnet to allow for a sign-sensitive measurement of the stray magnetic fields.

Both sample and NV are mounted on piezoelectric scanners ($\text{ANS}_{(\text{xyz})}100$, Attocube) placed on top of additional stepping modules ($\text{ANP}_{(\text{xyz})}101$, Attocube). These provide a total range of 5 mm in all directions through stepping, with an additional $\sim 40 \mu\text{m}$ in x and y through the scanners. When heating of the sample is needed, we mount the sample on a small Peltier element (TEC3-2.5, Thorlabs) with thermally conductive adhesive tape. The Peltier is then placed on top of one of the two scanners and controlled via a PID unit (TTC001, Thorlabs), allowing us to reach temperatures of ~ 360 K during the scanning process.

As we are using open-loop piezo scanners, we need to calibrate their physical displacement and determine the piezo non-linearity to achieve an accurate representation of distances in our stray field images. To do so, we perform atomic force microscopy measurements of a section of the patterned Cr_2O_3 sample on a commercial system (Bruker Dimension 3100), as shown in Fig. A.3a (left).

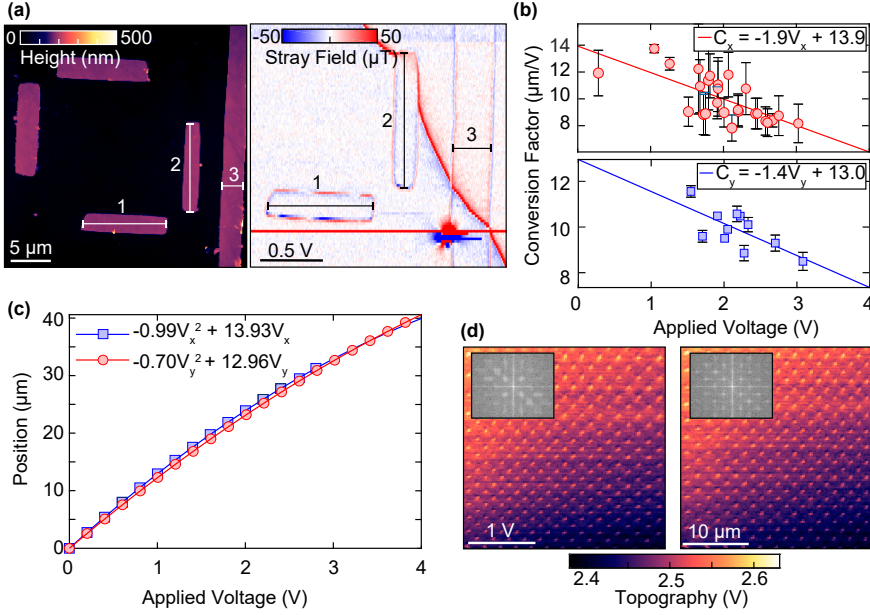


Figure A.3.: Calibration of the piezo position. (a) Atomic force microscopy (left) and NV magnetometry (right) images used to compare length scales and obtain the conversion factor from applied voltage to real distance. Error bars are estimated from the images in (a). (b) The conversion factor from applied voltage (V) to displacement (μm) as a function of the applied voltage for the x (top) and y (bottom) axes. (c) A plot of the position (as determined by integrating the conversion factor in (b)) as a function of the voltage applied in the x -direction (blue squares) and y -direction (red circles). The fit parameters are given in the top right inset. The bottom-right inset shows the resulting deformation of equally spaced lines in a 2D plot, with dark gray arrows shown for emphasis. (d) Topography images taken with scanning NV magnetometry over a test grating (TGT1, NT-MDT) pre- (left) and post-calibration (right). The insets show a 2D Fourier transform of the pattern.

If we assume the topography there is primarily sample topography and not due to the tip geometry, then we can use this as a calibration for our piezo. To do so, we compare the lengths and widths of the same structures measured in our confocal setup, as shown in Fig. A.3a (right). Rather than using the topography measured in our system, which is convolved with our very blunt TPSP tip, we use the magnetic field data, as the stray fields we measure arise from the very edge of the mesas. A few points of comparison are shown in Fig. A.3a. This procedure allows us to determine the conversion factor from the applied voltage (V) to physical piezo displacement (μm) for a reasonably wide range of piezo voltages, as shown in Fig. A.3b. Note that these data points are based on previously measured stray field images and, for this reason, do not represent an exhaustive study of the range of applied voltages. However, this subset should be sufficient to extract the non-linearity. Errors on individual points are calculated based on a readout error of $\pm 300\text{ nm}$ and $\pm 0.02\text{ V}$ for the AFM and

magnetometry data, respectively. The error on the x -axis is below the marker size. We integrate the fitting functions given in the legends to convert from our system coordinates (in applied voltage) to real coordinates (in μm) as shown in Fig. A.3c. We then obtain a non-linear conversion, which corrects for deformations arising from the piezo non-linearity. The non-linearity is clearly seen in the 2D topography images of a regular grid of sharp, silicon pillars shown in Fig. A.3d. Here, the original image (with scale in applied voltage) is shown in the left panel and the adjusted scaling conversion in the right panel. Though the improved regularity of the grid is somewhat difficult to see from the images themselves, taking a 2D Fourier transform of the image as shown in the inset aids the comparison. Here, the sharpness of the peaks reflects the regularity of the topographical pattern.

Through this characterization, the absolute position is calculated assuming that $0\text{ V} \rightarrow 0\text{ }\mu\text{m}$ and $4\text{ V} \rightarrow 40\text{ }\mu\text{m}$. However, we have additionally investigated the motion of the piezos using an interferometer system (IDS 3010/SMF, Attocube), and found that this is not necessarily the case. By mounting small mirrors off the side of the piezo scanner, we can measure the absolute displacement relative to the IDS sensors in the xy plane. Through this, we found that the piezos not only move more than the $40\text{ }\mu\text{m}$ in total but also that once it reaches a given position (where the ideal position by given in the applied voltage), the piezo will exhibit an additional creep of $100\text{--}200\text{ nm}$ over the first 90 s , which decays logarithmically. This creep is problematic for ensuring that we can repeatedly measure the same area of the sample. While we believe that the creep within a single scan is accounted for by our calibration, it is a likely source of drift between subsequent measurements. Another source of drift could be temperature fluctuations, though these have not yet been quantified. Most recently, the IDS measurement process has been used to create a closed-loop scanning mode, where the position of the piezos is read out via the IDS and used to modify the next voltage step in order to reach or remain at a given position. Unfortunately, this was not completed for the measurements shown in this thesis.

A.2.3. Temperature calibration

Many of our magnetometry results in Chap. 4 rely on heating the sample, which we achieve with a Peltier element described in the previous section. In this system, the temperature is regulated with a feedback cycle, where the feedback parameter is the resistance of a thermistor placed in contact with the Peltier surface. Though these thermistors (TH10K, Thorlabs) have been calibrated, we wish to verify the calibration for ourselves. In particular, as the temperature value registered by the thermistor depends on the thermal connection with the Peltier, we need to make sure that we are not biasing our results. To calibrate the measured resistance, we use a secondary thermal probe (Steinacher) placed in contact with the Peltier and near the sample. In Fig. A.4b, we summarize the result of the temperature measurements performed with the thermal probe (blue diamonds) and the TH10K (red squares), where we see good agreement, with slight deviations at lower temperatures. In an independent confirmation on a controlled heating plate (HP-155-T, UniTemp), the thermal probe showed a higher accuracy than the TH10K, showing that the pre-defined calibration can not always be trusted.

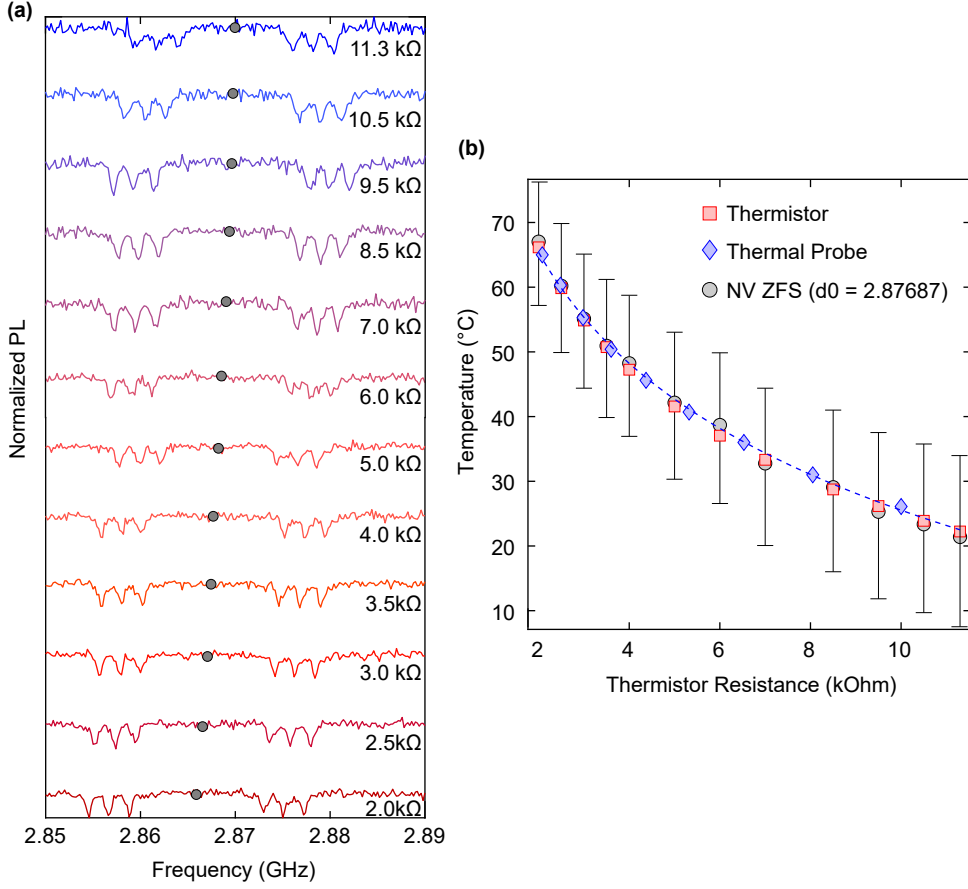


Figure A.4.: Calibration of the temperature. (a) Series of normalized, pulsed ODMR curves taken when in contact with the sample surface (here a 200 nm Cr_2O_3 film) for a Peltier temperature increasing from top (blue) to bottom (red). The ZFS of each ODMR curve is shown with a gray circle. We see a clear shift towards lower frequencies, consistent with an increase in temperature. (b) Temperature measured using a secondary thermal probe (blue diamonds) and the supposed value as measured by the thermistor (red squares) as a function of the thermistor resistance used to control the Peltier feedback loop. The temperature dependence, based on the ZFS extracted in (a) and converted according to Ref. [199], is shown with gray circles for a $d_0 = 2.87687$ GHz. The error bars show the change in the ZFS-based temperature estimate if d_0 varies by 1 MHz. The blue dashed line shows a logarithmic fit ($a \log(x) + b$, where $a = -24.7 \pm 0.3$ and $b = 82.5 \pm 1.1$) to the thermal probe data used to calibrate the temperature.

In these measurements, we are assuming that the sample is in thermal equilibrium with the Peltier. We believe this to be reasonable considering that the sample is mounted on the Peltier with thermally conductive tape. Furthermore, the entire

scanning system is placed inside a protective case to reduce thermal fluctuations and drafts that could cause rapid heat dissipation at the surface. We also attempted to verify this assumption quantitatively using the ZFS of the NV center as introduced in Chap. 2.2. We perform a series of pulsed ODMR measurements with our scanning probe in contact with the sample surface, in this case, a thin-film Cr_2O_3 sample. Here, rather than using continuous optical and MW excitation, we alternate the optical excitation and MW through short pulses. With these pulsed ODMR measurements, we can resolve the hyperfine structure of the NV center [85], which we fit to extract the ZFS. We repeat this procedure for different temperatures by setting the desired thermistor resistance. The pulsed ODMR measurements are summarized in Fig. A.4a, where we observe a shift of the ZFS, highlighted with black circles.

As discussed in Chap. 2.2, the NV ZFS depends linearly on the temperature (near room temperature) [54]. However, for broader temperature ranges, as shown in Fig. A.4, we need to examine the full temperature dependence, which can be described as a 5th order polynomial [199]:

$$D_0 = d_0 + d_1T + d_2T^2 + d_3T^3 + d_4T^3 + d_5T^5.$$

To convert the ZFS to a temperature, we use the values extracted in Ref. [199] but allow the d_0 term to vary. The results of this measurement series are summarized in Fig. A.4b (black circles) for a $d_0 = 2.87687$ GHz present excellent agreement with the other measurements. However, even a 1 MHz shift in d_0 can lead to drastic differences in the extracted temperature. We show this shift with the error bars in Fig. A.4b. Without better characterization of our NV center, it is difficult to use this method to determine the temperature. Furthermore, we have observed ODMR measurements that yield ZFS shifts corresponding to a temperature shift of multiple degrees despite the temperature of the Peltier not having changed. It is possible that the thermal contact between the diamond and the sample surface is considerably changed by the presence of contamination, which is extremely difficult to control. For this reason, we continue to rely on the thermal probe temperature calibration, which we fit to obtain a temperature calibration (blue dashed line).

A.3. Poissonian analysis of NV number

In Chap. 3.2, we found that scanning devices showing only a single pair of ODMR lines may still contain multiple NV centers. Based on our measured ODMR line statistics, let us perform a short analysis of the expected number of NVs per pillar. We will assume that the number of NVs per pillar follows a Poissonian distribution and that the orientation of the NV centers in the diamond is uncorrelated. In this case, the distribution of NV centers in a pillar is given by $P_{\text{Poiss}}(n_{\text{NV}}, \bar{n}_{\text{NV}})$, where n_{NV} is the number of NV centers, and \bar{n}_{NV} is the average value. Then the probability of measuring n_{ODMR} resonance pairs is given by:

$$\mathcal{P}(n_{\text{ODMR}} = 0) = P_{\text{Poiss}}(0, \bar{n}_{\text{NV}}) = e^{-\bar{n}_{\text{NV}}}, \quad (\text{A.1})$$

$$\mathcal{P}(n_{\text{ODMR}} = 1) = \sum_{i=1}^{\infty} P_{\text{Poiss}}(i, \bar{n}_{\text{NV}}) (1/4)^{i-1} = 4e^{-3\bar{n}_{\text{NV}}/4} \left(1 - e^{-\bar{n}_{\text{NV}}/4}\right), \quad (\text{A.2})$$

$$\mathcal{P}(n_{\text{ODMR}} > 1) = 1 - \mathcal{P}(n_{\text{ODMR}} = 0) - \mathcal{P}(n_{\text{ODMR}} = 1). \quad (\text{A.3})$$

Note that in Eq. A.2, we are summing over the probability of having any number NVs oriented in the same direction, where the $(1/4)^{i-1}$ factor appears due to the four possible NV orientations in the pillar. If we now solve these equations for \bar{n}_{NV} based on the observed ODMR lines, we obtain $\bar{n}_{\text{NV}} = 0.89 \pm 0.05$ NVs per device.

Based on this value, we are now able to determine the probability of a pillar containing a single NV center, given that we measure only one pair of ODMR lines. If we apply Bayes' Theorem and assume $\mathcal{P}(n_{\text{ODMR}} = 1 | n_{\text{NV}} = 1) = 1$, then we obtain:

$$\mathcal{P}(n_{\text{NV}} = 1 | n_{\text{ODMR}} = 1) = \frac{\mathcal{P}(n_{\text{ODMR}} = 1 | n_{\text{NV}} = 1) \mathcal{P}(n_{\text{NV}} = 1)}{\mathcal{P}(n_{\text{ODMR}} = 1)} \quad (\text{A.4})$$

$$= \frac{\bar{n}_{\text{NV}} e^{-\bar{n}_{\text{NV}}}}{4e^{-3\bar{n}_{\text{NV}}/4} (1 - e^{-\bar{n}_{\text{NV}}/4})}. \quad (\text{A.5})$$

By substituting the \bar{n}_{NV} found above, we see that $\mathcal{P}(n_{\text{NV}} = 1 | n_{\text{ODMR}} = 1) = 0.89$.

Of the 36 devices selected in Chap. 3.2, only 25 were verified to contain a single NV center via correlation measurements, thereby confirming the presence of multiple NVs with identical orientations, which cannot be distinguished by the ODMR spectrum alone. With these numbers, we find $\mathcal{P}(n_{\text{NV}} = 1 | n_{\text{ODMR}} = 1) = 0.69$, which is considerably smaller than the expected value. These skewed statistics could arise from NV centers whose position in the pillar leads to unfavorable coupling, and therefore a weak ODMR spectrum. For this reason, though the ODMR spectrum is useful, further characterization is necessary to ensure the presence of a single NV.

A.4. Approach curves

Throughout this thesis, we have repeatedly discussed the importance of determining the distance between NV and magnetic field source as this defines our spatial resolution and is also an important fitting parameter. For this reason, techniques to aid with the characterization of this quantity are of great interest. Here, we will explore the use of the NV PL drop upon approaching the sample to estimate d_{NV} [28, 118]. An example of such an approach curve is shown in Fig. A.5a. In Chap. 3.3.2, we have briefly discussed the origin of both the oscillations and the drop in the PL.

To use these approach curves as a way of determining the NV-to-sample spacing, we will first need to understand this behavior in more detail. The method used in the Reinhard group [118], which provides only a rough estimate, will not work well in this case as the oscillations they observed and analyzed far from contact (extending beyond what is seen in Fig. A.5a) are no longer visible within the noise level of the measurement.

Instead, we attempt to reproduce this behavior through simulations. Here, we use the parabolic pillar simulations discussed in Chap. 3.1.2 as a basis, and introduce a dielectric material near the end facet of the diamond pillar. In particular, we use a dielectric with an $n = 2.551$, corresponding to that of Cr_2O_3 . We then vary the distance between dielectric and diamond while recording $\mathcal{I}_{\text{na}}/\mathcal{I}_{\text{bd}}$. We integrate this value over the cone of the objective (NA = 0.8) and average over six wavelengths

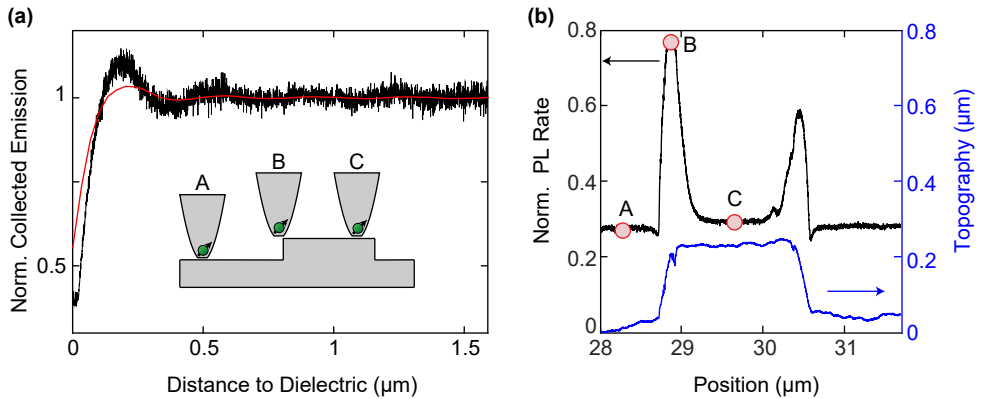


Figure A.5.: Approach curve over the Cr_2O_3 surface. (a) The PL rate (black), normalized to a value far from contact, and plotted as a function of the distance between the diamond tip and sample surface, as controlled using an ASC500 (Attocube). The simulated power collected within an NA = 0.8, is plotted in red as a function of the distance from the surface of a dielectric ($n = 2.551$). The power has been averaged over the 630 nm to 800 nm range and normalized. (b) PL rate (black) and topography (blue) when scanning over a topographic feature on the surface of Cr_2O_3 . The three points in the inset to (a) are highlighted here with red circles and labeled accordingly. Based on the change in PL between points A and B, we estimate a mesa height of 160 ± 20 nm, which is slightly smaller than shown in topography.

between 630 nm and 800 nm. The resulting curve, normalized to the value far from contact, is shown in Fig. A.5 in red. Here, we assume that the contact point in experiments corresponds to the dielectric being in direct contact with the entire diamond end facet as in the simulation.

In general, we observe a very similar behavior with weak oscillations up to ~ 250 nm, where the collected power increases before rapidly dropping off. However, for small distances, we see that the decay of the power and the in-contact values are quite different from the measured ones. This discrepancy hints towards additional factors not taken into account in these simulations. For example, these simulations assume perfect excitation of the emitter, which in reality, will vary depending on reflections within the pillar and from the dielectric surface.

However, we can still learn something about relative distances from the approach curve. As shown in the inset to Fig. A.5a, the distance between NV and the sample surface will change as one scans across a topographical structure. As the NV-to-sample distance increases, so should the measured PL rate. In Fig. A.5b, we show an example of the change in PL rate when scanning over a Cr_2O_3 mesa, normalized to the out-of-contact rate. In this figure, we also show the topography which we would like to characterize. For this measurement, the step height was calibrated based on previous comparisons to atomic force microscopy measurements as in Sec. A.2.2. We can then use the sharp drop-off of the PL rate in the approach curve to estimate the change in height required to obtain the observed change in PL. Using this technique, we extract a step height of 160 ± 20 nm, which is slightly smaller than what is shown in Fig. A.5b. Here, we use the left-hand side of the mesa, though we see that the right-hand side would give a much smaller estimate. The difference in the PL shift between these two sides could indicate a tilt in the pillar or an off-center NV center. Both cases would result in the NV center being closer to one edge of the mesa than the other. Though this technique is useful to gain a general sense of the distance between NV and sample, it requires further development to provide a quantitative value for d_{NV} or the height of topography on the sample surface.

A.5. Domain wall theory

A.5.1. Angular Profile Derivation

In Chap. 4.2.1, we introduced the angular profile of a 180° Bloch DW, with a surface ξ parallel to the xz plane. For posterity, we will derive the form given in Eq. 4.15.

To first see that the expression in Eq. 4.14 holds for any DW orientation (not just a Bloch DW shown in Sec. 4.2.1), let us insert the general form for $\mathbf{L} = (\cos \phi_{\text{DW}} \sin \theta, \sin \phi_{\text{DW}} \sin \theta, \cos \theta)$ into Eq. 4.13. Assuming a DW where ξ lies parallel to the xz plane and with a constant ϕ_{DW} , we find that $\partial_x \mathbf{L} = \partial_z \mathbf{L} = 0$. The remaining terms are then:

$$\mathcal{E} = \int \left[A \left(\cos \phi_{\text{DW}} \cos \theta \frac{d\theta}{dy}, \sin \phi_{\text{DW}} \cos \theta \frac{d\theta}{dy}, \sin \theta \frac{d\theta}{dy} \right)^2 + K(1 - \cos^2 \theta) \right] d\mathbf{r}.$$

Taking the dot product of the vector with itself, we then find:

$$\begin{aligned} \mathcal{E} &= \int A \left(\cos^2 \phi_{\text{DW}} \cos^2 \theta \left(\frac{d\theta}{dy} \right)^2 + \sin^2 \phi_{\text{DW}} \cos^2 \theta \left(\frac{d\theta}{dy} \right)^2 + \sin^2 \theta \left(\frac{d\theta}{dy} \right)^2 \right) d\mathbf{r} \\ &\quad + \int K \sin^2 \theta d\mathbf{r} \\ &= \int \left[A \left(\cos^2 \theta \left(\frac{d\theta}{dy} \right)^2 + \sin^2 \theta \left(\frac{d\theta}{dy} \right)^2 \right) + K \sin^2 \theta \right] d\mathbf{r} \end{aligned}$$

By combining the θ terms, we then finally arrive back at Eq. 4.14:

$$\mathcal{E} \left(\theta(y), \frac{d\theta(y)}{dy} \right) = \int \left[A \left(\frac{d\theta}{dy} \right)^2 + K \sin^2 \theta \right] d\mathbf{r},$$

where A is the exchange stiffness constant and K is the uniaxial anisotropy. In particular, this formulation of the problem satisfies the requirements for the Euler-Lagrange formalism. Therefore, to find the form of $\theta(y)$ that minimizes the total energy, we will need to solve the following:

$$\frac{\partial \mathcal{E}}{\partial \theta} - \frac{d}{dy} \frac{\partial \mathcal{E}}{\partial \theta_y} = 0, \tag{A.6}$$

where $\theta_y = \frac{\partial \theta}{\partial y}$. Inserting the form of \mathcal{E} above, we obtain

$$-2A \frac{d^2 \theta}{dy^2} + K \sin(2\theta) = 0. \tag{A.7}$$

Now, to solve this second-order differential equation, let us introduce a new function $f(y)$ where

$$\begin{aligned}
 \frac{\partial}{\partial y} f(y) &= \frac{\partial}{\partial y} [-A\theta_y^2 + K \sin^2 \theta], \\
 &= -2A \frac{d^2 \theta}{dy^2} \theta_y + 2K \sin \theta \cos \theta \theta_y, \\
 &= \left[-2A \frac{d^2 \theta}{dy^2} + K \sin(2\theta) \right] \theta_y, \\
 &= 0.
 \end{aligned} \tag{A.8}$$

Here, in the last step, we have applied Eq. A.7. As such, we can now solve this simple but equivalent problem instead. Let us integrate both sides of Eq. A.8:

$$\begin{aligned}
 \int_{-\infty}^{\infty} dy \left(\frac{d}{dy} f(y) \right) &= \int_{-\infty}^{\infty} 0 dy, \\
 \rightarrow [-A\theta_y^2 + K \sin^2 \theta]_{-\infty}^{\infty} &= [C]_{-\infty}^{\infty}.
 \end{aligned} \tag{A.9}$$

Far from the DW, we assume a homogeneous magnetization, such that $\theta_y = 0$. Furthermore, as $\theta(-\infty) = 0$ and $\theta(\infty) = \pi$ and so, applying these boundary conditions, we find that $C = 0$. Thus,

$$\begin{aligned}
 \theta_y^2 &= \frac{K \sin^2(\theta)}{A}, \\
 \rightarrow \frac{d\theta}{dy} &= \pm \sqrt{\frac{K}{A}} \sin \theta, \\
 \rightarrow \int \frac{d\theta}{\sin \theta} &= \pm \int \frac{dy}{\ell_m}.
 \end{aligned} \tag{A.10}$$

$$\tag{A.11}$$

Here, we have introduced $\ell_m = \sqrt{K/A}$, as in Chap. 4. Therefore, solving this simple integral problem, we find that the form of θ_y that minimizes the total energy is indeed given by

$$\theta(y) = 2 \arctan \left(e^{\frac{\pm(y_0 - y)}{\ell_m}} \right), \tag{A.12}$$

where y_0 is the position of the DW center. As we have made no assumptions about ϕ_{DW} here, in the absence of dipolar or DMI terms, this form will hold for any DW type.

A.5.2. Domain Wall Stray Field

Following the derivation of the DW profile, in Chap. 4.2.3 we gave the components of the stray field arising from the magnetization profile of a Bloch DW. In general, there are four additional terms that should be added to account for a general DW profile, which we outline here:

$$B_{x,N} = \frac{\mu_0 \sigma_m}{8\pi^2 \ell_m} \sin \phi_{\text{DW}} \operatorname{Re} \left[-\psi^{(0)} \left(\frac{2d + \pi \ell_m + 2ix}{4\pi \ell_m} \right) + \psi^{(0)} \left(\frac{2d + 3\pi \ell_m + 2ix}{4\pi \ell_m} \right) - \psi^{(0)} \left(\frac{2d + \pi \ell_m - 2ix}{4\pi \ell_m} \right) + \psi^{(0)} \left(\frac{2d + 3\pi \ell_m - 2ix}{4\pi \ell_m} \right) \right],$$

and

$$B_{z,N} = -\frac{i\mu_0 \sigma_m}{8\pi^2 \ell_m} \sin \phi_{\text{DW}} \operatorname{Im} \left[-\psi^{(0)} \left(\frac{2d + \pi \ell_m + 2ix}{4\pi \ell_m} \right) + \psi^{(0)} \left(\frac{2d + 3\pi \ell_m + 2ix}{4\pi \ell_m} \right) + \psi^{(0)} \left(\frac{2d + \pi \ell_m - 2ix}{4\pi \ell_m} \right) - \psi^{(0)} \left(\frac{2d + 3\pi \ell_m - 2ix}{4\pi \ell_m} \right) \right]. \quad (\text{A.13})$$

Recall that here, $\psi^{(0)}$ is the digamma function, i.e., the first derivative of the log gamma function, σ_m is the surface magnetization and d_{NV} is the distance between NV and surface. We do not fix ϕ_{DW} , thereby allowing for any mixture of Néel and Bloch DWs. As such, we see that the fitting function for a Néel wall, where $\phi_{\text{DW}} = \pm\pi/2$, is much more complex than that of a Bloch wall ($\phi_{\text{DW}} = 0$). To ensure that these analytic forms are indeed reasonable, we verify their form against micromagnetic simulations of the DW. The following discussion has been adapted from the SI in [140].

We simulate the DWs in MuMax3 [200] by approximating the surface magnetization of Cr_2O_3 as a thin slab, 1 nm thick, and with a magnetization $|M| = 10$ kA/m, exchange stiffness $A = 0.423$ pJ/m and uniaxial anisotropy of $K = 215.86$ J/m³.

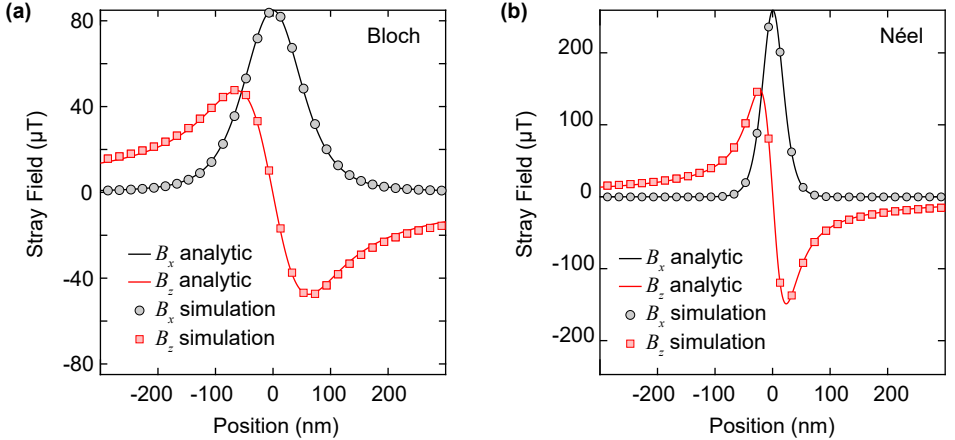


Figure A.6.: Verification of analytical stray field form. (a) Bloch wall stray field components B_x (black circles) and B_z (red squares) simulated for a 20 nm distance from the sample surface and compared to the calculated stray fields according to the analytical model (black and red lines, respectively). (b) The same plot as in (a), but for the Néel wall. We see excellent agreement between simulation and analytics in both cases, verifying the validity of our analytical stray field equations.

The total dimensions of the simulated sheet are $4096 \text{ nm} \times 32 \text{ nm} \times 1 \text{ nm}$, discretized to a grid of $1 \text{ nm} \times 2 \text{ nm} \times 1 \text{ nm}$ cells. We additionally include periodic boundary conditions to minimize artifacts.

To nucleate a DW in simulations, we start with a magnetization pointing upwards in one half of the simulation volume and downwards in the other. We allow the energy of the system to relax and simulate a time span of about $1 \mu\text{s}$ to ensure a static equilibrium. We then extract the magnetization profile of the DW and fit it with the profile described in Eq. 4.16, allowing us to obtain ℓ_m . By introducing DMI into the simulated system, one can also select between the Bloch and Néel configuration.

In the next step, we extract the stray field at a distance of 20 nm from the surface and compare this with the appropriate DW stray field equation given the ℓ_m obtained previously. For both the Bloch and Néel walls, we find excellent agreement between the numerical estimates and analytical approximations, as shown in Fig. A.6. We believe the analytical description to be more accurate in capturing the full extent of the sample as it considers an infinitely extended magnetic system, without the need of periodic boundary conditions as in the simulations.

A.6. Metropolis-Hastings algorithm

Here, our goal is to shortly describe the MH algorithm, which we use to fit the stray fields of both the mesa structures and the DW in Chap. 4. We have adapted this discussion from the SI of [140].

This algorithm is particularly useful for inferring the probability distributions of fit parameters in difficult-to-sample data sets [201, 202]. Therefore, it is appropriate for our analysis where the models involve many correlated parameters and exhibit multiple, local, good fits to our data. Such conditions make it difficult for gradient descent methods to determine a global minimum based on the mean squared error (MSE). Additionally, the analysis via the MH algorithm allows us to better estimate the uncertainty on the involved parameters by combining several datasets. For all analyses of the magnetic and sensor properties (parameters p) discussed in the main text, we fit the recorded stray field (data D) with a theoretical model using the following implementation of this iterative algorithm (with n steps):

1. A set of starting model parameters (p_{curr}) are defined together with a step size (d_i) for each parameter.
2. A new candidate set of parameters p_{new} is drawn from a set of proposal distributions. We use symmetric normal distributions centered around the current values p_{curr} , with a width $= 2d_i$. As the values are drawn randomly from these distributions, we realize a random walk over a range of reasonable starting parameters.
3. The model function is then computed for both parameter sets and compared with the measured data D to estimate the likelihood r_{curr} and r_{new} of the data, given p_{curr} or p_{new} , respectively. In particular, the likelihood is given by $r_{\text{new}(\text{curr})} \propto (R + 1)^{-(\nu+1)/2} \approx R^{-(\nu+1)/2}$, where $\nu = |D| - |p_{\text{new}(\text{curr})}|$ ($|\cdot|$ is the size of the set) and R is the MSE of our model. Often, additional prior knowledge is available on certain parameters (e.g., typical upper or lower bounds on parameters based on previous measurements), in which case, we multiply these to r following the Bayesian rule for the posterior. The probability for accepting p_{new} is then realized as follows:
 - Select a random value a uniformly distributed between 1 and 0.
 - **If** ($r_{\text{new}}/r_{\text{curr}} \geq a$): Accept the new parameters p_{new} and set $p_{\text{curr}} = p_{\text{new}}$.
 - **Else**: Keep the parameter set p_{curr} .
4. We draw a new candidate set based on p_{curr} and repeat this procedure n times.

In particular, our selection criteria prevent us from getting trapped in a given local minimum as we randomize the selection of better parameter sets through a . At the same time, we continuously improve the fit as better candidates, where $(r_{\text{new}}/r_{\text{curr}}) \geq 1$, are always accepted.

The typical evolution of a single parameter, normalized to its starting value, is shown in Fig. A.7 as a function of the iteration number. In the initial period, the parameters evolve quickly as the fit improves before settling to a stochastic walk around a particular value in a process known as thermalization. The iteration steps before

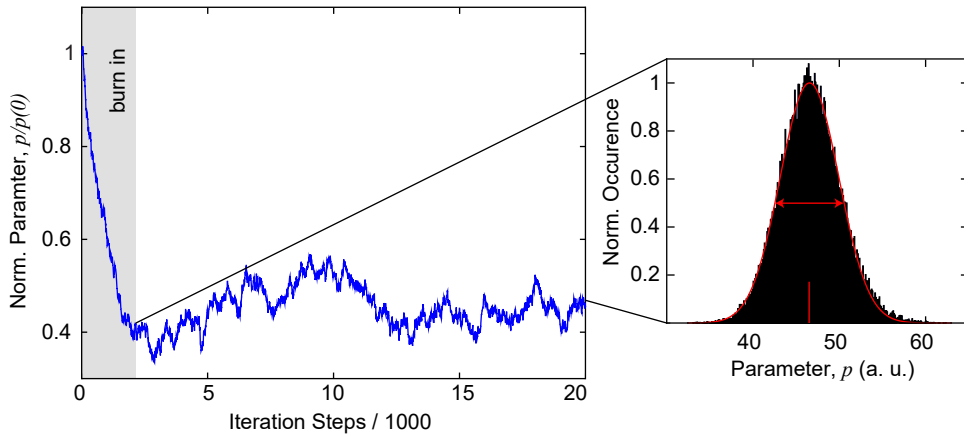


Figure A.7.: Typical single parameter evolution in the MH algorithm The parameter values relative to its starting value as a function of the iteration steps of the algorithm. The initial burn-in period is shown by the shaded area. The inset shows the histogram of values taken after the burn-in period, fitted with a Gaussian distribution, with the mean and FWHM shown with red bars.

reaching this point, shown in gray in Fig. A.7, are dropped when later examining the distribution of values and are referred to as the “burn-in region” [202]. Furthermore, we test for an underlying correlation of the steps by only considering every j^{th} value. The remaining steps are then processed into histograms for each parameter. In the last step, the resulting distributions are approximated by Gaussians to estimate a mean and a standard deviation for a given parameter based on the data and model used.

A.7. Error Analysis

In this section, we wish to summarize the various discussions of the error analyses throughout this thesis. We begin in Chap. 3, where the typical values we state for the TPSP parameters are given by the median of the measurement results that we have shown in histogram form throughout the chapter. The confidence intervals are taken to be the 1σ band, containing 68% of the data. As we have low statistics, choosing larger intervals will simply cover all the measurements. The errors on individual measurements are given by the uncertainties on the fitting parameters extracted in Matlab using the covariance matrix.

The majority of our analysis in Chapters 3 and 4 relies on the fitting of stray field data arising from magnetic textures such as DWs or at the edges of raised, topographical structures. For this reason, we have developed an analysis based on the MH algorithm that allows us to extract the uncertainty on our fitting parameters. The algorithm and how we extract these uncertainties are outlined in Appendix A.6. For individual stray field measurements, we state the mean and standard deviation extracted from Gaussian fits to the resulting probability distribution for each parameter. However, for magnetization measurements at room temperature, the value we state is the mean of all measurements taken under identical conditions, with the error stated being the standard deviation of these measurements. For the magnetic length, we take the 98th and 2nd percentile range extracted from the MH results for each measurement. The maximum of these bounds then gives the upper limit on ℓ_m .

One critical aspect in the stray field analysis, as discussed in Appendix A.2.2 is the characterization of the piezo non-linearity. This non-linearity plays a particularly important role in determining the angle of the DW in Sec. 4.3.1. In particular, to estimate the error, we compare the corrected mesa dimensions measured in our setup to those taken with AFM. On average, we observe a 10% error in the length and width of the mesas. Therefore, we take this value to be the uncertainty in the lateral position.

This error was independently confirmed by measurements of the piezo displacement for a given applied voltage using the Attocube IDS. Through simple error propagation, we then obtain $\delta k_{(1)} = \sqrt{2}k_{(1)}\Delta x$. Here, k (k_1) is the slope of the DW far from the mesa (on the mesa) to maintain consistency with the definitions in Chap. 4.3.1. Note that we assume $k = k_0$ far from the mesa. This $\delta k_{(1)}$ can then be converted to an error on $\sin(\theta_{1(2)})$ through further error propagation. This results in

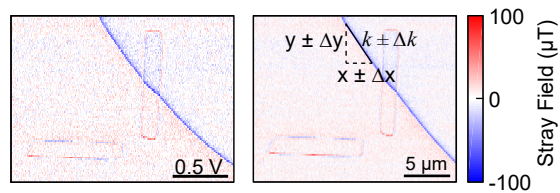


Figure A.8.: Determining the error for the DW angle. Stray field image of two mesas together with the DW plotted with the position in applied voltage (left) and the converted position in μm (right).

$$\delta \sin(\theta_{1(2)}) = \frac{\sqrt{2} \cos(\tan^{-1}(k_{(1)})) k_{(1)}}{1 + k_{(1)}^2} \Delta x, \quad (\text{A.14})$$

which is plotted as the error bars in Fig. 4.10b. We then use linear regression to obtain the final estimate of n_{mesa} . In experiments, the slope of the DW is determined by hand using the positions extracted from the stray field image. Independent confirmation of these slopes indicates that the readout error is small compared to the systematic error introduced through the calibration of the piezo motion.

The piezo non-linearity and the accuracy of our calibration will also play a role in the analysis of the stray fields as it defines the length scales of the magnetic systems and plays a role in the angle between NV center and DW, for example. However, we believe that these are well accounted for in the MH analysis by allowing for broad priors on these parameters. In general, based on experience, we believe that these systematic errors are small compared to the statistical error we state.

In Appendix A.2.3, we also discussed the calibration of the temperature in our measurement setup. We found that the secondary thermistor provides the more accurate representation of the temperature and therefore used these readings to calibrate our temperature. Though each measurement of the temperature shows a low readout error, the discrepancy between the methods shown in Fig. A.4 suggests a reasonable error on the absolute temperature of $\sim 2^\circ\text{C}$, which is reflected in our measurements of the magnetic length and surface magnetization as a function of temperature.

B. Additional Measurements

Throughout this thesis, we have focused on only one of several magnetic systems investigated over the last four years. Though our investigations of Cr_2O_3 represent the most prominent of these systems, for posterity, we would like to highlight two further magnetic studies. These are interesting systems in their own right and expand on different NV techniques while highlighting possible future avenues for NV magnetometry.

B.1. Artificial Spin ice

Students are generally introduced to the concept of electric charges or monopoles early on in their education. On the other hand, magnets are always taught as having a dipolar form due to the vanishing divergence of the magnetic field. Though the Maxwell equations preclude the existence of magnetic monopoles, they have long been theorized to exist. To date, no experimental evidence of true magnetic monopoles has been found.

Nonetheless, monopolar-like fields have been shown to exist in solid state systems, most famously in spin ice [203]. Spin ice materials such as dysprosium titanate ($\text{Dy}_2\text{Ti}_2\text{O}_7$) most commonly exhibit pyrochlore-like lattices consisting of interlinked tetrahedra with a magnetic ion at each vertex of the tetrahedron. They derive their name from water ice, which exhibits a very similar molecular structure. Just as in water ice [204], spin ice has a highly degenerate ground state, leading to many interesting properties.

More recently, there has been a move towards engineering systems that mimic these spin ices. Such systems, also called artificial spin ice (ASI), are a form of metamaterial in which the properties of the system are governed by the form rather than the underlying material properties [205, 206]. ASIs have been successfully engineered to reproduce all the relevant properties of natural spin ice and expand upon that observed in nature. This versatility has allowed researchers to explore interactions that are otherwise impossible to realize. ASIs have also drawn the attention of the spintronics community as promising structures for realizing complex computing due to their diverse ground state [207, 208].

In this section, we introduce the basic concepts of ASI, including the dynamics of these systems. To date, techniques such as MFM [209], SQUID [210], and XMCD [211] have been used to image the static magnetic structure of ASIs and their dynamics. Here, we explore these materials with NV magnetometry, using the stray field imaging techniques presented throughout the thesis. We harness the excellent spatial resolution and spin relaxation time of the NV center to explore the changes in the ASI behavior and investigate dynamics in ASIs on the nanoscale.

B.1.1. Introduction

As with any metamaterial, ASI is an engineered system whose magnetic properties are primarily defined by the fabrication parameters. In particular, ASI systems consist of micro- to nano-meter scale magnetic islands (most commonly permalloy, consisting of $\sim 80\%$ nickel and $\sim 20\%$ iron), fabricated on a non-magnetic substrate such that they form a lattice. One of the strengths of ASI is that it can be used to realize a wide range of lattice structures [206, 212]. Some of the first realizations, and still some of the most widely-studied lattices, are the Kagome and square geometries shown in Fig. B.1. Here, the magnetic islands are fabricated with a stadium shape, placed in close proximity.

In Chap. 4.1.1, we introduced three of the most common magnetic energy terms. These same terms will apply to ASI. However, as mentioned before, the magnetic properties of the whole are no longer determined by the permalloy itself. Due to the spatial dimensions of the permalloy islands, the magnetic orientation of these structures will be dominated by their shape anisotropy. Due to the flat elongated structure of the islands, the anisotropy will lead to an in-plane easy-axis lying along the long axis of the island. This strong anisotropy and the FM nature of permalloy lead the entire island to act as a single, macroscopic magnetic moment [205]. In this configuration, dipolar interactions between the effective moments will play an important role. In particular, due to the long-range nature of the dipolar interaction, the island moment experiences contributions from a large portion of the system. These contributions are the primary driving force for the large number of equivalent ground states and result in a complex phase diagram [213].

With this in mind, we can explore the basic magnetic structure of these ASIs. Let us begin with the square lattice. We model each island as a dumbbell-like dipole [203], with a positive magnetic charge (red) at one end and a negative one (blue) on the other, as shown in Fig. B.1. Ideally, the system would like to minimize the global dipolar interactions. This minimization is achieved with a “two-in, two-out” orientation, where two spins point towards the vertex and the remaining two point away. This “two-in, two-out” rule is also seen in water ice when one considers the orientation of the water molecules within the tetrahedron, hence the name spin ice. As many energetically equivalent magnetic configurations exist, the lowest energy state will be highly degenerate. However, even such a state will not produce the minimum dipolar

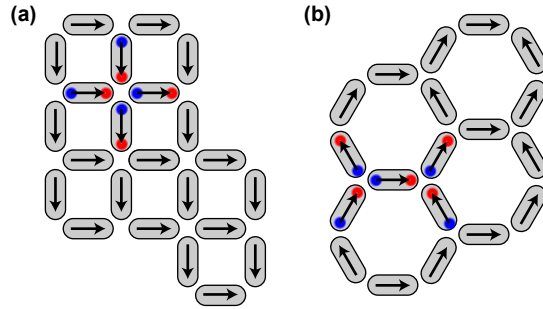


Figure B.1.: Two common ASI lattices. One possible, low-energy configuration of a (a) square ASI and (b) Kagome ASI. Each of the permalloy islands (gray) exhibits a macroscopic dipole behavior with a positive (red) and negative (blue) pole or charge. We associate this with an overall magnetic moment (black arrows).

interaction between every pair of elements [205], a situation known as geometric frustration.

For the Kagome lattice, the geometric frustration is even more evident. In the square lattice, we see that the given magnetic configuration leads to zero net magnetic charge at any one lattice site. If we try to realize such a 0 net charge vertex in the Kagome lattice, we will see that with only three moments, this is impossible. If we arrange any two of the three spins, the third spin will always lead to a net $+1$ or -1 charge. Though this structure can not realize a 0 charge vertex, the next-most favorable configuration is alternating $+1/-1$ charges, leading to overall neutrality. These lowest-energy magnetic configurations are those commonly said to satisfy the spin ice rules.

In motivating the interest in ASIs, we mentioned that they have been shown to exhibit pseudo-monopoles. It is important to emphasize once more that these are not “true” monopoles as they only exist within the solid-state system and are not an isolated source (or sink) of magnetic fields as with electric charges [203]. However, for simplicity, we will call them monopoles. As shown in Fig. B.2a, in the ground state, a square ASI lattice will exhibit zero net charge at each vertex. However, if one of the islands flips its orientation, we see that one vertex will then exhibit a -2 charge, while the neighboring vertex has a charge of $+2$. These

regions of excess magnetic charge are then what is referred to as the magnetic monopoles. Such excitations may be achieved through the application of an external stimulus, such as magnetic fields. In particular, by applying a magnetic field, these excitations have been used to demonstrate a complete flip of the magnetic state of a lattice [211]. Further flipping of moments as shown in Fig. B.2a can result in the monopoles splitting apart, becoming spatially isolated in the crystal and forming what is known as a Dirac chain.

For the Kagome lattice, we have already seen that the vertex charge is ± 1 . However, as the charge does not exceed that at any other point in the lattice, we do not consider these to be monopoles. Instead, we typically consider the total charge per island by summing the charge at the vertices on either end, which in the low energy state is 0. Flipping a single element as shown in Fig. B.2b leads to two regions with an excess charge of ± 2 , i.e., magnetic monopoles. Note that unlike in the square lattice case where the charge at the monopole vertex is always the same, as the monopoles

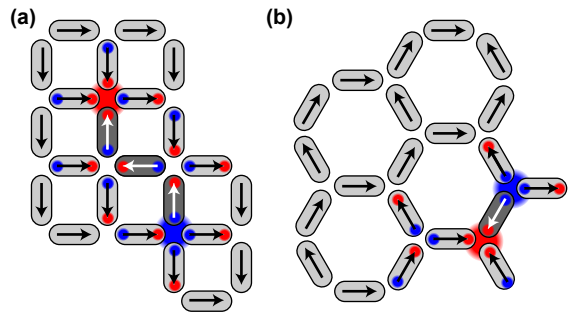


Figure B.2.: Monopoles in ASI lattices. Excitations of the ASI where the islands flip their orientation (dark gray with white arrow), resulting in an overall charge resembling a monopole at either end of the flipped chain, shown here for a (a) square ASI and (b) Kagome ASI. The resulting chain of flipped elements is known as a Dirac chain.

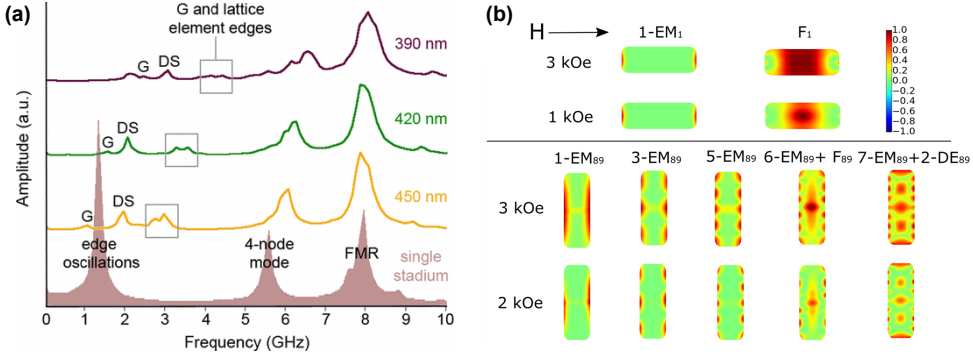


Figure B.3.: Spin wave modes in an ASI. (a) Simulated spin wave spectra of a square ASI containing 112 elements and a 6-island Dirac chain with associated monopole pair. The bottom spectrum shows the resonances of a single island. The top three curves show the shift in frequency as a function of the lattice spacing. The edge mode at 1.4 GHz is blue-shifted, as shown by the squares. Additional resonances showing oscillations of the monopole pair (G) or Dirac string (DS) also arise. Reprinted from [214] with permission from PRL 2013. (b) Spatial profiles of the magnetization dynamics in individual islands of a square ice lattice at given magnetic fields. The field direction is shown with the arrow. The frequencies of the modes increase towards the right. Here, the 1 refers to horizontal islands and 89 to vertical ones, and n-EM (n-DE) refers to an edge (Damon-Eshbach [215]) mode with n nodes, respectively. F is the fundamental mode. Reproduced with permission from [215].

propagate in the Kagome lattice, the vertex charge may change. However, the total charge is always the same.

While the ASI can be flipped by applying a magnetic field, single elements may flip spontaneously due to the temperature of the system. The flipping time t_f of an ASI moment will be described by the Arrhenius law:

$$\frac{1}{t_f} = \frac{1}{t_a} e^{-\frac{KV}{k_B T}}, \quad (\text{B.1})$$

where $1/t_a$ is the attempt frequency, K is the shape anisotropy constant, V is the volume of the macrospin, k_B is the Boltzmann constant, and T is the temperature. If the measurement time exceeds t_f , then the system is said to be thermally active or superparamagnetic [206]. This phenomenon is only observed in ferro-(ferri-) magnetic nanoparticles and depends very much on the shape parameters [216]. One may therefore tune between a static and a superparamagnetic regime not only by temperature but also geometry.

Understanding the collective behavior of an ASI is complicated but represents an active field of research. In addition to these single spin flips, simulations have identified many collective spin wave modes [214, 217]. Spin waves are magnetic excitations resulting in a collective precession of the spins. In typical ASIs, these spin wave modes tend to fall in the 1-100 GHz regime. Fig. B.3 shows a few examples of such

spin wave modes both for the collective lattice (a) and single islands (b) [215, 218]. These modes are, in part, in the 2-3 GHz regime and so may be resonant with the NV center spin transitions. As such, the spin noise-dependent T_1 time of the NV center may be used to access and directly image these spin modes.

B.1.2. The Samples

Let us now turn to a discussion of our investigations in ASI. We will introduce two samples provided to us by Naemi Leo and Kevin Hofhuis during their time in the Heydermann group at the ETH/PSI. In both samples, the ASI consists of permalloy islands fabricated on a silicon substrate and covered with a ~ 10 nm layer of Al. In particular, the structures are patterned into a permalloy wedge in which the thickness gradually decreases, as shown in Fig. B.4a. The sample from Kevin Hofhuis consists solely of square ASIs.

In the following sections, the focus will be on the sample received from Naemi Leo, on which the majority of measurements were performed. Here, several ASIs have been patterned, with different lattices and island separations, as shown in Fig. B.4b. An example of such an ASI WF, here with an element separation $D = 66$ nm, is shown in Fig. B.4c. This sample structure gives us access to several valuable parameters. For instance, the varying thickness and island separation allow us to probe different regimes of the Arrhenius law in Eq. B.1 by tuning the volume and interaction strength of the islands, respectively.

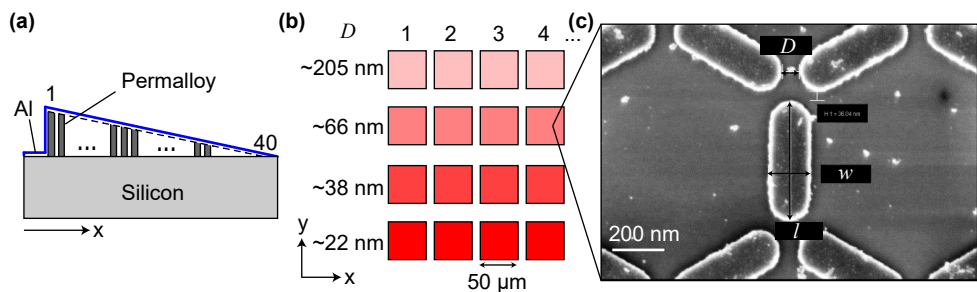


Figure B.4.: ASI sample. (a) Schematic of a wedged permalloy ASI sample. The permalloy is evaporated on a Si substrate and patterned into 40 WFs (along the x -direction), exhibiting different element separations in the y -direction. The permalloy is then capped with a ~ 10 nm Al layer to prevent degradation. The entire sample contains multiple lattices, but we will focus on the Kagome lattice. (b) Further schematic highlighting the WF layout. The element separation D is given to the left, and the WF number is written on top. Each WF is $50 \mu\text{m} \times 50 \mu\text{m}$. (c) An SEM image showing the structure of the $D = 66$ nm Kagome spin ice. Here, we highlight the definition of D . Each island has dimensions of $l \approx 470$ nm and $w \approx 160$ nm.

B.1.3. DC magnetometry

We will begin with some basic magnetometry images taken in our confocal scanning setup (see Appendix A.2.2) with single NV, tapered scanning probes.

We begin with measurements on a Kagome lattice taken on WF 14. Here the numbering refers to the WF position relative to the left-hand side of the sample in Fig. B.4a,b. Based on the approach curve technique outlined in Appendix A.4, we expect the permalloy thickness to be on the order of 10 nm. Here we focus on the WF with an island separation $D \approx 205$ nm. In Fig. B.5a, we show a map of the NV center PL while scanning across this WF.

We also make use of the iso-B imaging described in Chap. 2.2.2, with one addition: we use two MW driving frequencies to measure two different magnetic fields simultaneously. In particular, we apply a 3 mT bias field along the NV axis and drive with two MW sources set to 2.87 GHz and 2.7 GHz, corresponding to a ± 3 mT magnetic field along the NV axis relative to the bias field. Throughout the scan, we alternate between the two driving sources while simultaneously recording the corresponding PL with two counter windows. When subtracted from one another, the two resulting stray field images yield a map of the iso field lines at $\sim \pm 3$ mT, as shown in Fig. B.5b. In this image, we see regions of alternating positive and negative fields concentrated near the end caps of the magnetic islands. This results is consistent with the macroscopic dipole behavior of the islands. The inset to Fig. B.5b shows the expected stray field for ideal dipoles oriented as shown with black arrows. We obtain reasonable agreement with the iso-B imaging, verifying that we observe the expected spin ice rules seen in Fig. B.1a.

As we continue to thinner structures in the higher numbered WFs, we eventually reach WF 23, where we no longer see any magnetic contrast (see Fig. B.5d). However, we continue to see a drop in the NV PL over the islands, as seen in Fig. B.5c. Due to the strong magnetic moment of permalloy, it is unlikely that the stray fields would drop below the NV sensitivity even for a few nm thicknesses. Unfortunately, characterizing the exact height of the structures in this WF is made difficult by the Al capping layer. One possible explanation for this reduction in PL and simultaneous lack of stray magnetic field is the transition to superparamagnetic behavior. Due to the rapid flipping of the moments in time scales shorter than the measurement time, we would expect to see no DC stray field. We will try to verify this hypothesis with further measurements.

Switching now to full-field magnetometry, we observe one of the major difficulties when working with strong stray magnetic fields. In Fig. B.6a, we take a full ODMR curve at each point in a scan of WF 14 and plot the components parallel (left) and perpendicular (right) to the NV axis. Though we indeed obtain a general image of the stray fields arising from these permalloy structures, we see that at the caps of the stadium-shaped islands, the contrast drops, resulting in poor ODMR fits and incorrect pixels. As such, fully quantitative images on thick permalloy layers prove difficult. However, if we look at the perpendicular field strength at these points, they seem too small to explain such a drastic drop in contrast [31]. It is possible that additional factors, specifically having to do with the spin coherence time of the NV center, which we will explore in more detail in the next section.

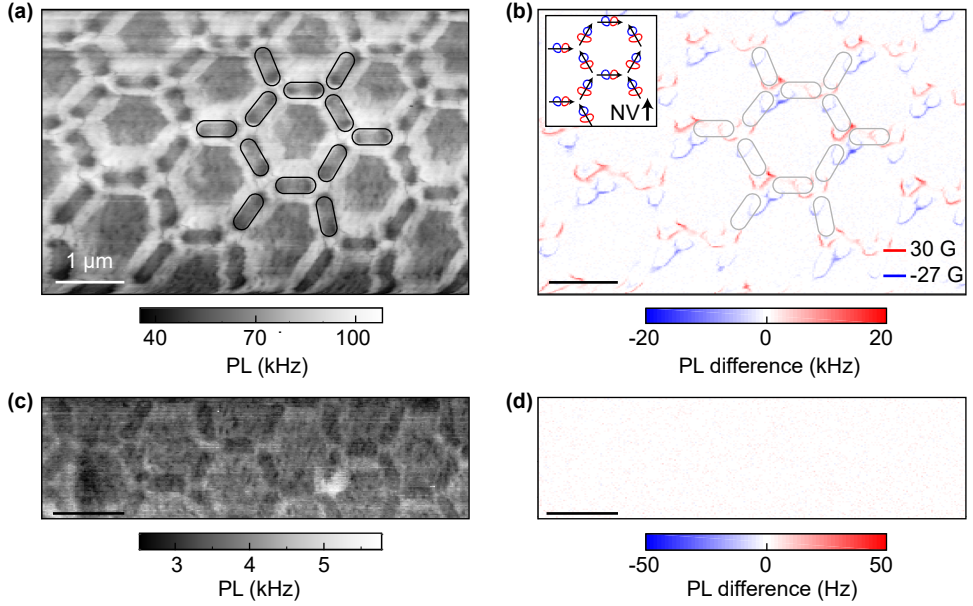


Figure B.5.: Iso-B imaging of the Kagome spin ice. (a) NV PL measured while scanning over WF 14 (with $D = 205$ nm) shows the position of the individual elements, highlighted in part by black outlines. (b) Iso-B imaging resulting from the difference of the PL measured when driving with two different MW frequencies. The blue (red) curves correspond to a field parallel to the NV of -27 G (30 G). We again highlight the corresponding island positions in gray. (c) A PL image taken over WF 23. We observe a faint drop in PL over the islands, but the lighter rings surrounding the islands, arising from the topography have nearly vanished. This suggests structures only a few nm in height. (d) Iso-B image of the area shown in (c). We see no stray fields, suggesting that these elements may be superparamagnetic. All scale bars represent 1 μm .

Moving again to the WFs with thinner structures, we observe a drastic change in behavior. In our measurements, the applied magnetic field has an in-plane component of ~ 1.5 mT. Under these conditions, we see that the islands in WF 22 now seem to be magnetized in the externally applied magnetic field direction, as shown in Fig. B.6b. Here, the direction of the in-plane component is shown by black arrows. In this regime, the magnetic moment of each island no longer lies along the long axis of the island, meaning that we are able to overcome the shape anisotropy through the applied field. However, even though we observe reasonable stray fields in Fig. B.6b, the same conditions produce no stray magnetic field in the next WF (23). By increasing the in-plane field even further, perhaps we could reach a regime where even WF 23 is magnetized along the field direction. If this is possible, we could perhaps narrow down the source of the reduction of PL on this WF. Nonetheless, we see that through the change in thickness, we can tune between different magnetic behaviors.

Though we have successfully imaged the spin ice rules in the Kagome lattice, we

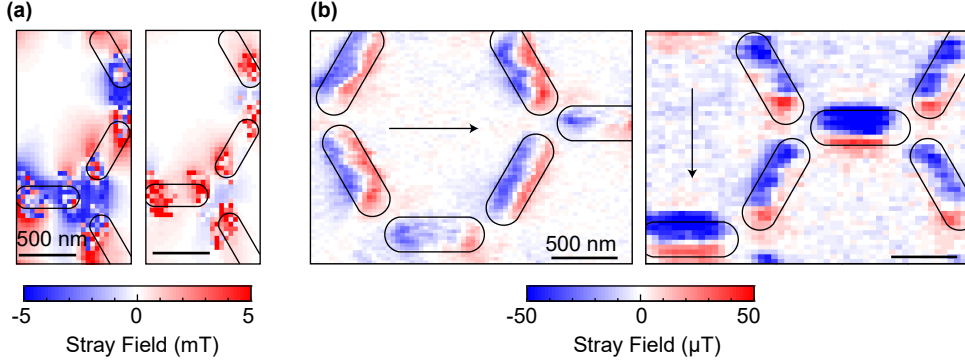
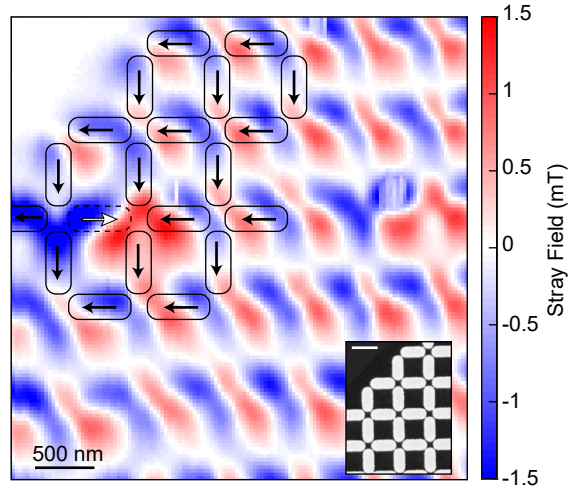


Figure B.6.: Full-field imaging of the Kagome lattice. (a) Full-field images of WF 14 ($D = 205$ nm) obtained by recording a full ODMR at each point and fitting the resonances to extract the field parallel (left) and perpendicular (right) to the NV. The island positions are highlighted in black. (b) Full-field feedback images of WF 22 ($D = 205$ nm) with an applied in-plane field (>1.5 mT), whose direction is shown with black arrows. We see that the elements all become magnetized in the same direction, along the magnetic field.

have not yet observed any monopoles. At this point, let us discuss the second sample, where we believe that we are indeed able to identify monopoles. Furthermore, scanning over the thick permalloy layers in this sample lead to difficulties in our ODMR imaging. Therefore, we switched to an NV scanning probe with an unusually deep NV in order to measure further from the sample where the field magnitude has dropped. Feedback imaging with this tip yielded the stray field image seen in Fig. B.7.

Figure B.7.: Observation of Dirac chains. Full-field feedback image taken over a square ASI. The position of the elements and assumed spin orientation is shown in black. One element at the left, shown with a dashed line and white arrow, appears to have switched, resulting in a monopole pair. There appears to be a second such flip in the same line, to the right side. The inset shows an SEM image of the sample.



Due to the small islands and island separation, obtaining a clear image of the topography is difficult. However, as we have imaged the edge of one of the WFs, we can overlay the island pattern based on atomic force microscopy measurements of the lattice (see the inset of Fig. B.7) to make sense of our observations. We highlight the most likely island configuration with black outlines. Here, we observe a sudden increase in the stray field at the left-hand side of this image. More importantly, if we examine the stray field produced by the nearby structures, it appears as if the horizontal island, highlighted with a dashed line and white arrow has flipped, leading to two monopoles. A second instance of this structure appears on the right-hand side of the same line of lattice elements. However, repeated measurements have shown no growth of the associated Dirac chain.

Thus far, we have successfully shown that the static magnetic structure of ASIs may be measured through NV magnetometry. Unfortunately, in the presence of strong magnetic fields, the NV center is at a disadvantage compared to many other imaging techniques, including MFM [209] and XMCD [211], which have been used to image the magnetic structure of ASIs in the past. On the other hand, the non-invasiveness of the technique allows us to access a wide range of magnetic behavior without influencing it. Specifically, near WF 22, where the thin structures are characterized by weak anisotropy, NV magnetometry has the potential to provide new insights. In particular, the question of superparamagnetic behavior remains to be answered.

B.1.4. AC magnetometry

Though other techniques may be better suited to measuring the strong stray fields and slow (order of seconds) flipping of moments in ASIs [211], NV magnetometry has the distinct advantage of being sensitive to high-frequency oscillations while simultaneously achieving nanoscale resolution. In particular, we will utilize the spin relaxation time of the NV center, which is affected by the spectral noise density resonant with the NV spin transitions [219]. This technique has successfully been used to characterize and image spin noise in permalloy [73] as well as yttrium iron garnet [220] and artificial AFM systems [183].

Our measurements consist of three stages, beginning with the initialization of the NV spin into the $|0\rangle$ state through a 2500 ns, 532 nm excitation pulse. The NV center is then allowed to evolve without any optical or MW driving for a time τ . Following this, the NV PL is read out with a 300 ns counter pulse before re-initializing the spin, as shown in Fig. B.8b. The resulting measurement is shown in Fig. B.8a, taken far from the sample surface (circles) and in contact over a permalloy island (squares). We additionally measure the NV PL at the end of the initialization to obtain the $|0\rangle$ -state PL level, which we use as a reference. Fitting the two PL decay curves with an exponential decay ($\propto e^{-t/T_1}$), we obtain the corresponding spin relaxation time, T_1 of the NV center. The T_1 time decreases strongly in contact, from 1.3 ± 3.0 ms to 100 ± 20 μ s.

While measuring the PL decay curve is by far the most accurate measure of the spin relaxation time, scanning an area of only a few μm^2 can take on the order of a day or more. Instead, we measure at a single time point yielding high contrast between the in-contact and out-of-contact T_1 measurements while short enough to guarantee reasonable scanning times. In our measurements, we repeat the pulse sequence shown

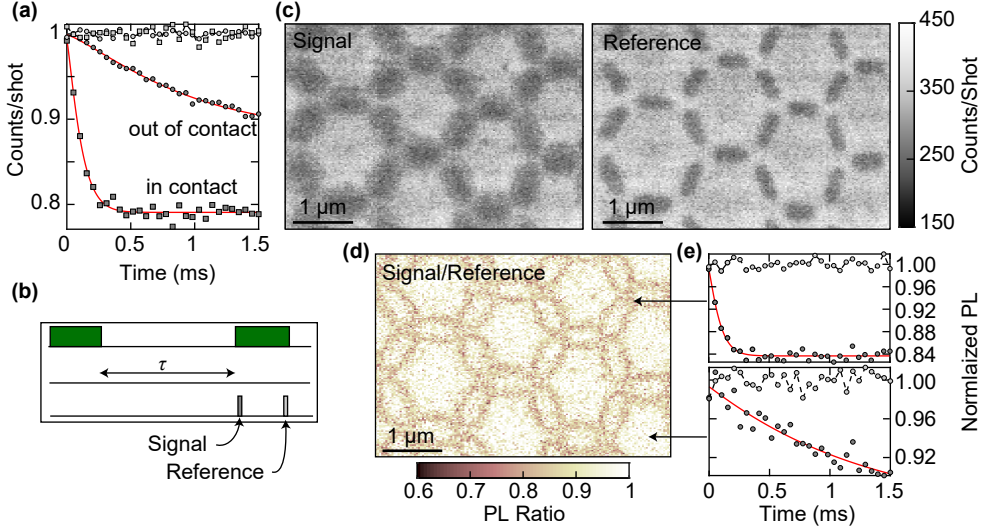


Figure B.8.: Measuring spin noise with the spin relaxation time of the NV center (a) Measurements of the NV PL as a function of time. When out of contact, the NV PL drops off exponentially with a $T_1 = 950 \pm 260 \mu\text{s}$ (dark gray circles). However, when scanning over an ASI island (dark gray squares), the T_1 time drops to $120 \pm 10 \mu\text{s}$. The light gray squares and circles represent a reference measurement taken after re-initializing the NV. (b) Pulse sequence used to measure the curves in (a). The top line is the 532 nm initialization of the NV before and after a wait time τ . The NV PL is then measured using two 300 ns counter windows at the beginning and end of the initialization pulse, resulting in the dark gray and light gray curves in (a), respectively. (c) PL images of the WF 21 Kagome lattice ($D = 205 \text{ nm}$) measured by the signal and reference counter windows following a fixed $\tau = 150 \mu\text{s}$. (d) The ratio of the two PL measurements in (c), showing a drop in relative PL at the edges of the islands, suggesting a drop in T_1 resulting from resonant spin noise. (e) Representative T_1 measurements taken at the approximate positions shown, fit with T_1 times of $100 \pm 20 \mu\text{s}$ (top) and $1.3 \pm 3.0 \text{ ms}$ (bottom).

in Fig. B.8b with a $\tau = 150 \mu\text{s}$, while scanning the NV across the sample. We then integrate the PL collected over repeated 300 ns counter windows. The resulting PL image is shown in Fig. B.8c (left). The reference image, based on the PL measured at the end of the optical initialization pulse, is shown in Fig. B.8c (right). Finally, we take the ratio of the values in these images to obtain qualitative maps of the NV spin relaxation time.

Shown in Fig. B.8d is the result of this single point T_1 imaging taken on the WF 21 of the $D = 205 \text{ nm}$ Kagome lattice, where we still expect to see static spin ice behavior. What we observe is a distinct drop in the PL ratio at the edges of each of the islands. We have also performed representative, full T_1 measurements at selected points around the islands, as shown in Fig. B.8e. Here, we see a clear distinction in the PL decay near the element cap and when far from the island.

These observations hint towards an oscillating magnetic field, resonant with the NV

spin transitions, located near the edges of the islands. There are a number of published discussions of the spin modes of very similar Kagome and square ASIs [215, 221, 222] (just to name a few) that show edge modes in the 2-10 GHz regime that we are interested in. However, these lowest frequency modes are typically localized near the end-caps of the islands where the interactions are the strongest, as shown in Fig. B.3b (top left). These modes are very different from our observations, which show a reduction in T_1 around the entire island. One possibility is that this reduction may not be due to spin wave modes but rather a decay of the magnetic properties of the islands near the edges following the lift-off procedure in fabrication. However, this drop in the T_1 time at the end caps of the islands could explain our loss in contrast seen in Fig. B.6a.

We have already seen a transition in the DC field behavior of the spin ice around the WF 22 mark, so let us examine this using our AC sensing. In Fig. B.9, we repeat the one-point T_1 PL imaging discussed above on WF 23. Now, rather than seeing contrast at the island edges, the strongest PL contrast is found at the center of each island. Again, this could be an indication that what we observe indeed comes from superparamagnetic behavior. If the Arrhenius law-based flipping of the magnetic moment of each island would be resonant with the NV transitions, we could explain the behavior we have observed - a reduced T_1 and PL on the islands as well as a lack of DC fields. Therefore, let us look into this in more detail.

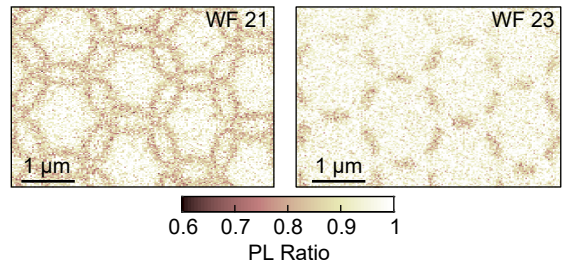


Figure B.9.: Comparing spin noise on WF 21 and 23. Comparison of PL ratio images (obtained as shown in Fig. B.8c,d) for WFs 21 and 23 on the $D = 205$ nm Kagome lattice. We see a clear shift in the PL reduction from the island edges to lying on the islands, which we associate with the shift to a superparamagnetic behavior.

In Eq. B.1, we give the general form of the flipping rate. If we approximate our structures as very flat ellipsoids, then we can make use of some common tricks for calculating K . In particular, $K = 1/2\mu_0 M_s^2 \Delta N$, where M_s is the saturation magnetization and ΔN is the difference in the demagnetizing factors for the ellipsoid. The latter may be calculated using elliptical integrals following Ref. [223]. Therefore, we calculate the demagnetizing factors corresponding to the a and b axes of our ellipsoid shape (assuming $a = 470$ nm, $b = 160$ nm, and $c = 3$ nm) and obtain $\Delta N = 0.0114$. Taking $\mu_0 M_s = 0.8$ T [224], we then find $K = 29$ N/m². Using the dimensions of the stadium shape to calculate the volume, and assuming an attempt frequency of 10 GHz [225], we obtain a flipping rate of 2.3 GHz at 23 °C, which is close to our typical measurement temperature. The flipping rate we extract here is quite close to resonant with our NV spin transitions. Of course, as we do not have an exact characterization of the permalloy thickness in this WF, we have assumed a thickness of 3 nm, which would need to be confirmed. In comparison, if we assume a thickness of 10 nm as we believe we have in WF 14, we would obtain a flipping rate of ~ 600 Hz. Unfortunately,

this is far too high to expect to see a static stray field, indicating that the thickness dependence in our estimate is not quite correct. A proper characterization of the permalloy thickness would be necessary for a confident statement.

In trying to make sense of our results, we also performed similar measurements while applying in-plane fields as in Fig. B.6c,d. According to simulations, the in-plane magnetic field should allow us to tune through any possible magnetic resonances. We could expect to see a change in the T_1 behavior once the assumed spin wave modes exceed the NV resonances or vice versa. Alternatively, if we manage to sufficiently raise the superparamagnetic energy barrier on WF 23, we would expect to see behavior more like that seen on WF 21. Unfortunately, up to in-plane fields of ~ 3.5 mT, we see no change in behavior.

Many questions still exist surrounding these measurements. Though they could not be answered within the scope of my Ph.D., these are interesting problems that could help us understand not only ASI systems but potentially also the NV center itself.

B.1.5. Conclusions

In our investigation of ASIs, we have explored two ASI lattices: the honeycomb-like Kagome lattice and, briefly, the square lattice. We used NV magnetometry to image the stray fields of the individual, permalloy lattice elements and observed that they do indeed follow the spin ice rules. In the square ASI, we additionally identified two pairs of magnetic monopoles.

We then discussed how the spin relaxation time of the NV might be used to identify spin noise in magnetic systems and applied this to the Kagome lattice. A reduction in the T_1 time, which changed depending on the thickness of the magnetic islands, was observed. However, the origin of this reduction is still unclear. For the thinner islands, we believe that the lack of magnetic moment and localized drop in T_1 time could indicate superparamagnetic behavior in the islands.

Unfortunately, a lack of simulation expertise made a theoretical explanation of difficult. Though initial steps were carried out with the help of Dr. Sebastian Gliga, reprioritization of other projects on both sides prevented any results from nucleating. Furthermore, unclear whether the T_1 reduction is indeed probing the desired physics. Additional influences on the T_1 , such as the charge state, have not been taken into account here [110]. Generally, more care should be taken to account for the NV charge state and compare the T_1 decay of each of the spin states [62]. A comparison with recent T_1 -based studies of spin noise at DWs [183] could also help in this regard.

Moreover, the spin ice community already has access to many excellent techniques for investigating static magnetization and large-scale dynamics, including MFM, Brillouin light scattering, and PEEM-XMCD. Nonetheless, the NV still exhibits the advantage of being sensitive to both DC and AC fields at the nanoscale. As few experimental verifications of spin modes on the level of individual spin ice islands exist, this is an area where NV magnetometry could prove useful.

The 2D imaging of spin wave modes through T_1 techniques with the NV is also an attractive avenue of research in systems other than ASIs. For example, first steps towards imaging FM resonances in isolated permalloy disks were conducted early on in my Ph.D. Fig. B.10 shows the results of full T_1 decay curves measured while scanning across a $5\mu\text{m}$ permalloy disk. Here, we see a pattern emerge in the disk,

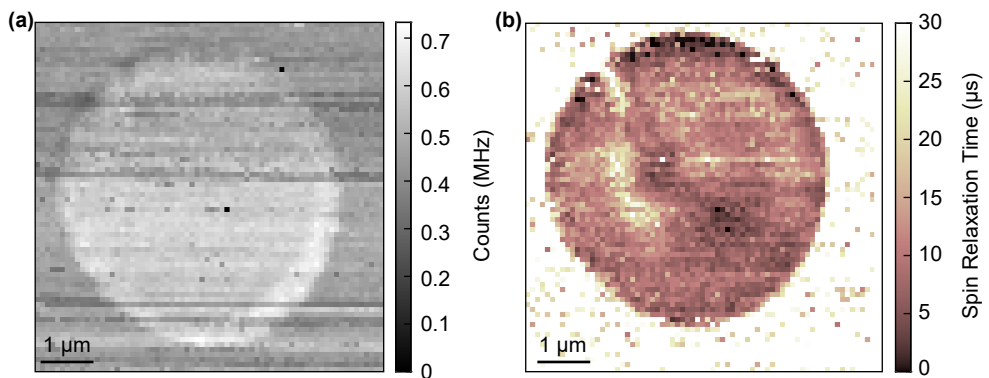


Figure B.10.: T_1 imaging over a permalloy disk. (a) PL image of a permalloy disk taken concurrently with the T_1 image. (b) Image of the permalloy disk taken by performing a full T_1 measurement at each pixel. Here, we see a clear change in the length of the T_1 time (though the fitting is often poor due to a low number of measurement points per T_1 curve) over the disk. The structure in the top left appears to have some correspondence to a slight change in PL in (a), but otherwise, there are no apparent changes in PL or topography that would lead to this change in T_1 time.

again hinting towards some magnetic influence. Though a bias field was applied, it is unclear whether the field was sufficient to remove the magnetic vortices known to inhabit such permalloy disks. Apart from creating strong field gradients that could influence our measurements, these magnetic vortices are also known to produce spin waves of their own [226]. To narrow down the origin of this signal in the future, T_1 measurements could be combined with additional measurement techniques [73]. Additionally, driving the system, whether it be an ASI or a permalloy disk, can be a valuable tool for controlling the behavior of the system. Most importantly, any experimental results should be combined with support from simulations, which has been missing thus far.

B.2. Skyrmions

Within the rapidly growing field of spintronics, one avenue of great interest involves magnetic skyrmions [2]. These are nanoscale magnetic textures characterized by their spiral magnetism and topological properties [227]. The interest in skyrmions has been driven in part by the fact that they may be generated and moved through the application of spin currents or electric fields [8] and can exist in a number of materials and at a range of temperatures and magnetic fields. As such, the use of skyrmions in computing applications has recently been proposed, where they may be used as logical bits for storing and transferring information. Moreover, they show unique transport phenomena such as the skyrmion Hall effect [228, 229].

However, due to their tiny spatial extent, imaging these magnetic structures can prove quite challenging. Here, NV scanning magnetometry again proves valuable due to its nanoscale spatial resolution. In the last years, following the measurements we present here, multiple nanoscale studies of skyrmions using scanning NV magnetometry have been published, characterizing fluctuations of the skyrmion boundary [22], identifying the chirality (the rotation direction) of skyrmions [77] as well as identifying the effect of disorder on skyrmions in ultrathin films [23]. Through these studies, NV magnetometry has been established as a useful technique in this field.

B.2.1. Introduction

Magnetic skyrmions belong to the same class of magnetic defects as DWs and, therefore, we can use much of what we have learned about DWs in Chap. 4 also to discuss skyrmions. Let us consider a 180° DW, which we wrap around such that the ends of the wall touch. In this way, we would form a “bubble” domain with the spins pointing in one direction inside the bubble and the opposite direction outside the bubble. If we now shrink the bubble until only a single spin in the center points opposite to those on the outside, we find that we obtain the magnetic structure shown in Fig. B.11. However, just as there are multiple types of DWs, there can be multiple types of skyrmions. Fig. B.11a shows a Bloch skyrmion, but one can also define a Néel skyrmion with either right-handed or left-handed chirality (see Fig. B.12b). Though the boundary between a bubble domain and a skyrmion is a disputed topic, one common definition is that a true skyrmion will contain only a single central spin pointing opposite to its boundary [8, 230]. An additional defining feature of a skyrmion is that its magnetic structure can be mapped onto the entirety of a sphere, as shown in Fig. B.11c for the Néel case.

This mapping can be understood by only considering the orientation of the magnetic moments. If we then assign the top of the sphere to moments pointing along $+z$ and the bottom to moments along $-z$, we can match each arrow in Fig. B.11b to a point on this sphere. In particular, we see that the magnetic moments of a skyrmion cover the sphere exactly once. This property is also known as the topological charge or winding number of a skyrmion. Mathematically, this is given by the following [8]:

$$N = \frac{1}{4\pi} \int \boldsymbol{\mu} \cdot \left(\frac{\partial \boldsymbol{\mu}}{\partial x} \times \frac{\partial \boldsymbol{\mu}}{\partial y} \right) dx dy, \quad (\text{B.2})$$

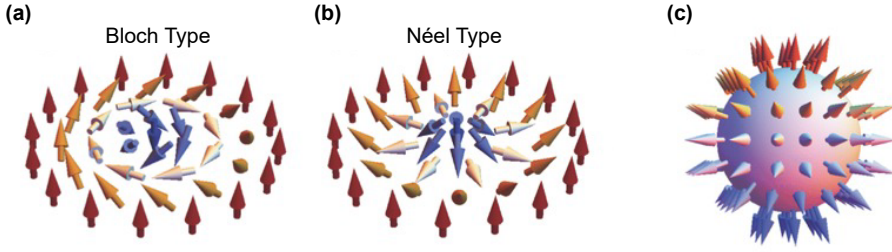


Figure B.11.: Skyrmion structure. A simple schematic of the magnetic moments that build up a (a) Bloch skyrmion and (b) Néel skyrmion. (c) Spins of a Néel skyrmion projected onto a sphere where the top of the sphere has the magnetic moment pointing up and the bottom has the magnetic moment pointing down. In this way, we see that we can cover the entire sphere exactly once. Adapted with permission from [231]

where μ is the unit vector of the magnetization. Using this definition, each of the structures in Fig. B.11 has an associated winding number $|N| = 1$. Most importantly, this topological charge is quantized, and moving from one N to another requires us to overcome a large energy barrier [232]. For this reason, the skyrmion is said to be topologically stable. This is one of the properties that make skyrmions so attractive.

However, if the transformation of a skyrmion is so energetically expensive, one could ask how skyrmions can form in the first place. If we look back at our description of magnetic energy terms in Chap. 4.1.1, we realize that the highly localized twist of the spins in a skyrmion is energetically unfavorable when considering exchange and out-of-plane uniaxial anisotropy. Instead, in FMs, this would favor a uniform, out-of-plane orientation. Therefore, there must be a missing element, which leads to a rotation of the spins. Dipolar interactions will favor an antiparallel alignment of the spins and so, will play a role here. However, most commonly, this missing element is the Dzyaloshinskii-Moriya interaction or DMI. In particular, we will consider DMI arising from the interface between two materials.

Interfacial DMI comes from a breaking of inversion symmetry at the interface between, for example, a magnetic layer and a heavy metal layer [233]. The resulting interaction term can be described using the following Hamiltonian form:

$$H_{DM} = -\mathbf{D}_{12} \cdot (\mathbf{S}_1 \times \mathbf{S}_2), \quad (\text{B.3})$$

where \mathbf{D}_{12} is the DMI vector resulting between two spins \mathbf{S}_1 and \mathbf{S}_2 , as shown in Fig. B.12a. One way in which this interaction term appears is due to superexchange. Superexchange is an angle-dependent exchange interaction between two magnetic spins and mediated by a secondary atom, commonly a nearby metallic atom. This description additionally requires the metallic layer to exhibit a strong spin-orbit coupling (SOC) and inversion symmetry to be broken, the latter of which is easily achieved at an interface [234]. The form in Eq. B.3 then leads to a preference for the two spins to lie perpendicular to each other through a rotation around the \mathbf{D}_{12} vector [233].

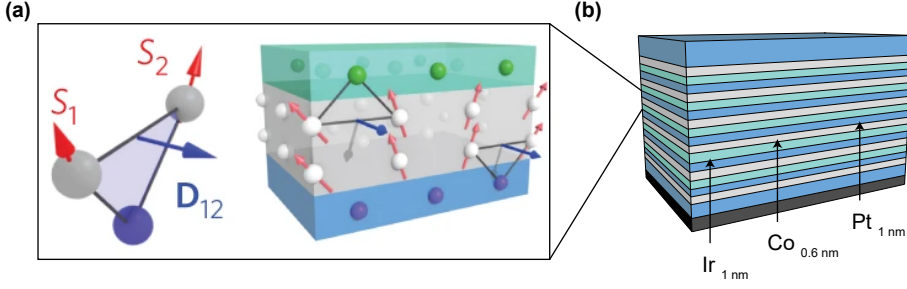


Figure B.12.: Achieving DMI-stabilized skyrmions. (a) Schematic showing how the interaction between two atoms belonging to a magnetic material (gray), and mediated by a third metallic atom (blue), leads to a DMI between the magnetic moments. S_1 and S_2 will rotate around the DMI vector to achieve an angle as close to 90° as possible. Reproduced from [235] with permission from Springer 2016. (b) The sample provided to us by the Hug group, consisting of five repetitions of $\text{Ir}_1/\text{Co}_{0.6}/\text{Pt}_1$, where the subscripts refer to the thickness of the layer in nm. Here, Ir is shown in green, Co in gray, and Pt in blue. The stack is capped by two thicker Pt layers and grown on a sapphire substrate

For sufficiently strong DMI, therefore, the rotation of spins in a skyrmion (typically Néel skyrmions) will be energetically favorable.

B.2.2. Imaging skyrmions

For our study of skyrmions, we focus on multilayer materials; specifically, Ir/Co/Pt stacks, where Ir and Pt are heavy metals with large SOC and Co is a common FM. We received a multilayer stack from colleagues at EMPA in the group of Hans Hug, consisting of five repetitions of 0.6 nm of Co, sandwiched between 1 nm of Ir and Pt as shown in Fig. B.12b. Due to the asymmetry of the interfaces (Ir on one side, Pt on the other), the resulting DMI at the two interfaces does not cancel out, leading to an overall DMI term [236]. The entire sample is grown on a sapphire substrate with thick Pt capping layers on either end of the stack.

However, without prior magnetic preparation, the sample will be in a magnetic domain state. Therefore, to generate the expected Néel skyrmions at room temperature, one must first saturate the Co layers by placing the sample in an out-of-plane magnetic field exceeding 100 mT, and then slowly reduce the field amplitude [237]. We achieve this by bringing the sample to within ~ 5 mm of a large, $5 \text{ cm} \times 5 \text{ cm} \times 2 \text{ cm}$ permanent magnet and then carefully removing the magnet without changing its orientation relative to the sample. All this is done with the sample mounted in our room temperature, confocal scanning NV magnetometry setup (see Appendix A.2.2). We then apply a bias field along the NV axis of ~ 2.2 mT to perform quantitative imaging.

Following this preparation process, we perform iso-B imaging of the sample by setting the MW driving to 8.4 MHz and 9.8 MHz from the lower NV spin resonance, corresponding to a field of 3 mT and 3.5 mT respectively, relative to the bias field. We then measure the corresponding NV PL while scanning the sample and upon subtracting the resulting two PL images, we obtain the image seen in Fig. B.13a. Here, we see

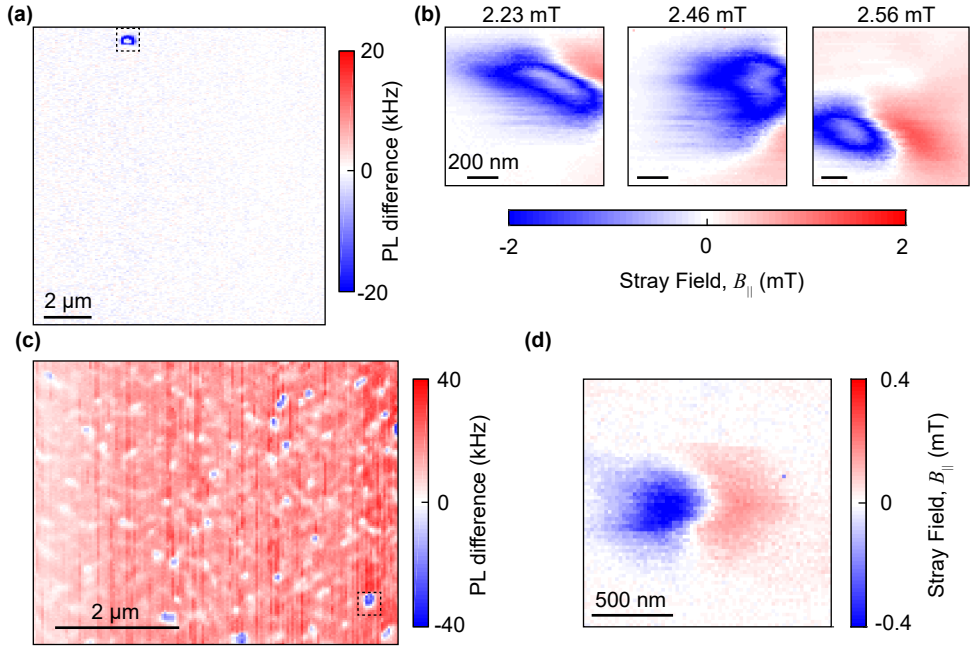


Figure B.13.: Imaging skyrmions and bubble domains. (a) Iso-B image showing the difference in PL measured after magnetizing the multilayer sample, showing a single contour corresponding to 3 mT. (b) Full-field images taken by measuring pixel-by-pixel ODMR curves, showing a small, magnetic structure. By applying increasing magnetic fields (noted above each image), the shape of the structure changes. Due to the size and field dependence, this is likely a bubble domain. (c) Iso-B image taken after a second initialization. Here, the iso-B lines should be at 2.7 mT and 1.5 mT, but unfortunately, we do not see clear lines but rather a continuous background with localized disturbances. (d) Full-field image taken at the position highlighted with a dashed box in (c).

a single field line, approximately 500 nm in diameter. Following a second preparation round, and measuring fields of 2.75 mT and 1.57 mT, we observe considerably more magnetic structures, as shown in Fig. B.13c.

In the next step, we perform quantitative imaging of selected regions of these iso-B images, highlighted here by dashed boxes. The resulting stray field images were obtained by measuring a full ODMR trace at each point and plotting the stray field components parallel to the NV axis as shown in Fig. B.13b,d. We observe compact magnetic structures, again approximately 500 nm in extent. Furthermore, these structures tend to be quite asymmetric, a property which has also been shown in other NV magnetometry studies, where these distortions are attributed to disorder in the magnetic system. The disorder may, for example, stem from thickness-dependent variations in DMI [23] observed in our samples [237].

In Fig. B.13b, we image the same structure in three different external applied fields

and observe a distinct change in the shape and size of the texture. Together with the larger extent of these structures, the magnetic-field dependence hints towards a bubble domain rather than a skyrmion. However, comparing the structure in Fig. B.13d to other observations of skyrmions with NV magnetometry in a similar material, we observe a generally similar stray field pattern [22]. Further measurements of other areas in the same sample preparation iteration yield similar structures, though the shape may change. However, based on MFM measurements [237], we expect the skyrmion radius to be around 10-20 nm. To explain such a broadening of the skyrmion stray field, we would require an NV center hundreds of nm from the sample surface. While this is not impossible, based on our characterization of typical NV-to-sample distances in Chap. 3.3.2, it is improbable. For this reason, even these structures may be bubble domains rather than true skyrmions. While we are near the level of spatial resolution one would need to resolve such 20 nm-radius skyrmions, these studies would still benefit from further improvements in the NV spatial resolution.

B.2.3. Conclusions

In this section, we have explored skyrmions and how the NV center may be used to image these nanoscale structures. We targeted Néel skyrmions, hosted in five repetitions of an Ir/Co/Pt stack. We performed both iso-B and full stray field imaging of skyrmion-like magnetic structures, though based on their large radius and magnetic field behavior, we believe they might be bubble domains. However, they may still be exhibit skyrmionic properties. Therefore, confirming the skyrmionic nature of these structures would be an important step for the future. To do so, one can map out the spin structure using vector magnetometry [22], or one can use the skyrmion Hall effect. This effect leads to skyrmion motion perpendicular to an applied current [228, 229]. In particular, one could use current pulses and take NV magnetometry-based “snapshots” following each pulse to visualize the motion of the skyrmions.

Of particular interest for future studies are skyrmions in even ultra-thin film systems. Moving to a single repeat of the Ir/Co/Pt would allow us to reach a regime of magnetic imaging where, for example, the magnetic properties of the MFM tips could cause changes in skyrmions while imaging. Not only this but such single repeat materials are much closer to what one would expect to use in technological applications. For this reason, many recent investigations of skyrmions have focused on ultra-thin film systems [23, 238]. Furthermore, using the AC magnetometry capabilities of the NV could also be of interest. Already PL measurements have yielded information about the dynamics of skyrmions [22]. Expanding on these measurements with more sophisticated techniques such as those touched upon in Sec. B.1 could allow us to learn more about these technologically relevant structures. Here, NV magnetometry would allow us to access these skyrmion dynamics on the relevant nanoscale.

C. Bibliography

- [1] B. Dieny, I. L. Prejbeanu, K. Garello, P. Gambardella, P. Freitas, R. Lehn-dorff, W. Raberg, U. Ebels, S. O. Demokritov, J. Akerman, A. Deac, P. Pirro, C. Adelmann, A. Anane, A. V. Chumak, A. Hirohata, S. Mangin, S. O. Valenzuela, M. C. Onbaşlı, M. d'Aquino, G. Prenat, G. Finocchio, L. Lopez-Diaz, R. Chantrell, O. Chubykalo-Fesenko, and P. Bortolotti, *Opportunities and challenges for spintronics in the microelectronics industry*, [Nature Electronics](#) **3**, 446–459 (2020).
- [2] A. Fert and F. N. Van Dau, *Spintronics, from giant magnetoresistance to magnetic skyrmions and topological insulators*, [Comptes Rendus Physique](#) **20**, 817 (2019).
- [3] E. Gerstner, *Nobel Prize 2007: Fert and Grünberg*, [Nature Physics](#) **3**, 754 (2007).
- [4] T. Kawahara, K. Ito, R. Takemura, and H. Ohno, *Spin-transfer torque RAM technology: Review and prospect*, [Microelectronics Reliability](#) **52**, 613–627 (2012).
- [5] A. Manchon, J. Železný, I. Miron, T. Jungwirth, J. Sinova, A. Thiaville, K. Garello, and P. Gambardella, *Current-induced spin-orbit torques in ferromagnetic and antiferromagnetic systems*, [Reviews of Modern Physics](#) **91**, 035004 (2019).
- [6] M. Foerster, O. Boulle, S. Esefelder, R. Mattheis, and M. Kläui, *Domain wall memory device*, [Handbook of Spintronics](#) pp. 1387–1441 (2016).
- [7] S. S. P. Parkin, M. Hayashi, and L. Thomas, *Magnetic domain-wall racetrack memory*, [Science](#) **320**, 190 (2008).
- [8] K. Everschor-Sitte, J. Masell, R. M. Reeve, and M. Kläui, *Perspective: Magnetic skyrmions—Overview of recent progress in an active research field*, [Journal of Applied Physics](#) **124**, 240901 (2018).
- [9] X. Zhang, M. Ezawa, and Y. Zhou, *Magnetic skyrmion logic gates: conversion, duplication and merging of skyrmions*, [Scientific Reports](#) **5**, 9400 (2015).
- [10] D. A. Allwood, *Magnetic domain-wall logic*, [Science](#) **309**, 1688 (2005).
- [11] K. Jhuria, J. Hohlfeld, A. Pattabi, E. Martin, A. Y. Arriola Córdova, X. Shi, R. Lo Conte, S. Petit-Watelot, J. C. Rojas-Sanchez, G. Malinowski, S. Mangin, A. Lemaître, M. Hehn, J. Bokor, R. B. Wilson, and J. Gorchon, *Spin-orbit torque switching of a ferromagnet with picosecond electrical pulses*, [Nature Electronics](#) **3**, 680–686 (2020).

- [12] V. Baltz, A. Manchon, M. Tsoi, T. Moriyama, T. Ono, and Y. Tserkovnyak, *Antiferromagnetic spintronics*, [Reviews of Modern Physics](#) **90**, 015005 (2018).
- [13] K. Olejník, T. Seifert, Z. Kašpar, V. Novák, P. Wadley, R. P. Campion, M. Baumgartner, P. Gambardella, P. Němec, J. Wunderlich, J. Sinova, P. Kužel, M. Müller, T. Kampfrath, and T. Jungwirth, *Terahertz electrical writing speed in an antiferromagnetic memory*, [Science Advances](#) **4**, eaar3566 (2018).
- [14] P. Němec, M. Fiebig, T. Kampfrath, and A. V. Kimel, *Antiferromagnetic opto-spintronics*, [Nature Physics](#) **14**, 229–241 (2018).
- [15] N. A. Spaldin and R. Ramesh, *Advances in magnetoelectric multiferroics*, [Nature Materials](#) **18**, 203–212 (2019).
- [16] T. Kosub, M. Koppe, F. Radu, O. G. Schmidt, and D. Makarov, *All-electric access to the magnetic-field-invariant magnetization of antiferromagnets*, [Physical Review Letters](#) **115**, 097201 (2015).
- [17] T. Kosub, M. Koppe, R. Hühne, P. Appel, B. Shields, P. Maletinsky, R. Hübner, M. O. Liedke, J. Fassbender, O. G. Schmidt, and D. Makarov, *Purely antiferromagnetic magnetoelectric random access memory*, [Nature Communications](#) **8**, 13985 (2017).
- [18] J.-L. Wang, W. Echtenkamp, A. Mahmood, and C. Binek, *Voltage controlled magnetism in Cr_2O_3 based all-thin-film systems*, [Journal of Magnetism and Magnetic Materials](#) **486**, 165262 (2019).
- [19] O. Kazakova, R. Puttock, C. Barton, H. Corte-León, M. Jaafar, V. Neu, and A. Asenjo, *Frontiers of magnetic force microscopy*, [Journal of Applied Physics](#) **125**, 060901 (2019).
- [20] M. J. Martínez-Pérez and D. Koelle, *NanoSQUIDS: Basics and recent advances*, [Physical Sciences Reviews](#) **2** (2017).
- [21] S.-W. Cheong, M. Fiebig, W. Wu, L. Chapon, and V. Kiryukhin, *Seeing is believing: Visualization of antiferromagnetic domains*, [npj Quantum Materials](#) **5**, 1–10 (2020).
- [22] A. Jenkins, M. Pelliccione, G. Yu, X. Ma, X. Li, K. L. Wang, and A. C. B. Jayich, *Single-spin sensing of domain-wall structure and dynamics in a thin-film skyrmion host*, [Physical Review Materials](#) **3**, 083801 (2019).
- [23] I. Gross, W. Akhtar, A. Hrabec, J. Sampaio, L. J. Martínez, S. Chouaieb, B. J. Shields, P. Maletinsky, A. Thiaville, S. Rohart, and V. Jacques, *Skyrmion morphology in ultrathin magnetic films*, [Physical Review Materials](#) **2**, 024406 (2018).
- [24] J.-P. Tetienne, T. Hingant, L. Martínez, S. Rohart, A. Thiaville, L. H. Diez, K. Garcia, J.-P. Adam, J.-V. Kim, J.-F. Roch, I. Miron, G. Gaudin, L. Vila, B. Ocker, D. Ravelosona, and V. Jacques, *The nature of domain walls in ultrathin ferromagnets revealed by scanning nanomagnetometry*, [Nature Communications](#) **6**, 6733 (2015).

-
- [25] I. Gross, W. Akhtar, V. Garcia, L. J. Martínez, S. Chouaieb, K. Garcia, C. Carrétéro, A. Barthélémy, P. Appel, P. Maletinsky, J.-V. Kim, J. Y. Chauleau, N. Jaouen, M. Viret, M. Bibes, S. Fusil, and V. Jacques, *Real-space imaging of non-collinear antiferromagnetic order with a single-spin magnetometer*, [*Nature* **549**, 252 \(2017\)](#).
 - [26] P. Appel, B. J. Shields, T. Kosub, N. Hedrich, R. Hübner, J. Faßbender, D. Makarov, and P. Maletinsky, *Nanomagnetism of magnetoelectric granular thin-film antiferromagnets*, [*Nano Letters* **19**, 1682 \(2019\)](#).
 - [27] F. Casola, T. van der Sar, and A. Yacoby, *Probing condensed matter physics with magnetometry based on nitrogen-vacancy centres in diamond*, [*Nature Reviews Materials* **3**, 17088 \(2018\)](#).
 - [28] P. Maletinsky, S. Hong, M. S. Grinolds, B. Hausmann, M. D. Lukin, R. L. Walsworth, M. Loncar, and A. Yacoby, *A robust scanning diamond sensor for nanoscale imaging with single nitrogen-vacancy centres*, [*Nature Nanotechnology* **7**, 320 \(2012\)](#).
 - [29] P. Appel, E. Neu, M. Ganzhorn, A. Barfuss, M. Batzer, M. Gratz, A. Tschöpe, and P. Maletinsky, *Fabrication of all diamond scanning probes for nanoscale magnetometry*, [*Review of Scientific Instruments* **87**, 063703 \(2016\)](#).
 - [30] T. X. Zhou, R. J. Stöhr, and A. Yacoby, *Scanning diamond NV center probes compatible with conventional afm technology*, [*Applied Physics Letters* **111**, 163106 \(2017\)](#).
 - [31] L. Rondin, J.-P. Tetienne, T. Hingant, J.-F. Roch, P. Maletinsky, and V. Jacques, *Magnetometry with nitrogen-vacancy defects in diamond*, [*Reports on Progress in Physics* **77**, 056503 \(2014\)](#).
 - [32] N. Hedrich, D. Rohner, M. Batzer, P. Maletinsky, and B. J. Shields, *Parabolic diamond scanning probes for single-spin magnetic field imaging*, [*Physical Review Applied* **14**, 064007 \(2020\)](#).
 - [33] D. Le Sage, K. Arai, D. R. Glenn, S. J. DeVience, L. M. Pham, L. Rahn-Lee, M. D. Lukin, A. Yacoby, A. Komeili, and R. L. Walsworth, *Optical magnetic imaging of living cells*, [*Nature* **496**, 486–489 \(2013\)](#).
 - [34] G. Davies and M. Hamer, *Optical studies of the 1.945 eV vibronic band in diamond*, [*Proceedings of the Royal Society of London. A. Mathematical and Physical Sciences* **348**, 285 \(1976\)](#).
 - [35] G. Balasubramanian, I. Y. Chan, R. Kolesov, M. Al-Hmoud, J. Tisler, C. Shin, C. Kim, A. Wojcik, P. R. Hemmer, A. Krueger, T. Hanke, A. Leitenstorfer, R. Bratschitsch, F. Jelezko, and J. Wrachtrup, *Nanoscale imaging magnetometry with diamond spins under ambient conditions*, [*Nature* **455**, 648 \(2008\)](#).
 - [36] F. Dolde, H. Fedder, M. W. Doherty, T. Nöbauer, F. Rempp, G. Balasubramanian, T. Wolf, F. Reinhard, L. C. L. Hollenberg, F. Jelezko, and J. Wrachtrup, *Electric-field sensing using single diamond spins*, [*Nature Physics* **7**, 459–463 \(2011\)](#).

- [37] J. Michl, J. Steiner, A. Denisenko, A. Bülau, A. Zimmermann, K. Nakamura, H. Sumiya, S. Onoda, P. Neumann, J. Isoya, and J. Wrachtrup, *Robust and accurate electric field sensing with solid state spin ensembles*, [Nano Letters](#) **19**, 4904 (2019).
- [38] J. Teissier, A. Barfuss, P. Appel, E. Neu, and P. Maletinsky, *Strain coupling of a nitrogen-vacancy center spin to a diamond mechanical oscillator*, [Physical Review Letters](#) **113** (2014).
- [39] S. Knauer, J. P. Hadden, and J. G. Rarity, *In-situ measurements of fabrication induced strain in diamond photonic-structures using intrinsic colour centres*, [npj Quantum Information](#) **6** (2020).
- [40] P. Neumann, I. Jakobi, F. Dolde, C. Burk, R. Reuter, G. Waldherr, J. Honert, T. Wolf, A. Brunner, J. H. Shim, D. Suter, H. Sumiya, J. Isoya, and J. Wrachtrup, *High-precision nanoscale temperature sensing using single defects in diamond*, [Nano Letters](#) **13**, 2738 (2013).
- [41] C. Foy, L. Zhang, M. E. Trusheim, K. R. Bagnall, M. Walsh, E. N. Wang, and D. R. Englund, *Wide-field magnetic field and temperature imaging using nanoscale quantum sensors*, [ACS Applied Materials and Interfaces](#) **12**, 26525 (2020).
- [42] P. Wang, S. Chen, M. Guo, S. Peng, M. Wang, M. Chen, W. Ma, R. Zhang, J. Su, X. Rong, F. Shi, T. Xu, and J. Du, *Nanoscale magnetic imaging of ferritins in a single cell*, [Science Advances](#) **5**, eaau8038 (2019).
- [43] G. Kucsko, P. C. Maurer, N. Y. Yao, M. Kubo, H. J. Noh, P. K. Lo, H. Park, and M. D. Lukin, *Nanometre-scale thermometry in a living cell*, [Nature](#) **500**, 54 (2013).
- [44] Y.-C. Chen, P. S. Salter, S. Knauer, L. Weng, A. C. Frangeskou, C. J. Stephen, S. N. Ishmael, P. R. Dolan, S. Johnson, B. L. Green, G. W. Morley, M. E. Newton, J. G. Rarity, M. J. Booth, and J. M. Smith, *Laser writing of coherent colour centres in diamond*, [Nature Photonics](#) **11**, 77–80 (2017).
- [45] J. P. Hadden, V. Bharadwaj, B. Sotillo, S. Rampini, R. Osellame, J. D. Witmer, H. Jayakumar, T. T. Fernandez, A. Chiappini, C. Armellini, M. Ferrari, R. Ramponi, P. E. Barclay, and S. M. Eaton, *Integrated waveguides and deterministically positioned nitrogen vacancy centers in diamond created by femtosecond laser writing*, [Optics Letters](#) **43**, 3586–3589 (2018).
- [46] A. Haque and S. Sumaiya, *An overview on the formation and processing of nitrogen-vacancy photonic centers in diamond by ion implantation*, [Journal of Manufacturing and Materials Processing](#) **1**, 6 (2017).
- [47] J. O. Orwa, C. Santori, K. M. C. Fu, B. Gibson, D. Simpson, I. Aharonovich, A. Stacey, A. Cimmino, P. Balog, M. Markham, D. Twitchen, A. D. Greentree, R. G. Beausoleil, and S. Prawer, *Engineering of nitrogen-vacancy color centers in high purity diamond by ion implantation and annealing*, [Journal of Applied Physics](#) **109**, 083530 (2011).

-
- [48] P. Deák, B. Aradi, M. Kaviani, T. Frauenheim, and A. Gali, *Formation of nv centers in diamond: A theoretical study based on calculated transitions and migration of nitrogen and vacancy related defects*, [*Physical Review B* **89**, 075203 \(2014\)](#).
- [49] M. W. Doherty, J. Michl, F. Dolde, I. Jakobi, P. Neumann, N. B. Manson, and J. Wrachtrup, *Measuring the defect structure orientation of a single NV centre in diamond*, [*New Journal of Physics* **16**, 063067 \(2014\)](#).
- [50] D. Zheng, N. D. Lai, X. Xu, F. Treussart, and J. Roch, *Orientation of the spin of a single nv color center in a diamond nanocrystal, and analysis of its optical transition dipoles*, [*IEEE Xplore* p. 1–2 \(2009\)](#).
- [51] J. R. Maze, A. Gali, E. Togan, Y. Chu, A. Trifonov, E. Kaxiras, and M. D. Lukin, *Properties of nitrogen-vacancy centers in diamond: the group theoretic approach*, [*New Journal of Physics* **13**, 025025 \(2011\)](#).
- [52] A. Gali, *Ab initio theory of the nitrogen-vacancy center in diamond*, [*Nanophotonics* **8**, 1907 \(2019\)](#).
- [53] M. L. Goldman, M. W. Doherty, A. Sipahigil, N. Y. Yao, S. D. Bennett, N. B. Manson, A. Kubanek, and M. D. Lukin, *State-selective intersystem crossing in nitrogen-vacancy centers*, [*Physical Review B* **91**, 165201 \(2015\)](#).
- [54] V. M. Acosta, A. Jarmola, E. Bauch, and D. Budker, *Optical properties of the nitrogen-vacancy singlet levels in diamond*, [*Physical Review B* **82** \(2010\)](#).
- [55] L. Robledo, H. Bernien, T. v. d. Sar, and R. Hanson, *Spin dynamics in the optical cycle of single nitrogen-vacancy centres in diamond*, [*New Journal of Physics* **13**, 025013 \(2011\)](#).
- [56] M. W. Doherty, N. B. Manson, P. Delaney, F. Jelezko, J. Wrachtrup, and L. C. Hollenberg, *The nitrogen-vacancy colour centre in diamond*, [*Physics Reports* **528**, 1 \(2013\)](#).
- [57] B. Shields, Q. Unterreithmeier, N. de Leon, H. Park, and M. Lukin, *Efficient readout of a single spin state in diamond via spin-to-charge conversion*, [*Physical Review Letters* **114** \(2015\)](#).
- [58] S. D. Subedi, V. V. Fedorov, J. Peppers, D. V. Martyshkin, S. B. Mirov, L. Shao, and M. Loncar, *Laser spectroscopic characterization of negatively charged nitrogen-vacancy (NV^-) centers in diamond*, [*Optical Materials Express* **9**, 2076–2087 \(2019\)](#).
- [59] N. Aslam, G. Waldherr, P. Neumann, F. Jelezko, and J. Wrachtrup, *Photo-induced ionization dynamics of the nitrogen vacancy defect in diamond investigated by single-shot charge state detection*, [*New Journal of Physics* **15**, 013064 \(2013\)](#).
- [60] K. J. Brown, E. Chartier, E. M. Sweet, D. A. Hopper, and L. C. Bassett, *Cleaning diamond surfaces using boiling acid treatment in a standard laboratory chemical hood*, [*Journal of Chemical Health Safety* **26**, 40 \(2019\)](#).

- [61] Y. Mita, *Change of absorption spectra in type-Ib diamond with heavy neutron irradiation*, [Physical Review B](#) **53**, 11360 (1996).
- [62] D. Rohner, *Towards single spin magnetometry at mK temperatures*, [Ph.D. thesis](#) (2020).
- [63] D. M. Toyli, D. J. Christle, A. Alkauskas, B. B. Buckley, C. G. Van de Walle, and D. D. Awschalom, *Measurement and control of single nitrogen-vacancy center spins above 600 K*, [Physical Review X](#) **2**, 031001 (2012).
- [64] L. J. Rogers, R. L. McMurtrie, M. J. Sellars, and N. B. Manson, *Time-averaging within the excited state of the nitrogen-vacancy centre in diamond*, [New Journal of Physics](#) **11**, 063007 (2009).
- [65] J. Kölbl, *Dressed states of a strain-driven spin in diamond*, [Ph.D. thesis](#), University of Basel (2020).
- [66] A. Barfuss, *Hybrid spin-nanomechanics with single spins in diamond mechanical oscillators*, [Ph.D. thesis](#), University of Basel (2017).
- [67] M. H. Alkahtani, F. Alghannam, L. Jiang, A. Almethen, A. A. Rampersaud, R. Brick, C. L. Gomes, M. O. Scully, and P. R. Hemmer, *Fluorescent nanodiamonds: past, present, and future*, [Nanophotonics](#) **7**, 1423 (2018).
- [68] N. Bar-Gill, L. Pham, C. Belthangady, D. Le Sage, P. Cappellaro, J. Maze, M. Lukin, A. Yacoby, and R. Walsworth, *Suppression of spin-bath dynamics for improved coherence of multi-spin-qubit systems*, [Nature Communications](#) **3**, 858 (2012).
- [69] J. Wrachtrup, S. Y. Kilin, and A. P. Nizovtsev, *Quantum computation using the ^{13}C nuclear spins near the single NV defect center in diamond*, [Optics and Spectroscopy](#) **91**, 429 (2001).
- [70] Y. Wu, Y. Wang, X. Qin, X. Rong, and J. Du, *A programmable two-qubit solid-state quantum processor under ambient conditions*, [npj Quantum Information](#) **5** (2019).
- [71] A. Jarmola, V. M. Acosta, K. Jensen, S. Chemerisov, and D. Budker, *Temperature- and magnetic-field-dependent longitudinal spin relaxation in nitrogen-vacancy ensembles in diamond*, [Physical Review Letters](#) **108** (2012).
- [72] G.-Q. Liu, X. Feng, N. Wang, Q. Li, and R.-B. Liu, *Coherent quantum control of nitrogen-vacancy center spins near 1000 Kelvin*, [Nature Communications](#) **10** (2019).
- [73] T. van der Sar, F. Casola, R. Walsworth, and A. Yacoby, *Nanometre-scale probing of spin waves using single electron spins*, [Nature Communications](#) **6**, 7886 (2015).
- [74] M. Lesik, T. Plisson, L. Toraille, J. Renaud, F. Occelli, M. Schmidt, O. Salord, A. Delobbe, T. Debuisschert, L. Rondin, P. Loubeyre, and J.-F. Roch, *Magnetic measurements on micrometer-sized samples under high pressure using designed NV centers*, [Science](#) **366**, 1359 (2019).

-
- [75] L. Thiel, Z. Wang, M. A. Tschudin, D. Rohner, I. Gutiérrez-Lezama, N. Ubrig, M. Gibertini, E. Giannini, A. F. Morpurgo, and P. Maletinsky, *Probing magnetism in 2D materials at the nanoscale with single-spin microscopy*, [*Science* **364**, 973 \(2019\)](#).
 - [76] V. M. Acosta, E. Bauch, M. P. Ledbetter, A. Waxman, L.-S. Bouchard, and D. Budker, *Temperature dependence of the nitrogen-vacancy magnetic resonance in diamond*, [*Physical Review Letters* **104**, 070801 \(2010\)](#).
 - [77] Y. Dovzhenko, F. Casola, S. Schlotter, T. X. Zhou, F. Büttner, R. L. Walsworth, G. S. D. Beach, and A. Yacoby, *Magnetostatic twists in room-temperature skyrmions explored by nitrogen-vacancy center spin texture reconstruction*, [*Nature Communications* **9**, 2712 \(2018\)](#).
 - [78] B. J. Maertz, A. P. Wijnheijmer, G. D. Fuchs, M. E. Nowakowski, and D. D. Awschalom, *Vector magnetic field microscopy using nitrogen vacancy centers in diamond*, [*Applied Physics Letters* **96**, 092504 \(2010\)](#).
 - [79] D. Broadway, S. Lillie, S. Scholten, D. Rohner, N. Dontschuk, P. Maletinsky, J.-P. Tetienne, and L. Hollenberg, *Improved current density and magnetization reconstruction through vector magnetic field measurements*, [*Physical Review Applied* **14** \(2020\)](#).
 - [80] L. Thiel, *Nanoscale magnetometry with a single spin in diamond at cryogenic temperatures*, [*Ph.D. thesis*](#), University of Basel (2019).
 - [81] P. Appel, M. Ganzhorn, E. Neu, and P. Maletinsky, *Nanoscale microwave imaging with a single electron spin in diamond*, [*New Journal of Physics* **17**, 112001 \(2015\)](#).
 - [82] J.-P. Tetienne, T. Hingant, J.-V. Kim, L. H. Diez, J.-P. Adam, K. Garcia, J.-F. Roch, S. Rohart, A. Thiaville, D. Ravelosona, and V. Jacques, *Nanoscale imaging and control of domain-wall hopping with a nitrogen-vacancy center microscope*, [*Science* **344**, 1366–1369 \(2014\)](#).
 - [83] R. S. Schoenfeld and W. Harneit, *Real time magnetic field sensing and imaging using a single spin in diamond*, [*Physical Review Letters* **106**, 030802 \(2011\)](#).
 - [84] J. M. Taylor, P. Cappellaro, L. Childress, L. Jiang, D. Budker, P. R. Hemmer, A. Yacoby, R. Walsworth, and M. D. Lukin, *High-sensitivity diamond magnetometer with nanoscale resolution*, [*Nature Physics* **4**, 810 \(2008\)](#).
 - [85] A. Dréau, M. Lesik, L. Rondin, P. Spinicelli, O. Arcizet, J.-F. Roch, and V. Jacques, *Avoiding power broadening in optically detected magnetic resonance of single NV defects for enhanced DC magnetic field sensitivity*, [*Physical Review B* **84** \(2011\)](#).
 - [86] D. Hopper, H. Shulevitz, and L. Bassett, *Spin readout techniques of the nitrogen-vacancy center in diamond*, [*Micromachines* **9**, 437 \(2018\)](#).

- [87] M. Kaviani, P. Deák, B. Aradi, T. Frauenheim, J.-P. Chou, and A. Gali, *Proper surface termination for luminescent near-surface nv centers in diamond*, [Nano Letters](#) **14**, 4772 (2014).
- [88] J. Wrachtrup, F. Jelezko, B. Grotz, and L. McGuinness, *Nitrogen-vacancy centers close to surfaces*, [MRS Bulletin](#) **38**, 149–154 (2013).
- [89] Z.-H. Wang, G. de Lange, D. Ristè, R. Hanson, and V. V. Dobrovitski, *Comparison of dynamical decoupling protocols for a nitrogen-vacancy center in diamond*, [Physical Review B](#) **85**, 155204 (2012).
- [90] J. F. Barry, J. M. Schloss, E. Bauch, M. J. Turner, C. A. Hart, L. M. Pham, and R. L. Walsworth, *Sensitivity optimization for NV-diamond magnetometry*, [Reviews of Modern Physics](#) **92**, 015004 (2020).
- [91] N. H. Wan, B. J. Shields, D. Kim, S. Mouradian, B. Lienhard, M. Walsh, H. Bakhru, T. Schröder, and D. Englund, *Efficient extraction of light from a nitrogen-vacancy center in a diamond parabolic reflector*, [Nano Letters](#) **18**, 2787 (2018).
- [92] P. Appel, *Scanning nanomagnetometry : Probing magnetism with single spins in diamond*, [Ph.D. thesis](#), University of Basel (2017).
- [93] M. Radtke, E. Bernardi, A. Slablab, R. Nelz, and E. Neu, *Nanoscale sensing based on nitrogen vacancy centers in single crystal diamond and nanodiamonds: achievements and challenges*, [Nano Futures](#) **3**, 042004 (2019).
- [94] E. Marchiori, L. Ceccarelli, N. Rossi, L. Lorenzelli, C. L. Degen, and M. Poggio, *Technical review: Imaging weak magnetic field patterns on the nanometer-scale and its application to 2D materials*, [arXiv:2103.10382 \[cond-mat, physics:quant-ph\]](#) (2021).
- [95] R. P. Mildren and J. R. Rabeau, *Optical engineering of diamond*, ([Wiley](#)) (2013).
- [96] S. Mi, M. Kiss, T. Graziosi, and N. Quack, *Integrated photonic devices in single crystal diamond*, [Journal of Physics: Photonics](#) **2**, 042001 (2020).
- [97] J. P. Hadden, J. P. Harrison, A. C. Stanley-Clarke, L. Marseglia, Y.-L. D. Ho, B. R. Patton, J. L. O’Brien, and J. G. Rarity, *Strongly enhanced photon collection from diamond defect centers under microfabricated integrated solid immersion lenses*, [Applied Physics Letters](#) **97**, 241901 (2010).
- [98] M. Jamali, I. Gerhardt, M. Rezai, K. Frenner, H. Fedder, and J. Wrachtrup, *Microscopic diamond solid-immersion-lenses fabricated around single defect centers by focused ion beam milling*, [Review of Scientific Instruments](#) **85**, 123703 (2014).
- [99] D. Riedel, D. Rohner, M. Ganzhorn, T. Kaldewey, P. Appel, E. Neu, R. Warburton, and P. Maletinsky, *Low-loss broadband antenna for efficient photon collection from a coherent spin in diamond*, [Physical Review Applied](#) **2** (2014).

-
- [100] T.-Y. Huang, R. R. Grote, S. A. Mann, D. A. Hopper, A. L. Exarhos, G. G. Lopez, G. R. Kaighn, E. C. Garnett, and L. C. Bassett, *A monolithic immersion metalens for imaging solid-state quantum emitters*, [*Nature Communications* **10**, 2392 \(2019\)](#).
- [101] L. Li, E. H. Chen, J. Zheng, S. L. Mouradian, F. Dolde, T. Schröder, S. Karaveli, M. L. Markham, D. J. Twitchen, and D. Englund, *Efficient photon collection from a nitrogen vacancy center in a circular bullseye grating*, [*Nano Letters* **15**, 1493 \(2015\)](#).
- [102] S. A. Momenzadeh, R. J. Stoehr, F. Favaro de Oliveira, A. Brunner, A. Denisenko, S. Yang, F. Reinhard, and J. Wachtrup, *Nanoengineered diamond waveguide as a robust bright platform for nanomagnetometry using shallow nitrogen vacancy centers*, [*Nano Letters* **15**, 165 \(2015\)](#).
- [103] M. Pelliccione, A. Jenkins, P. Ovartchaiyapong, C. Reetz, E. Emmanouilidou, N. Ni, and A. C. Bleszynski Jayich, *Scanned probe imaging of nanoscale magnetism at cryogenic temperatures with a single-spin quantum sensor*, [*Nature Nanotechnology* **11**, 700 \(2016\)](#).
- [104] P. Fuchs, M. Challier, and E. Neu, *Optimized single-crystal diamond scanning probes for high sensitivity magnetometry*, [*New Journal of Physics* **20**, 125001 \(2018\)](#).
- [105] K. Drexhage, *Influence of a dielectric interface on fluorescence decay time*, [*Journal of Luminescence* **1**, 693 \(1970\)](#).
- [106] B. J. Hausmann, M. Khan, Y. Zhang, T. M. Babinec, K. Martinick, M. McCutcheon, P. R. Hemmer, and M. Lončar, *Fabrication of diamond nanowires for quantum information processing applications*, [*Diamond and Related Materials* **19**, 621 \(2010\)](#).
- [107] T. P. M. Alegre, C. Santori, G. Medeiros-Ribeiro, and R. G. Beausoleil, *Polarization-selective excitation of nitrogen vacancy centers in diamond*, [*Physical Review B* **76** \(2007\)](#).
- [108] T. Yamada, H. Yoshikawa, H. Uetsuka, S. Kumaragurubaran, N. Tokuda, and S.-i. Shikata, *Cycle of two-step etching process using ICP for diamond MEMS applications*, [*Diamond and Related Materials* **16**, 996 \(2007\)](#).
- [109] L. Xie, T. X. Zhou, R. J. Stöhr, and A. Yacoby, *Crystallographic orientation dependent reactive ion etching in single crystal diamond*, [*Advanced Materials* **30**, 1705501 \(2018\)](#).
- [110] D. Bluvstein, Z. Zhang, and A. C. B. Jayich, *Identifying and mitigating charge instabilities in shallow diamond nitrogen-vacancy centers*, [*Physical Review Letters* **122**, 076101 \(2019\)](#).
- [111] A. Gruber, A. Dräbenstedt, C. Tietz, L. Fleury, J. Wrachtrup, and C. von Borczyskowski, *Scanning confocal optical microscopy and magnetic resonance on single defect centers*, [*Science* **276**, 2012 \(1997\)](#).

- [112] P. Grünwald, *Effective second-order correlation function and single-photon detection*, [New Journal of Physics](#) **21**, 093003 (2019).
- [113] C. Kurtsiefer, S. Mayer, P. Zarda, and H. Weinfurter, *Stable solid-state source of single photons*, [Physical Review Letters](#) **85**, 290 (2000).
- [114] A. Golubev, *Exponentially modified peak functions in biomedical sciences and related disciplines*, [Computational and Mathematical Methods in Medicine](#) **2017**, 1 (2017).
- [115] D. Rohner, *Enhancing collection efficiency of nitrogen vacancy center fluorescence using a solid immersion lens*, MSc. Thesis (2013).
- [116] S. Hong, M. S. Grinolds, L. M. Pham, D. Le Sage, L. Luan, R. L. Walsworth, and A. Yacoby, *Nanoscale magnetometry with NV centers in diamond*, [MRS Bulletin](#) **38**, 155 (2013).
- [117] B. C. Buchler, T. Kalkbrenner, C. Hettich, and V. Sandoghdar, *Measuring the quantum efficiency of the optical emission of single radiating dipoles using a scanning mirror*, [Physical Review Letters](#) **95**, 063003 (2005).
- [118] S. Ernst, D. M. Irber, A. M. Waeber, G. Braunbeck, and F. Reinhard, *A planar scanning probe microscope*, [ACS Photonics](#) **6**, 327 (2019).
- [119] M. Batzer, *Optimization of single crystalline all diamond scanning probes for quantum sensing applications*, [Ph.D. thesis](#), University of Basel (2019).
- [120] D. Rohner, J. Happacher, P. Reiser, M. A. Tschudin, A. Tallaire, J. Achard, B. J. Shields, and P. Maletinsky, *(111)-oriented, single crystal diamond tips for nanoscale scanning probe imaging of out-of-plane magnetic fields*, [Applied Physics Letters](#) **115**, 192401 (2019).
- [121] E. Neu, P. Appel, M. Ganzhorn, J. Miguel-Sánchez, M. Lesik, V. Mille, V. Jacques, A. Tallaire, J. Achard, and P. Maletinsky, *Photonic nano-structures on (111)-oriented diamond*, [Applied Physics Letters](#) **104**, 153108 (2014).
- [122] E. D. Herbschleb, H. Kato, Y. Maruyama, T. Danjo, T. Makino, S. Yamasaki, I. Ohki, K. Hayashi, H. Morishita, M. Fujiwara, and N. Mizuochi, *Ultra-long coherence times amongst room-temperature solid-state spins*, [Nature Communications](#) **10** (2019).
- [123] S. Sangtawesin, B. L. Dwyer, S. Srinivasan, J. J. Allred, L. V. Rodgers, K. De Greve, A. Stacey, N. Dontschuk, K. M. O'Donnell, D. Hu, D. A. Evans, C. Jaye, D. A. Fischer, M. L. Markham, D. J. Twitchen, H. Park, M. D. Lukin, and N. P. de Leon, *Origins of diamond surface noise probed by correlating single-spin measurements with surface spectroscopy*, [Physical Review X](#) **9** (2019).
- [124] M. Batzer, M. Batzer, B. Shields, E. Neu, C. Widmann, C. Giese, C. Nebel, P. Maletinsky, and P. Maletinsky, *Single crystal diamond pyramids for applications in nanoscale quantum sensing*, [Optical Materials Express](#) **10**, 492–500 (2020).

-
- [125] I. V. Fedotov, L. V. Doronina-Amitonova, A. A. Voronin, A. O. Levchenko, S. A. Zibrov, D. A. Sidorov-Biryukov, A. B. Fedotov, V. L. Velichansky, and A. M. Zheltikov, *Electron spin manipulation and readout through an optical fiber*, [Scientific Reports](#) **4**, 5362 (2014).
 - [126] A. Smirnov, V. M. Yasinskii, D. S. Filimonenko, E. Rostova, G. Dietler, and S. K. Sekatskii, *True tapping mode scanning near-field optical microscopy with bent glass fiber probes*, [Scanning](#) **2018**, 3249189 (2018).
 - [127] F. Fávaro de Oliveira, S. A. Momenzadeh, Y. Wang, M. Konuma, M. Markham, A. M. Edmonds, A. Denisenko, and J. Wrachtrup, *Effect of low-damage inductively coupled plasma on shallow nitrogen-vacancy centers in diamond*, [Applied Physics Letters](#) **107**, 073107 (2015).
 - [128] A. Hirohata, Y. Keisuke, Y. Nakatani, I.-L. Prejbeanu, B. Di'eny, P. Pirro, and B. Hillebrands, *Review on spintronics: Principles and device applications*, [Journal of Magnetism and Magnetic Materials](#) **509**, 166711 (2020).
 - [129] S. Bader and S. Parkin, *Spintronics*, [Annual Review of Condensed Matter Physics](#) **1**, 71 (2010).
 - [130] P. Wadley, B. Howells, J. Železný, C. Andrews, V. Hills, R. P. Campion, V. Novák, K. Olejník, F. Maccherozzi, S. S. Dhesi, S. Y. Martin, T. Wagner, J. Wunderlich, F. Freimuth, Y. Mokrousov, J. Kuneš, J. S. Chauhan, M. J. Grzybowski, A. W. Rushforth, K. W. Edmonds, B. L. Gallagher, and T. Jungwirth, *Electrical switching of an antiferromagnet*, [Science](#) **351**, 587–590 (2016).
 - [131] N. Eastaugh, V. Walsh, T. Chaplin, and R. Siddall, *The Pigment Compendium: A Dictionary of Historical Pigments* (Elsevier) (2004).
 - [132] I. Dzyaloshinskii, *On the magneto-electrical effect in antiferromagnets*, [JETP](#) **10**, 628 (1960).
 - [133] D. Astrov, *The magnetoelectric effect in antiferromagnetics*, [JETP](#) **11**, 708 (1960).
 - [134] C. A. Brown, *Magnetoelectric domains in single crystal chromium oxide*, [Ph.D. thesis](#), Imperial College (1969).
 - [135] S. Shtrikman and D. Treves, *Observation of the magnetoelectric effect in Cr_2O_3 powders*, [Physical Review](#) **130**, 986 (1963).
 - [136] M. Fiebig, D. Fröhlich, G. Sluyterman v. L., and R. V. Pisarev, *Domain topography of antiferromagnetic Cr_2O_3 by second-harmonic generation*, [Applied Physics Letters](#) **66**, 2906 (1995).
 - [137] P. Schoenherr, L. M. Giraldo, M. Lilienblum, M. Trassin, D. Meier, and M. Fiebig, *Magnetoelectric force microscopy on antiferromagnetic 180° domains in Cr_2O_3* , [Materials](#) **10**, 1051 (2017).
 - [138] A. Hubert and R. Schaäfer, *Magnetic Domains The Analysis of Magnetic Microstructures* (Berlin Springer Berlin) (2014).

- [139] G. Catalan, J. Seidel, R. Ramesh, and J. F. Scott, *Domain wall nanoelectronics*, [Reviews of Modern Physics](#) **84**, 119 (2012).
- [140] N. Hedrich, K. Wagner, O. V. Pylypovskiy, B. J. Shields, T. Kosub, D. D. Sheka, D. Makarov, and P. Maletinsky, *Nanoscale mechanics of antiferromagnetic domain walls*, [Nature Physics](#) **17**, 574 (2021).
- [141] S. Mu and K. D. Belashchenko, *Influence of strain and chemical substitution on the magnetic anisotropy of antiferromagnetic Cr_2O_3 : An ab-initio study*, [Physical Review Materials](#) **3**, 034405 (2019).
- [142] O. V. Pylypovskiy, A. V. Tomilo, D. D. Sheka, J. Fassbender, and D. Makarov, *Boundary conditions for the Néel order parameter in a chiral antiferromagnetic slab*, [Physical Review B](#) **103**, 134413 (2021).
- [143] S. Mu, A. L. Wysocki, and K. D. Belashchenko, *First-principles microscopic model of exchange-driven magnetoelectric response with application to Cr_2O_3* , [Physical Review B](#) **89**, 174413 (2014).
- [144] M. Fiebig, *Revival of the magnetoelectric effect*, [Journal of Physics D: Applied Physics](#) **38**, R123 (2005).
- [145] X. He, Y. Wang, N. Wu, A. N. Caruso, E. Vescovo, K. D. Belashchenko, P. A. Dowben, and C. Binek, *Robust isothermal electric control of exchange bias at room temperature*, [Nature Materials](#) **9**, 579–585 (2010).
- [146] L. Fallarino, A. Berger, and C. Binek, *Magnetic field induced switching of the antiferromagnetic order parameter in thin films of magnetoelectric chromia*, [Physical Review B](#) **91**, 054414 (2015).
- [147] T. H. O'dell, *The electrodynamics of magneto-electric media*, volume XI (North-Holland) (1970).
- [148] K. Siratori, K. Kohn, and E. Kita, *Magnetoelectric effect in magnetic materials*, [Acta Physica Polonica A](#) **81**, 431 (1991).
- [149] E. J. Samuelsen, M. T. Hutchings, and G. Shirane, *Inelastic neutron scattering investigation of spin waves and magnetic interactions in Cr_2O_3* , [Solid State Communications](#) **7**, 1043–1045 (1969).
- [150] H. V. Gomonay and V. M. Loktev, *Shape-induced phenomena in finite-size antiferromagnets*, [Physical Review B](#) **75**, 174439 (2007).
- [151] K. L. Dudko, V. V. Eremenko, and L. M. Semenenko, *Magnetostriction of antiferromagnetic Cr_2O_3 in strong magnetic fields*, [Physica Status Solidi \(b\)](#) **43**, 471 (1971).
- [152] J. B. Goodenough, *Direct cation-cation interactions in several oxides*, [Physical Review](#) **117**, 1442 (1960).
- [153] Y.-Y. Li, *Superexchange interactions and magnetic lattices of the rhombohedral sesquioxides of the transition elements and their solid solutions*, [Physical Review](#) **102**, 1015 (1956).

-
- [154] S. Shi, A. L. Wysocki, and K. D. Belashchenko, *Magnetism of chromia from first-principles calculations*, [Physical Review B](#) **79**, 104404 (2009).
 - [155] J. O. Artman, J. C. Murphy, and S. Foner, *Magnetic anisotropy in antiferromagnetic corundum-type sesquioxides*, [Physical Review](#) **138**, A912 (1965).
 - [156] C. W. Abert, *Discrete mathematical concepts in micromagnetic computations*, [Ph.D. thesis](#), University of Hamburg (2013).
 - [157] M. S. Wornle, P. Welter, M. Giraldo, T. Lottermoser, M. Fiebig, P. Gambardella, and C. L. Degen, *Coexistence of Bloch and Néel walls in a collinear antiferromagnet*, [Physical Review B](#) **103**, 094426 (2021).
 - [158] S. Cao, N. Wu, W. Echtenkamp, V. Lauter, H. Ambaye, T. Komesu, C. Binek, and P. A. Dowben, *The surface stability of $\text{Cr}_2\text{O}_3(0001)$* , [Journal of Physics: Condensed Matter](#) **27**, 255003 (2015).
 - [159] A. L. Wysocki, S. Shi, and K. D. Belashchenko, *Microscopic origin of the structural phase transitions at the $\text{Cr}_2\text{O}_3(0001)$ surface*, [Physical Review B](#) **86**, 165443 (2012).
 - [160] O. Bikondoa, W. Moritz, X. Torrelles, H. J. Kim, G. Thornton, and R. Lindsay, *Impact of ambient oxygen on the surface structure of $\alpha\text{-Cr}_2\text{O}_3(0001)$* , [Physical Review B](#) **81** (2010).
 - [161] N. Spaldin, *Analogy between the magnetic dipole moment at the surface of a magnetoelectric and the electric charge at the surface of a ferroelectric*, [JETP](#) **159** (2021).
 - [162] K. D. Belashchenko, *Equilibrium magnetization at the boundary of a magnetoelectric antiferromagnet*, [Physical Review Letters](#) **105**, 147204 (2010).
 - [163] Y. Kota, H. Imamura, and M. Sasaki, *Strain-induced Néel temperature enhancement in corundum-type Cr_2O_3 and Fe_2O_3* , [Applied Physics Express](#) **6**, 113007 (2013).
 - [164] S. Mu, A. L. Wysocki, and K. D. Belashchenko, *Effect of substitutional doping on the Néel temperature of Cr_2O_3* , [Physical Review B](#) **87**, 054435 (2013).
 - [165] P. Borisov and W. Kleemann, *Exchange bias and ferromagnetic coercivity in heterostructures with antiferromagnetic Cr_2O_3* , [Journal of Applied Physics](#) **110**, 033917 (2011).
 - [166] D. Astrov, *Magnetoelectric effect in chromium oxide*, [Soviet Physics JETP](#) **13**, 730 (1961).
 - [167] T. Martin and J. Anderson, *Magneto-electric annealing effects of Cr_2O_3* , [Physics Letters](#) **11**, 109 (1964).
 - [168] E. G. Tveten, T. Müller, J. Linder, and A. Brataas, *Intrinsic magnetization of antiferromagnetic textures*, [Physical Review B](#) **93**, 104408 (2016).

- [169] S. Foner, *High-field antiferromagnetic resonance in Cr_2O_3* , [Physical Review](#) **130**, 183 (1963).
- [170] A. Parthasarathy and S. Rakheja, *Dynamics of magnetoelectric reversal of an antiferromagnetic domain*, [Physical Review Applied](#) **11**, 034051 (2019).
- [171] Y. Kota and H. Imamura, *Narrowing of antiferromagnetic domain wall in corundum-type Cr_2O_3 by lattice strain*, [Applied Physics Express](#) **10**, 013002 (2016).
- [172] *Slasi: Spin-lattice simulation tool* (2019).
- [173] S. Selzer, U. Atxitia, U. Ritzmann, D. Hinzke, and U. Nowak, *Inertia-free thermally driven domain-wall motion in antiferromagnets*, [Physical Review Letters](#) **117**, 107201 (2016).
- [174] S. K. Kim and Y. Tserkovnyak, *Landau-Lifshitz theory of thermomagnonic torque*, [Physical Review B](#) **92**, 020410(R) (2015).
- [175] K. D. Belashchenko, O. Tchernyshyov, A. A. Kovalev, and O. A. Tretiakov, *Magnetoelectric domain wall dynamics and its implications for magnetoelectric memory*, [Applied Physics Letters](#) **108**, 132403 (2016).
- [176] M. Street, W. Echtenkamp, T. Komesu, S. Cao, P. A. Dowben, and C. Binek, *Increasing the Néel temperature of magnetoelectric chromia for voltage-controlled spintronics*, [Applied Physics Letters](#) **104**, 222402 (2014).
- [177] A. Mahmood, W. Echtenkamp, M. Street, J.-L. Wang, S. Cao, T. Komesu, P. A. Dowben, P. Buragohain, H. Lu, A. Gruverman, A. Parthasarathy, S. Rakheja, and C. Binek, *Voltage controlled Néel vector rotation in zero magnetic field*, [Nature Communications](#) **12**, 1674 (2021).
- [178] S. P. Pati, N. Shimomura, T. Nozaki, T. Shibata, and M. Sahashi, *Néel temperature of Cr_2O_3 in $\text{Cr}_2\text{O}_3/\text{Co}$ exchange-coupled system: Effect of buffer layer*, [Journal of Applied Physics](#) **117**, 17D137 (2015).
- [179] K. Hono, Y. K. Takahashi, G. Ju, J.-U. Thiele, A. Ajan, X. Yang, R. Ruiz, and L. Wan, *Heat-assisted magnetic recording media materials*, [MRS Bulletin](#) **43**, 93–99 (2018).
- [180] X. Marti, I. Fina, C. Frontera, J. Liu, P. Wadley, Q. He, R. J. Paull, J. D. Clarkson, J. Kudrnovský, I. Turek, J. Kuneš, D. Yi, J.-H. Chu, C. T. Nelson, L. You, E. Arenholz, S. Salahuddin, J. Fontcuberta, T. Jungwirth, and R. Ramesh, *Room-temperature antiferromagnetic memory resistor*, [Nature Materials](#) **13**, 367–374 (2014).
- [181] S. Loth, S. Baumann, C. P. Lutz, D. M. Eigler, and A. J. Heinrich, *Bistability in atomic-scale antiferromagnets*, [Science](#) **335**, 196–199 (2012).
- [182] R. Cheng, M. Li, A. Sapkota, A. Rai, A. Pokhrel, T. Mewes, C. Mewes, D. Xiao, M. De Graef, and V. Sokalski, *Magnetic domain wall skyrmions*, [Physical Review B](#) **99**, 184412 (2019).

-
- [183] A. Finco, A. Haykal, R. Tanos, F. Fabre, S. Chouaieb, W. Akhtar, I. Robert-Philip, W. Legrand, F. Ajejas, K. Bouzehouane, N. Reyren, T. Devolder, J.-P. Adam, J.-V. Kim, V. Cros, and V. Jacques, *Imaging non-collinear antiferromagnetic textures via single spin relaxometry*, [Nature Communications](#) **12**, 767 (2021).
 - [184] J. C. Slonczewski, *Theory of Bloch-line and Bloch-wall motion*, [Journal of Applied Physics](#) **45**, 2705 (1974).
 - [185] Q. Meier, M. Fechner, T. Nozaki, M. Sahashi, Z. Salman, T. Prokscha, A. Suter, P. Schoenherr, M. Lilienblum, P. Borisov, I. Dzyaloshinskii, M. Fiebig, H. Luetkens, and N. Spaldin, *Search for the magnetic monopole at a magnetoelectric surface*, [Physical Review X](#) **9**, 011011 (2019).
 - [186] N. Jones, *How to stop data centres from gobbling up the world's electricity* (2018).
 - [187] E. H. Chen, H. A. Clevenson, K. A. Johnson, L. M. Pham, D. R. Englund, P. R. Hemmer, and D. A. Braje, *High-sensitivity spin-based electrometry with an ensemble of nitrogen-vacancy centers in diamond*, [Physical Review A](#) **95**, 053417 (2017).
 - [188] D. R. Glenn, R. R. Fu, P. Kehayias, D. Le Sage, E. A. Lima, B. P. Weiss, and R. L. Walsworth, *Micrometer-scale magnetic imaging of geological samples using a quantum diamond microscope*, [Geochemistry, Geophysics, Geosystems](#) **18**, 3254 (2017).
 - [189] J. B. McKinnon, D. Melville, and E. W. Lee, *The antiferromagnetic-ferromagnetic transition in iron-rhodium alloys*, [Journal of Physics C: Solid State Physics](#) **3**, S46 (1970).
 - [190] S. O. Mariager, L. L. Guyader, M. Buzzi, G. Ingold, and C. Quitmann, *Imaging the antiferromagnetic to ferromagnetic first order phase transition of FeRh*, [arXiv:1301.4164 \[cond-mat\]](#) (2013).
 - [191] L. J. Swartzendruber, *The Fe-Rh (iron-rhodium) system*, [Bulletin of Alloy Phase Diagrams](#) **5**, 456 (1984).
 - [192] M.-T. Suzuki, T. Koretsune, M. Ochi, and R. Arita, *Cluster multipole theory for anomalous Hall effect in antiferromagnets*, [Physical Review B](#) **95**, 094406 (2017).
 - [193] T. Higo, H. Man, D. B. Gopman, L. Wu, T. Koretsune, O. M. J. van 't Erve, Y. P. Kabanov, D. Rees, Y. Li, M.-T. Suzuki, S. Patankar, M. Ikhlas, C. L. Chien, R. Arita, R. D. Shull, J. Orenstein, and S. Nakatsuji, *Large magneto-optical Kerr effect and imaging of magnetic octupole domains in an antiferromagnetic metal*, [Nature Photonics](#) **12**, 73–78 (2018).
 - [194] G. Nava Antonio, I. Bertelli, B. G. Simon, R. Medapalli, D. Afanasiev, and T. van der Sar, *Magnetic imaging and statistical analysis of the metamagnetic phase transition of FeRh with electron spins in diamond*, [Journal of Applied Physics](#) **129**, 223904 (2021).

- [195] Y. Wang, M. M. Decker, T. N. G. Meier, X. Chen, C. Song, T. Grünbaum, W. Zhao, J. Zhang, L. Chen, and C. H. Back, *Spin pumping during the antiferromagnetic–ferromagnetic phase transition of iron–rhodium*, [Nature Communications](#) **11**, 275 (2020).
- [196] S. Nakatsuji, N. Kiyohara, and T. Higo, *Large anomalous hall effect in a non-collinear antiferromagnet at room temperature*, [Nature](#) **527**, 212–215 (2015).
- [197] Y. Chu, N. de Leon, B. Shields, B. Hausmann, R. Evans, E. Togan, M. J. Burek, M. Markham, A. Stacey, A. Zibrov, A. Yacoby, D. Twitchen, M. Loncar, H. Park, P. Maletinsky, and M. Lukin, *Coherent optical transitions in implanted nitrogen vacancy centers*, [Nano Letters](#) **14**, 1982 (2014).
- [198] M. Radtke, R. Nelz, A. Slablab, and E. Neu, *Reliable nanofabrication of single-crystal diamond photonic nanostructures for nanoscale sensing*, [Micromachines](#) **10**, 718 (2019).
- [199] X.-D. Chen, C.-H. Dong, F.-W. Sun, C.-L. Zou, J.-M. Cui, Z.-F. Han, and G.-C. Guo, *Temperature dependent energy level shifts of nitrogen-vacancy centers in diamond*, [Applied Physics Letters](#) **99**, 161903 (2011).
- [200] A. Vansteenkiste, J. Leliaert, M. Dvornik, M. Helsen, F. Garcia-Sanchez, and B. Van Waeyenberge, *The design and verification of MuMax3*, [AIP Advances](#) **4**, 107133 (2014).
- [201] W. M. Bolstad, *Bayesian statistics using conjugate priors*, [Understanding Computational Bayesian Statistics](#) pp. 61–100 (2009).
- [202] C. P. Robert, *The Metropolis-Hastings algorithm*, [Wiley StatsRef: Statistics Reference Online](#) pp. 1–15 (2015).
- [203] C. Castelnovo, R. Moessner, and S. L. Sondhi, *Magnetic monopoles in spin ice*, [Nature](#) **451**, 42 (2008).
- [204] L. Pauling, *The structure and entropy of ice and of other crystals with some randomness of atomic arrangement*, [Journal of the American Chemical Society](#) **57**, 2680 (1935).
- [205] R. F. Wang, C. Nisoli, R. S. Freitas, J. Li, W. McConville, B. J. Cooley, M. S. Lund, N. Samarth, C. Leighton, V. H. Crespi, and P. Schiffer, *Artificial ‘spin ice’ in a geometrically frustrated lattice of nanoscale ferromagnetic islands*, [Nature](#) **439**, 303 (2006).
- [206] S. H. Skjærvø, C. H. Marrows, R. L. Stamps, and L. J. Heyderman, *Advances in artificial spin ice*, [Nature Reviews Physics](#) **2**, 13 (2019).
- [207] H. Arava, P. M. Derlet, J. Vijayakumar, J. Cui, N. S. Bingham, A. Kleibert, and L. J. Heyderman, *Computational logic with square rings of nanomagnets*, [Nanotechnology](#) **29**, 265205 (2018).
- [208] J. H. Jensen, E. Folven, and G. Tufte, *Computation in artificial spin ice*, [The 2018 Conference on Artificial Life](#) (2018).

-
- [209] S. Ladak, D. E. Read, G. K. Perkins, L. F. Cohen, and W. R. Branford, *Direct observation of magnetic monopole defects in an artificial spin-ice system*, [*Nature Physics* **6**, 359–363 \(2010\)](#).
- [210] M. Wyss, S. Gliga, D. Vasyukov, L. Ceccarelli, G. Romagnoli, J. Cui, A. Kleibert, R. L. Stamps, and M. Poggio, *Stray-field imaging of a chiral artificial spin ice during magnetization reversal*, [*ACS Nano* **13**, 13910 \(2019\)](#).
- [211] A. Farhan, P. M. Derlet, A. Kleibert, A. Balan, R. V. Chopdekar, M. Wyss, J. Perron, A. Scholl, F. Nolting, and L. J. Heyderman, *Direct observation of thermal relaxation in artificial spin ice*, [*Physical Review Letters* **111**, 057204 \(2013\)](#).
- [212] G.-W. Chern, C. Reichhardt, and C. Nisoli, *Realizing three-dimensional artificial spin ice by stacking planar nano-arrays*, [*Applied Physics Letters* **104**, 013101 \(2014\)](#).
- [213] L. Anghinolfi, H. Luetkens, J. Perron, M. G. Flokstra, O. Sendetskyi, A. Suter, T. Prokscha, P. M. Derlet, S. L. Lee, and L. J. Heyderman, *Thermodynamic phase transitions in a frustrated magnetic metamaterial*, [*Nature Communications* **6**, 8278 \(2015\)](#).
- [214] S. Gliga, A. Kákay, R. Hertel, and O. G. Heinonen, *Spectral analysis of topological defects in an artificial spin-ice lattice*, [*Physical Review Letters* **110**, 117205 \(2013\)](#).
- [215] Y. Li, G. Gubbiotti, F. Casoli, F. J. T. Gonçalves, S. A. Morley, M. C. Rosamond, E. H. Linfield, C. H. Marrows, S. McVitie, and R. L. Stamps, *Brillouin light scattering study of magnetic-element normal modes in a square artificial spin ice geometry*, [*Journal of Physics D: Applied Physics* **50**, 015003 \(2016\)](#).
- [216] S. Krause, G. Herzog, T. Stapelfeldt, L. Berbil-Bautista, M. Bode, E. Y. Vedmedenko, and R. Wiesendanger, *Magnetization reversal of nanoscale islands: How size and shape affect the arrhenius prefactor*, [*Physical Review Letters* **103**, 127202 \(2009\)](#).
- [217] V. S. Bhat, F. Heimbach, I. Stasinopoulos, and D. Grundler, *Magnetization dynamics of topological defects and the spin solid in a Kagome artificial spin ice*, [*Physical Review B* **93**, 140401 \(2016\)](#).
- [218] D. M. Arroo, J. C. Gartside, and W. R. Branford, *Sculpting the spin-wave response of artificial spin ice via microstate selection*, [*Physical Review B* **100**, 214425 \(2019\)](#).
- [219] J.-P. Tetienne, T. Hingant, L. Rondin, A. Cavallès, L. Mayer, G. Dantelle, T. Gacoin, J. Wrachtrup, J.-F. Roch, and V. Jacques, *Spin relaxometry of single nitrogen-vacancy defects in diamond nanocrystals for magnetic noise sensing*, [*Physical Review B* **87**, 235436 \(2013\)](#).

- [220] H. Zhang, M. J. H. Ku, F. Casola, C. H. R. Du, T. van der Sar, M. C. Onbasli, C. A. Ross, Y. Tserkovnyak, A. Yacoby, and R. L. Walsworth, *Spin-torque oscillation in a magnetic insulator probed by a single-spin sensor*, [Physical Review B](#) **102**, 024404 (2020).
- [221] I. Panagiotopoulos, *Confined spin wave spectra of Kagome artificial spin ice arrays*, [Journal of Magnetism and Magnetic Materials](#) **422**, 227 (2017).
- [222] X. Zhou, G.-L. Chua, N. Singh, and A. O. Adeyeye, *Large area artificial spin ice and anti-spin ice $\text{Ni}_8\text{OFe}_2\text{O}$ structures: Static and dynamic behavior*, [Advanced Functional Materials](#) **26**, 1437 (2016).
- [223] J. A. Osborn, *Demagnetizing factors of the general ellipsoid*, [Physical Review](#) **67**, 351 (1945).
- [224] M. Dekker, *Chapter 2: Magnetic materials and their characteristics* (2004).
- [225] V. Kapaklis, U. B. Arnalds, A. Farhan, R. V. Chopdekar, A. Balan, A. Scholl, L. J. Heyderman, and B. Hjörvarsson, *Thermal fluctuations in artificial spin ice*, [Nature Nanotechnology](#) **9**, 514–519 (2014).
- [226] S. Mayr, L. Flajšman, S. Finizio, A. Hrabec, M. Weigand, J. Förster, H. Stoll, L. J. Heyderman, M. Urbánek, S. Wintz, and J. Raabe, *Spin-wave emission from vortex cores under static magnetic bias fields*, [Nano Letters](#) **21**, 1584 (2021).
- [227] Y. Tokura and N. Kanazawa, *Magnetic skyrmion materials*, [Chemical Reviews](#) (2020).
- [228] N. Nagaosa and Y. Tokura, *Topological properties and dynamics of magnetic skyrmions*, [Nature Nanotechnology](#) **8**, 899 (2013).
- [229] W. Jiang, X. Zhang, G. Yu, W. Zhang, X. Wang, M. Benjamin Jungfleisch, J. Pearson, X. Cheng, O. Heinonen, K. L. Wang, Y. Zhou, A. Hoffmann, and S. te Velthuis, *Direct observation of the skyrmion hall effect*, [Nature Physics](#) **13**, 162 (2016).
- [230] A. B. Bogatyřev and K. L. Metlov, *What makes magnetic skyrmions different from magnetic bubbles?*, [Journal of Magnetism and Magnetic Materials](#) **465**, 743–746 (2018).
- [231] N. Kanazawa, S. Seki, and Y. Tokura, *Noncentrosymmetric magnets hosting magnetic skyrmions*, [Advanced Materials](#) **29**, 1603227 (2017).
- [232] S.-G. Je, H.-S. Han, S. K. Kim, S. A. Montoya, W. Chao, I.-S. Hong, E. E. Fullerton, K.-S. Lee, K.-J. Lee, M.-Y. Im, and J.-I. Hong, *Direct demonstration of topological stability of magnetic skyrmions via topology manipulation*, [ACS Nano](#) **14**, 3251 (2020).
- [233] A. Fert, V. Cros, and J. Sampaio, *Skyrmions on the track*, [Nature Nanotechnology](#) **8**, 152 (2013).

-
- [234] T. Moriya, *Anisotropic superexchange interaction and weak ferromagnetism*, [*Physical Review* **120**, 91](#) (1960).
- [235] C. Moreau-Luchaire, C. Moutafis, N. Reyren, J. Sampaio, C. a. F. Vaz, N. Van Horne, K. Bouzehouane, K. Garcia, C. Deranlot, P. Warnicke, P. Wohlhüter, J.-M. George, M. Weigand, J. Raabe, V. Cros, and A. Fert, *Additive interfacial chiral interaction in multilayers for stabilization of small individual skyrmions at room temperature*, [*Nature Nanotechnology* **11**, 444–448](#) (2016).
- [236] A. Hrabec, N. A. Porter, A. Wells, M. J. Benitez, G. Burnell, S. McVitie, D. McGrouther, T. A. Moore, and C. H. Marrows, *Measuring and tailoring the Dzyaloshinskii-Moriya interaction in perpendicularly magnetized thin films*, [*Physical Review B* **90**, 020402\(R\)](#) (2014).
- [237] M. Baćani, M. A. Marioni, J. Schwenk, and H. J. Hug, *How to measure the local Dzyaloshinskii-Moriya interaction in skyrmion thin-film multilayers*, [*Scientific Reports* **9**, 3114](#) (2019).
- [238] A. S. Varentcova, S. von Malottki, M. N. Potkina, G. Kwiatkowski, S. Heinze, and P. F. Bessarab, *Toward room-temperature nanoscale skyrmions in ultrathin films*, [*npj Computational Materials* **6**, 1–11](#) (2020).

Acknowledgments

As any former doctoral student can tell you, a Ph.D. is an arduous journey. Luckily it is not one I had to take alone. I am absolutely indebted to all those who supported me along the way and who made my journey all the more enjoyable. While what follows is far from an exhaustive list of those who deserve thanks, I would like to take this time to express my gratitude to the many individuals who made a particularly large impact on my Ph.D.

Of course, none of this would have been possible without the support of my supervisor. Dear Patrick, thank you for giving me this opportunity and accepting me into the group. Through your guidance and optimism, I've been able to navigate the more frustrating parts of a Ph.D. and come out on the other side satisfied with what we've achieved. I am always amazed at the time and effort you put into the group, whether this be providing comments for papers and theses or proposing and guiding experiments. This is definitely a defining factor for the success of the group. Thank you also to my second supervisor, Martino. Your support over the last years has been greatly appreciated, and it's always great to know that you were there with advice if I needed it. To round out my committee, I am also very grateful that Toeno agreed to the position of external referee. Reading a 150-page thesis is a large commitment and should by no means be taken for granted. I have always enjoyed your valuable input on past projects when we were able to meet in person, be it in Montpellier or Lausanne.

To the entire Quantum Sensing group, past and present, I couldn't have done it without you! Whether it be assisting in experiments, letting me borrow devices, giving feedback, or simply listening, you have all helped keep me sane over the last four years. A particularly large thank you to all of those who also agreed to read through this monstrosity of a thesis! Also, to the inhabitants of 3.13, thank you for all the interesting conversations and entertaining distractions - I couldn't have asked for better office mates. I would also like to thank Beat, Mara, and Mark at this point, not only for your scientific and personal support but also for being such a great D&D team! You all made the experience so special and really helped me get through the challenging period of writing papers and preparing my thesis.

Of course, I have to mention the RT crew in particular. Dear Brendan, your constant support, patience, and willingness to listen to me let out steam are more than I could have hoped for. Whether it be how to align an AOM setup or how to make the best Feuerzangenbowle, you have been my go-to for advice for the last four years. I'm so glad that you haven't tired of sharing your experience! Outside the lab, having gotten to learn Baaseldütsch with you and work on the rooftop garden are experiences that have made this time so much more enjoyable. Kai, I know we haven't always seen eye to eye, but I am incredibly grateful for all of your support and expertise. The amount of time and effort you have put into the RT setup and measurements is by no means self-explanatory for a post-doc, and we really couldn't

have asked for a better person to push forward our experiments. Your knowledge and constant curiosity have really been a massive driving force in the last years. To Paul, though you haven't been in the team very long, I am absolutely confident that the setup is in good hands! I have no doubt that you'll do an amazing job. Last but not least, to Patrick (Pappel). You were the first to introduce me to the RT setup, and I am so grateful for all of your help in getting me introduced to the group and the experiments. I certainly wouldn't be where I am now without your support.

Thank you as well to everyone who has supplied me with samples over the years, as without you, this work would never have been possible. In particular, to our collaborators in Dresden – Denys Makarov, Denis Sheka, Oleksandr (Sasha) Pylypovskyi and Tobias Kosub. Thank you for all the discussions in the last year(s) and of course for providing us with all of these amazing Cr_2O_3 samples. A special thank you to Sasha for always responding so quickly and even taking time out of your weekends to answer my questions! All of your help and input is greatly appreciated. Though they will likely never read this, so much of this thesis has been supported by the hard work of the members of the electronics and mechanical workshops, so I would be remiss not to also thank them. They never cease to impress with their incredible competence and creativity.

Finally, I need to thank all of my family. Though they might be far away, they have supported me every step of the way, and I always know that they are my biggest fans. Nadja, thank you for agreeing to read through 150 pages of something you know very little about! And to Pady. I think you suffered the most during this process, having to listen to every complaint and frustration. Without your endless support, I would never have made it this far. I owe you so much.

Curriculum Vitae

Personal Details

Name	Natascha Hedrich
Date of Birth	5 of July 1991
Place of Birth	Uxbridge, Ontario, Canada
Email	natascha.hedrich@unibas.ch

Education

2016 – 2021	University of Basel, PhD in Experimental Physics PhD thesis in the group of Prof. P. Maletinsky <i>Exploring antiferromagnetic domain wall mechanics through scanning nitrogen vacancy magnetometry</i>
2014 – 2016	ETH Zurich, Master of Science in Physics Master thesis in the group of Prof. A. Imamoglu <i>Towards optomechanics with MoSe₂</i>
2014 – 2009	Thompson Rivers University, Bachelor of Science in Physics and Mathematics (Honors) Bachelor thesis with Prof. R. Taylor <i>Applications of the Remez algorithm to digital all-pass filters</i>

Publications

- [239] N. Hedrich, K. Wagner, P. V. Pylypovskiy, B. J. Shields, T. Kosub, D. D. Sheka, D. Makarov, P. Maletinsky *Nanoscale mechanics of antiferromagnetic domain walls*, [Nature Physics](#) **17**, 574-577 (2021)
- [240] N. Hedrich, D. Rohner, M. Batzer, P. Maletinsky, B. J. Shields *Parabolic diamond scanning probes for single-spin magnetic field imaging*, [Physical Review Applied](#) **14**, 064007 (2020)
- [241] P. Appel, B. J. Shields, T. Kosub, N. Hedrich, R. Hübner, J. Faßbender, D. Makarov, P. Maletinsky, *Nanomagnetism of magnetoelectric granular thin-film antiferromagnets*, [Nano Letters](#) **19**, 1682-1687 (2019)

July 19, 2021